

J. Schröder, D. Lupascu, D. Balzani  
(Editors)

**Proceedings of the First Seminar on  
The Mechanics of  
Multifunctional Materials**

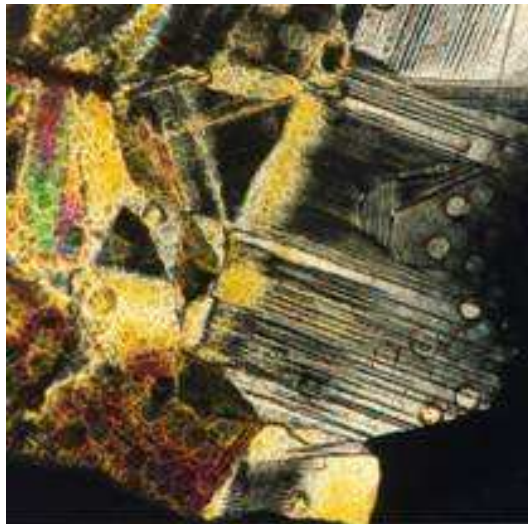


Universität Duisburg-Essen  
Ingenieurwissenschaften  
Abt. Bauwissenschaften  
Institut für Mechanik  
Prof. Dr.-Ing. J. Schröder

**Bericht Nr. 5**

**Proceedings**  
of the First Seminar on  
**THE MECHANICS OF  
MULTIFUNCTIONAL MATERIALS**

J. Schröder, D. Lupascu, D. Balzani (Eds.)



**Physikzentrum Bad Honnef**

**May 7 - 10, 2007**

Report No. 5  
Institute of Mechanics  
Faculty for Engineering Sciences  
Division Civil Engineering  
University of Duisburg-Essen

**Editors:**

Prof. Dr.-Ing. habil. Jörg Schröder  
University of Duisburg-Essen  
Faculty for Engineering Sciences  
Division Civil Engineering  
Institute of Mechanics  
D-45117 Essen

Prof. Dr. rer. nat. Doru C. Lupascu  
Dresden University of Technology  
Institute of Material Science  
D-01062 Dresden

Dr.-Ing. Daniel Balzani  
University of Duisburg-Essen  
Faculty for Engineering Sciences  
Division Civil Engineering  
Institute of Mechanics  
D-45117 Essen

© Prof. Dr.-Ing. habil. Jörg Schröder  
Institut für Mechanik  
Abteilung Bauwissenschaften  
Fakultät für Ingenieurwissenschaften  
Universität Duisburg-Essen  
Universitätsstraße 15  
45117 Essen

No part of this work may be reproduced, stored in a retrieval system or transmitted in any form or by any means, electronic, mechanical, photocopying, recording or otherwise, without prior written permission of the Publisher.

ISBN-10	3-9809679-1-3
ISBN-13	978-3-9809679-1-4
EAN	9783980967914

# Preface

Multifunctional materials establish innovative perspectives in automotive and aeronautical engineering, space technology, light weight construction, mechanical engineering, modern measurement and control technology, and many other applications. Therefore, industrial interest in the understanding, modeling and computer simulation of such materials has promoted the research activities in this field.

The scope of this seminar is to bring together scientists that are working on multifunctional materials encouraging interaction among both young and established researchers. We are glad to note that the seminar provides presentations from many fields of multifunctional materials such as phase transitions, magnetism, ferro- and piezoelectricity, shape memory alloys, and microheterogeneity. About 50 attendees participate in the Seminar at the Physikzentrum Bad Honnef which has been serving as the main meeting point of the German Physical Society since 1976. Located close to Germany's oldest nature preserve with beautiful views on the Rhine river the place offers the perfect platform for intensive discussions.

The Proceedings at hand provide extended abstracts of nearly 40 lecturers presenting at the Seminar. We thank all authors and participants for their cooperation and contribution to this workshop.

The Organizers

Jörg Schröder  
Doru Lupascu  
Daniel Balzani



## Contents

<i>T. Antretter, T. Waitz and F. D. Fischer</i>	
The Morphology of Martensite in Nano-Structured Ni-Ti Alloys . . . . .	1
<i>T. Bartel, K. Hackl</i>	
On the influence of phase-transformations on the experimental determination of micromechanical model-parameters . . . . .	5
<i>M. Böhl and S. Reese</i>	
Computational testing of shape memory polymer networks . . . . .	9
<i>M. Brünig</i>	
An anisotropic damage model for micro-heterogeneous materials . . . . .	13
<i>D. Christ and S. Reese</i>	
FE modelling of shape memory alloys in the framework of large strains . . . . .	17
<i>M. Enderlein, M. Kuna and A. Ricoeur</i>	
A micromechanical material model for ferroelectrics and its application to crack problems . . . . .	21
<i>F. Felten and G. A. Schneider</i>	
The electric permeability of cracks in PZT determined by Scanning Probe Force Microscopy . . . . .	26
<i>X. Feng, G. Fischer, H. A. Crostack and B. Svendsen</i>	
Experimental and theoretical investigation of Portevin-Le Châtelier deformation bands . . . . .	31
<i>R. Gärtner, M. Fleischer and R. Schmidt</i>	
3D Finite Element Model for calculation of effective Material properties . . . . .	35
<i>A. Haug, P. R. Onck, E. Van der Giessen</i>	
Development of Inter- and Intragranular Stresses during Switching of Ferroelectric Polycrystals . . . . .	39
<i>U. Hoppe and K. Hackl</i>	
Numerical simulation of microstructures in finite plasticity using relaxed energies . .	43
<i>S. Ilic and K. Hackl</i>	
Application of multiscale FEM to the simulation of heterogeneous materials . . . . .	47
<i>L. Jański, M. Kuna, A. Meyer, M. Scherzer and P. Steinhorst</i>	
Modellierung von Risswachstum in piezoelektrischen Materialien mittels moderner adaptiver FEM-Lösungsstrategien . . . . .	52
<i>H. Jelitto, F. Gehrig, G. A. Schneider, C. Häusler, P. Neumeister and H. Balke</i>	
Stable Crack Growth in Piezoelectric Ceramics and PZT/Electrode Interfaces . . . .	56
<i>M. Kamlah, B. Laskewitz and D. Zhou</i>	
Ferroelectric Ceramics: Basic Properties and Modeling Methods . . . . .	60
<i>S. Klinkel</i>	
A constitutive model for hysteresis effects in ferroelectric ceramics . . . . .	64

<i>D. M. Kochmann, W. J. Drugan and R. S. Lakes</i>	
Stability and Performance of Composite Materials Having a Negative-Stiffness Phase	69
<i>W. S. Kreher and A. Yu. Belov</i>	
Modeling linear properties and nonlinear response of ferroelectric/ferroelastic polycrystalline materials	73
<i>R. Lammering and A. Vishnevsky</i>	
Investigation of Local Strain and Temperature Behavior of Superelastic NiTi Wires	77
<i>S. Lentzen, R. Schmidt and D. Weichert</i>	
Geometrically, electrically and thermally nonlinear thermopiezomechanics	83
<i>K. Linnemann and S. Klinkel</i>	
A Nonlinear Constitutive Model for Magnetostrictive Materials	87
<i>D. C. Lupascu</i>	
Microstructural Parameters and Semiconductor Properties at the Origin of the Macroscopic Behavior of Ferroelectrics	91
<i>A. Menzel, A. Arockiarajan and S.M. Sivakumar</i>	
On the modelling of domain switching in ferroelastic materials	95
<i>R. Müller, D. Gross and D. Schrade</i>	
Simulation of domain structure evolution in ferroelectric materials	99
<i>P. Neumeister and H. Balke</i>	
3-d microscopic model for PZT-ceramics accounting for different crystallographic phases	103
<i>O. Papes</i>	
Investigation of large strains and fracture in single crystal silicon structures by means of a mixed atomistic - continuum mechanical approach	107
<i>J. Popp, V. Böhm, V. Naletova, I. Zeidis and K. Zimmermann</i>	
Locomotion systems based on magnetisable, highly elastic materials	118
<i>M. Richter and B. W. Zastrau</i>	
On the determination of the overall elastic material behaviour of textile reinforced concrete with micro- and macro-cracks using homogenisation	122
<i>D. Rosato and C. Miehe</i>	
An Incremental Variational Formulation for the Coupled Electromechanical Response of Piezoceramics	126
<i>J. Schröder, H. Romanowski and I. Kurzhofer</i>	
A computational meso-macro transition procedure for electro-mechanical coupled ceramics	127
<i>R. Steinhausen, C. Pientschke and H. Beige</i>	
Herstellung und Charakterisierung von piezoelektrischen Gradientenkeramiken	131
<i>I. Temizer and P. Wriggers</i>	
A Database Approach to Homogenization	135

<i>A. Ungethüm and R. Lammering</i>	
Simulation of temperature and stress induced phase transformation of shape memory alloys using cellular automaton and the finite element method . . . . .	139
<i>K. Weinberg</i>	
A theory for Kirkendall void growth in MEMS . . . . .	143
<i>C. Wellmann and P. Wriggers</i>	
Homogenization of granular materials modeled through a three-dimensional Discrete Element Model . . . . .	147
<i>K. Wippler and M. Kuna</i>	
Numerische und analytische dreidimensionale Fundamentallösungen für Piezoelektrika zur Anwendung in der BEM . . . . .	151
<i>D. Zhou, M. Kamlah, Z. Wang, B. Laskewitz and Y. Gan</i>	
Ferroelectric and Ferroelastic Properties of Piezoceramics: An Experimental Investigation . . . . .	156
<i>H.D. Alber and P. Zhu</i>	
Traveling wave solutions for phase field models for diffusionless phase transitions in ferroelectrics	
<i>E. Stein and G. Sagar</i>	
Theory and computation of a micro-macro monocrystalline model for martensitic phase transformation at finite strains	



# THE MORPHOLOGY OF MARTENSITE IN NANO-STRUCTURED NI-TI ALLOYS

Thomas Antretter<sup>1</sup>, Thomas Waitz<sup>2</sup> and Franz D. Fischer<sup>1</sup>

<sup>1</sup>Institute of Mechanics, Montanuniversität Leoben  
Franz-Josef Straße 18, A-8700 Leoben, Austria  
e-mail: antrette@unileoben.ac.at

<sup>2</sup> Institute of Materials Physics, University of Vienna  
Boltzmanngasse 5, A-1090 Vienna, Austria  
e-mail: waitz@ap.unvie.ac.at

**Abstract.** *Nano-structured NiTi instantaneously transforms from fcc austenite via an intermediate phase (the R-phase) into monoclinic B19' martensite. At a grain size less than a critical limit of about 50nm no transformation can be observed even upon cooling down to cryogenic temperatures. In slightly larger grains the martensite appears as a laminate of alternating twin-related Bain correspondence variants. For grain diameters in the order of 100nm it becomes more likely to observe two such martensite laminates whose arrangement relative to each other, as it appears in a micrograph, gives the impression of a "herring-bone pattern". This term has widely been adopted in the literature for this particular formation. This paper focuses on the prediction of the resulting morphology, which is determined by the energies involved, i.e. the chemical and mechanical contributions as well as interface energies. The elastic strain energy as well as the interface energies generated by the transformation eigenstrains of the newly created phases are evaluated. Various arrangements are calculated and compared with each other in terms of their impact on the total energy balance. Such an approach allows to determine an optimum configuration minimizing the total energy introduced into the system. The herring-bone morphology is also compared with the case of a single laminate as an alternative energy release mechanism. The parameters defining the geometry of the laminates such as the twin band thickness or the laminate width are computed and verified by means of high-resolution TEM images.*

## Introduction

NiTi alloys are the most important practically used shape memory alloys. In contrast to their conventional coarse-grained counterparts, bulk nanocrystalline NiTi alloys attract considerable attention as advanced functional material [1]. In nanograins of NiTi a unique path of atomic scale twinning is encountered [2]. A variety of martensite arrangements allows to accommodate the newly created phase in order to maximize the energy release triggered by the transformation. It is the objective of the present study to investigate the dependence of the martensitic morphology on the grain size of nanocrystalline NiTi alloys by numerical as well as experimental means using transmission electron microscopy (TEM). Martensitic phase transformations are characterized by the formation of multiple symmetry related variants of the martensite building complex microstructures on different length scales [3]. The eigenstrains that occur during

the transformation from the parent austenitic phase to the martensite of lower crystalline symmetry enforce arrangements of fine mixtures of compensating variants that minimize the free energy [4]. The twinned martensitic microstructure strongly depends on the crystallography of the transformation. Similarly, a small grain size of the parent phase can impose geometrical constraints that might significantly affect the martensitic morphology [5].

Fig. 1a and b show TEM bright field images of grains of different size (diameter of about 50 and 100 nm, respectively) that contain B19' martensite. Atomic scale twinning of the martensite leads to an ultrahigh density of the twins. The twins have equal volume fractions, and their average width is about 2 nm. Different martensitic morphologies are observed in grains of different size: In small enough grains frequently a single laminate of a twinned martensite sequence is encountered (see Fig. 1a). In grains in the order of 100 nm, a banded structure of two such laminates V1 and V2, separated by junction planes indicated by the dashed lines, is observed (see Fig. 1b). The angle between the twin boundary planes (i.e. the solid lines) is  $125^\circ$ . The width of the variant V2 is about 22% of the grain size (measured in a direction normal to the dashed lines).

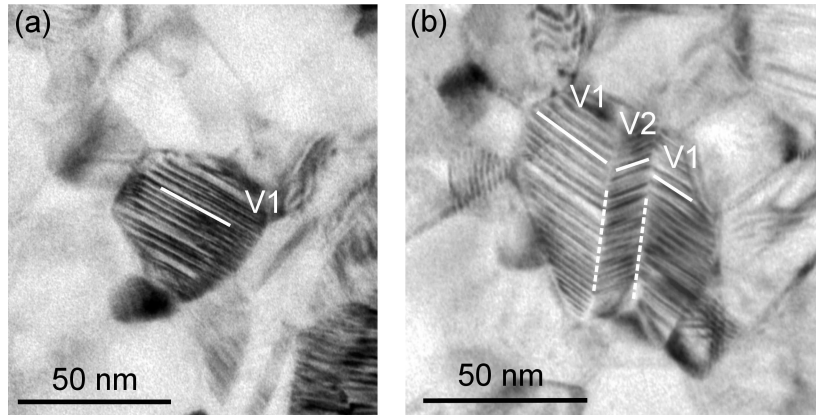


Figure 1: TEM micrographs of martensitic nanograins in NiTi. Atomic scale compound twins of B19' are indicated by solid white lines. (a) Single variant of twinned martensite. (b) Herringbone morphology of two variants V1 and V2 of twinned martensite (dashed lines indicate the junction planes of V1 and V2).

## Modeling and Results

For the time being a two-dimensional approach has been chosen in order to enable parametric studies in a cost-effective way. Fig. 2a shows the geometry of a circular grain embedded in a continuum of austenite that is assumed to remain untransformed. The model is characterized by the parameters  $\delta$  denoting the grain diameter, the width  $B$  of the central laminate and the twin band width  $d$ . Each laminate is composed of a series of alternating Bain correspondence variants (BCV) highlighted by different shades of gray in Fig. 2a. The junction plane between the two laminates as well as all twin planes between Bain variants, which are perpendicular to the projection plane appear as lines in this view. The current model comprises three sections of twin-related martensite laminates, the central one including an angle of  $125^\circ$  with its neighbors. The transformation eigenstrain components for each Bain variant can be calculated in a coordinate system aligned with the projection plane. As an example the eigenstrains for BCV1 are given here:  $\varepsilon_{T,11} = -0.039$ ,  $\varepsilon_{T,22} = 0.076$ ,  $\gamma_{T,12} = -0.105$ . Note that also out-of-plane contributions of the transformation strain tensor are expected which will add to the total strain

energy. The finite element mesh has been arranged in such a way that it already contains all the characteristic features of the transformed geometry, i.e. twin planes always coincide with element edges. This guarantees sharp interfaces and captures jumps in the stress distribution. 6-node triangular elements with quadratic shape functions have been chosen, suitable for resolving the stress singularities at the corners of the interface sufficiently well. The transforming grain is assumed to be embedded in an infinitely extended austenitic matrix. Realistically, the stress fields generated by the transformation will decay to zero far away from the boundary of the grain. It is thus admissible to place the grain in the center of a circular patch with a diameter of  $10\delta$  without having to cope with undesirable boundary effects at the perimeter of the finite element model. Relatively large elements can be used in the zones far away from the grain where no significant gradients have to be expected (see Fig. 2b). The transformation itself is simulated as anisotropic thermal expansion, the expansion coefficients thus representing the transformation eigenstrains calculated above.

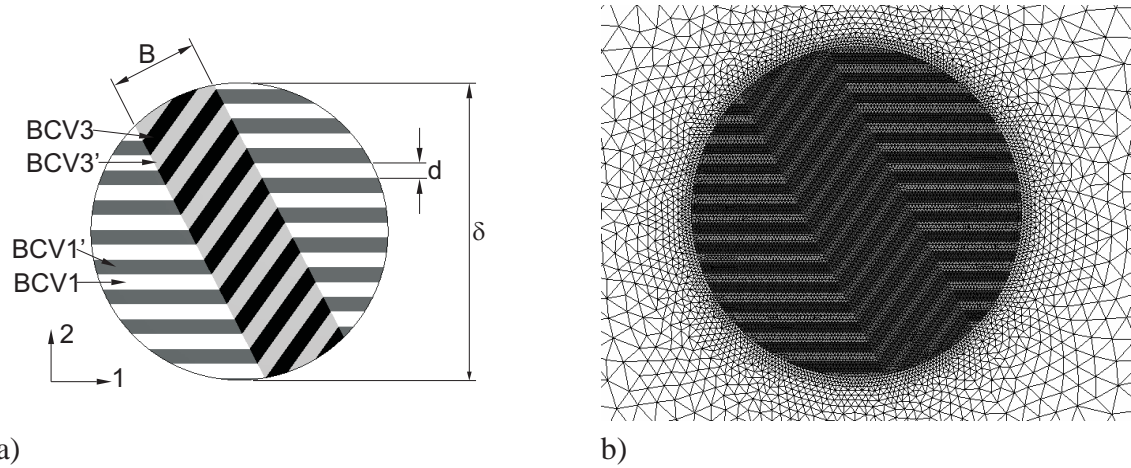


Figure 2: (a) Geometrical parameters describing the herring-bone pattern of a fully transformed grain. The surrounding austenitic matrix is not displayed. (b) Detail of the finite element mesh in and around the grain.

As a direct result of the numerical calculations the strain energy input into the material can be worked out. A total energy balance, however, also requires taking into account the chemical interface energies at the twin planes as well as the grain boundary and the phase boundary between the two different martensite laminates. These contributions have to be added to the strain energy in a subsequent postprocessing step. For the specific magnitudes of the chemical surface energies the reader is referred to [6]. Given the transformation strains of the martensite variants the total energy introduced by the phase change depends on two geometric parameters, i.e. the fraction of each laminate defined by  $B/\delta$  and the relative twin band width  $d/\delta$ . An automated preprocessing procedure enables to create finite element models for various combinations of these parameters. The resulting total energy  $E_b$  per grain volume as a function of  $B/\delta$  and  $d/\delta$  is shown in Fig. 3a for  $\delta = 50\text{nm}$  and Fig. 3b for  $\delta = 100\text{nm}$ . These cases are also compared with a single laminate of BCV1 and BCV1', where the central section disappears. For the case of the smaller grain the energy minimum is found for  $B/\delta = 0.3$  and  $d/\delta = 0.05$ , i.e.  $d = 2.5\text{nm}$ . This ratio  $d/\delta$  shifts to lower values as the grain grows while the absolute magnitude of  $d$  slowly increases. For  $d = 100\text{nm}$  the optimum twin-band width  $d$  is at about  $3.5\text{nm}$ . These values correspond well to the dimensions found in the micrographs depicted in Fig. 1. The energy consumption relative to the grain volume is higher in the case of the smaller grain making it more difficult for the grain to transform. For the case of  $\delta = 100\text{nm}$  shown in Fig. 3b the herring-bone morphology

consisting of three alternating laminates is energetically more favorable than its single-layered counterpart indicated by the dashed line with the white open markers. However, as the grain diameter tends to smaller values this energetic advantage disappears. Eventually, for small enough grains (e.g.  $\delta=50\text{nm}$ ) the single-layered pattern prevails.

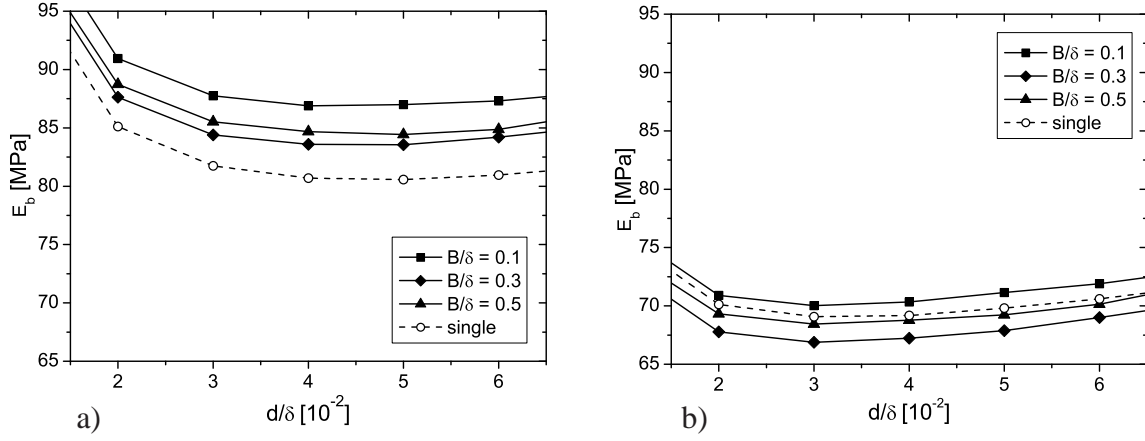


Figure 3: Total energy per grain volume as a function of the relative twin band width evaluated for (a)  $\delta=50\text{nm}$ , and (b)  $\delta=100\text{nm}$ .

## Conclusions

The morphology of a NiTi nanograin is to a large extent determined by the total energy minimum after martensitic transformation. In terms of this energy a herring-bone pattern of two martensite laminates is compared with the case of a single laminate. For the herring-bone microstructure the width  $B$  of the central section as well as the twin band-width  $d$  has then been quantified for a given grain diameter  $\delta$ . The calculated morphology expressed in terms of the ratios  $B/\delta$  and  $d/\delta$  is in good agreement with the experimental evidence.

## REFERENCES

- [1] T. Waitz, V. Kazyknanov and H.-P. Karnthaler, Martensitic phase transformations in nanocrystalline NiTi studied by TEM, *Acta Materialia* **52**, 137–147 (2004).
- [2] K.F. Hane and T.W. Shield, Microstructure in the cubic to monolitic transition in Titanium-Nickel shape memory alloys, *Acta Materialia* **47**, 2603–2617 (1999).
- [3] J.M. Ball and R.D. James, Fine phase mixtures as minimizers of energy, *Archive for Rational Mechanics and Analysis* **100**, 13–52 (1987).
- [4] K. Bhattacharya, *Microstructure of Martensite. Why it forms and how it gives rise to the shape-memory effect*, Oxford University Press, New York (2003).
- [5] F.D. Fischer, T. Schaden, F. Appel and H. Clemens, Mechanical twins, their development and growth, *European Journal of Mechanics* **A22**, 709–726 (2003).
- [6] T. Waitz, T. Antretter, F.D. Fischer, N.K. Simha and H.P. Karnthaler, Size effects on the martensitic phase transformation of NiTi nanograins, *J. Mech. Phys. Solids*, in print (2006).

# ON THE INFLUENCE OF PHASE-TRANSFORMATIONS ON THE EXPERIMENTAL DETERMINATION OF MICROMECHANICAL MODEL-PARAMETERS

T.Bartel<sup>1</sup>, K.Hackl<sup>1</sup>

<sup>1</sup>Institute of Mechanics, Ruhr-Universitaet Bochum, Universitaetsstr. 150, 44780 Bochum  
e-mail: Thorsten.Bartel@rub.de  
e-mail: Klaus.Hackl@rub.de

**Abstract.** *Our work aims at the analysis of phase-transformations within solid materials and their influence on the macroscopic material-behavior. Precisely, we study local phenomena showing up in experiments on shape-memory alloys and give explanations validated by global FE-computations. In this context, we determine the necessity to perform macroscopic computations in order to be able to fit microscopic model-parameters to experimental data. Moreover, the assembly of experiments itself may cause phase-transformations which highly affects the material-response of the subsequent test. The underlying material-model [1] is based on the specification of a microstructure which might be induced by external loads and thermal changes, respectively. It provides not only effective stresses but determines the development of different phase-variants along with their corresponding volume fraction as well. In the context of shape-memory alloys (SMA), pseudoelasticity and pseudoplasticity is captured for any type of transformation, e.g. cubic-tetragonal or cubic-monoclinic.*

## Micromechanical model

The micromechanical is based on the definition of energy-densities

$$\psi_I = \frac{1}{2} (\epsilon_I - \epsilon_I^t) : \mathbf{C}_I : (\epsilon_I - \epsilon_I^t) - C_I \quad (1)$$

for each phase-variant  $I$ , where  $\epsilon_I^t$  denotes so-called transformation-strains,  $\mathbf{C}_I$  represent different material tensors and  $C_I$  chemical energies depending on temperature  $T$ , heat capacity and latent heat.

Due to mathematical and physical reasons it is unavoidable to allocate different strain-states  $\epsilon_I$  to each present phase. Precisely, this procedure prevents the averaged energy-density on the microscale, namely

$$\psi = \sum_{I=0}^{NV} \theta_I \psi_I(\epsilon_I) \quad , \quad (2)$$

to become non-convex. Here, we tacitly introduced the volume fractions  $\theta_I$  of each phase as well as the total number of phases  $NV$ . Furthermore, the arrangement of different phases is subjected to physical patterns as depicted in Fig. 1. The same figure shows a specified, roof-like perturbation of the local, homogeneous displacement-field based on the chosen microstructure, which allows for a relaxation of the averaged energy-density. The perturbation-field consists

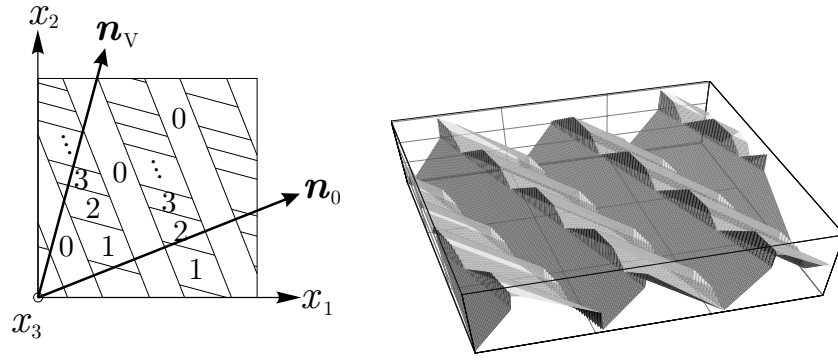


Figure 1: Specified microstructure, associated perturbation-field

of additional parameters  $\mathbf{u}_I$ , which are referred to as amplitudes of perturbation, and  $\mathbf{n}_0$  and  $\mathbf{n}_V$  as unit-vectors representing the alignment of the introduced laminates.

Based on this procedure, one exemplarily obtains

$$\boldsymbol{\varepsilon}_A = \boldsymbol{\varepsilon} + \frac{1}{\theta_A} \mathbf{n}_A \otimes_S \mathbf{u}_A \quad (3)$$

$$\boldsymbol{\varepsilon}_I = \boldsymbol{\varepsilon} - \frac{1}{\theta_M} \mathbf{n}_A \otimes_S \mathbf{u}_A + \frac{1}{\theta_I} \mathbf{n}_M \otimes_S (\mathbf{u}_I - \mathbf{u}_{I-1}) \quad (4)$$

with

$$\mathbf{a} \otimes_S \mathbf{b} := \frac{1}{2} (\mathbf{a} \otimes \mathbf{b} + \mathbf{b} \otimes \mathbf{a}) \quad (5)$$

as strain-measures within each phase-domain. In total, an amount of  $4NV + 6$  additional parameters

$$\mathcal{V} = (\theta_1, \theta_2, \dots, \theta_{NV}, \mathbf{u}_0, \mathbf{u}_1, \mathbf{u}_2, \dots, \mathbf{u}_{NV-1}, \mathbf{n}_0, \mathbf{n}_V) \quad (6)$$

has been introduced, which are now separated into *elastic* variables

$$\mathcal{V}_{el} = (\mathbf{u}_0, \mathbf{u}_1, \mathbf{u}_2, \dots, \mathbf{u}_{NV-1}) \quad (7)$$

and *dissipative* variables

$$\mathcal{V}_{diss} = (\theta_1, \theta_2, \dots, \theta_{NV}, \mathbf{n}_0, \mathbf{n}_V) \quad (8)$$

The minimization process

$$\psi_{rel}(\boldsymbol{\varepsilon}, \mathbf{p}) = \min \{ \psi; \mathcal{V}^{el} \} \quad (9)$$

yields the so-called relaxed energy density  $\psi_{rel}$ , which represents an approximation of the rank-one convex hull. A sophisticated analysis on upper and lower bounds of such energy-densities is included in [2].

The treatment of all inelastic variables  $\mathbf{p} = \mathcal{V}^{diss}$  is based on the definition of a so-called dissipation functional  $\Delta$ , which measures the amount of dissipated power caused by a change of  $p_i$ . Assuming the actual velocities  $\dot{p}_i$  to be minimizers of the total power  $\mathcal{L} = \dot{\psi}_{rel} + \Delta$  provides

$$\mathbf{0} \in \frac{\partial \mathcal{L}}{\partial \dot{\mathbf{p}}} \quad , \quad (10)$$

from which evolution-laws  $\dot{p}_i(\boldsymbol{\varepsilon}, T)$  can be derived. A comprehensive treatise on this matter can be found in [3].

## Numerical results

In this manner, material–point computations can be performed providing results as shown in Fig. 2 which represents the behavior of a material undergoing cubic–monoclinic transformations (e.g. NiTi) subjected to uniaxial tension.

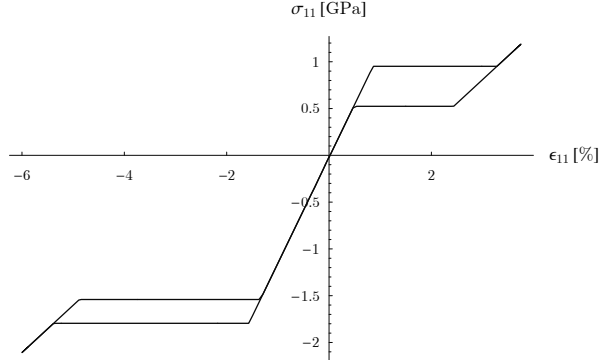


Figure 2: stress–strain diagram (cubic–monoclinic, uniaxial load)

Even though our model is based on physically well defined quantities and hardly contains any phenomenological approaches (see [4] for another example), one inevitably has to adapt certain quantities like the shape and size of the hysteresis to reality.

Usually, material–point computations are compared to experimental results obtained by tension–tests for example. Yet, Fig. 3 reveals a severe problem concerning this matter. Both experiments

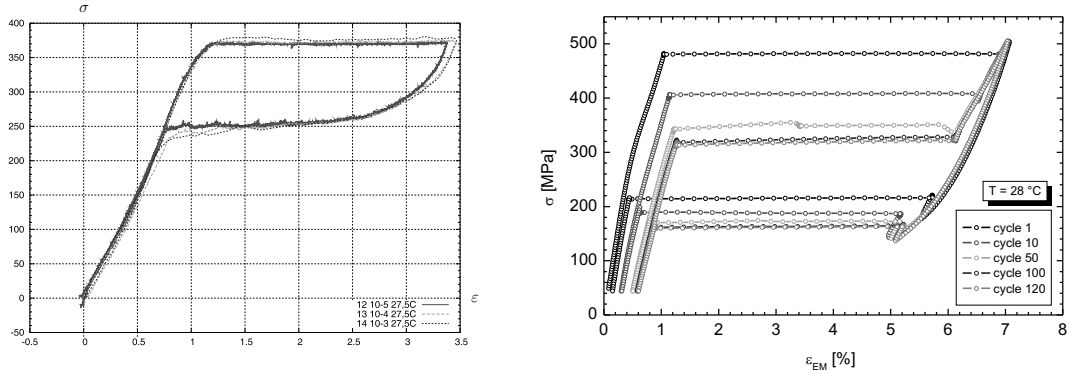


Figure 3: experimental results of tension tests (by courtesy of C. Grabe, J. Olbricht)

represent the local behavior of NiTi but provide completely different values regarding stress–plateaus and size and shape of the hysteresis. Obviously, phase–transformations do affect experiments in such a way that the determination of local material–parameters is much more difficult than one may expect. Furthermore it shows that material–point computations are not sufficient for the simulation of the local material response of such specimens.

## FE–simulations

In order to investigate the reasons for the difference of the material response in the aforementioned tests, the material model has been implemented into the FEM. We claim now that

there is just one way to fit parameters to the outcome of experiments sufficiently, namely to simulate the entire experiment. This also includes the simulation of the assembly, for example the clamping of the specimen. Fig. 4 provides a first hint on the influence of the assembly on the results of an experiment.

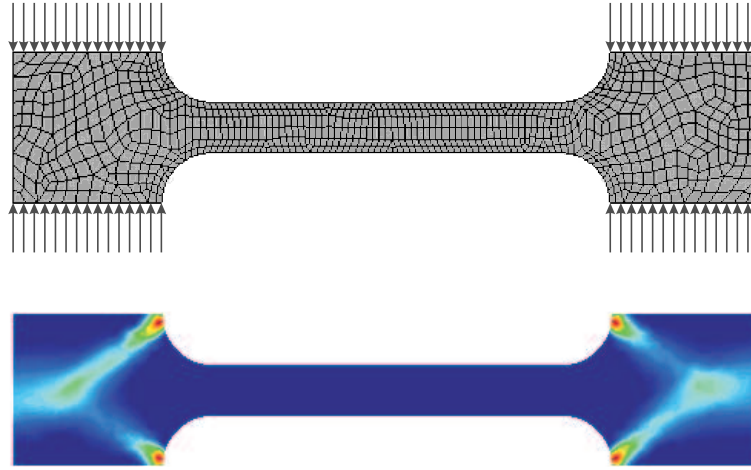


Figure 4: distribution of martensite-variant 1 due to clamping

## Conclusion

Our FE-analyses reveal that for instance the clamping of a specimen on the chuck jaws already causes phase-transformations, which presumably will have an effect on the following tension-test. In this context, also materials scientists hold such processes responsible for certain phenomena like "artificial" stress-drops. The most common feature is the initiation of phase-transformations in the regions where external loads are applied. In further process, the transformation-zones will spread from the ends to the center of the specimen, not vice versa as one may expect. Due to the fact that displacements are measured at the center the test may not be considered as significant anymore.

## REFERENCES

- [1] T. Bartel, K. Hackl, A Micromechanical Model for Martensitic Transformations in Single Crystals, submitted to J.Mech.Phys.Sol.
- [2] S. Govindjee, K. Hackl, R. Heinen, An upper bound to the free energy of mixing by twin-compatible lamination for  $n$ -variant martensitic phase-transformations, Continuum Mech. Thermodyn. **18**, 443–453 (2007)
- [3] A mathematical model for rate-independent phase-transformations with hysteresis. Proceedings of the Workshop on Models of Continuum Mechanics in Analysis and Engineering.
- [4] S. Stupkiewicz, H. Petryk, Modelling of laminated microstructures in stress-induced martensitic transformations, J.Mech.Phys.Sol. **50**, 2303–2331 (2002)

## COMPUTATIONAL TESTING OF SHAPE MEMORY POLYMER NETWORKS

M. Böl and S. Reese

Institute of Solid Mechanics  
e-mail: m.boel@tu-bs.de / s.reese@tu-bs.de

**Abstract.** *Shape memory properties provide a very attractive insight into materials science, opening unexplored horizons and giving access to unconventional functions in different materials like metals, ceramics and polymers. In this regard, the biomedical field, always in search of materials that display unconventional properties able to satisfy the severe specifications required by their implantation, is showing great interest in shape memory materials, especially in shape memory polymers (SMPs), whose mechanical properties make them extremely attractive for many biomedical applications. However, diverse characteristics as e.g. their biocompatibility, particularly for long-term applications, has not yet been fully established and is therefore the object of controversy. Also their mechanical behaviour is still part of research. The shape memory properties can be quantified by cyclic thermomechanical investigations. One cycle includes the "programming" of the sample and the recovery of its permanent shape. To describe the aforementioned phenomenon, in this paper a three-dimensional thermoviscoelastic model is proposed. The model is based on a physical understanding of the material behaviour and a mechanical interpretation of the stress-strain-temperature changes observed during thermomechanical loading. The main focus of this work is the influence of both, the material constants and heat transfer boundary conditions on the response of shape memory polymers. Therefore we illustrate different general simulations as well as some examples of application.*

### Introduction

Shape memory materials are defined by their capacity to recover strains by the application of external stimuli such as heat, magnetic fields or electric currents, see e.g. [1].

Diverse metallic, ceramic and polymeric materials exhibit the shape memory effect. The use of a particular shape memory material depends strongly on the desired recovery characteristics. Shape memory ceramics typically exhibit quick shape recovery over very small strain increments and large stress levels. Shape memory alloys show larger recoverable strain levels at moderate timescales and high stresses. Shape memory polymers in contrast possess the highest recoverable strain levels (several hundred percents) but the slowest activation times and the smallest stress levels, cp. [1-5].

Shape memory polymers are a special kind of polymers where the so-called glass transition is used to recover the original shape of a structure. This procedure is schematically shown in Figure 1. We start from the stress- and stretch-free state at the high temperature level  $\Theta_{\text{high}}$  (see point IV in Figure 1 (a)). The stent has its initial structure, see point IV, Figure 1 (b). Increasing the loading the stent shows the classical rubber-like material behaviour, i.e. large stretches can be obtained. At a certain point I one holds the loading fixed and begins to decrease

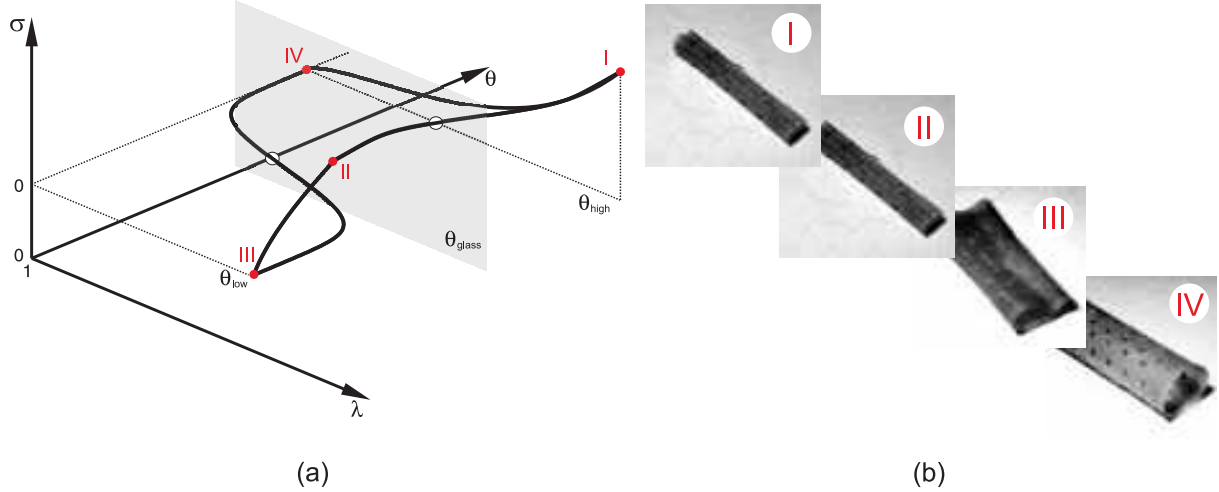


Figure 1: Material characteristics of shape memory polymers. (a)  $\sigma$ - $\lambda$ - $\Theta$  diagram of SMPs and (b) schematic of the shape memory effect in polymers as defined by four critical temperatures of a polymer stent.

the temperature. Near the glass transition temperature  $\Theta_{\text{glass}}$  the material behaviour begins to change. In particular, the deformation reached up to this point is frozen. The lowest temperature  $\Theta_{\text{low}}$  is reached at point II. At this point the loading is reduced until zero, see point III. However, the system is deformed if one compares with the initial state. If the temperature is kept at  $\Theta_{\text{low}}$  the stent maintain its deformed shape. Only if the temperature increases to  $\Theta_{\text{high}}$  the material "remembers" its initial shape and deforms back to this state, i.e. point IV.

### Macromechanical constitutive model

In order to model the described material behaviour constitutively we save at each temperature above  $\Theta_{\text{glass}}$  the deformation state. Therefore we split the Helmholtz energy in to parts. The first one ( $W_r(\mathbf{b}, \Theta)$ ) describes the rubber-like behaviour above  $\Theta_{\text{glass}}$ . Herein  $\mathbf{b} = \mathbf{F}\mathbf{F}^T$  is the classical left Cauchy Green tensor. Below the glass transition temperature the material behaves glassy-like, specified by second contribution  $W_g(\mathbf{b}_e, \Theta)$ . Here, the left Cauchy Green tensor  $\mathbf{b}_e = \mathbf{F}\mathbf{C}_f^{-1}\mathbf{F}^T$  is modified by  $\mathbf{C}_f^{-1}$ , the inverse right Cauchy Green tensor, including the "frozen" deformations.

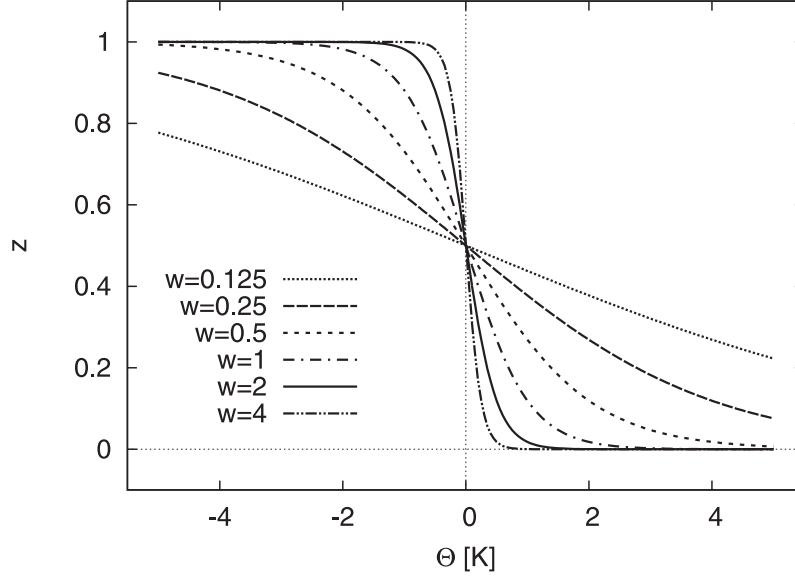
Both, from the physical as well as from the numerical point of view it is important to state that the glass transition does not happen abruptly. Quite the contrary, the transition process takes place in a certain temperature range. In order to take this into account we apply the complete Helmholtz energy as

$$W(\mathbf{b}, \mathbf{b}_e, \Theta) = (1 - z) W_r(\mathbf{b}, \Theta) + z W_g(\mathbf{b}_e, \Theta) \quad (1)$$

where  $z$  describes the glass transition by means of the formula

$$z = \frac{1}{2} \left( 1 - \frac{\exp(w \Delta\theta) - \exp(-w \Delta\theta)}{\exp(w \Delta\theta) + \exp(-w \Delta\theta)} \right) \quad (2)$$

In Equation (2)  $\Delta\theta = \theta - \theta_{\text{glass}}$  denotes the difference between the current temperature  $\Theta$  and the glass transition temperature  $\theta_{\text{glass}}$ . Furthermore  $w$  describes the transition width between the rubber-like and glassy-like state. The influence of this parameter is shown in Figure 2. It can be recognised that for lower values of  $w$  the transition is much more smoother than for higher ones.

Figure 2: Influence of the width parameter  $w$ 

### Finite element simulations

To study the shape memory effect we apply here a simple simulation of a cylindric tube, representing schematically a polymer stent. In Figure 3 (a) the loading conditions of the stent

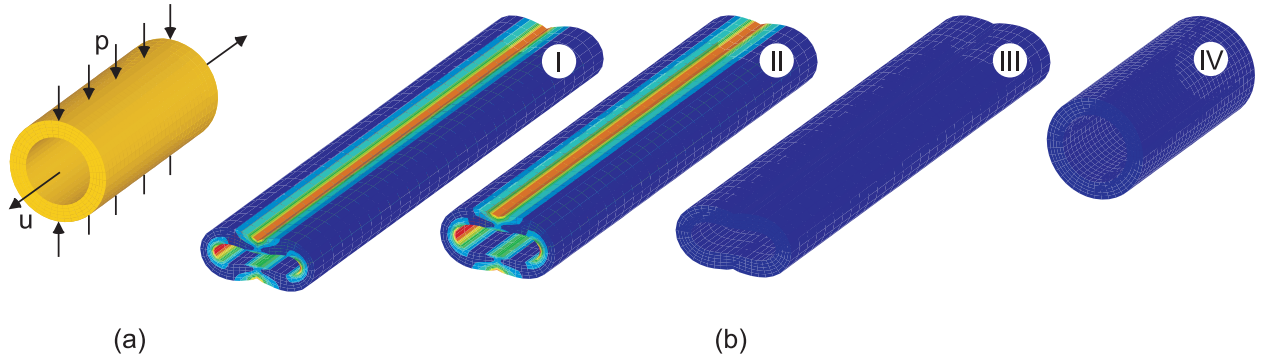


Figure 3: Themomechanical cycle, representing the shape memory effect: (a) System with loading conditions and (b) different deformation states during the load history.

are shown. It is loaded by a tension displacement  $u$  in combination with a compression load  $p$ . Further the system is loaded during the shape memory cycle by a thermal load  $\Theta$ . In Figure 3 (b)<sub>I–IV</sub> the results are shown. Analogue to Figure 1 we start in point IV, the undeformed state. Then the system is loaded by mechanical loads and fixed in point I. Next, the temperature is decreased until  $\Theta_{\text{low}}$  is reached in point II. During keeping the temperature constant at  $\Theta_{\text{low}}$  all loads are taken away from the stent, cp. point III. By increasing the temperature the material "remembers" its initial shape, i.e. point IV.

### Conclusions

In the present contribution we present a new approach for the modelling of shape memory polymers. The results show that the suggested method is a powerful tool to simulate the deformation behaviour of SMPs in various situations. In the future the concept should be further compared with experimental results.

## REFERENCES

- [1] K. Otsuka and C. M. Wayman, Shape Memory Materials. New York: Cambridge University Press, (1998).
- [2] A. Lendlein and S. Kelch, Shape-Memory Polymers, *Angewandte Chemie International Edition* **41**, 2034–2057 (2002).
- [3] A. Lendlein and R. Langer, Biodegradable, Elastic Shape Memory Polymers for Potential Biomedical Applications, *Science* **296**, 1673–1676 (2002).
- [4] Y. Liu, K. Gall, M. L. Dunn and P. McCluskey, Thermomechanical recovery couplings of shape memory polymers in flexure, *Smart Materials and Structures* **12**, 947–954 (2003).
- [5] A. Lendlein, A. M. Schmidt, M. Schroeter and R. Langer, Shape-Memory Polymer Networks from Oligo( $\epsilon$ -caprolactone) Dimethacrylates, *Journal of Polymer Sciences* **43**, 1369–1381 (2005).

## AN ANISOTROPIC DAMAGE MODEL FOR MICRO-HETEROGENEOUS MATERIALS

**Michael Brünig**

Lehrstuhl für Baumechanik-Statik, University of Dortmund  
D-44221 Dortmund, Germany  
e-mail: michael.bruenig@uni-dortmund.de

**Abstract.** *The paper deals with the modelling of temperature and rate-dependent behavior of anisotropically damaged micro-heterogeneous materials. Based on the concepts of continuum damage mechanics, a yield function as well as a separate damage criterion are presented and rate-dependent constitutive equations are discussed.*

### Introduction

In many engineering applications materials undergo progressive deterioration of their mechanical and functional properties under the action of various loading conditions both during the manufacturing process and in the working environment. On the microscale this damage process is the irreversible transformation of the microstructure via nucleation, propagation and coalescence of microdefects. Therefore, damage is intrinsically a multiscale problem where microdefects in a localized region have strong influence on the macroscale response of the solid. Modelling damage evolution and predicting macroscopic material properties is the objective of damage mechanics. In the present paper the macroscopic temperature and rate-dependent behavior of micro-heterogeneous materials is discussed using an anisotropic continuum damage approach taking into account a set of internal variables.

### Theoretical framework

The continuum damage mechanics approach is based on the introduction of damaged and corresponding fictitious undamaged configurations [1], [2]. The effective undamaged configurations are used to formulate the thermo-elastic-plastic constitutive equations of the undamaged matrix material. The effective specific Helmholtz free energy is additively decomposed into a thermo-elastic and a thermo-plastic part

$$\bar{\phi}(\mathbf{A}^{el}, \gamma, \Theta) = \bar{\phi}^{el}(\mathbf{A}^{el}, \Theta) + \bar{\phi}^{pl}(\gamma, \Theta) \quad (1)$$

where  $\mathbf{A}^{el}$  represents the elastic strain tensor,  $\gamma$  denotes a scalar plastic internal variable and  $\Theta$  is the absolute temperature. This leads to the definition of the effective Kirchhoff stress tensor

$$\bar{\mathbf{T}} = \rho_o \frac{\partial \bar{\phi}^{el}}{\partial \mathbf{A}^{el}} = 2G \mathbf{A}^{el} + \left(K - \frac{2}{3}G\right) \text{tr} \mathbf{A}^{el} \mathbf{1} - 3K \alpha_T (\Theta - \Theta_o) \mathbf{1} . \quad (2)$$

where  $\rho_o$  denotes the initial mass density,  $G$  and  $K$  represent the shear and bulk modulus of the material and  $\alpha_T$  is the coefficient of thermal expansion.

The rate-dependent plastic material behavior is assumed to be governed by the dynamic yield condition

$$f^{pl} = a \bar{I}_1 + \sqrt{\bar{J}_2} - c(\gamma, \dot{\gamma}, \Theta) = 0. \quad (3)$$

In Eq. (3)  $a$  represents the hydrostatic stress coefficient while  $\bar{I}_1 = \text{tr} \bar{\mathbf{T}}$  is the first invariant of the effective stress tensor (2) and  $\bar{J}_2 = \frac{1}{2} \text{dev} \bar{\mathbf{T}} \cdot \text{dev} \bar{\mathbf{T}}$  denotes the second invariant of its deviator. In addition,  $c(\gamma, \dot{\gamma}, \Theta)$  represents the rate- and temperature-dependent equivalent stress measure.

In the present analysis, the equivalent stress is expressed as a specific function of equivalent plastic strain, equivalent plastic strain rate and temperature using the multiplicative decomposition [3]

$$c(\gamma, \dot{\gamma}, \Theta) = \tilde{c}(\gamma) f_1(\dot{\gamma}) f_2(\Theta) \quad (4)$$

In Eq. (4) the reference equivalent effective stress can numerically be simulated by the power law

$$\tilde{c}(\gamma) = \tilde{c}_o \left( \frac{H_o \gamma}{n \tilde{c}_o} + 1 \right)^n \quad (5)$$

where  $\tilde{c}_o$  represents the initial yield stress,  $H_o$  denotes the initial hardening modulus and  $n$  means the hardening exponent. It is determined using quasistatic tests at constant reference temperature  $\Theta_o$ . The experimentally observed increasing dependence of the equivalent stress on the equivalent plastic strain rate  $\dot{\gamma}$  is described by the strain rate hardening function

$$f_1(\dot{\gamma}) = 1 + d \left( \frac{\dot{\gamma} - \dot{\gamma}_o}{\dot{\gamma}_o} \right)^m \quad (6)$$

where  $d$  and  $m$  are constitutive parameters which can be obtained from a series of dynamic experiments at different strain rates and constant temperature and the reference inelastic strain rate  $\dot{\gamma}_o$  is given by the quasistatic reference test. In addition, the decrease in equivalent stress with increasing temperature is taken into account by the thermal softening function

$$f_2(\Theta) = 1 - b \left( \frac{\Theta - \Theta_o}{\Theta_m} \right)^q. \quad (7)$$

In Eq. (7)  $b$  and  $q$  are constitutive parameters which can be determined from a series of isothermal tests at different constant temperatures  $\Theta$  and very low strain rates (quasistatic experiments) and  $\Theta_m$  denotes the melting temperature.

Moreover, to be able to compute plastic strain rates the plastic potential function

$$g^{pl}(\bar{\mathbf{T}}, \gamma, \Theta) = \sqrt{\bar{J}_2} - c_o(\gamma, \Theta) \quad (8)$$

is introduced which takes into account the temperature-dependent scalar effective stress measure

$$c_o(\gamma, \Theta) = \tilde{c}(\gamma) f_2(\Theta). \quad (9)$$

This leads to the isochoric plastic strain rate

$$\dot{\mathbf{H}}^{pl} = \dot{\lambda} \frac{\partial g^{pl}}{\partial \bar{\mathbf{T}}} = \dot{\gamma} \bar{\mathbf{N}} \quad (10)$$

where  $\dot{\lambda}$  is a non-negative scalar-valued factor,  $\bar{\mathbf{N}} = \frac{1}{\sqrt{2 \bar{J}_2}} \text{dev} \bar{\mathbf{T}}$  represents the normalized deviatoric strain direction and the internal variable  $\dot{\gamma} = \frac{1}{\sqrt{2}} \dot{\lambda}$  denotes the equivalent plastic strain rate.

The anisotropically damaged configurations are considered to formulate the inelastic constitutive equations of the damaged aggregate. In particular, the specific Helmholtz free energy of the damaged material sample is additively decomposed into three parts:

$$\phi(\mathbf{A}^{el}, \mathbf{A}^{da}, \gamma, \mu, \Theta) = \phi^{el}(\mathbf{A}^{el}, \mathbf{A}^{da}, \Theta) + \phi^{pl}(\gamma, \Theta) + \phi^{da}(\mu, \Theta). \quad (11)$$

The thermoelastic part of the free energy of the damaged material  $\phi^{el}$  is expressed in terms of the elastic and damage strain tensors,  $\mathbf{A}^{el}$  and  $\mathbf{A}^{da}$ , whereas the thermo-plastic part,  $\phi^{pl}$  due to plastic hardening, and the thermo-damaged part,  $\phi^{da}$  due to damage strengthening, take into account the respective internal effective plastic and damage state variables,  $\gamma$  and  $\mu$ . This leads to the definition of the Kirchhoff stress tensor

$$\mathbf{T} = \rho_o \frac{\partial \phi^{el}}{\partial \mathbf{A}^{el}} = 2(G + \eta_2 \text{tr} \mathbf{A}^{da}) \mathbf{A}^{el} + [(K - \frac{2}{3}G + 2\eta_1 \text{tr} \mathbf{A}^{da}) \text{tr} \mathbf{A}^{el} + \eta_3 (\mathbf{A}^{da} \cdot \mathbf{A}^{el})] \mathbf{1} \\ + \eta_3 \text{tr} \mathbf{A}^{el} \mathbf{A}^{da} + \eta_4 (\mathbf{A}^{el} \mathbf{A}^{da} + \mathbf{A}^{da} \mathbf{A}^{el}) - 3 K \alpha_T (\Theta - \Theta_o) \mathbf{1} \quad (12)$$

where  $\eta_1, \dots, \eta_4$  are material constants which describe the deterioration of the elastic properties by the occurrence of damage [4].

The rate-dependent damage material behavior is assumed to be governed by the dynamic damage condition

$$f^{da}(\tilde{\mathbf{T}}, \sigma) = I_1 + \tilde{\beta} \sqrt{\tilde{J}_2} - \sigma(\mu, \dot{\mu}, \Theta) = 0 \quad (13)$$

which is a function of the first stress invariant,  $I_1 = \text{tr} \mathbf{T}$  and of the anisotropic stress measure  $\tilde{J}_2 = \frac{1}{2} \text{dev} \tilde{\mathbf{T}} \cdot \mathcal{P} \text{dev} \tilde{\mathbf{T}}$  where the anisotropic nature of the problem is characterized by the directional dependence of the projection tensor  $\mathcal{P}$ .

The equivalent stress is expressed as a specific function of damage accumulation, rate of damage accumulation and temperature using the multiplicative decomposition [3]

$$\sigma(\mu, \dot{\mu}, \Theta) = \tilde{\sigma}(\mu) f_3(\dot{\mu}) f_2(\Theta). \quad (14)$$

In Eq. (14) the reference stress is numerically simulated by the linear relations

$$\tilde{\sigma}(\mu) = \sigma_o + H_1^{da} \mu \quad \text{if } 0 \leq \mu < f_c \quad (\text{isotropic damage}) \quad (15)$$

or

$$\tilde{\sigma}(\mu) = \sigma_o + H_1^{da} f_c + H_2^{da} (\mu - f_c) \quad \text{if } \mu \geq f_c \quad (\text{anisotropic damage}) \quad (16)$$

where  $\sigma_o$  represents the initial damage strength,  $H_1^{da}$  and  $H_2^{da}$  denote the respective damage softening moduli and  $f_c$  means the critical void volume fraction characterizing the onset of anisotropic damage by predominant void coalescence leading to microcracks. The equivalent stress is determined using quasistatic tests at constant reference temperature  $\Theta_o$ . The experimentally observed increasing dependence of the equivalent stress on the equivalent damage strain rate  $\dot{\mu}$  is described by the damage rate hardening function

$$f_3(\dot{\mu}) = 1 + h \left( \frac{\dot{\mu} - \dot{\mu}_o}{\dot{\mu}_o} \right)^r. \quad (17)$$

In Eq. (17)  $h$  and  $r$  are constitutive parameters which can be obtained from a series of dynamic experiments at different damage rates and constant temperature and the reference damage rate

$\dot{\mu}_o$  is given by the quasistatic reference test. Furthermore, to be able to compute damage strain rates, the damage potential function

$$g^{da}(\tilde{\mathbf{T}}, \mu, \Theta) = \alpha I_1 + \beta \sqrt{\tilde{J}_2} - g_o(\mu, \Theta) \quad (18)$$

is also formulated in the terms of stress invariants and  $g_o(\mu, \Theta)$  represents a temperature dependent scalar stress measure. In Eq. (18)  $\alpha$  and  $\beta$  denote kinematically based damage parameters [2]. This leads to the nonassociated damage rule

$$\dot{\mathbf{H}}^{da} = \dot{\mu} \frac{\partial g^{da}}{\partial \tilde{\mathbf{T}}} = \dot{\mu} \alpha \mathbf{1} + \dot{\mu} \beta \frac{1}{2\sqrt{\tilde{J}_2}} \mathcal{P} \operatorname{dev} \tilde{\mathbf{T}}. \quad (19)$$

The first term in the right hand part in Eq. (19) represents the rate of inelastic volumetric deformations caused by the isotropic growth of microvoids whereas the second term models the anisotropic evolution of damage strain rates which takes into account the significant dependence of the evolution of size, shape and orientation of microcracks and micro-shearbands on the direction of the current stress state.

## Conclusion

A general framework for the modelling of temperature and rate-dependent deformation processes of anisotropically damaged elastic-plastic materials has been presented. This continuum damage mechanics approach may be used in numerical simulations of progressive deterioration of multifunctional properties of micro-heterogeneous materials.

## REFERENCES

- [1] G.Z. Voyiadjis, T. Park, The kinematics of damage for finite strain elastic-plastic solids, *Int. J. Eng. Sci.* **37**, 803–830 (1999).
- [2] M. Brünig, An anisotropic ductile damage model based on irreversible thermodynamics, *Int. J. Plasticity* **19**, 1679–1713 (2003).
- [3] M. Brünig, Continuum framework for the rate-dependent behavior of anisotropically damaged ductile metals, *Acta Mechanica* **186**, 37–53 (2006).
- [4] K. Hayakawa, S. Murakami, Y. Liu, An irreversible thermodynamics theory for elastic-plastic-damage materials, *Eur. J. Mech., A/Solids* **17**, 13–32 (1998).

## FE MODELLING OF SHAPE MEMORY ALLOYS IN THE FRAMEWORK OF LARGE STRAINS

Daniel Christ<sup>1</sup>, Stefanie Reese<sup>1</sup>

<sup>1</sup>Institute of Solid Mechanics, Braunschweig University of Technology, D-38106 Braunschweig, Germany  
e-mail: d.christ@tu-bs.de / s.reese@tu-bs.de

**Abstract.** *In this contribution we present a finite deformation material model for shape memory alloys. In the current state the model is able to describe the effect of pseudoelasticity and pseudoplasticity. At the end of the paper a finite element simulation of a NiTi stent is carried out.*

### Introduction

Shape memory alloys (SMA) can undergo diffusionless and reversible phase transformations between a higher-ordered austenite phase and a lower-ordered martensite phase as a result of changes in temperature and/or the state of stress. Consequently, SMA exhibits several macroscopic phenomena not present in traditional materials (e.g. pseudoelasticity and the shape memory effect). These unique features of SMA have found numerous applications in industrial and medical technologies. The increasing use in commercially valuable applications has motivated a vivid interest in the development of accurate constitutive models to describe the behaviour of SMA. Meanwhile, a large number of material models has been developed to describe the complex behaviour of SMA, particularly the effect of pseudoelasticity. These models follow three different approaches depending on whether a formulation at the micro, the meso or the macro scale is used. The micro level models are generally based on the description of micro scale effects such as nucleation, interface motion or twin growth. They consider phase volume fraction as a consequence of interface movements (e.g. [1, 2]). The meso level models combine micro mechanical aspects (such as habit planes, martensite variants, etc.) and macro scale thermodynamics. The constitutive equations are defined at the micro scale. The response on the macro level is obtained due to the use of proper homogenization techniques (e.g. [3, 4]). The macro level models deal with macroscopic quantities, which lead to a description of the global mechanical behaviour [5, 6, 7]. One of the advantages of the latter type of models is their convenient implementation into a FE code. Therefore they are widely used in structural engineering applications. Although a lot of these material models have been implemented into the finite element method, only a few of them are derived in the framework of finite deformation [8, 9, 10]. The goal of this work is to propose a three-dimensional material model which is able to reproduce the pseudoelastic behaviour within the large strain regime.

### Continuum mechanical model

At the continuum mechanical level we introduce the deformation gradient

$$\mathbf{F} := \mathbf{F}_e \mathbf{F}_t \Rightarrow \mathbf{F}_e = \mathbf{F} \mathbf{F}_t^{-1} \quad (1)$$

and its decomposition into an elastic part  $\mathbf{F}_e$  and a "transformation" part  $\mathbf{F}_t$  which describes the phase transformation from austenite to martensite. This multiplicative split of the deformation gradient  $\mathbf{F}$  is known from crystal plasticity (e.g. [11]). In the same manner we decompose the transition part  $\mathbf{F}_t$  according to

$$\mathbf{F}_t := \mathbf{F}_{t_e} \mathbf{F}_{t_d} \Rightarrow \mathbf{F}_{t_e} = \mathbf{F}_t \mathbf{F}_{t_d}^{-1} \quad (2)$$

where  $\mathbf{F}_{t_e}$  is used to model the energy storage and the second term  $\mathbf{F}_{t_d}$  expresses in conjunction with the Helmholtz free energy the physical dissipation during the phase transformation. The Helmholtz free energy is defined as

$$\Psi = \Psi_e(\mathbf{C}_e, z) + \Psi_t(\mathbf{C}_{t_e}). \quad (3)$$

The first term  $\Psi_e$  includes the energy storage in the material at elastic deformations due to mechanical loading and  $\Psi_t$  represents the energy storage during the phase transition. Exploiting the principle of material objectivity the Helmholtz free energy depends only on the "elastic" right Cauchy-Green tensors

$$\mathbf{C}_e = \mathbf{F}_e^T \mathbf{F}_e = \mathbf{F}_t^{-T} \mathbf{C} \mathbf{F}_t^{-1}, \quad (4)$$

$$\mathbf{C}_{t_e} = \mathbf{F}_{t_e}^T \mathbf{F}_{t_e} = \mathbf{F}_{t_d}^{-T} \mathbf{C}_t \mathbf{F}_{t_d}^{-1}. \quad (5)$$

Due to the use of the martensitic volume fraction  $z$  it is considered that two different phases coexist during the phase transition.  $z$  has always a value between 0 and 1 whereby  $z = 0$  denotes pure austenite and  $z = 1$  pure martensite. Certainly the material behaviour of shape memory alloys is strongly temperature dependent so that in general the temperature should be considered as an additional independent variable. However, in the present contribution we focus mainly on the effect of pseudoelasticity which may be displayed under approximately isothermal conditions. Therefore we choose to treat the temperature as a constant. Assuming isothermal conditions the Clausius-Duhem form of the entropy inequality takes the form  $\mathbf{S} \cdot \frac{1}{2} \dot{\mathbf{C}} - \dot{\Psi} \geq 0$  where  $\mathbf{S}$  denotes the second Piola-Kirchhoff stress tensor. We insert (3) into the inequality and obtain the form

$$\mathbf{S} \cdot \frac{1}{2} \dot{\mathbf{C}} - \frac{\partial \Psi_e}{\partial \mathbf{C}_e} \cdot \dot{\mathbf{C}}_e - \frac{\partial \Psi_e}{\partial z} \dot{z} - \frac{\partial \Psi_t}{\partial \mathbf{C}_{t_e}} \cdot \dot{\mathbf{C}}_{t_e} \geq 0. \quad (6)$$

In analogy to former publications [5, 7] the martensitic volume fraction  $z$  can be expressed in terms of the Green-Lagrange strain  $\mathbf{E}_t := \frac{1}{2}(\mathbf{C}_t - \mathbf{1})$ :

$$z := \omega_\gamma ||\mathbf{E}_t|| \quad (7)$$

Here,  $\omega_\gamma$  is a material parameter which describes the length of the stress-strain hysteresis. The material time derivative of  $z$  is then computed by means of the relation

$$\dot{z} = \omega_\gamma \frac{\mathbf{E}_t}{||\mathbf{E}_t||} \cdot \frac{1}{2} \dot{\mathbf{C}}_t = \omega_\gamma \left( \mathbf{F}_t \frac{\mathbf{E}_t}{||\mathbf{E}_t||} \mathbf{F}_t^T \right) \cdot \mathbf{d}_t \quad (8)$$

where the deformation rate tensor  $\mathbf{d}_t$  is defined by  $\mathbf{d}_t := \frac{1}{2} \mathbf{F}_t^{-T} \dot{\mathbf{C}}_t \mathbf{F}_t^{-1}$ . We further rewrite the deformation rates  $\dot{\mathbf{C}}_e$  and  $\dot{\mathbf{C}}_{t_e}$  in the format

$$\dot{\mathbf{C}}_e = -\mathbf{l}_t^T \mathbf{C}_e + \mathbf{F}_t^{-T} \dot{\mathbf{C}} \mathbf{F}_t^{-1} - \mathbf{C}_e \mathbf{l}_t, \quad (9)$$

$$\dot{\mathbf{C}}_{t_e} = -\mathbf{l}_{t_d}^T \mathbf{C}_{t_e} + \mathbf{F}_{t_d}^{-T} \dot{\mathbf{C}}_t \mathbf{F}_{t_d}^{-1} - \mathbf{C}_{t_e} \mathbf{l}_{t_d}. \quad (10)$$

In this context the definitions  $\mathbf{l}_t := \dot{\mathbf{F}}_t \mathbf{F}_t^{-1}$  and  $\mathbf{l}_{td} := \dot{\mathbf{F}}_{td} \mathbf{F}_{td}^{-1}$  have been used. For the next step we assume that  $\Psi_e$  and  $\Psi_t$  are isotropic functions of  $\mathbf{C}_e$  and  $\mathbf{C}_{te}$ , respectively. One consequence of this specialisation is the coaxiality of  $\mathbf{C}_e$  and  $\partial\Psi_e/\partial\mathbf{C}_e$  as well as of  $\mathbf{C}_{te}$  and  $\partial\Psi_t/\partial\mathbf{C}_{te}$ . After the application of several rules from tensor calculus and the exploitation of the symmetry of  $\partial\Psi_e/\partial\mathbf{C}_e$  and  $\partial\Psi_t/\partial\mathbf{C}_{te}$  the Clausius-Duhem inequality (6) is transformed into the relation

$$\left( \mathbf{S} - 2 \mathbf{F}_t^{-1} \frac{\partial\Psi_e}{\partial\mathbf{C}_e} \mathbf{F}_t^{-T} \right) \cdot \frac{1}{2} \dot{\mathbf{C}} + (\mathbf{M} - \mathbf{X}) \cdot \mathbf{d}_t + \mathbf{M}_t \cdot \mathbf{d}_{td} \geq 0 \quad (11)$$

The introduced material parameter  $\Delta\Psi$  considers the difference of the internal energy and the entropy between the austenitic and the martensitic phase [7]. Due to the coaxiality also the Mandel stress tensors  $\mathbf{M} := 2 \mathbf{C}_e (\partial\Psi_e/\partial\mathbf{C}_e)$  and  $\mathbf{M}_t := 2 \mathbf{C}_{te} (\partial\Psi_t/\partial\mathbf{C}_{te})$  are symmetric.  $\mathbf{X} := 2 \mathbf{F}_{te} (\partial\Psi_t/\partial\mathbf{C}_{te}) \mathbf{F}_{te}^T + \omega_\gamma \Delta\Psi \mathbf{F}_t (\mathbf{E}_t / \|\mathbf{E}_t\|) \mathbf{F}_t^T$  is the so-called back stress tensor. The final form of the Clausius-Duhem inequality is sufficiently satisfied by the relation

$$\mathbf{S} = 2 \mathbf{F}_t^{-1} \frac{\partial\Psi_e}{\partial\mathbf{C}_e} \mathbf{F}_t^{-T} \quad (12)$$

for the second Piola-Kirchhoff stress tensor  $\mathbf{S}$  and the evolution equations

$$\mathbf{d}_t = \dot{\lambda} \frac{\mathbf{M}^D - \mathbf{X}^D}{\|\mathbf{M}^D - \mathbf{X}^D\|} = \frac{\partial\Phi_{\text{SMA}}}{\partial\mathbf{M}}, \quad (13)$$

$$\mathbf{d}_{td} = \dot{\lambda} \frac{b}{\mu_t} \mathbf{M}_t^D. \quad (14)$$

The phase transition function  $\Phi_{\text{SMA}}$  is given in the continuum mechanical context via

$$\Phi_{\text{SMA}} = \|\mathbf{M}^D - \mathbf{X}^D\| - \sqrt{\frac{2}{3}} k. \quad (15)$$

$k$  is a further material parameter which describes the half height of the stress-strain hysteresis. Further on the Kuhn-Tucker conditions  $\dot{\lambda} \geq 0$ ,  $\Phi_{\text{SMA}} \leq 0$  and  $\dot{\lambda} \Phi_{\text{SMA}} = 0$  have to be fulfilled. The numerical implementation of the derived material model into a FE code is very challenging and comprehensive. On this account we refer to [12] wherein the derivation of the implementation is presented in detail.

## Numerical results

In this chapter we present a finite element simulation of a medical stent. The geometry and discretisation of the stent are given by the white structure in Fig. 1. The stent is stretched at the tip. The end of the joints at the opposite side of the tip are fixed in longitudinal direction but can move in radial direction. Additionally, a radial displacement is applied on the outer surface of the stent by an analytical function. Due to the function the "bottom" of the stent is fixed in radial direction and the ends on the top overlap. The deformed stent is plotted within the initial geometry in Fig. 1 which well illustrates the large deformation of the stent at the end of the loading. Additionally, it shows the distribution of the phase transformation  $z$  in the stent structure. Although the radius of the stent decreases to a tenth of its initial value the end of the phase transformation ( $z = 1$ ) is still not reached. It is obvious that the deformation of the stent is very large and a simulation of the stent with a model derived in the framework of small strains leads to erroneous results. Using the large deformation model this problem is overcome. Certainly the numerical effort is higher. However, the additional cost is in no proportion to the cost caused by a denied or only delayed admittance.

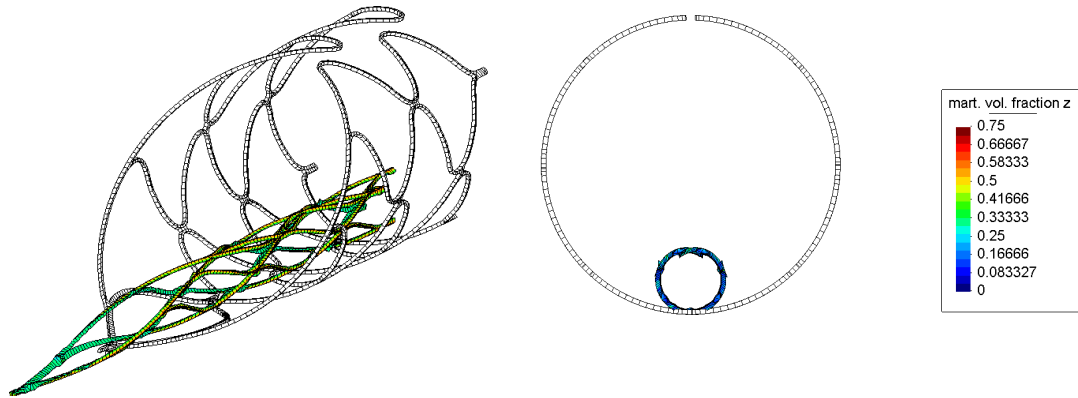


Figure 1: Stent geometry in the initial (white) and the deformed (coloured) state and the distribution of the martensitic volume fraction at the end of loading

## REFERENCES

- [1] F. Falk, *Int J Eng Sci* 27 (1998) 277-284
- [2] J. Ball and R. James, *Phil Trans Phys Sci Eng* 338 (1992) 389-450
- [3] C. Lexcellent and B. C. Goo and Q. P. Sun and J. Bernadini, *Acta Mater* 44 (1996) 3773-3780
- [4] G. J. Hall and S. Govindjee, *J Mech Phys Solid* 50 (2002) 501-530
- [5] B. Raniecki and C. Lexcellent, *Eur J Mech Solid* 13 (1994) 21-50
- [6] A. Souza and E. Mamiya and N. Zouain, *Eur J Mech Solid* 17 (1998) 789-806
- [7] D. Helm and P. Haupt, *Int J Solid Struct* 40 (2003) 827-849
- [8] A. Masud and Mohammad Panahandeh and F. Auricchio, *Comput. Methods Appl. Mech. Engrg.* 148 (1997) 23-37
- [9] F. Auricchio, *Int J Plast* 17 (2001) 971-990
- [10] C. Mueller and O. T. Bruhns, *Mater Sci A* 5 (2004) 260-271
- [11] E. H. Lee, *J Appl Mech* 36 (1969) 1-6
- [12] D. Christ and S. Reese, *Proceedings of SPIE Vol 6170: Smart Structures and Materials 2006: Active Materials: Behavior and Mechanics*, W. D. Armstrong (Ed.), San Diego, USA, February, 247-257, 2006

# A MICROMECHANICAL MATERIAL MODEL FOR FERROELECTRICS AND ITS APPLICATION TO CRACK PROBLEMS

M. Enderlein<sup>1</sup>, M. Kuna<sup>1</sup>, A. Ricoeur<sup>1</sup>

<sup>1</sup>Institute of Mechanics and Fluid Dynamics  
TU Bergakademie Freiberg, 09596 Freiberg  
Marco.Enderlein@imfd.tu-freiberg.de, Meinhard.Kuna@imfd.tu-freiberg.de,  
Andreas.Ricoeur@imfd.tu-freiberg.de

**Abstract.** *A micromechanical model for the simulation of domain switching processes in ferroelectric ceramics is described in this paper. Based on the model, phenomena occurring at crack tip zones under cyclic electromechanical loading can be explained.*

## Introduction

Ferroelectric ceramics are used in a wide variety of applications. Often they are subjected to cyclic electromechanical loading. Under these loading conditions fatigue cracking may occur in the material, leading to failure of the component. It turned out that fatigue crack propagation can be found even under purely electrical loading. The reason for this phenomenon lies in additional mechanical stresses, induced by inelastic strains due to switching of ferroelectric domains. To describe such effects a micromechanical material model similar to [2] is developed and implemented into a finite element environment. The model is verified by simulating typical ferroelectric material hystereses. The simulation of an electromechanically loaded DCB-specimen provides an insight into the microstructural processes at a crack tip.

## Micromechanical model

The material model is based on the constitutive equations for linear piezoelectric material [3]. They are extended by introducing the total strain  $\varepsilon_{ij}^{\text{tot}}$  and the total dielectric displacement  $D_i^{\text{tot}}$ , which both consist of a linear part ( $\varepsilon_{ij}$ ,  $D_i$ ) and a non-linear part (irreversible strain  $\varepsilon_{ij}^{\text{irr}}$ , irreversible polarization  $P_i^{\text{irr}}$ ). Hence, the extended constitutive equations can be formulated as:

$$\sigma_{ij} = c_{ijkl} (\varepsilon_{kl}^{\text{tot}} - \varepsilon_{kl}^{\text{irr}}) - e_{ijk} E_k \quad (1)$$

$$D_i^{\text{tot}} = e_{ikl} (\varepsilon_{kl}^{\text{tot}} - \varepsilon_{kl}^{\text{irr}}) + \kappa_{ij} E_j + P_i^{\text{irr}} \quad (2)$$

with the material tensors  $c_{ijkl}$ ,  $e_{ijk}$ ,  $\kappa_{ij}$ , the stress tensor  $\sigma_{ij}$  and the electrical field vector  $E_i$ . The evolution of the non-linear terms is found by the description of the ferroelectric and ferroelastic domain switching processes in the microstructure. Therefore, a representative volume element (RVE) is considered, representing a typical domain structure as can be found for instance in a grain. Restricting to plain problems and assuming the existence of both  $90^\circ$  and  $180^\circ$  domain walls, such a structure consists of four domain variants  $N$  with polarization directions shifted by  $90^\circ$  each. Defining their volume fraction  $v^{(N)}$ , effective material tensors are built:

$$c_{ijkl} = \sum_{N=1}^4 c_{ijkl}^{(N)} v^{(N)}, \quad e_{ijk} = \sum_{N=1}^4 e_{ijk}^{(N)} v^{(N)}, \quad \kappa_{ij} = \sum_{N=1}^4 \kappa_{ij}^{(N)} v^{(N)}. \quad (3)$$

Furthermore, the following relations can be derived:

$$\varepsilon_{ij} = \sum_{N=1}^4 \varepsilon_{ij}^{(N)} v^{(N)}, \quad \varepsilon_{ij}^{\text{irr}} = \sum_{N=1}^4 \varepsilon_{ij}^{\text{irr}(N)} v^{(N)} \Rightarrow \varepsilon_{ij}^{\text{tot}} = \sum_{N=1}^4 \varepsilon_{ij}^{\text{tot}(N)} v^{(N)} \quad (4)$$

$$D_i = \sum_{N=1}^4 D_i^{(N)} v^{(N)}, \quad P_i^{\text{irr}} = \sum_{N=1}^4 P_i^{\text{irr}(N)} v^{(N)} \Rightarrow D_i^{\text{tot}} = \sum_{N=1}^4 D_i^{\text{tot}(N)} v^{(N)}, \quad (5)$$

assuming, that  $\sigma_{ij}$  and  $E_i$  are the same for each variant in the RVE (REUSS approximation).

Domain wall motion describes the change in the volume fraction of specific domain variants due to  $\pm 90^\circ$  or  $180^\circ$  switching of individual unit cells within the domain. Considering one unit cell, changes of the spontaneous polarization  $\Delta P_i^{\text{sp}}$  and, for  $\pm 90^\circ$  switching, changes of the spontaneous strain  $\Delta \varepsilon_{ij}^{\text{sp}}$  are associated with the reorientation:

$$\Delta P_i^{\text{sp}} = b P^0 \begin{pmatrix} \sin \left( \alpha + \frac{1}{2} \beta \right) \\ -\cos \left( \alpha + \frac{1}{2} \beta \right) \end{pmatrix}, \quad \Delta \varepsilon_{ij}^{\text{sp}} = -\varepsilon_D \begin{pmatrix} \cos 2\alpha & \sin 2\alpha \\ \sin 2\alpha & -\cos 2\alpha \end{pmatrix}. \quad (6)$$

In Eqs. (6)  $\alpha$  describes the orientation of the unit cell with respect to the global coordinate system. The parameter  $b$  depends on the switching angle  $\beta$ . It is  $b = \mp \sqrt{2}$  for  $\beta = \pm 90^\circ$  and  $b = -2$  for  $\beta = 180^\circ$ .  $P^0$  is the absolute value of the spontaneous polarization. The spontaneous strain value  $\varepsilon_D$  can be calculated from the lattice parameters of a unit cell [4]. Together with the change of the volume fraction  $dv^{(N)}$  of the variant  $N$ ,  $\Delta \varepsilon_{ij}^{\text{sp}}$  and  $\Delta P_i^{\text{sp}}$  yield the homogenized irreversible strain and polarization on the macroscopic level.

The evolution of the volume fractions  $v^{(N)}$  within a specific RVE is controlled by an energy criterion [1], which states that a unit cell switches, if the dissipative work  $w^{\text{diss}}$  exceeds a critical value  $w^{\text{crit}}$ :

$$w^{\text{diss}} \geq w^{\text{crit}}. \quad (7)$$

This means for our model, that the volume fraction of a variant decreases for the benefit of another variant depending on the switching mode if Eq. (7) is fulfilled. The dissipative work can be calculated for each variant from the change of the specific internal energy, yielding the following expression:

$$w^{\text{diss}(N)} = \sigma_{ij} \varepsilon_{ij}^{(N)} + \sigma_{ij} \Delta \varepsilon_{ij}^{\text{sp}(N)} + E_i D_i^{(N)} + E_i \Delta P_i^{\text{sp}(N)}. \quad (8)$$

As critical work, the values  $w_{\pm 90^\circ}^{\text{crit}} = \sqrt{2} P^0 E_c$  and  $w_{180^\circ}^{\text{crit}} = 2 P^0 E_c$  are used, with the coercive field strength  $E_c$ . The amount of decrease  $dv^{(N)}$  is calculated by the evolution equation:

$$dv^{(N)} = dv_0 \frac{w^{\text{diss}(N)}}{w^{\text{crit}}} \quad (9)$$

whereby the reference volume fraction  $dv_0$  is a model parameter.

To implement the material model into a finite element environment, it is assumed that each integration point of a finite element represents one specific RVE. The equilibrium conditions of the finite elements can be derived from the principle of virtual electromechanical work. Within that principle, the irreversible variables appear as residual strains and polarization, resulting in additional mechanical and electrical nodal loads in the algebraic system of equations. To solve

the system an incremental procedure must be used, since  $\varepsilon_{ij}^{\text{irr}}$  and  $P_i^{\text{irr}}$  depend on the load history. Additional iterations have to be performed within each load step until a stable state is reached among the domain variants, i.e. no further switching processes occur under constant loading conditions.

## Numerical Results

To verify the model, the typical ferroelectric and ferroelastic material hystereses are investigated. As can be seen from Fig. 1, a good agreement is found between simulation and experimental results for the material BaTiO<sub>3</sub>. Especially the characteristic values of  $E_c$ , the remanent strain  $\varepsilon_{ij}^r$  and remanent polarization  $P_i^r$  are represented well.

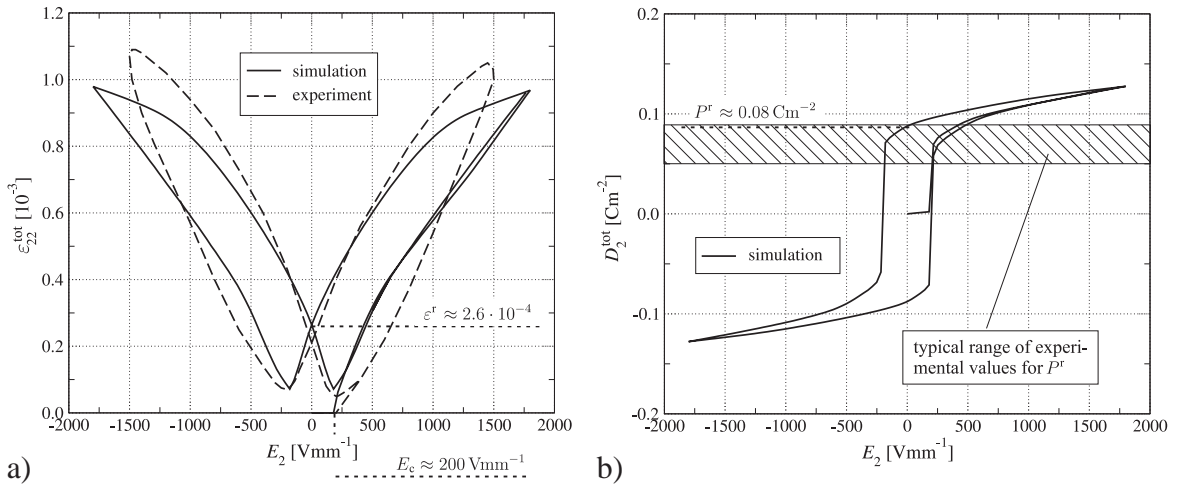


Figure 1: Strain-electrical field hysteresis (a) and dielectric hysteresis (b), comparison between simulation and experimental results

Based on these results, a pre-poled DCB-specimen under cyclic electrical and static mechanical loading is investigated. The polarized state is characterized by a specific distribution of the volume fractions of all domain variants and is determined at first by simulating the poling process. For the fracture simulation an electrical field is applied opposite to the poling direction and perpendicular to the crack.

The electrical field causes domain switching in the specimen. If the applied field is weak, these effects are restricted to a small region at the crack tip. However, if the field exceeds  $E_c$  domain switching takes place in the whole specimen except from the blades. Thus, there is a region around the crack tip where the sign of the polarization switches and high residual stresses occur. To characterize the loading situation in that region, the normal stress distribution along the ligament is analyzed. As can be seen from Fig. 2a,  $\sigma_{22}$  is close to zero for electrical fields below the coercive field strength. For  $E \geq E_c$ , when the main part of domain switching takes place,  $\sigma_{22}$  rises rapidly, showing an asymptotic behavior when approaching the crack tip. The results clearly reveal that electrically induced tensile stresses arise in front of the crack due to ferroelectric domain switching processes. Based on the curves in Fig. 2a stress intensity factors  $K_I(E)$  are calculated, assuming that the stress singularity in front of the crack tip follows approximately  $\sigma_{22} \approx r^{-0.5}$ , so that the well known relation of linear elastic fracture mechanics  $K_I = \lim_{r \rightarrow 0} \sigma_{22} \sqrt{2\pi r}$  (on the ligament) can be applied. The calculated values of  $K_I$  are shown in Fig. 2b by the curve depicted with triangle symbols. If  $E_c$  is exceeded, the stress intensity factor steeply increases, reaching soon the typical values of the fracture toughness of

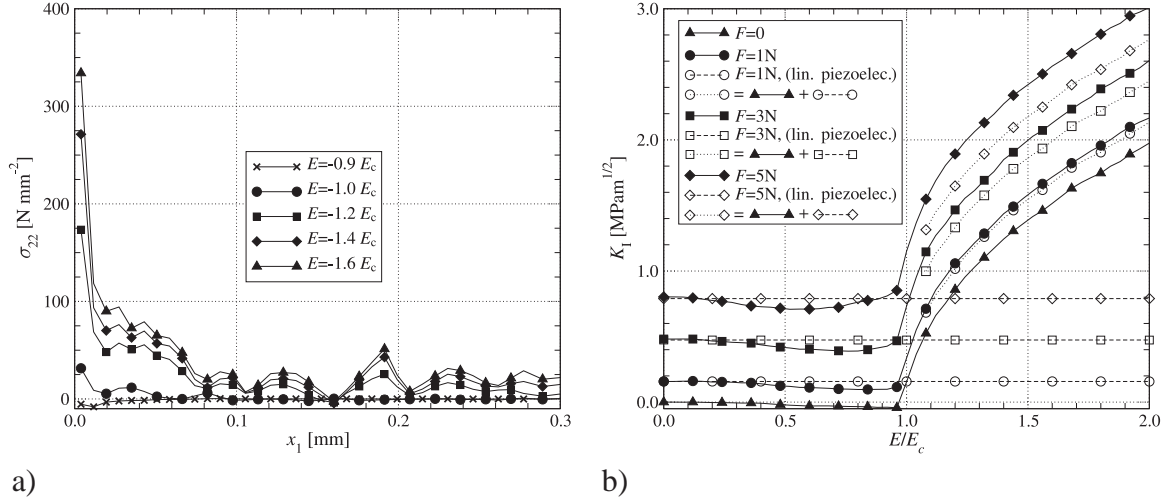


Figure 2: Distribution of stress  $\sigma_{22}$  at the ligament for different electrical fields  $E$  (a) and stress intensity factors  $K_I(E)$  depending on the static mechanical load  $F$  (b)

ferroelectric ceramics. By means of these results experimental observations can be explained, where crack propagation is found, when an electrical field is applied above  $E_c$  and opposite to the original poling direction [5].

Besides the curve for pure electrical loading some result are shown in Fig. 2b, originating from analyses where a static mechanical crack opening load has been applied in addition to the electrical field. As expected the curves (solid lines) lie above the one depicted by triangles.  $K_I$  is composed of two parts now, a mechanically induced part (dashed lines), which is found in linear piezoelectric calculations, too, and an electrically induced part, as discussed above. The domain switching is supported by the additional mechanical load, i.e. the electrically induced part is bigger than with pure electrical loading. This fact can be seen from Fig. 2b, comparing the solid lines with the dotted lines, which stand for the superposition of the pure mechanical load (dashed lines) and the pure electrical load (triangular symbols).

## Conclusions

It has been shown that the developed model is capable to explain observations from fracture mechanics experiments concerning the crack propagation under cyclic electromechanical loading. Besides the shown results the model is used for further simulations, e. g. to investigate the influence of the poling state around the crack tip on the dielectric intensity factor  $K_{IV}$ .

## REFERENCES

- [1] S. C. Hwang, C. S. Lynch and R. M. McMeeking, Ferroelectric/ferroelastic interactions and a polarization switching model, *Acta metallurgica et materialia* **43**, 2073–2084 (1995).
- [2] M. Kamlah, A. C. Liskowsky, R. M. McMeeking and H. Balke, Finite element simulation of a polycrystalline ferroelectric based on a multidomain single crystal switching model, *International Journal of Solids and Structures* **42**, 2949–2964 (2005).
- [3] V. Z. Parton and B. A. Kudryavtsev, *Electromagnetoelasticity*, Gordon and Breach Science Publishers, New York (1988).

- [4] A. Ricoeur and M. Kuna, A micromechanical model for the fracture process zone in ferroelectrics, *Computational Material Sciences* **27**, 235–249 (2003).
- [5] I. Westram, A. Ricoeur, A. Emrich, J. Rödel and M. Kuna, Fatigue crack growth law for ferroelectrics under cyclic electrical and combined electromechanical loading, *Journal of the European Ceramic Society*, **27**, 2485-2494 (2007).

## THE ELECTRIC PERMEABILITY OF CRACKS IN PZT DETERMINED BY SCANNING PROBE FORCE MICROSCOPY

Frank Felten<sup>1,2</sup> and Gerold A. Schneider<sup>1</sup>

<sup>1</sup>Hamburg University of Technology, Institute of Advanced Ceramics,  
Denickestr. 15, 21073 Hamburg, Germany  
e-mail: g.schneider@tu-harburg.de

<sup>2</sup> (now with Robert Bosch GmbH, Corporate Sector Research and Advanced Engineering,  
Applied Research 1 - Materials, Robert-Bosch-Platz 1, Gerlingen-Schillerhöhe, Germany)  
e-mail: frank.felten@de.bosch.com

**Abstract.** *The choice of the electric boundary condition at the faces of an crack in a ferroelectric body with high permittivity has a major influence on the theoretically predicted energy release rates and field intensity factors. Especially when electrical impermeability is assumed, large effects in retarding crack growth are predicted, being in disagreement with experimental observations. Therefore in the presented work an indentation crack in a poled lead zirkonate titanate (PZT) ceramic subjected to electric fields up to 0.5 kV/mm is investigated. Using high resolution scanning probe microscopy the crack opening displacement and the electrical potential distribution around the crack are determined. From these, the potential difference across the crack and thus the electric field within the crack are determined as a function of the applied electric field. Furthermore, the data allow for calculating the field intensity factors, the energy release rate and the effective dielectric constant of the crack filling medium. Latter could be determined to be constant having an average value of 21. It is shown by means of a Griffith crack that for the value of 21 the effect in retarding crack growth is already negligible when assuming the total energy release rate as a fracture criterion.*

### Introduction

Ferroelectric ceramics are widely used as actuators and sensors. Unfortunately they show distinct brittleness and thus they are very susceptible to failure by cracking. To permit the assessment of the durability and reliability of ferroelectrics, suitable fracture mechanics concepts are necessary, which take both mechanical and electrical loading into account. A large number of theoretical papers have been published concerning the electric and stress fields near cracks in dielectric and piezoelectric materials. Almost all of these efforts are based on the assumption that non-conducting cracks in dielectric and piezoelectric materials with high dielectric constants can be treated as completely impermeable. This feature leads to predictions of significant reductions of the crack tip energy release rate (ERR) when electric fields are applied together with mechanical loads compared to the value that prevails due to the applied load alone. Since the ERR is known to control crack propagation in brittle ceramics, this model implies that an applied electric field will make it much less likely that a crack will propagate. On the other hand, experimental work shows that this predicted effect is greatly overestimated (see e.g. [1] and ref. herein). McMeeking [2] has emphasized that the assumption of impermeability of the

crack is a deficiency since the resulting calculations of the ERR and crack tip stress and field intensity factors is probably misleading. A more suitable assumption is the boundary condition introduced by Hao and Shen [3] which takes the potential difference across the opened crack into account and allows for choosing an appropriate permeability of the crack by the dielectric constant of the crack filling medium. In a first approach Schneider et al. [4] experimentally determined this permittivity by means of a radial indentation crack using Kelvin Probe Force Microscopy (KFM) [6] and Atomic Force Microscopy (AFM). Whereas in [4] only one relatively low applied electric field was used, in the study presented here (from [5]), the methodology is extended and the permeability is studied at different applied electric fields up to 0.5 kV/mm. Furthermore, this procedure allows for checking the existence of an saturation effect of the electric field interior to the crack due to dielectric breakdown as proposed e.g. by Landis [7].

## Experimental

The experimental setup is shown schematically in Fig. 1. The specimen used is a commercial PZT (Vibrit1100, Siemens, Germany). The slab of width  $250\mu\text{m}$  is prepared from a commercially trimorph designed for industrial looms. This structure is of some convenience because a voltage can be applied easily using the existing electrodes on the sides of the slab. After proper surface preparation, a crack of overall size of  $2a = 517\mu\text{m}$  is introduced by Vickers indentation. Afterwards, the sample is fixed in a custom made holder and aligned under the AFM (Dimension 3000, Nanoscope IIIa, Digital Instruments, U.S.A).

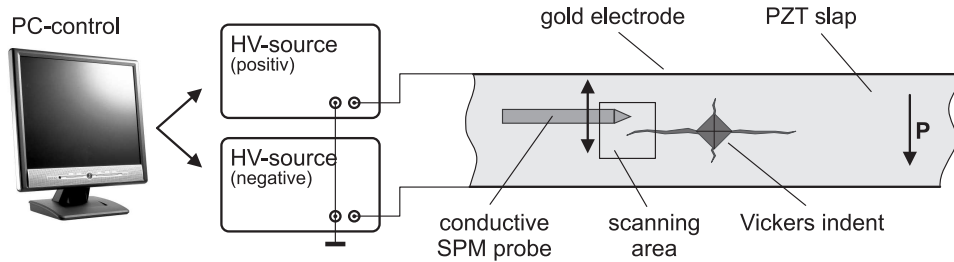


Figure 1: Experimental setup (schematic)

First the crack opening displacement (COD) is measured using semi-contact AFM without a voltage applied to the specimen, since the voltage reduces the image quality. It will be shown later (Fig. 3), that the influence of the field on the COD is negligible. Beginning with the crack tip region, a series of overlapping images are acquired sequentially. The full crack opening  $2u_2$  is determined by evaluating the section scans of the height images as described in [8] and the distance from the crack tip is determined by superposing the overlapping images. After applying the voltage using two computer controlled HV-sources, the surface potential around the crack is measured by KFM. After increasing the applied voltage the KFM measurement is repeated.

The surface potential measured shows a distinct drop across the crack, Fig. 2 (line B). To quantify the drop  $\Delta\phi$  we extrapolate linearly the potential curves from both sides of the crack and measure the vertical distance between these lines. This is necessary due to principal resolution limitations in KFM as described in [4] (and ref. herein). The applied electric field is determined by evaluating the negative potential gradient at sufficient distance from the crack, in Fig. 2 (line A). Repeating this method at different positions and different applied voltages we finally get the potential drop as a function of both the distance from the crack tip and the remote electric field.

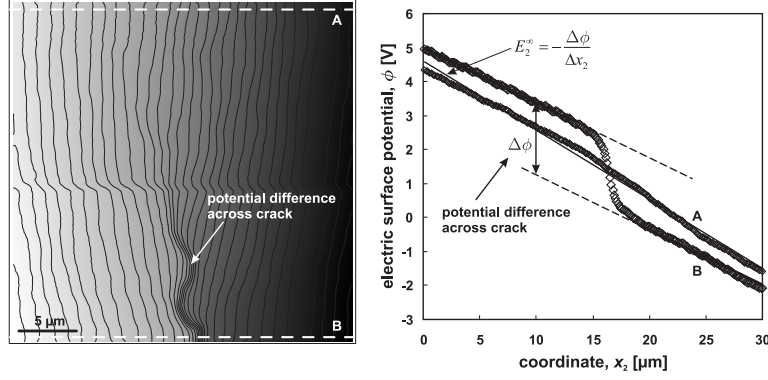


Figure 2: About determining the potential difference across the crack (shown for  $E_2^\infty = 200$  kV/mm). Left: KFM potential map. Right: Section scans illustrating how to evaluate  $E_2^\infty$  and  $\Delta\phi$ .

## Results and Discussion

The fracture mechanics framework based on Suo et al. [9] describes the correlation between field intensity factors  $\mathbf{K} = (K_{II}, K_I, K_{III}, K_D)^T$  and crack face displacement fields  $\mathbf{U} = (u_1, u_2, u_3, \phi)^T$  predicting a square root shape near the tip:

$$\Delta\mathbf{U}(r') = \sqrt{\frac{2r'}{\pi}} \mathbf{H} \mathbf{K} \quad \text{with} \quad \Delta\mathbf{U} = \mathbf{U}^+ - \mathbf{U}^- \quad (1)$$

Here,  $r'$  is the distance from the crack tip and the indices "+" and "-" depicting the upper and lower crack face, respectively.  $\mathbf{H}$  is the Irwin-matrix taking into account the material properties as well as the crack orientation with respect to the poling direction. The element values are given in [4]. Regarding their predicted shape at the crack tip, the COD  $\Delta u_2$  as well as the potential drop  $\Delta\phi$  are analyzed in Fig. 3.

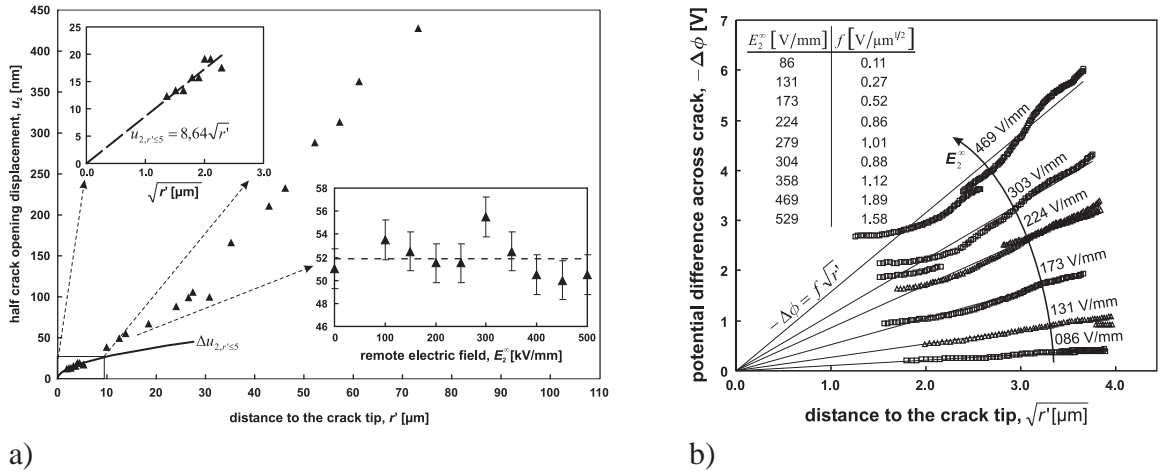


Figure 3: a) Crack opening displacement (COD). Insert top left: COD plotted vs. the square root of the distance from the crack tip. Insert right: COD at approx.  $r' = 12$   $\mu\text{m}$  showing that there is no significant influence of the remote electric field on the COD. b) Potential difference vs. square root of the distance from the tip with table giving proportionality factors of the fitted trends.

The linear behavior at the crack tip implies a good agreement with the parabolic shape at the tip from Eq. (1). From the square root functions the field intensity factors can now be easily

obtained by inverting Eq. (1). Hence, the total energy release rate (ERR)  $G$  can be calculated using  $\mathbf{H}$  and the results for  $\mathbf{K}$  with:

$$G = 1/4 \mathbf{K} \mathbf{H} \mathbf{K}^T \quad (2)$$

To finally analyze the results regarding the electric permittivity interior to the crack  $\varepsilon^*$  the electric field inside the crack,

$$E_2^* = -\frac{\Delta\phi}{\Delta U_2}, \quad (3)$$

must be determined from the results given in Fig. 3 and correlated to the applied electric field. With  $\varepsilon_{22}^\sigma$  being the material permittivity measured at constant stress and  $b$  and  $a$  being the long and short axis of the Griffith crack, it is [4]:

$$E_2^* = -\frac{H_{44}\varepsilon_{22}^\sigma}{H_{44}\varepsilon^* - 2(b/a)} E_2^\infty, \quad (4)$$

Hence, the field inside the crack is predicted to be proportional to the applied field. In Fig. 4a the field from Eq. (3) is plotted vs. the applied field confirming the proportionality in a wide regime. By comparing the experimentally determined proportionality factor with the one from Eq. (4) the effective permittivity of the crack medium is determined to be approx.  $\varepsilon^* = 21\varepsilon_0$  as indicated in the figure. Note, that electric fields up to 100 kV/mm are found without significant saturation effects or any dielectric breakdown. Thus, as an important result, a maximum field must be assumed to be  $>100$  kV/mm.

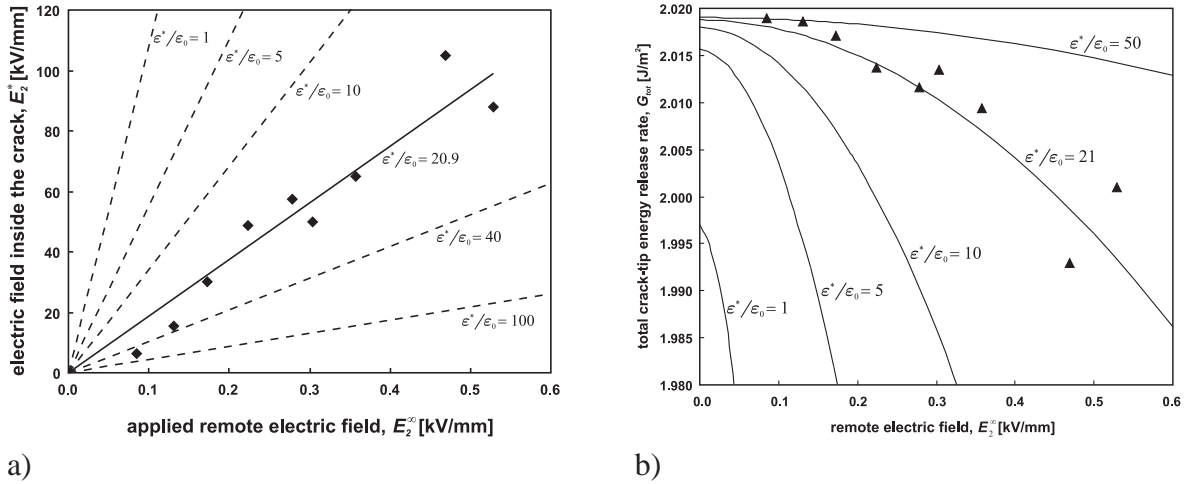


Figure 4: a) Electric field interior to the crack vs. remote electric field. b) Total ERR as a function of remote field. Both: Lines are calculated for a Griffith crack of same length with the dielectric constant of the crack filling medium as parameter.

Fig. 4b shows total ERR calculated from Eq. (2) as a function of applied field. The plotted parabolas are theoretically predicted for a Griffith crack with the dielectric constant of the crack's interior as a parameter. The experimental results again are in good agreement with the predictions when  $\varepsilon^*/\varepsilon_0$  is assumed to be 21. Furthermore, the reduction of the ERR due to the applied electric field is only 1.5% of the maximum value. Hence, the effect in retarding crack growth is negligibly small for the high permeability found from the experiment. The

raised permittivity can thus be used to describe the discrepancies between theory and fracture experiments within the already existing fracture mechanics framework.

## REFERENCES

- [1] G. A. Schneider, Influence of Electric Field and Mechanical Stresses on the Fracture of Ferroelectrics, accepted for publication in *Annual Reviews of Materials Research* **37** (2007).
- [2] R. M. McMeeking, Towards a fracture mechanics for brittle piezoelectric and dielectric materials, *Int. J. Frac.* **108**, 25–41 (2001).
- [3] T.-H. Hao and Z.-Y. Shen, A New Electric Boundary Condition of Electric Fracture Mechanics and its Applications, *Eng. Frac. Mech.* **47**[6], 793–802 (1994).
- [4] G. A. Schneider, F. Felten and R. M. McMeeking, The electrical potential difference across cracks in PZT measured by Kelvin Probe Microscopy and the implications for fracture, *Acta mater.* **51**[8], 2235–2241 (2003).
- [5] F. Felten, Anwendung der Rastersondenmikroskopie zur Bestimmung bruchmechanischer Parameter und lokaler piezoelektrischer Eigenschaften von Ferroelektrika, Dissertation, Shaker Verlag (ISBN 978-3-8322-5837-5) (2006)
- [6] H. O. Jacobs, H. F. Knapp and A. Stemmer, Practical aspects of Kelvin probe force microscopy, *Rev. Sci. Instrum.* **30**[3], 1756–1760 (1999).
- [7] C. M. Landis, Energetically consistent boundary conditions for electromechanical fracture, *Int. J. Solids Struct.* **41**, 6291–6315 (2004); Corrigendum: **42**, 2461–2463 (2004).
- [8] O. Raddatz, G. A. Schneider and N. Claussen, Modelling of R-Curve Behaviour in Ceramic/Metal Composites, *Acta mater.* **46**, 6381–6395 (1998).
- [9] Z. Suo, C.-M. Kuo, D. M. Barnett and J. R. Willis, Fracture Mechanics for Piezoelectric Ceramics, *J. Mech. Phys. Solids* **4**[4], 739–765 (1992).

## EXPERIMENTAL AND THEORETICAL INVESTIGATION OF PORTEVIN-LE CHÂTELIER DEFORMATION BANDS

X. Feng<sup>1,2</sup>, G. Fischer<sup>1</sup>, H. A. Crostack<sup>1</sup>, B. Svendsen<sup>2</sup>

<sup>1</sup>Chair of Quality Management  
University of Dortmund, Germany  
email: xfeng@rif.fuedo.de

<sup>2</sup>Chair of Mechanics  
University of Dortmund, Germany  
e-mail: bob.svendsen@udo.edu

**Abstract.** *The basis of plastic deformation of metals is the formation and motion of dislocations. One of the methods to reduce the ductility and improve the strength of pure metals is to introduce foreign atoms in metallic solid solutions in order to obstruct the dislocation motion. In some regimes of temperature and loading rate, the interaction of such foreign atoms with dislocations can result in a negative strain-rate sensitivity, dynamic instability and deformation localization, leading to the nucleation and propagation of so-called Portevin-Le Chelier (PLC) bands. From a technological point of view, the development of such bands results in a reduction of surface quality and strength, and therefore is undesirable. In this paper, the propagation of PLC deformation bands in Al alloys are studied experimentally and theoretically. The morphology and kinematics of PLC bands are investigated using both mechanical and thermal measurement methods. The latter is based on the use of a thermal camera which captures the temperature changes resulting from mechanical dissipation and heating produced during nucleation and propagation of PLC bands. On the modeling side, attention is focused on the influence of model parameters and the geometry of specimen as well as on the thermomechanical coupling.*

### Introduction

A common technological method to increase the strength of pure metals is to introduce foreign atoms in metallic solid solutions in order to obstruct the dislocation motion. In some regimes of temperature and loading-rate, the interaction of such foreign atoms with dislocations can result in a negative strain-rate sensitivity, dynamic instability and deformation localization, leading to the nucleation and propagation of so-called Portevin-Le Châtelier (PLC) bands. From a technological point of view, the development of such bands results in a reduction of surface quality and strength, and therefore is undesirable. From the appearance of the recorded load serration, three types of PLC bands have been commonly distinguished [3]: type-A bands, which are nucleated near one specimen grip during a slight yield point, and then propagate continuously along the specimen with only slight load fluctuations; type-B bands, which are also nucleated near one grip, but propagate discontinuously along the specimen accompanied by rather regular load serration; and type-C bands, which are nucleated at random sites along the specimen length and cause strong regular load drops at rather high frequency. The unstable

plastic flow is basically traced back to a negative strain-rate sensitivity (SRS) of the flow stress, namely a decrease of the flow stress with increasing applied strain-rate. Such an anomalous behavior may be induced by the dynamic strain ageing (DSA) within certain ranges of loading rates and temperatures [2, 5, 6, 8].

In this short work, an example of the experimental results of a detailed investigation of the morphology and kinematics of PLC bands by means of high-speed infrared camera are presented. In addition, simulation results based on the model of Estrin [4, 7] and the finite-element method are shown. The development of temperature due to mechanical dissipation is modeled as well.

## Experimental results

The material investigated in this study is a technical AlMg3 alloy [1]. The composition is Al-3.11%Mg-0.26%Si-0.22%Fe-0.18%Mn(wt%). This material was prepared by cold-rolling into 1.5mm sheets. The specimens manufactured from these sheets were ground and polished followed by annealing in air at 673K for 2 hours and quenching into water. Tensile test were carried out using an miniaturized testing machine at room temperature. Strain gauges with a 1.5mm gauge length were used to measure the strain on the back side of specimens. Concurrently, a high-speed infrared camera is used to detect the change of temperature of the specimen on the surface of a specimen. The plastic deformation of metal is accompanied by a dissipation of the major part of the mechanical energy into heat. This dissipation generally results in an increase in temperature. The IR camera has a maximum full frame-rate of 880Hz, a pixel resolution of  $256 \times 256$ , and a temperature sensitivity of 12mK. On this basis, experimental

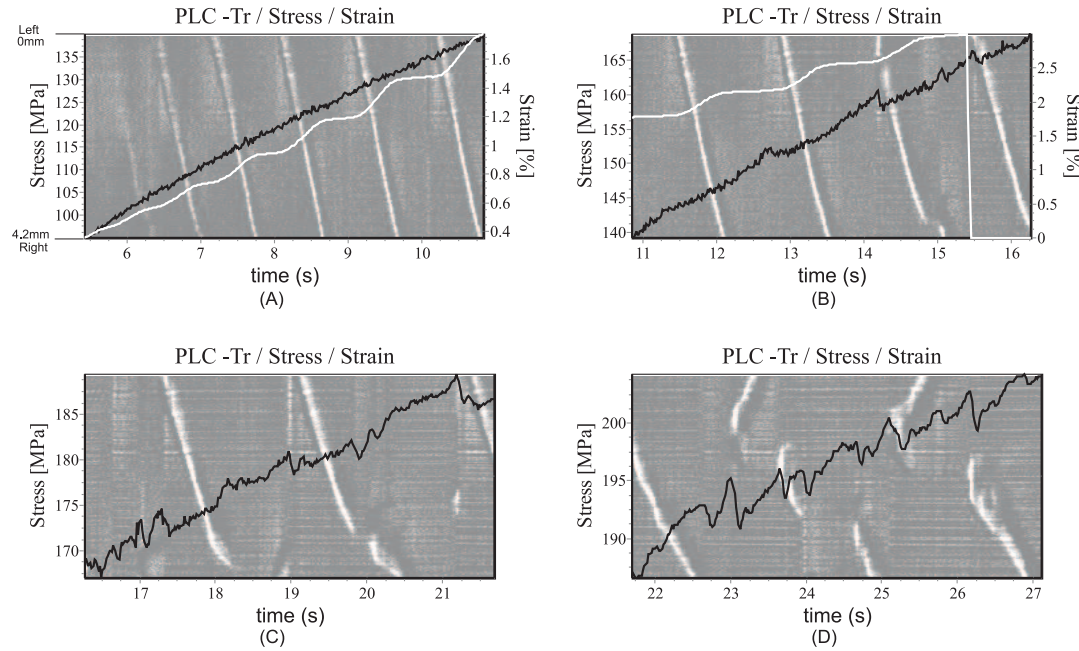


Figure 1: Experimental results on the nucleation and propagation of PLC bands at  $\dot{\epsilon} = 0.27\%/s$  (strain rate) correlated in time with stress (black) and strain (white) results. A picture of the band trajectories (bright areas) is shown in the background.

results are obtained for example on the nucleation of PLC bands is often observed in regions of stress concentration and high stress gradients. Existing bands may expand to form a new band propagating towards the other side of the specimen. In Fig. 1A, the top corresponds to

the left side of infrared camera and the bottom corresponds to the right side. Some PLC bands are nucleated at the grip area of specimen and propagate through this field of view from left to the right side. Newly-formed bands are stronger than older ones, implying that the strain increment due to the band is increasing with strain. When the strain reaches about 2.5%, the band begins to break down. After a short time, it then resumes its motion at the same position (memory effect). The slope of the trajectory of a PLC band (i.e. the average band velocity) decreases exponentially with strain and time. On the other hand, the average band velocity increases with the applied external strain-rate following a power law relation (in a given range of plastic strain). The power law exponent between band velocity and external strain rate has been determined experimentally at 0.72. For this determination, a strain gauge at the center of specimen was used. As shown in Fig. 1 (A), a PLC band causes a strain increment when a PLC band enters the range of strain gauge. Considering the stress curve in Fig. 1A, the jumps are weak, and as the strain goes up, their amplitude increases (in Fig. 1B, C, D in turn). In the peak area of each stress serration, a PLC band is nucleated, and starts to propagate where stress gradients are present. In Fig. 1C, breaks in the band propagation appear more frequently than in Fig. 1B. The common aspect here is that the PLC bands continues to propagate after a break in the same direction. This situation changes in Fig. 1D. New PLC bands nucleate in the middle of specimen and propagate in two directions. These break more frequently or propagate only over a short distance. Correspondingly, jumps in the stress occur more frequently.

### Simulation results

An upper-bound estimate of this temperature increase is given by assuming the process is adiabatic. In this work, this estimate is combined with the Estrin model [3, 4] for the PLC effect. In this model, dynamic strain ageing is described by accounted for by taking the evolution of solute concentration into account. This model was implemented as a user material subroutine in ABAQUS. The instability is triggered in the current specimen in the notch region. Results of simulation are shown in Fig. 2. Band angles predicted in the simulations (about  $55^\circ$ ) agree well



Figure 2: The morphology of simulated PLC bands based on Estrin model.

with the experimental value (about  $60^\circ$ ). The corresponding stress development as a function of time is shown in Fig. 3A. Coupling arises between temperature and deformation in the sense that increased temperature enhances the mobility of foreign atoms and dislocations, which in turn leads to enhanced plastic strain and so a further increase in temperature. In order to show the influence of coupling, the stress-time curve was simulated with and without coupling (see Fig. 3). In area I (see Fig. 3B), there is no distinctive difference between both curves (see Fig. 3A and Fig. 3B). But in area II, the larger serration magnitude in coupling case compared to the no-coupling case is evident (Fig. 3B).

In summary, the coupling of temperature and strain leads to the following consequences:

- The stress jumps are more pronounced than without coupling;

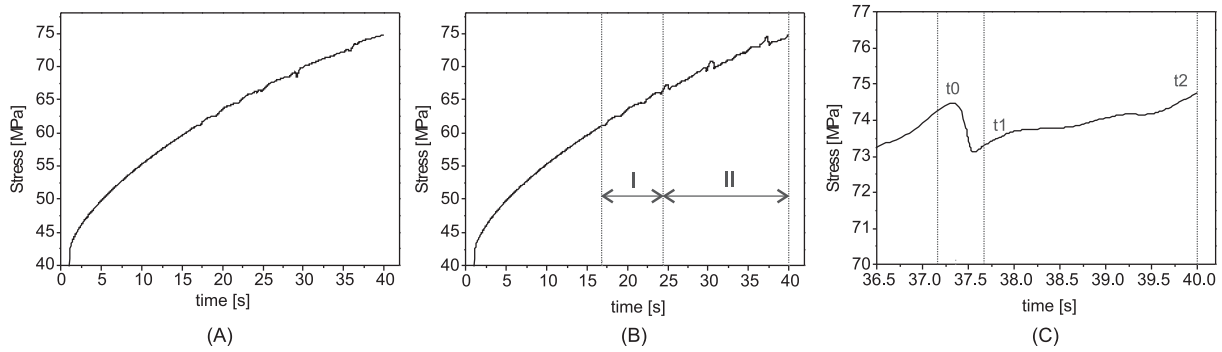


Figure 3: Simulated stress development in time. (A) without coupling, (B) with coupling, (C) blow-up of stress development in the coupling case.

- The propagation of PLC bands is interrupted more frequently;
- Several bands occur;
- At high external strain, PLC bands are nucleated only in the middle area.

In most cases, the above phenomena are also observed in the experiments (Fig. 1D). In work in progress, the alternative model of Hähner ([8]) is also being investigated and will be reported on in future work.

## REFERENCES

- [1] J. Balik, P. Lukac. Portevin-Le Châtelier instabilities in Al-3Mg conditioned by strain rate and strain. *Acta metal. Mater*, 41(5):1447-1454, 1993.
- [2] A. H. Cottrell. Effect of Solute Atoms on the Behaviour of Dislocation: in Report of a Conference of Strength of Solids. *Physical Society, London*, 30-38, 1948.
- [3] Y. Estrin, L. P. Kubin. Plastic Instabilities: Classification und Physical Mechanisms. *Res Mechanica*, 23:197-221, 1988.
- [4] Y. Estrin, P. G. McCormick. Modelling the transient flow behaviour of dynamic strain ageing materials. *Acta Metall. Mater*, 39:2977-2983, 1991.
- [5] P. Hähner, A. Ziegenbein, E. Rizzi, and H. Neuhäuser. Spatio-temporal analysis of Portevin-Le Châtelier deformation bands: theory, simulation and experiment. *Physical Review B* 2002, 65(13):134109, 2002.
- [6] F. B. Klose, A. Ziegenbein, J. Weidenmüller, H. Neuhäuser, and P. Hähner. Portevin-Le Châtelier effect in strain and stress controlled tensile tests. *Computational Materials Science*, 26:80-86, 2003.
- [7] C. P. Ling, P. G. McCormick. The effect of temperature on strain rate sensitivity in an Al-Mg-Si alloy. *Acta Metal. Mater*, 41:3127-3131, 1993.
- [8] E. Rizzi, P. Hähner. On the Portevin-Le Châtelier effect: theoretical modelling and numerical results. *International Journal of Plasticity*, 20:121-165, 2004.

## 3D FINITE ELEMENT MODEL FOR CALCULATION OF EFFECTIVE MATERIAL PROPERTIES

Roland Gärtner<sup>1</sup>, Sigurd Kubel<sup>2</sup>, Mario Fleischer<sup>1</sup> and Rolf Schmidt<sup>1</sup>

<sup>1</sup> Technische Universität Dresden, Institut für Festkörpermechanik, Germany  
TU-Dresden Institut für Festkörpermechanik 01062 Dresden  
e-mail: roland.gaertner@gmail.com

<sup>2</sup> GWT-TUD GmbH, FB Technische Mechanik, Germany

**Abstract.** *This work presents a method for the numerical homogenization of three-dimensional, periodically heterogeneous structures, which makes it possible to calculate effective, anisotropic and homogeneous alternative material parameters. Thus the efforts in calculating of such structures can be reduced tremendously. The finite element model consists of a periodic Unit Cell, which represents the periodicity of the complete structure in all directions.*

### Introduction

Many materials feature heterogeneous structures caused by variably distributed physical parameters such as density, Young's-Modulus, conductivity etc. This can be found in two or multi phase materials, a typical example are composite materials. Furthermore heterogeneity can be caused geometrically as occurs in stiffened plates or material featuring cellular structure like cancellous bone, wood or packaging material. In the structure of heterogeneous material one can distinguish different scales. We assume that we can at least determine one length scale  $L$  for the material or the component and one length scale  $l$  for the inhomogeneities. If the dimensions are approximately of the same level ( $\frac{L}{l} \approx 1$ ) one should solve this problem using conventional methods. The effort of a calculation with conventional methods cannot be justified in case of the opposite relation ( $\frac{L}{l} \rightarrow \infty$ ). In this case the homogenization results in a description of the material or structure independent from the size of inhomogeneities, which can reduce the DOF of our model and thus the calculation costs tremendously.

For many heterogeneous materials periodical or approximately periodical structures can be found. Cell methods use a periodically repeating Unit Cell also Representative Volume Element (RVE) to perform homogenization. Fundamental works such as [1] und [4] deal with fibre reinforced composites to describe two-dimensional homogenization. Homogenization by Unit Cells is possible, if one can find a underlying periodic structure and the material properties of all constituents are known. To perform the calculation of homogenized, effective material properties we implemented the following steps:

- Determination of the RVE, containing all geometric information about the structure
- Identification of the fundamental material law and properties of the constituents
- Application of suitable boundary conditions on the RVE and static analysis
- Calculation of effective material properties

To solve the homogenization problem we used the finite element method, because there are no restrictions to geometry, material properties, number of phases or size.

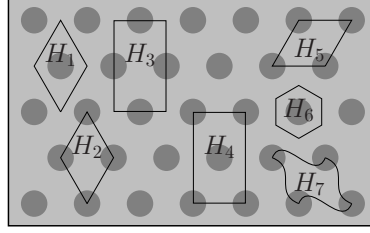


Figure 1: Some possible RVE on a 2D hexagonal device (see [3]).

### Homogenization using the unit cell method for linear elastic material

Firstly a so called *Unit Cell* or *Representative Volume Element* RVE, which features all necessary information about the periodicity of the microstructure, needs to be defined. Thus the the object under consideration marks the smallest possible cell, from which the whole structure can be rebuilt. Fig. 1 shows some possible RVE's for hexagonal arrangement of fibres in a matrix. The selection of the RVE is arbitrary. Obviously  $H_6$  will lead to the smallest model. But in case we want to study the behavior of the microstructure it can be helpful choosing a RVE like  $H_4$ , which can also visualize interaction between the fibres.

Regards in this paper are limited to linear elasticity. The general formulation of HOOK's-law as given by YOUNG combines the second order CAUCHY stress tensor  $\sigma$  and the classical linearized strain tensor  $\varepsilon$ .

$$\sigma = E \cdot \varepsilon \quad (1)$$

Herein  $E$  is the fourth order elasticity tensor, with 81 elements. From the symmetries in  $\sigma$  and  $\varepsilon$  the number of independent elements reduces to 36. Another restriction can be derived from the existence of the elastic potential  $U$  (stored strain energy), which reduces the number of independent components of the elasticity tensor to 21. These restrictions enable a reformulation of the generalized HOOKE's law Eq.(1) in matrix notation (VOIGT's notation, see also [5]).

$$\vec{\sigma} = \underline{C} \cdot \vec{\varepsilon} \quad (2)$$

With  $\vec{\sigma} = (\sigma_{11}\sigma_{22}\sigma_{33}\sigma_{12}\sigma_{23}\sigma_{13})^T$  the  $(6 \times 1)$ -stress vector,  $\underline{C}$  the  $(6 \times 6)$ -elasticity matrix and  $\vec{\varepsilon} = (\varepsilon_{11}\varepsilon_{22}\varepsilon_{33}\varepsilon_{12}\varepsilon_{23}\varepsilon_{13})^T$  the  $(6 \times 1)$ -strain vector. In heterogeneous material the terms in Eq.(2) are functions of the coordinates  $x_i$ .

$$\vec{\sigma}(\vec{x}) = \underline{C}(\vec{x}) \cdot \vec{\varepsilon}(\vec{x}) \quad (3)$$

The basic idea of homogenization is to find a globally homogeneous medium equivalent to the underlying heterogeneous structure. This is reached if the stored strain energy in both cases is equal. In case for one RVE that means

$$U_{RVE} = \frac{1}{2} \int_{(V_{RVE})} \vec{\sigma}^T(\vec{x}) \cdot \vec{\varepsilon}(\vec{x}) dV = \frac{1}{2} \int_{(V_{RVE})} \langle \vec{\sigma} \rangle^T \cdot \langle \vec{\varepsilon} \rangle dV. \quad (4)$$

In Eq.(4)  $\langle \vec{\sigma} \rangle$  and  $\langle \vec{\varepsilon} \rangle$  represent the averaged stresses and strains for the homogenized material in this case we can write HOOK's-law as

$$\langle \vec{\sigma} \rangle = \underline{C}^* \cdot \langle \vec{\varepsilon} \rangle. \quad (5)$$

Adopting Eq.(5) to the right hand side of Eq.(4) leads to

$$U_{RVE} = \frac{V_{RVE}}{2} \langle \vec{\sigma} \rangle^T \cdot \langle \vec{\varepsilon} \rangle = \frac{V_{RVE}}{2} \langle \vec{\varepsilon} \rangle^T \cdot \underline{C}^* \cdot \langle \vec{\varepsilon} \rangle. \quad (6)$$

If the left hand side of Eq.(4) can be solved numerically this leads to a system of independent equations, from which the elements of  $\underline{C}^*$  can be calculated.

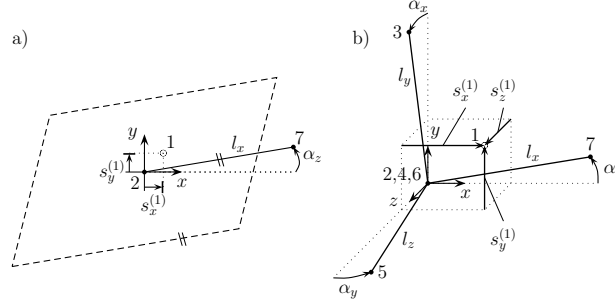


Figure 2: Deformed structure and auxiliary construction a) 2D-case, b) 3D-case (without schematic RVE).

We implemented an auxiliary construction (see Fig. 2), which is independent from the RVE, to apply displacements on the boundary of the RVE, from which the strain state can be calculated easily. The displacement on the boundary of the RVE can be divided in two parts.

$$\vec{u}_{bound} = \vec{u}^{(h)} + \vec{u}^{(f)} \quad (7)$$

The first part  $\vec{u}^{(h)}$  (homogeneous displacement) can be directly retrieved from the displacements implemented via the auxiliary construction (see Eq.(8)) the second part  $\vec{u}^{(f)}$  will be explained later.

$$\vec{u}^{(h)} = \begin{bmatrix} s_x \cdot x + \sin(\alpha_y) \cdot z + (\cos(\alpha_y) - 1) \cdot x + (\cos(\alpha_z) - 1) \cdot x + \sin(\alpha_z) \cdot y \\ s_y \cdot y + \sin(\alpha_z) \cdot x + (\cos(\alpha_z) - 1) \cdot y + (\cos(\alpha_x) - 1) \cdot y + \sin(\alpha_x) \cdot z \\ s_z \cdot z + \sin(\alpha_x) \cdot y + (\cos(\alpha_x) - 1) \cdot z + (\cos(\alpha_y) - 1) \cdot z + \sin(\alpha_y) \cdot x \end{bmatrix} \quad (8)$$

Under assumption of small strains and linearization we can calculate the strain vector

$$\vec{\varepsilon} = [s_x \quad s_y \quad s_z \quad \alpha_x \quad \alpha_y \quad \alpha_z]^T. \quad (9)$$

Thus we can define different strain states simply by changing the displacements in the points (nodes) 1, 3, 5 or 7 of the auxiliary construction.

To correctly handle the boundary conditions for the RVE we need to consider  $\vec{u}^{(f)}$  the *fluctuations*, which can be understood as perturbation in the strain field caused by inhomogeneities of the heterogeneous structure. As shown in Fig. 3 an arbitrary point  $Q$  and its corresponding point  $P$  on the opposite face feature the same fluctuation after deformation (Eq.10).

$$\overrightarrow{Q'Q''} = \overrightarrow{P'P''} = \vec{u}^{(f)} \quad (10)$$

As we use the CE-command, provided by ANSYS to formulate constrained equations, to apply the homogeneous displacements to the boundary of the RVE, we can easily extend these equations with the fluctuation. Therefore we use additional elements MASS21, each of those corresponds to a pair of nodes on opposite faces of the RVE. To preserve periodicity in the deformed structure the fluctuations have to be equal for corner nodes (and in 3D case for corresponding edges respectively). To eliminate rigid body movement within the fluctuation we chose  $\vec{u}^{(f)} = 0$  on the corner nodes.

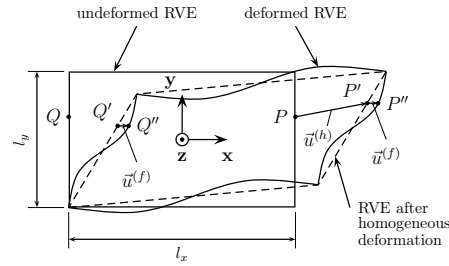


Figure 3: Different states of deformation, for simplification shown in the 2D case.

## Conclusions

Within a project in hearing research we applied the described model to calculate effective material properties of stereocilia. These are small structures on hair cells essential in the hearing process. They feature a periodically heterogeneous micro structure displayed in Fig. 4. With this homogenization procedure it was possible to calculate orthotropic material behavior for stereocilia only from their microstructure and data for the linear elastic properties of the constituents as provided in literature [2] or estimated. In the applied case our model is limited to the restrictions of continuum mechanics. However an extension to nanomechanical problems as well as to non-linear problems can be implemented within the model.

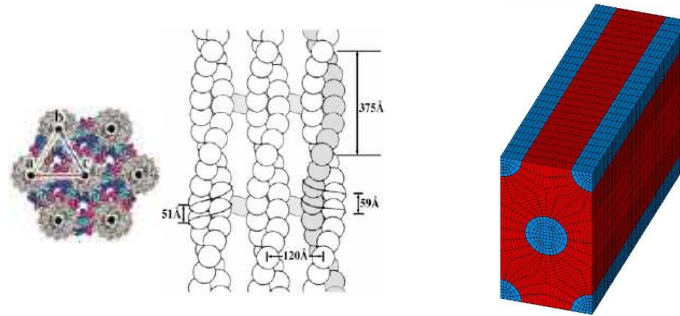


Figure 4: Microstructure of stereocilia as depicted in [6] and the deduced FE-model for the RVE.

## REFERENCES

- [1] Böhm, H. J.; A short introduction to basic aspects of continuum micromechanics, Lecture Notes, European Advanced Summer School, National University of Ireland, Galway, 1998
- [2] Janmey, P. A. et al.; Actin Filaments, Biophysics Textbook Online, Mai 2004
- [3] Li, S.; General unit cells for micromechanical analyses of unidirectional composites, Composites: Part A 32, **815-826**, Elsevier Science Ltd., 2001
- [4] Lukkassen, D. et al.; Some engineering and mathematical aspects on the homogenization method, Composite Engineering, Vol. 5, No. 5, **519-531**, Jan. 1995
- [5] Ting, T. C. T.; Anisotropic Elasticity - Theory and Applications, Oxford University Press, New York Oxford, 1996
- [6] Volkmann, N. et al.; An Atomic Model of Actin Filaments Cross-linked by Fimbrin and its Implications for Bundle Assembly and Function, The Journal of Cell Biology, Vol. 153, **947-956**, The Rockefeller University Press, Mai 2001

## DEVELOPMENT OF INTER- AND INTRAGRANULAR STRESSES DURING SWITCHING OF FERROELECTRIC POLYCRYSTALS

A. Haug<sup>1</sup>, Patrick R. Onck<sup>2</sup>, Erik Van der Giessen<sup>2</sup>

<sup>1</sup>Materialpruefanstalt Universitaet Stuttgart  
Pfaffenwaldring 32, 70569 Stuttgart, Germany  
e-mail: anja.haug@mpa.uni-stuttgart.de

<sup>2</sup> University of Groningen, Materials Science Center  
Nyenborgh 4, 9747 AG Groningen, The Netherlands  
e-mail: p.r.onck@rug.nl, e.van.der.Giessen@rug.nl

**Abstract.** *In polycrystalline ferroelectrics, as used in a wide range of applications, electric and stress fields interact so as to maintain compatibility. We study the influence of grain-to-grain interactions on the overall and local switching behaviour and in particular the induced stresses inside grains and across grain boundaries. The behaviour inside each grain is represented by the single-crystal model of [1] and the polycrystal response is obtained through a two-dimensional multi-grain model in which grains are represented individually. We investigate the effect of random grain orientations, both in the plane of consideration and in three directions.*

### Introduction

Calculations for example of ferroelectric device performans are carried out in two dimensions (2D) in order to minimize time and cost. This eliminates the geometrical three dimensionality of the problem but retains the fact that each individal crystal is a three-dimensional (3D) entity. One way to resolve this is to study 2D model polycrystals with a planar crystallography or to leave the 3D crystals be subjected to 2D deformations. A special case in the latter approach is to have all grains share the same direction normal to the plane of consideration. We investigate the effect of the way in which a random 2D polycrystal of 3D grains is constructed. In doing so, we emphasize how the grain–grain interactions affect the distributions of strain, polarization and stresses inside the grains.

### Single crystal model

The model we use for a single crystal is described in detail by [1]. Each grain is considered to comprise a number of different domains, corresponding to the possible directions of spontaneous polarization. Note that we do not explicitly account for the geometry of the domains inside the crystals, but use a 'smeared out' representation instead. Switching is modelled by the reduction of a domain and the increase of another domain by the same amount. The change is accompanied by a characteristic rate change in remanent polarization and remanent strain. Switching is governed by the thermodynamic driving force which is dual to the dissipative work rate. For numerical convenience, we adopt a power-law relation between the driving force and the incremental volume fraction [2].

## Multi-grain model

Although homogenization schemes such as the self-consistent method [1] can describe the overall response of ferroelectric polycrystalline materials quite accurately, they are limited in picking-up the stress fluctuations inside grains [3]. To capture the interactions between adjacent grains in detail, we adopt the multi-grain model proposed in [3] in which a polycrystal is represented by an aggregate of discrete grains. In the 2D studies here, the grains are assumed to be hexagons. Grain boundaries are simply lines along which the crystal orientation changes discontinuously; mechanical and electrical displacement, traction and charge are continuous across grain boundaries. Each grain is meshed with a grid of triangular finite elements, refined near grain boundaries, as illustrated in the inset of Fig. 1.

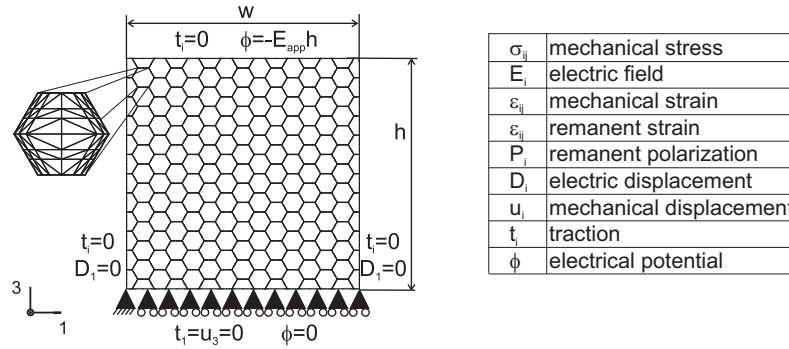


Figure 1: Definition of multi-grain model with boundary conditions.

Adopting the multi-grain concept, a rectangular piece of polycrystalline material, representing a typically experimental setup, is considered (Fig. 1). The electrical potential,  $\phi$ , has the value  $E_{app}/h$  on the top and its value is zero on the bottom. On the lateral sides  $D_1 = 0$  to decouple the material from the surrounding area. The displacement in  $x_3$ -directions,  $u_3$ , of the nodes on the bottom is zero and the left corner node is also fixed in the  $x_1$ -direction in order to prevent rigid body motion. All other sides are traction free,  $t_i = 0$  ( $i = 1, 3$ ).

In the  $x_2$ -direction normal to the plane of consideration, the electric field ( $E_2 = 0$ ) and the mechanical stress ( $\sigma_{2i} = 0$ ) is prescribed to vanish.

## Results

Results are presented for samples comprising 187 grains, each discretized by 72 triangular elements. The values of the modelling parameters for the switching systems as well as the material constants with respect to crystallographic axes can be found in Table 1 of [1]. The global components of the material tensors and for the switching necessary tensors are computed from its orientation, as specified by the Euler angles  $(\phi_g, \theta_g, \psi_g)$ . Two types of orientation distributions are considered. In one of these, the Euler angles are generated at random: the so-called 3D grain orientation. From these, 2D grain orientations are constructed such that the normals of the switching systems are pointing in the  $x_2$  direction, i.e.  $\theta_g = \psi_g = 0$ ; this leaves only the rotation  $\phi_g$  about the  $x_2$  axis as a random variable. Thus, by construction, both 3D and 2D grain orientations are nominally isotropic in the  $x_1$ - $x_3$  plane. In the same spirit, all six domains are assumed to be equally present in each grain. The parameters used in the power law are the same as in [3].

All results are normalized by  $D_0$ ,  $E_0$ ,  $\gamma_0$  or  $\tau_0$ ;  $D_0$  and  $E_0$  are the values at the onset of switching for purely electrical loading; similarly,  $\gamma_0$  and  $\tau_0$  mark the start of switching under

purely mechanical loading [1, 3].

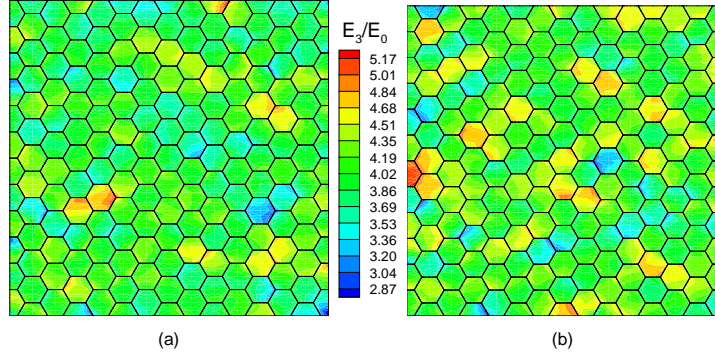


Figure 2: Distribution of  $E_3/E_0$  at  $E_{app} = 4E_0$  for a case with (a) 2D grain orientations and (b) 3D grain orientations.

First, in Fig. 2, we demonstrate that the internal electric field is affected by the different grain orientations. The magnitudes of the electric field are in the same range, but with different spatial distributions. In both calculations the highest and lowest fields can be found along the grain boundaries.

In Fig. 3 is macroscopic response plotted. The macroscopic displacement  $D^{mac}$ , and the macroscopic strain,  $\varepsilon^{mac}$ , are plotted versus the applied electric field. The macroscopic electric displacement is calculated as the total charge on the top divided by the area  $w$  of the top surface, and the macroscopic strain is computed from the average displacement  $u_3$  along the top of the sample divided by the cell height  $h$ . The hysteresis loop is not changed much when allowing for 3D grain orientations. In contrast, the mechanical response is much more sensitive. The butterfly loop of the 3D orientation is shifted to lower values compared with the 2D orientation. The microscopic values are given at the integration stations as averages over 14 different real-

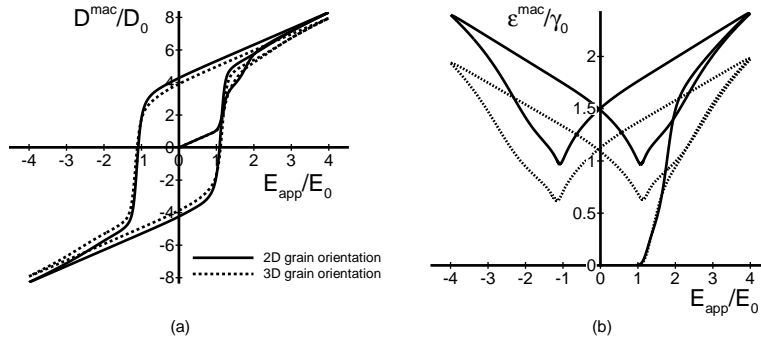


Figure 3: Comparison of the macroscopic response predicted for a 2D grain orientation (full line) and 3D grain orientation (dashed line) under plane stress conditions. (a) electrical response (hysteresis loop) and (b) mechanical response (butterfly loop).

izations for  $\varepsilon_{33}^R$ ,  $P_3^R$ ,  $\sigma_{33}$  and  $\varepsilon_{33}$  —all in the direction of the applied field— at the peak applied electric field of  $4E_0$ . Remanent strain and polarization show a bimodal distribution for the 2D grain orientation. This arises directly from the orientation dependence of these quantities. The peak at the right end of the distributions vanish for the 3D grain orientation. The minimum remanent parameters are smaller for the 3D grain orientation. The reduction is so strong that

even elements with no remanent strain occur. This arises due to the larger number of switching systems which can be activated. The unimodal strain histogram in Fig. 4c has a higher peak for the 3D grain orientation and, in addition, is narrower. This is attributed to the grain–grain constraints being stronger as there are more possibilities for orientation mismatch. The histograms of the normal stress in loading direction are basically identical, Fig. 4d.

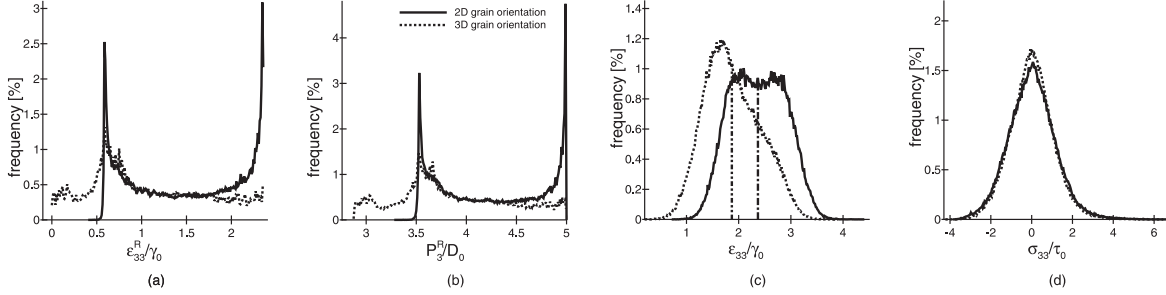


Figure 4: Frequency distributions of (a)  $\varepsilon_{33}^R/\gamma_0$ , (b)  $P_3^R/D_0$ , (c)  $\varepsilon_{33}/\gamma_0$  and (d)  $\sigma_{33}/\tau_0$  at  $E_{app} = 4E_0$  for 14 realizations of 2D grain orientations (full line) and 3D grain orientations (dashed) under plane stress conditions. The dash-dotted and dash-double-dotted lines in (c) indicate the median of  $\varepsilon_{33}/\gamma_0$  of the 2D and 3D grain orientation, respectively.

An extensive discussion can be found in [3]. Also the influence of the plane strain - plane stress condition is discussed there.

\*

#### Acknowledgement

This research has been carried out within the research programme “Evolution of the microstructure of materials” which is financially supported by the Netherlands foundation for Fundamental Research on Matter (FOM) and the Netherlands Institute for Metals Research (NIMR).

#### REFERENCES

- [1] J. E. Huber, and N. A. Fleck, and C. M. Landis, and R. M. McMeeking, A constitutive model for ferroelectric polycrystals, *Journal of the Mechanics and Physics of Solids* **47**, 1663–1697 (1999).
- [2] J. E. Huber, and N. A. Fleck, Multi-axial electrical switching of a ferroelectric: theory versus experiment, *Journal of the Mechanics and Physics of Solids* **49**, 785–811 (2001).
- [3] A. Haug, and J. E. Huber, and P. R. Onck, and E. Van der Giessen, Multigrain analysis versus self consistent estimates of ferroelectric polycrystals, *Journal of the Mechanics and Physics of Solids* **44**, 2066–2078 (2007).

## NUMERICAL SIMULATION OF MICROSTRUCTURES IN FINITE PLASTICITY USING RELAXED ENERGIES

Ulrich Hoppe<sup>1</sup> and Klaus Hackl<sup>2</sup>

Lehrstuhl für Allgemeine Mechanik, Ruhr-Universität Bochum  
Gebäude IA 3/126, 44780 Bochum, Deutschland

<sup>1</sup>e-mail: ulrich.hoppe@rub.de

<sup>2</sup>e-mail: klaus.hackl@rub.de

**Abstract.** *The convexity of energy functionals for inelastic materials is analyzed on the basis of an incremental variational principle. Non-quasiconvex problems give rise to microstructures and often exhibit mesh-dependent results when being solved by standard solution methods, e. g., FEM. A partial rank-one convexification enables a reduction of the mesh-dependency and allows to predict the occurrence and distribution of microstructures independent of the numerical realization.*

### Introduction

The formulation of constitutive equations in finite elasticity is confined by several restrictions. Besides the standard principles, e. g., the second law of thermodynamics or the principle of material frame indifference, convexity of the energy function guarantees the existence of solutions of the boundary value problem under consideration and is directly connected to material stability. While there is only one notion of convexity for one-dimensional functions,  $f : \mathbb{R} \rightarrow \mathbb{R}$ , generalized definitions are needed for the vectorial case,  $f : \mathbb{R}^n \rightarrow \mathbb{R}$ , [1,6].

Inelastic materials cannot be directly analyzed with respect to their convexity properties. This requires a variational formulation that is based on an incremental variational principle. For *generalized standard materials* the constitutive equations can be derived from a free energy and a dissipation function. The incremental problem implicitly depends on the internal variables at the beginning and the end of a time step. By means of an incremental variational principle the internal variables can be eliminated, resulting in a so-called condensed energy function, which only depends on the deformation gradient. The condensed energy is used to study the convexity properties of the problem.

As an example a problem from single crystal plasticity is considered. Finite element simulations involving a representative volume element under periodic boundary conditions give mesh-dependent solutions showing laminar microstructures. A consecutive refinement of the mesh size results in a greater number of oscillations of the displacement field. The spatial wavelength of these oscillations tends toward zero, exhibiting meaningless results in the limit. By convexification of the energy function the mesh dependency can be substantially reduced, while the occurrence and distribution of microstructures can be predicted in a well defined and physically meaningful manner.

## Single-slip elastoplasticity

Inelastic materials are characterized by dissipation, which is nonrecoverable energy expended via change of the internal variables. The internal variables measure the intrinsic state of the material produced by plastic deformation, hardening, damage, or phase-transformations. Standard generalized dissipative models with internal variables  $\mathbf{K}$  are typically described by two potentials: The specific Helmholtz free energy  $W(\mathbf{F}, \mathbf{K})$ , and a dissipation-functional  $\Delta(\mathbf{K}, \dot{\mathbf{K}})$ . The latter is used to define the evolution laws of the internal variables. By means of a time-incremental approach [3] the corresponding boundary value problem can be formulated in a proper variational framework. The advantage of this formulation is, that in a time-incremental setting it reduces to a pure minimization problem which can be analyzed by variational calculus. Explicit minimization with respect to the internal variables results in a condensed energy potential  $W_{\mathbf{K}_0}^{cond}(\mathbf{F})$ , not always given in a closed form.

In the context of single-slip crystal plasticity the internal variables  $\mathbf{K} = \{\gamma, p\}$  consist of the scalar plastic slip  $\gamma$  and a hardening parameter  $p$ . The free energy density function is chosen to be of a neo-Hookean type and depends on the deformation gradient  $\mathbf{F}$  only through its elastic part  $\mathbf{F}_e$ , which is in accordance with the finite deformation setting. The free energy density reads

$$W(\mathbf{F}, \gamma, p) = U(j) + \frac{\mu}{2} \text{tr}(\mathbf{F}_e^T \mathbf{F}_e) + \frac{a}{2} p^2, \quad U(j) = \frac{\Lambda}{4} (j)^2 - \frac{\Lambda + 2\mu}{2} \ln(j), \quad (1)$$

where the symbols  $\mu$ ,  $\Lambda$  and  $a$  denote material parameters and  $j = \det \mathbf{F}_e$ . The dissipation-function is chosen as

$$\Delta(\gamma, p, \dot{\gamma}, \dot{p}) = \begin{cases} r|\dot{\gamma}| & \text{if } |\dot{\gamma}| + \dot{p} \leq 0 \\ \infty & \text{else} \end{cases}. \quad (2)$$

For this particular example the minimization with respect to the internal variables can be carried out explicitly and a closed form of the condensed potential  $W_{\mathbf{K}_0}^{cond}$  is obtained

$$W_{\gamma_o, p_o}^{cond}(\mathbf{F}) = U(\det \mathbf{F}) + \frac{\mu}{2} \left[ \text{tr} \mathbf{F}^T \mathbf{F} - 2\gamma_o C_{sn} + \gamma_o^2 C_{ss} - \frac{(\max\{0, |C_{sn} - \gamma_o C_{ss}| - \frac{\tau_{crit} - a p_o}{\mu}\})^2}{C_{ss} + a/\mu} \right],$$

where,  $C_{sn}$ ,  $C_{ss}$  denote the components of the deformation tensor  $\mathbf{C} = \mathbf{F}^T \mathbf{F}$  in the direction of the slip-system vectors  $s$  and  $n$  (see [3] for details).

For a particular range of material parameters the condensed energy fails to be rank-one convex and, hence, fails to be quasiconvex. As a consequence, microstructures may be obtained as solutions of boundary value problems. The occurrence of microstructures can be demonstrated by direct finite element simulation using representative volume elements under periodic boundary conditions. Figure 1 shows two typical results of these simulations: Oscillations in the plastic slip field  $\gamma$ , forming first and second order laminates. These oscillations are highly mesh-dependent. The number of laminates grows towards infinity when the mesh becomes finer and finer.

The mesh-dependency and the accompanying material instability phenomena can be avoided by replacing the nonconvex condensed energy by a suitable relaxed energy. Because of its simple algorithmic structure and its ability to provide sufficient information to reconstruct the microstructure, we use the rank-one relaxation  $R^{(k)} W^{cond}(\mathbf{F})$  as the underlying relaxation technique. The numerical algorithm can be formulated as a restricted optimization problem. For example, in the 2-dimensional case and  $k = 1$  the objective function

$$\tilde{W}^{cond}(x, \mathbf{F}) := (1 - \lambda) W^{cond}(\mathbf{F} - \lambda \mathbf{a} \otimes \mathbf{b}) + \lambda W^{cond}(\mathbf{F} + (1 - \lambda) \mathbf{a} \otimes \mathbf{b}) \quad (3)$$

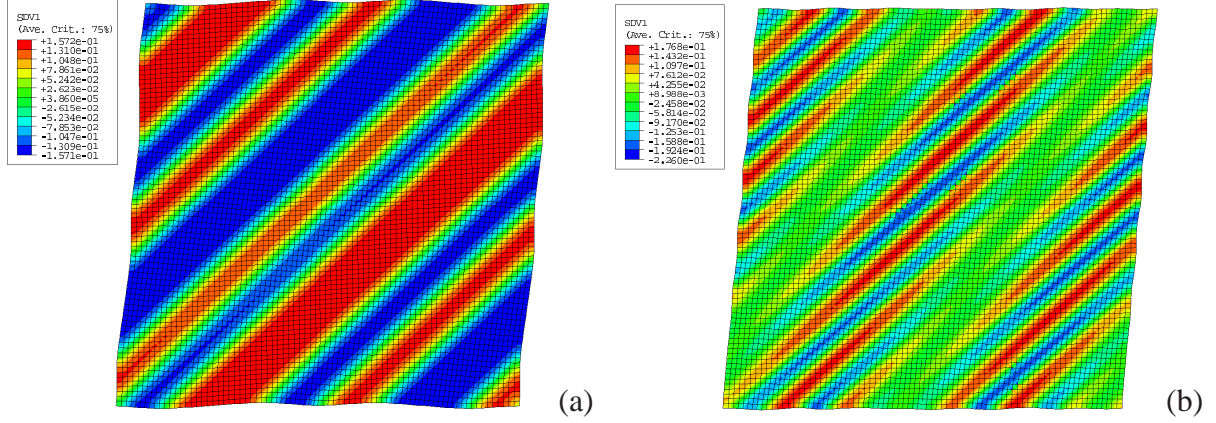


Figure 1: Single-slip plasticity: (a) First order laminates and (b) Second order laminates by direct finite element simulation assuming periodic boundary conditions.

depends on 4 optimization variables, for example,

$$x = (\lambda, \rho, \alpha, \beta), \quad \text{representing} \quad \mathbf{a} = \rho \begin{pmatrix} \cos(\alpha) \\ \sin(\alpha) \end{pmatrix}, \quad \mathbf{b} = \begin{pmatrix} \cos(\beta) \\ \sin(\beta) \end{pmatrix}. \quad (4)$$

The vectors  $\mathbf{a}$  and  $\mathbf{b}$  form the rank-one matrix  $\mathbf{a} \otimes \mathbf{b}$  and the scalar  $\lambda$  determines the volume fraction of the two phases of the first order laminate. The relaxed energy is obtained by solving the minimization problem

$$R^{(1)}W^{cond}(\mathbf{F}) = \min_{x \in \mathcal{B}} \tilde{W}^{cond}(x, \mathbf{F}) \quad (5)$$

for a given deformation gradient  $\mathbf{F}$  and a domain  $\mathcal{B}$  of  $x$  defined by

$$\mathcal{B} = \{x \in \mathbb{R}^4 \mid 0 \leq \lambda \leq 1, 0 \leq \rho, 0 \leq \alpha \leq \pi, 0 \leq \beta \leq 2\pi, \det(\mathbf{F}_i) > 0\}, \quad (6)$$

where  $\mathbf{F}_i$  denotes the deformation gradient of the  $i$ th phase. Corresponding minimization problems can be set up for higher order laminations. Although the realization of an algorithm for higher order laminates is straight forward, the exponentially growing number of optimization variables strongly limits its practical application. Already for low order laminates the numerical search for the minimizer of (5) turns out to be difficult, because the objective function may have several local extrema and the inequalities in (6) impose nonlinear constraints, which require a special treatment. Different procedures have been used to solve the minimization problem numerically. Probabilistic global search procedures have shown to be efficient and sufficiently robust. The procedure can be essentially improved by using starting values obtained from a rigid elastic model [5].

The rank-one relaxation of the simple shear problem has been computed using first-order and second-order laminates. In a finite element framework the above mentioned algorithm has to be performed in every material point (e.g. Gauss point) and within every time step. As a result of the numerical rank-one relaxation not only the energy and the volume fractions, but also the rank-one matrices are obtained from which sufficient information about the orientation of the laminar microstructure can be gathered. Figure 2 (a) shows the evolution of the volume fraction  $\lambda$  for the first order laminate obtained for a simple shear test. Figure 2 (b) compares approximations of the polyconvex hull  $W_{\delta,r}^{pc}(\mathbf{F})$ , realized with a procedure described in [2,4], and the second-order laminate hull  $R^{(2)}W(\mathbf{F})$ , realized by the algorithm described above. Both approximations almost coincide and significantly lower the energy. The good agreement suggests that the quasiconvex hull of  $W^{cond}$  can be realized by second order laminates.

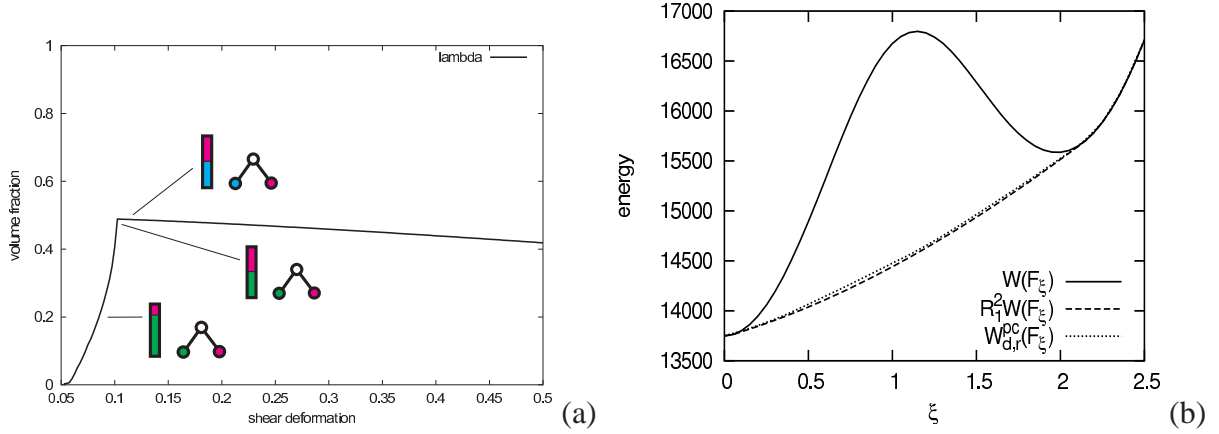


Figure 2: (a) Evolution of the volume fraction parameter  $\lambda$  for a first-order laminate; (b) Polyconvex envelope and second-order laminate hull for the condensed energy density in single-slip plasticity

## Conclusion

This work presents an approach to the calculation of microstructures for inelastic materials based on a reduced incremental variational principle. In essence, the condensed functional is of the same form as in nonlinear elasticity and can be analyzed by standard methods from the direct calculus of variations and convex analysis. It is demonstrated, that finite element simulations of non-quasiconvex problems may result in mesh-dependent solutions possibly showing a laminar microstructure. By rank-one relaxation of the reduced energy the formation of microstructures can be predicted in an essentially mesh-independent manner.

## REFERENCES

- [1] Ball, J. M. , Convexity conditions and existence theorems in nonlinear elasticity. *Arch. Rational Mech. Analysis*, (1977) 63:337–403.
- [2] Bartels S., Carstensen C., Hackl K., and Hoppe U., Effective relaxation for microstructures simulations: algorithms and applications. *Comp. Meth. Appl. Meth. Eng.*, 193, No. 48-51 (2004) 5143-5175.
- [3] Carstensen, C., Hackl, K., and Mielke, A., Nonconvex potentials and microstructures in finite-strain plasticity. *Proc. Roy. Soc. London (A)*, (2002), Vol. 458, pp. 299-317.
- [4] Carstensen, C.; Hackl, K.; Hoppe, U.; Orlando, A., Computational microstructures in phase transition solids and finite-strain elastoplasticity. *GAMM-Mitt.* 29 No. 2, (2006) pp. 215-246.
- [5] Conti S., Relaxation of single-slip single-crystal plasticity with linear hardening, in: *Multiscale Materials Modeling*, Eds. P. Gumbsch, Fraunhofer IRB, Freiburg, (2006), pp. 30-35.
- [6] Morrey C.B., Quasi-convexity and the lower semicontinuity of multiple integrals. *Pacific J. Math.*, 2 (1952) 25-53.

## APPLICATION OF MULTISCALE FEM TO THE SIMULATION OF HETEROGENEOUS MATERIALS

Sandra Ilic<sup>1</sup> and Klaus Hackl<sup>2</sup>

Institute of Mechanics  
Ruhr University of Bochum  
D-44780 Bochum, Germany  
<sup>1</sup>e-mail: sandra.ilic@rub.de  
<sup>2</sup>e-mail: klaus.hackl@rub.de

**Abstract.** *In this paper our intention is to show applications of multiscale FEM in modelling of two different kinds of heterogeneous materials. The subject of the first example is the simulation of solution-precipitation creep which is a diffusional process occurring in polycrystals if pressure and temperature are in a specific range. In the second example the overall material properties of cancellous bone are evaluated. As this material contains a liquid phase, dynamical investigations on a representative volume element are carried out.*

### Concept of the multiscale FEM

Multiscale FEM is based on the theory of homogenisation for which it is specific that real material properties have to be replaced by effective ones, obtained by examination of a representative volume element (RVE). The method is applicable only if the ratio of characteristic lengths of macroscale which is related to the simulated body and microscale which is related to the RVE tends to zero. In this case according to the concept of volume average the macrodeformation gradient  $\bar{\mathbf{F}}$  and first Piola Kirchhoff macrostress tensor  $\bar{\mathbf{P}}$  are defined by the expressions:

$$\bar{\mathbf{F}} = \frac{1}{V} \left[ \int_{\mathcal{B}} \mathbf{F} dV - \int_{\mathcal{L}} \mathbf{x} \otimes \mathbf{N} dA \right] = \frac{1}{V} \int_{\partial \mathcal{B}} \mathbf{x} \otimes \mathbf{N} dA, \quad (1)$$

$$\bar{\mathbf{P}} = \frac{1}{V} \int_{\mathcal{B}} \mathbf{P} dV = \frac{1}{V} \int_{\partial \mathcal{B}} \mathbf{t} \otimes \mathbf{X} dA. \quad (2)$$

Here  $\mathcal{B}$  is the RVE with volume  $V$ ,  $\partial \mathcal{B}$  is its boundary,  $\mathcal{L}$  is a boundary of voids inside RVE,  $\mathbf{N}$  is the normal vector on the surface and  $\mathbf{t}$  traction. In usual notation macroquantities are denoted by symbols with overbar and microquantities without it. It should be still stressed that the macrodeformation gradient  $\bar{\mathbf{F}}$  and the macrostress tensor  $\bar{\mathbf{P}}$  given by (1) and (2) additionally have to satisfy Hill's macrohomogeneity condition:

$$\bar{\mathbf{P}} : \dot{\bar{\mathbf{F}}} = \frac{1}{V} \int_{\mathcal{B}} \mathbf{P} : \dot{\mathbf{F}} dV. \quad (3)$$

This condition states that macropower has to be equal to volume average of micropower and its solutions define the boundary conditions on the microlevel [1].

In the following we will concentrate only on modelling of materials with periodic microstructure. For that particular case it is suitable to express the microdeformations dependent on the vector of microfluctuations  $\tilde{\mathbf{w}}$ :

$$\mathbf{x} = \bar{\mathbf{F}}\mathbf{X} + \tilde{\mathbf{w}} \quad (4)$$

which yields following superposition:

$$\mathbf{F} = \nabla \mathbf{x} = \bar{\mathbf{F}} + \nabla \tilde{\mathbf{w}} = \bar{\mathbf{F}} + \tilde{\mathbf{F}}. \quad (5)$$

One other consequence of assumption (4) is that microfluctuations must satisfy periodic and tractions antiperiodic boundary conditions on the periodic boundary of the RVE.

### Modelling of solution-precipitation creep

Solution-precipitation creep is a deformation process typical for polycrystalline material under specific pressure and temperature. It is based on diffusion of material particles within intercrystalline space which becomes very intensive in presence of a fluid phase and can lead to large deformations if an extended time period is observed.

In order to give a continuum-mechanical formulation of the problem, the behaviour of a polycrystal consisting of disjoint crystals  $\Omega_i$  with boundary  $\partial\Omega_i$  is analysed. Deformation of each crystal is decomposed into one elastic and one inelastic part yielding a multiplicative decomposition of deformation gradient:

$$\phi = \phi_i^E \circ \phi_i^I, \quad \mathbf{F} = \mathbf{F}_i^E \mathbf{F}_i^I. \quad (6)$$

The material formulation of the problem relies on the functional of total power given as

$$L = \dot{E} + \Delta \quad (7)$$

where  $E$  denotes stored elastic energy and  $\Delta$  dissipation. The stored elastic energy can be expressed via the Helmholtz free-energy  $\psi(\mathbf{F}^E)$  as

$$E = \sum_i \int_{\bar{\Omega}_i} \psi(\mathbf{F}(\mathbf{F}_i^I)^{-1}) \, d\bar{V} = \sum_i \int_{\Omega_i} \psi(\mathbf{F}(\mathbf{F}_i^I)^{-1}) J_i^I \, dV. \quad (8)$$

Here  $\bar{\Omega}_i = \phi_i^I(\Omega_i)$  is the volume of the inelastically deformed grain, and  $J_i^I$  the Jacobian corresponding to inelastic deformation  $\mathbf{F}_i^I$ . For definition of the dissipation term it is necessary to note that during the process two kinds of motion occur: material transport along the crystal boundaries and motion of the crystal boundary itself caused by solution/precipitation of material. If the velocity of material transport is denoted by  $\mathbf{Q}_i$  and normal velocity of boundary by  $v_i^n$ , the dissipation term becomes:

$$\Delta = \sum_i \int_{\partial\bar{\Omega}_i} \left[ \frac{\gamma}{2} \mathbf{Q}_i^2 + \frac{\kappa}{2} (v_i^n)^2 \right] \, d\bar{S} = \sum_i \int_{\partial\Omega_i} \left[ \frac{\gamma}{2} \mathbf{Q}_i^2 + \frac{\kappa}{2} (v_i^n)^2 \right] J_i^I |(\mathbf{F}_i^I)^{\text{T}-1} \mathbf{N}_i| \, dS. \quad (9)$$

Here  $\kappa$  and  $\gamma$  are inelastic constants such that  $\kappa/\gamma \ll d^2$ , where  $d$  corresponds to a characteristic dimension of a grain. As a consequence of mass conservation, the types of motion described above depend on each other and they must satisfy following coupling condition:

$$v_i^n = \bar{\nabla} \cdot \mathbf{Q}_i. \quad (10)$$

Having in mind equations (8)-(10) the Lagrangian obtains the final form

$$L = \sum_i \left[ \frac{d}{dt} \int_{\Omega_i} \psi \left[ \mathbf{F} (\mathbf{F}_i^I)^{-1} \right] J_i^I dV + \int_{\partial\Omega_i} \left[ \frac{\gamma}{2} \mathbf{Q}_i^2 + \frac{\kappa}{2} (v_i^n)^2 + \alpha_i (v_i^n - \bar{\nabla} \cdot \mathbf{Q}_i) \right] J_i^I \left| (\mathbf{F}_i^I)^{T-1} \mathbf{N}_i \right| dS \right], \quad (11)$$

where  $\alpha_i$  is Lagrange multiplier for which it can be shown that it is a smooth approximation of normal component of Eshelby tensor [2].

In order to investigate the influence of solution-precipitation creep on the deformation of a sample of real dimensions the following simulation is carried out. On the macrolevel of multiscale method one square plate with side length 20mm and load  $p = 1$  kN/mm is observed (Fig.1.a). Vertical displacements on lower boundary and horizontal displacements on the left one are constrained. For simulation of a random polycrystalline structure in each Gauss point of the plate one RVE with arbitrary orientation in plane is attached. Overall material behaviour is defined by free energy density of Neo-Hookean material and mixed variational formulation due to Simo, Taylor and Pister. On the microlevel a polycrystal consisting of nine crystals is chosen (Fig.1.b). The behaviour of the material on this level is defined by the Lagrangian (11). Final results of tests are displacements on the boundary of the plate. In Figure 1.c horizontal displacements on the right boundary are denoted by  $u$  and vertical displacements on the upper boundary by  $v$ . Inelastic constants  $\kappa$  and  $\gamma$  are chosen in such a way that monitoring of deformations is possible over several time steps.

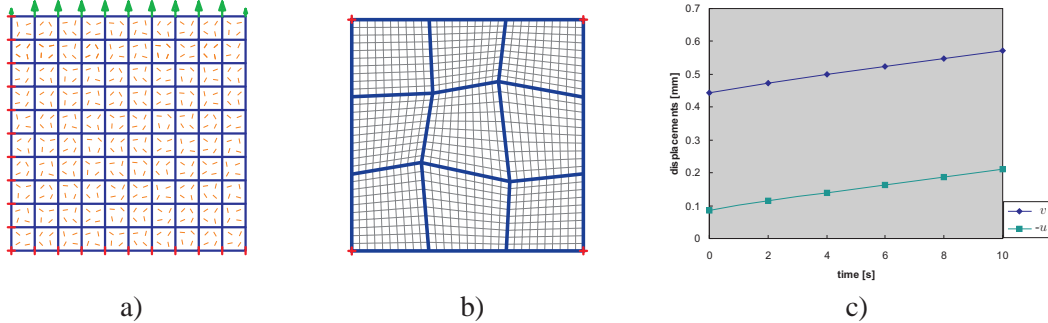


Figure 1: a) Tension test of a plate. b) Polycrystalline RVE. c) Resulting displacements on the boundary of plate for assumed material parameters:  $E = 23$  kN/mm<sup>2</sup>,  $\nu = 0.16$ ,  $\gamma = 50000$  kNs/mm<sup>5</sup>,  $\kappa = 1000$  kNs/mm<sup>3</sup>.

## Investigation of properties of cancellous bone

Cancellous bone is a two component structure consisting of bone frame and interstitial blood-marrow. The study of its properties is important as it can yield early detecting of osteoporosis whose general indications are that the bone frame get thinner and partially disappears. In that case porosity of the material can increase from normal value of 72% until even 95%. Opposed to the previous example here linear material behaviour and dynamic excitation will be observed requiring a formulation of the problem in complex domain.

An important property of RVE in this case is that it consists of a solid and a fluid phase. The state of the stress  $\sigma$  and strain  $\epsilon$  in any point of solid phase  $\Omega_s$  is defined by

$$-\omega^2 \rho_s \mathbf{u} - \nabla \cdot \sigma_s = 0, \quad \sigma_s = \mathcal{C}_s : \epsilon, \quad (12)$$

where  $\omega$  is the excitation frequency,  $\mathbf{u}$  the displacement field,  $\rho_s$  the density of solid material and  $\mathbf{C}_s$  is the complex material tensor dependent on complex bulk and shear modulus whose imaginary parts have to be calculated according to relations:  $K_s^I = \frac{\delta}{\pi} K_s^R$ ,  $\mu_s^I = \frac{\delta}{\pi} \mu_s^R$ , where for blood-marrow the logarithmic decrement takes the value  $\delta = 0.1$ . The state inside the fluid phase  $\Omega_f$  is defined by:

$$-\omega^2 \rho_f \mathbf{u} - \nabla \cdot \boldsymbol{\sigma}_f = \mathbf{0}, \quad \boldsymbol{\sigma}_f = K_f \nabla \cdot \mathbf{u} \mathbf{I} + 2i\omega\eta \boldsymbol{\epsilon} + i\omega\xi \nabla \cdot \mathbf{u} \mathbf{I}. \quad (13)$$

In this expressions viscosity coefficients  $\eta$ ,  $\xi$ , bulk modulus  $K_f$  and density  $\rho_f$  determine fluid properties and  $\mathbf{I}$  denotes the unit tensor. Coupling between phases of the RVE is given by the condition that displacements on interface of materials have to be compatible:

$$\mathbf{u}_s = \mathbf{u}_f \quad \text{on} \quad \Gamma = \Omega_s \cap \Omega_f. \quad (14)$$

Overall viscoelastic behaviour is described by the constitutive law

$$\boldsymbol{\sigma} = \bar{\mathbf{C}} : \boldsymbol{\epsilon} \quad (15)$$

and in our investigations we study the change of the effective elasticity tensor  $\bar{\mathbf{C}}$  dependent on the geometry of solid phase. For that purpose a RVE consisting of solid frame with thin walls and liquid corn is observed. In Figure 2.a an example of intermediate results on the microscale is shown. Here periodic boundary conditions for microfluctuations as well as compatibility condition (14) are satisfied. In order to illustrate final results in Figure 2.b change of two components of tensor  $\bar{\mathbf{C}}$  with respect to porosity is shown. Our further intention is to propose alternative models of RVE and to simulate such tests where sound attenuation of cancellous bone can be identified.

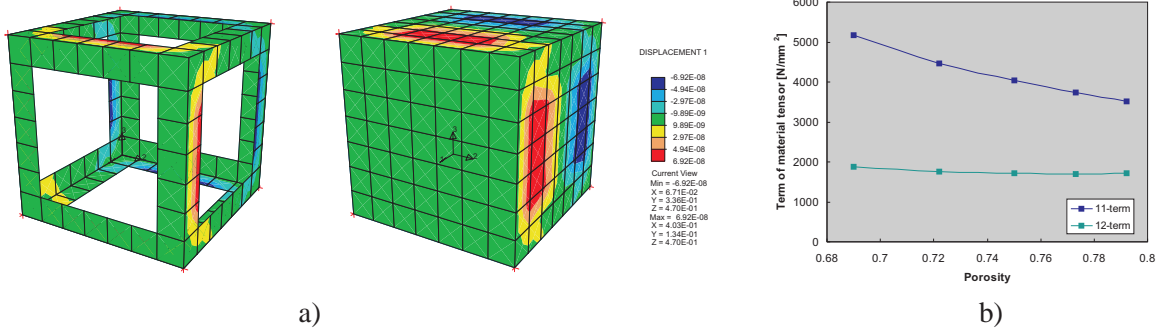


Figure 2: a) Example of calculations on microscale. b) Change of terms  $\bar{C}_{11}$  and  $\bar{C}_{12}$  of effective elasticity tensor with respect to porosity. Results are obtained using following values:  $\rho_f = 950 \text{ kg/m}^3$ ,  $K_f = 2.00 \times 10^9 \text{ Pa}$ ,  $\eta = 1.5 \text{ Ns/m}^2$ ,  $\xi = 0 \text{ Ns/m}^2$ ,  $\rho_s = 1960 \text{ kg/m}^3$ ,  $K_s^R = 2.04 \times 10^{10} \text{ Pa}$ ,  $\mu_s^R = 3.47 \times 10^{10} \text{ Pa}$ ,  $\omega = 100 \text{ kHz}$ .

## Conclusions

Application of multiscale FEM enables one to simulate behaviour of materials with different microstructure, illustrated here by two examples. In the first case deformation of a macroscopic sample caused by solution-precipitation creep is observed. Such numerical simulations are needed as due to its extremely slow nature this process is almost inaccessible experimentally. In the second case we are interested in evaluation of the effective elasticity tensor of a cancellous bone. Calculations are carried out for different geometry of the solid phase of RVE in order to analyse the influence of increasing porosity on material properties.

## REFERENCES

- [1] J. Schröder, Homogenisierungsmethoden der nichtlinearen Kontinuumsmechanik unter Beachtung von Stabilitätsproblemen, Habilitationsschrift, Universität Stuttgart, (2000).
- [2] K. Hackl, and S. Ilıc, Solution-precipitation creep–continuum mechanical formulation and micromechanical modelling, *Archive of Applied Mechanics* **74**, 773–779 (2005).

## MODELLIERUNG VON RISSWACHSTUM IN PIEZOELEKTRISCHEN MATERIALIEN MITTELS MODERNER ADAPTIVER FEM-LÖSUNGSSTRATEGIEN

**Łukasz Jański<sup>1</sup>, Peter Steinhorst<sup>2</sup>, Matthias Scherzer<sup>1</sup>,  
Meinhard Kuna<sup>1</sup> und Arnd Meyer<sup>2</sup>**

<sup>1</sup>TU Bergakademie Freiberg, Institut für Mechanik und Fluidodynamik  
Lampadiusstraße 4, D-09596 Freiberg  
e-mail: Lukasz.Janski@imfd.tu-freiberg.de

<sup>2</sup>TU Chemnitz, Fakultät für Mathematik  
Reichenhainer Straße 39, D-09107 Chemnitz  
e-mail: peter.steinhorst@mathematik.tu-chemnitz.de

**Abstract.** *Im vorliegenden Beitrag werden die theoretischen Grundlagen eines numerischen Werkzeuges zur Modellierung des Risswachstums in piezoelektrischen Scheiben dargestellt. Die Methodik basiert auf modernen adaptiven FE-Lösern, dem Einsatz asymptotischer Lösungen sowie auf der Interaction-Integral-Technik. Die Intensitätsfaktoren dienen zur Bewertung des bruchmechanischen Verhaltens. Die theoretischen Grundlagen werden im Vortrag durch die Ergebnisse numerischer Berechnungen ergänzt. Es wird gezeigt, dass die adaptive FEM mit zunehmender Netzverfeinerung gegen die exakte analytische Rissspitzenlösung konvergiert, so dass die Spannungsintensitätsfaktoren mit großer Genauigkeit bestimmt werden können. Die für die Interaction-Integral-Technik notwendige IRWIN-Matrix wird in Abhängigkeit von der Polungsrichtung des transversal-isotropen Materialverhaltens berechnet.*

### Einleitung

In moderne adaptive mechanische Systeme werden heutzutage eine Vielzahl von piezoelektrischen Sensoren und Aktuatoren integriert. Die Konstruktion dieser adaptronischen Systeme erfordert nicht nur die Sicherstellung der Funktionalität, sondern auch die Gewährleistung von Festigkeit, Bruchsicherheit und Ermüdung. Deshalb ist es notwendig, effiziente Techniken zur bruchmechanischen Charakterisierung von Piezomaterialien zu entwickeln. Für stationäre Risse in homogenen piezoelektrischen Strukturen existieren bereits bewährte FE-Techniken [1]. Fragen der Ermüdungsrissausbreitung unter elektromechanischen Wechselbelastungen sind noch weitgehend ungeklärt. Die vorliegende Arbeit widmet sich gerade dieser Thematik: Entwicklung eines numerischen Werkzeuges zur Modellierung von Risswachstum in piezoelektrischen Scheiben (ebener Verzerrungszustand). Hervorzuheben ist hierbei die Verwendung von modernen iterativen Lösungsverfahren, die fehlergesteuerte Netzverfeinerungsstrategien nutzen und mit deren Hilfe Risswachstum effektiv simuliert werden kann, wobei lokale asymptotische Rissspitzenlösungen sowie die Interaction-Integral-Technik eingesetzt werden. Der Beitrag stellt eine Erweiterung der in [2], [3] für elastisches Material entwickelten numerischen Verfahren auf piezoelektrische Strukturen dar.

## Numerisches Lösungsverfahren

Um die elektromechanischen Bilanzgleichungen [4] einer piezoelektrischen Struktur zu Lösen, wird die Finite-Elemente-Methode benutzt. Den Ausgangspunkt zur Konstruktion eines FE-Werkzeuges stellt die Variationsformulierung

$$\begin{aligned} a(u_\alpha, v_\beta) + b(\varphi, v_\beta) &= F(v_\beta) \quad \forall v_\beta \in V \\ b(\psi, u_\alpha) - c(\psi, \varphi) &= -G(\psi) \quad \forall \psi \in U \end{aligned} \quad (1)$$

dar. Hierbei sind  $V$  und  $U$  Räume der Funktionen, die zum HILBERT-Raum  $H^1(\Omega)$  gehören und entsprechende DIRICHLETSche Randbedingungen erfüllen. Die gesuchten Koordinaten  $u_\alpha$  des mechanischen Verschiebungsvektors und das elektrische Potential  $\varphi$  gehören ebenso zu den entsprechenden Räumen  $V$  oder  $U$ . Die Finite-Elemente-Diskretisierung des Problems (1) führt auf ein algebraisches, lineares Gleichungssystem mit einer quadratischen Matrix, die symmetrisch, aber indefinit ist. Es wird eine verallgemeinerte BRAMBLE-PASCIAK Methode [5] benutzt, um aus der indefiniten quadratischen Matrix eine positiv-definite zu machen. Die Methode basiert auf einer geeigneten Wahl des Vorkonditionierers. Da man im Rahmen der FE-Diskretisierung mit der adaptiven Netzverfeinerung arbeitet, wird ein hierarchischer Vorkonditionierer verwendet. Die adaptive Netzverfeinerung sichert eine optimale Finite-Elemente-Dichte in unterschiedlichen Teilen des Vernetzungsgebietes. Das vorkonditionierte, algebraische, lineare Gleichungssystem wird schließlich mit der Methode der konjugierten Gradienten iterativ gelöst. Es ist zu betonen, dass im Rahmen des vorgestellten Algorithmus kein Zusammenbau einer Gesamtsteifigkeitsmatrix stattfindet. Nur die Steifigkeitsmatrizen derjenigen Elemente, die in einem adaptiven Schritt einer Änderung unterliegen, werden aktualisiert.

## Asymptotische Lösung

Um die Bruchparameter im Rahmen einer FE-Lösung mit der notwendigen Genauigkeit zu bestimmen, muss die Gestalt der physikalischen Felder in der unmittelbaren Nähe einer Rissspitze bekannt sein. Diese asymptotischen Felder lassen sich mit dem von MUSSCHELICH-WILI in [6] und LEKHNITSKII in [7] vorgeschlagenen Formalismus konstruieren (siehe [4]) und haben die Form

$$\begin{aligned} \sigma_{\alpha\beta}(r, \theta) &= \sum_{M=I,II,IV} K_M r^{-0.5} \bar{\sigma}_{\alpha\beta}^M(\theta) \quad , \\ D_\alpha(r, \theta) &= \sum_{M=I,II,IV} K_M r^{-0.5} \bar{D}_\alpha^M(\theta) \quad , \\ u_\alpha(r, \theta) &= \sum_{M=I,II,IV} K_M r^{0.5} \bar{u}_\alpha^M(\theta) \quad , \\ \varphi(r, \theta) &= \sum_{M=I,II,IV} K_M r^{0.5} \bar{\varphi}^M(\theta) \end{aligned} \quad (2)$$

für homogenes piezoelektrisches Material. Dabei sind  $r$  und  $\theta$  die Koordinaten eines polaren Koordinatensystems mit dem Ursprung in der Rissspitze,  $\sigma_{\alpha\beta}$  die Koordinaten des Spannungstensors,  $D_\alpha$  die Koordinaten des Vektors der dielektrischen Verschiebung,  $u_\alpha$  die Koordinaten des Verschiebungsvektors und  $\varphi$  das elektrische Potential. Die Felder (2) weisen die klassische

Rissingularität auf, deren Koeffizienten die mechanischen  $K_I$ ,  $K_{II}$  und der dielektrische  $K_{IV}$  Intensitätsfaktoren sind.

### Interaction-Integral

Für die Berechnung der Intensitätsfaktoren  $K_I$ ,  $K_{II}$  und  $K_{IV}$  wird die Interaction-Integral-Technik [8] benutzt. Im Folgenden wird zuerst eine spezielle Schreibweise der Funktionen (2) eingeführt. Alle diese Funktionen lassen sich als eine Summe

$$\Psi = \sum_{M=I,II,IV} K_M \Psi^M \quad (3)$$

wiedergeben. Hierbei entspricht  $\Psi$  einem der physikalischen Felder in (2). Somit erhält man für das elektromechanische Interaction-Integral [1], [8]

$$J^{NM} = \int_C (H^{NM} n_1 - \sigma_{\alpha\beta}^N u_{\alpha,1}^M n_\beta + D_\alpha^N E_1^M n_\alpha) dC \quad (4)$$

mit  $N, M = I, II, IV$  und

$$H^{NM} = \frac{1}{2} c_{\alpha\beta\omega\delta} \epsilon_{\alpha\beta}^N \epsilon_{\omega\delta}^M - \frac{1}{2} \kappa_{\alpha\beta} E_\alpha^N E_\beta^M - e_{\alpha\beta\omega} \epsilon_{\beta\omega}^N E_\alpha^M. \quad (5)$$

Hierbei ist  $C$  eine beliebige Integrationskontur, die an gegenüberliegenden Rissufern startet und endet sowie die Risspitze umläuft.  $n_\alpha$  sind die Koordinaten des Normalenvektors zur Integrationskontur,  $\epsilon_{\alpha\beta}$  die Koordinaten des Verzerrungstensors,  $E_\alpha$  die Koordinaten des Vektors des elektrischen Feldes.  $c_{\alpha\beta\omega\delta}$ ,  $\kappa_{\alpha\beta}$  und  $e_{\alpha\beta\omega}$  stellen die entsprechenden Koordinaten der elastischen, dielektrischen und piezoelektrischen Materialtensoren dar. In (4) kann auch anstelle einer Funktion aus (2) die FE-Lösung des behandelten Problems mit unbekannten Intensitätsfaktoren eingesetzt werden. Die entsprechenden Interaction-Integrale bezeichnen wir dann mit  $J^{(FEM)M}$  und  $J^{N(FEM)}$ . Auf diese Weise lassen sich die gesuchten Intensitätsfaktoren  $K_N$  aus der FE-Lösung mit Hilfe des linearen Gleichungssystems

$$J^{(FEM)M} + J^{M(FEM)} = \sum_{N=I,II,IV} Y_{MN} K_N \quad (6)$$

bestimmen. Hierbei ist  $Y_{MN}$  die IRWIN-Matrix, welche die Beziehung

$$G = \sum_{N=I,II,IV} \sum_{M=I,II,IV} \frac{1}{2} K_M Y_{MN} K_N \quad (7)$$

zwischen den Intensitätsfaktoren und der elektromechanischen Energiefreisetzungsrate  $G$  herstellt.

### Ergebnisse

Die in diesem Text dargestellten theoretischen Grundlagen eines numerischen Werkzeuges zur Modellierung des Risswachstums in piezoelektrischen Scheiben werden im Vortrag durch die numerischen Ergebnisse ergänzt. Es wird nachgewiesen, dass die adaptive FEM mit zunehmender Netzverfeinerung gegen die exakte analytische Risspitzenlösung konvergiert. Die charakteristische Gestalt der elektromechanischen Felder in der unmittelbaren Nähe der Risspitze wird für Piezomaterialien dargestellt. Die in der Interaction-Integral-Technik verwendete

IRWIN-Matrix wird in Abhängigkeit von der Polungsrichtung des transversal-isotropen Materialverhaltens präsentiert. Im Vortrag wird bewiesen, dass die Spannungsintensitätsfaktoren mit großer Genauigkeit mit der Anwendung des in diesem Text vorgestellten numerischen Werkzeuges bestimmt werden können.

### **Zusammenfassung und Ausblick**

Es wurden die theoretischen Grundlagen zur Entwicklung eines numerischen Werkzeuges für die Modellierung des Risswachstums in einer piezoelektrischen Scheibe dargestellt. Der numerische Algorithmus basiert auf der adaptiven Finiten-Elemente-Methode. Die Intensitätsfaktoren dienen zur Bewertung des bruchmechanischen Verhaltens. Diese Faktoren kann man mit der Interaction-Integral-Technik auf effektive Weise im Postprocessing bestimmen. Die theoretischen Grundlagen werden im Vortrag durch die numerischen Ergebnisse ergänzt. Die weitere Arbeit besteht in der Formulierung eines Bruchkriteriums sowie in der Einbeziehung des adaptiv-iterativen Solvers in die Simulation von Risswachstum.

### **REFERENCES**

- [1] M. Kuna, Finite element analyses of cracks in piezoelectric structures: a survey, *Archive of Applied Mechanics* **76**, 725–745 (2006).
- [2] F. Rabold, A. Meyer, M. Scherzer und M. Kuna, Finite-Elemente-Simulation von Risswachstum mittels effizienter adaptiv-iterativer Solver, *DVM-Bericht* **236**, 171–181 (2004).
- [3] A. Meyer, F. Rabold und M. Scherzer, Efficient finite element simulation of crack propagation using adaptive iterative solvers, *Communications in Numerical Methods in Engineering* **22**, 93–108 (2006).
- [4] Q.-H. Qin, *Fracture Mechanics of Piezoelectric Materials*, WIT Press (2001).
- [5] A. Meyer und T. Steidten, Improvements and Experiments on the Bramble-Pasciak Type CG for Mixed Problems in Elasticity, Preprint-Reihe des Chemnitzer Sonderforschungsbereiches 393 (Numerische Simulation auf massiv parallelen Rechner) TU Chemnitz-Zwickau, Fakultät für Mathematik **01-13**, (2001).
- [6] N.I. Mučhelichwili, *Einige Grundaufgaben zur mathematischen Elastizitätstheorie*, VEB Fachbuchverlag Leipzig (1971).
- [7] S.G. Lekhnitskii, *Theory of Elasticity of an Anisotropic Body*, Mir Publishers Moscow (1981).
- [8] M. Enderlein, A. Ricoeur und M. Kuna, Finite element techniques for dynamic crack analysis in piezoelectrics, *International Journal of Fracture* **134**, 191–208 (2005).

## STABLE CRACK GROWTH IN PIEZOELECTRIC CERAMICS AND PZT/ELECTRODE INTERFACES

H. Jelitto<sup>1</sup>, F. Gehrig<sup>1</sup>, G. A. Schneider<sup>1</sup>, C. Häusler<sup>2</sup>, P. Neumeister<sup>2</sup>, and H. Balke<sup>2</sup>

<sup>1</sup>Hamburg University of Technology, Institute of Advanced Ceramics  
Denickestr. 15, D-21073 Hamburg  
e-mail: h.jelitto@tu-harburg.de

<sup>2</sup> Technische Universität Dresden, Institut für Festkörpermechanik  
D-01062 Dresden

**Abstract.** *The total (linear) energy release rate for crack growth in PZT ceramics and metal/ceramics interfaces is experimentally determined using a special modulation technique. In order to achieve stable crack growth a very stiff testing machine has been developed.*

### Introduction

The fracture behavior of piezo ceramics under electromechanical loads is of particular interest, since these materials are used in sensors and actuators in versatile technical fields. Therefore, the fracture behavior of piezoelectric ceramics (PZT) as well as metal/PZT interfaces is examined in four point bending under mechanical and electric loading and conditions of controlled crack growth. The experiments are performed in a custom made very stiff testing machine. A special modulation technique allows for the in-situ determination of the mechanical compliance  $C_m$ , the capacitance  $C_e$ , and the piezoelectric compliance  $C_p$  of the specimen as a function of the crack length. By calculating the derivatives of these generalized compliances with respect to the crack surface area we get the linear part of the total energy release rate.

### Stable crack growth in PZT bulk material

The two cases 'insulating crack' and 'conducting crack' with the given field orientations in Fig. 1 are measured in PZT with stable crack advance. In both cases we have homogeneous poling parallel or anti-parallel to the electric far field. Previous experiments have shown that the crack is semi-permeable to the electric field, because the relative permittivity in the crack interior is not 1 but around 30 [1]. The geometrical set-up for the insulating crack is shown in Fig. 2.

The total (linear) energy release rate is given in Eq. (1) representing a generalized Irwin-Kies-relation. Its derivation from the corresponding thermodynamic potential was done by Z. Suo [2]. The index  $V$  stands for constant voltage and  $F$  for constant force. We have

$$G_{tot} = \frac{F^2}{2} \frac{\partial C_m^V}{\partial A} + \frac{V^2}{2} \frac{\partial C_e^F}{\partial A} + FV \frac{\partial C_p}{\partial A}, \quad (1)$$

$$C_e^F = \left( \frac{\partial Q}{\partial V} \right)_F, \quad C_m^V = \left( \frac{\partial \Delta}{\partial F} \right)_V, \quad C_p = \left( \frac{\partial Q}{\partial F} \right)_V = \left( \frac{\partial \Delta}{\partial V} \right)_F \quad (2)$$

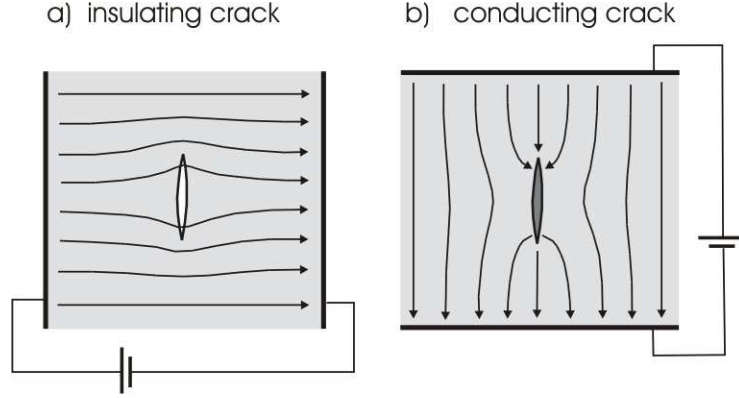


Figure 1: The two relevant configurations of poled piezoelectric ceramics with crack and electric field distribution, a) for an insulating semi-permeable crack and b) for a conducting crack.

where  $F$ ,  $V$ ,  $Q$ ,  $\Delta$  and  $A$  are force, voltage, charge, displacement, and crack surface area. The generalized compliances  $C_e^F$ ,  $C_m^V$ , and  $C_p$  are the capacitance, the mechanical compliance and the piezoelectric compliance, and are measured according to Eqs. (2).

Scrutinizing the modulation technique and the experimental results we found that the small displacement modulation with an amplitude of about 30 nm yields pure linear elastic response of the material. Thus, we measure solely the intrinsic toughness due to the creation of new crack surface. It means that the linear elastic energy release rate is separated from dissipative processes like domain switching. Fig. 3 gives an example for stable crack advance in PZT (PIC151)-bulk material. The diagram shows the mechanical, the piezoelectric, and the electric contribution  $G_m^V$ ,  $G_p$ , and  $G_e^F$  of the total linear energy release rate. Here, the sample is loaded by an additional external field of 375 V/mm, perpendicular to the crack surface. The sum of the three contributions yield a value around zero J/m<sup>2</sup>, which would not be physically meaningful. Thus, the total linear energy release rate is not a good fracture criterion but more likely the mechanical part of it. This was proposed before also by Park and Sun [3].

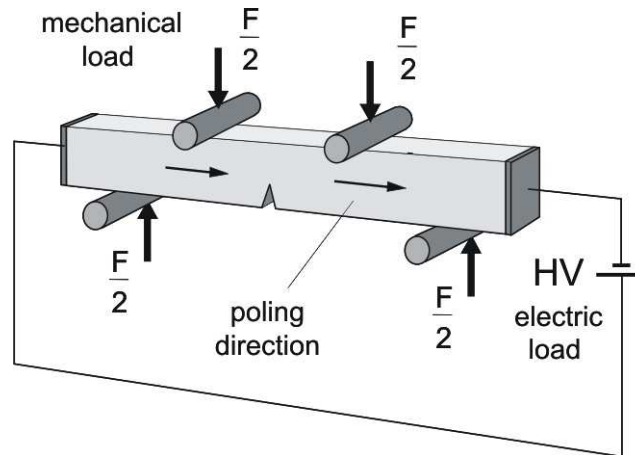


Figure 2: Schematic four point bending set-up for the insulating crack.

In the case of PZT-bulk material the effect of an external electric field is quite different for the insulating and for the conducting crack. Having an insulating crack electric fields between -500 and 500 V/mm yield changes of  $G_m^V$  of the order of 10 %. This is much less than theoretically

predicted for the impermeable crack, implying that the interior of the crack is highly permeable to electric fields, as said before. In the case of a conducting crack (see also Heyer et al. [4]), realized with a NaCl-solution in the crack interior, the effect of a corresponding electric field is of the order of 100 %. For example, with the appropriate field direction the crack grows slowly by its own without any mechanical loading, which is in agreement with theoretical predictions. (For the conducting crack only the  $K$ -factors were evaluated.)

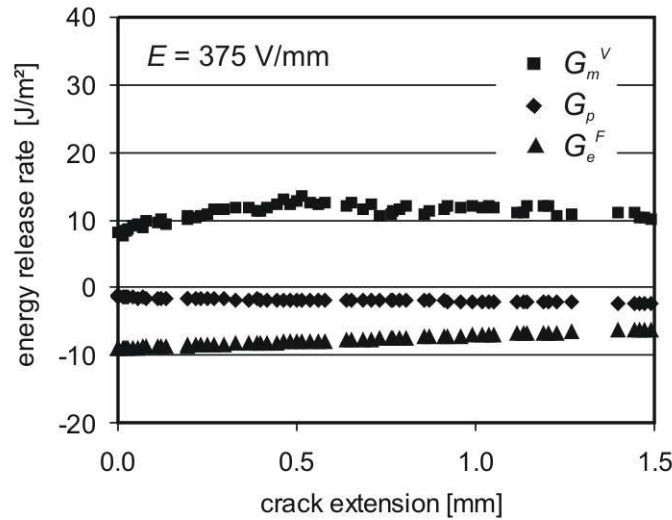


Figure 3: Linear contributions to the total energy release rate.

### Stable crack growth in metal/ceramics interfaces

The modulation method was applied also for metal/ceramic interfaces in commercial piezoelectric actuators. For PZT-bulk material as well as for the interfaces in multilayer actuators the experimental data are compared with FEM-calculations, taking into account the piezoelectric coupling and the layout of the inner metal electrodes of the actuator. The theoretical and experimental data agree quite well. Technically it is more difficult to achieve stable crack advance in metal/ceramic interfaces than in PZT-bulk material, because in the first case the fracture toughness is much lower (compare Figs. 3 and 4).

An example of the linear energy release rate measured along one of the inner electrodes of a multilayer actuator is given in Fig. 4. The polarization of the actuator was not alternating like in the commercial case but unidirectional. The external electric field, applied parallel to the direction of the poling field, was switched on and off in order to see an effect on the energy release rate. If there is any effect, it is rather small. When switching off the electric field at about 2.2 mm crack extension, it seems that  $G_m^V$  goes down a little bit by the order of 10 %. Also here the crack is semi-permeable. Furthermore, it can be seen that the total linear energy release rate, given by the continuous line, is not a valid fracture criterion. An appropriate criterion is given more likely by  $G_m^V$  or by the sum  $G_m^V + G_p$ . (The problem that  $G_m^V$  for example is not invariant to variable transformation is not addressed here.)

In the current experiments with interfacial crack growth mechanical mixed mode loading is investigated in an experiment of asymmetric three point bending with stable crack advance.

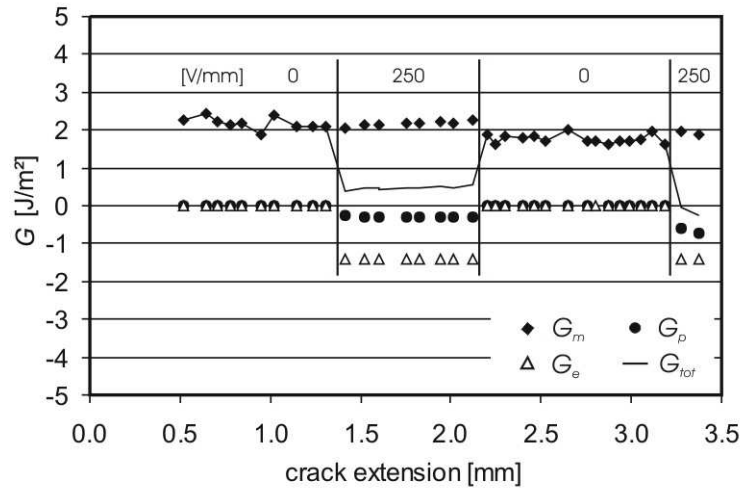


Figure 4: Energy release rate for crack growth in a metal ceramic interface.

The notch is shifted away from the middle position between the lower support rollers, yielding a combination of the stress intensity factors  $K_I$  and  $K_{II}$ . During the measurement the crack does not bend off but stays in the interface. The crack morphology depends on the poling configuration.

Thus, a new method is presented which allows for the determination of the total linear energy release rate including the mechanical, the electric, and the piezoelectric contribution for crack growth in piezoelectric ceramics. A paper [5], describing the experiments in detail for the case of PZT-bulk material, has been accepted for publication and two other papers are in preparation.

## REFERENCES

- [1] G. A. Schneider, F. Felten and R. M. McMeeking, The electrical potential difference across cracks in PZT measured by Kelvin Probe Microscopy and the implications for fracture, *Acta Mater.* **51**, 2235–2241 (2003).
- [2] Z. Suo, Mechanics concepts for failure in ferroelectric ceramics, *Smart structures and materials*, ASME 1991 AD-Vol. **24**/AMD-Vol. **123**, 1–6 (1991).
- [3] S. Park and C.-T. Sun, Fracture criteria for piezoelectric ceramics, *J. Am. Ceram. Soc.* **78**, 1475–1480 (1995).
- [4] V. Heier, G. A. Schneider, H. Balke, J. Drescher and H.-A. Bahr, A fracture criterion for conducting cracks in homogeneously poled piezoelectric PZT-PIC151 ceramics, *Acta Mater.* **46**, 6615–6622 (1998).
- [5] H. Jelitto, F. Felten, M. V. Swain, H. Balke and G. A. Schneider, Measurement of the total energy release rate for cracks in PZT under combined mechanical and electrical loading, *J. Appl. Mech.*, accepted for publication.

## FERROELECTRIC CERAMICS: BASIC PROPERTIES AND MODELING METHODS

Marc Kamlah<sup>1</sup>, Bernd Laskewitz<sup>1</sup>, and Dayu Zhou<sup>1</sup>

<sup>1</sup>Forschungszentrum Karlsruhe, Institut für Materialforschung II  
Hermann-von-Helmholtz-Platz 1, D-76344 Eggenstein-Leopoldshafen  
e-mail: kamlah@imf.fzk.de

**Abstract.** *After a short historic note on ferroelectrics, we will introduce the basic mesoscopic domain mechanisms typical of these materials and their relation to macroscopic hysteresis phenomena and piezoelectric properties. After this introduction, we will present a micromechanical finite element simulation of a ferroelectric volume element, where each grain exhibits single crystal behavior for the switching of its domains. Next, we will turn to macroscopic constitutive modeling. We will present a phenomenological as well as a micromechanically based model. We will present applications of these models to the analysis of poling processes of piezoceramic devices.*

### Introduction

In most cases, the piezoelectric effect is utilized by means of ferroelectric ceramics. The electromechanical coupling properties of these materials are caused by distinct features of their perovskite microstructure. Below the Curie temperature, each grain possesses a substructure of so-called domains, being regions of uniform orientation of the micro-dipoles of the crystallographic unit cells. Upon application of electric fields and mechanical stresses of sufficient magnitude, these domains can be reoriented. In particular, the so-called poling process by strong electric fields leads to the orientation of the domains in the direction of the field resulting in a macroscopic piezoelectric effect from the microscopic piezoelectric contributions of the domains.

### Domains and Switching Mechanisms in Ferroelectrics

*Piezoelectricity* is a phenomenon related to a distinct anisotropy of the microstructure, the *polar symmetry*, and, additionally, to a high degree of *order* of this anisotropy. Despite of the random orientation of their lattice axes, certain polycrystals possessing the so-called *perovskite structure* may exhibit piezoelectric coupling below the Curie temperature. Inside each grain of such a material, there are *domains* with different orientation of the polar symmetry and the capability for piezoelectricity is caused by *ferroelectricity*. This means that the orientations of these domains may be *switched* by electric or mechanical loads of sufficient magnitude. By the *poling process*, the orientation of domains is ordered in the direction of a strong electric field leading to a net *remanent* polarization and piezoelectric properties on the level of the polycrystal, see Fig. 1. For a detailed discussion see [1].

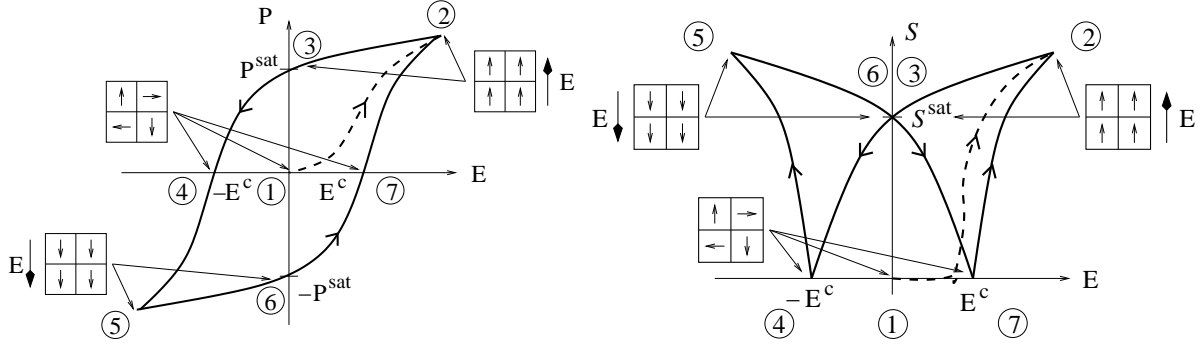


Figure 1: Schematic sketch with idealized domain states indicating the microscopic origin of the macroscopic dielectric and butterfly hystereses as the materials response to a cycling electric field with amplitudes of approximately twice the coercive field strength  $E^c$ . The ferroelectric material exhibits macroscopic piezoelectric properties in the poled states 2-3 and 5-6.

### Micromechanical Volume Element

As shown in the previous section, there is a clear understanding of the microscopic domain switching processes underlying the macroscopic behaviour of ferroelectric materials. Micromechanical concepts allow for the physical modeling of processes on the grain level and their impact on the properties of the polycrystalline aggregate. In this sense, a two-dimensional volume element under plane strain conditions has been considered, see the left panel of Fig. 2. Grain to grain interaction and electromechanical field coupling are taken into account by the finite element method. Each finite element is identified with a ferroelectric grain possessing single crystal properties for the switching of its domains according to the model by Huber *et al.* [2]. By means of this model, the influence of grain to grain interaction and of the orientation distribution of the lattice axes of the grains can be discussed, see [3]. As a example, the right panel of Fig. 2 shows the strain response of the polycrystalline aggregate to the poling process.

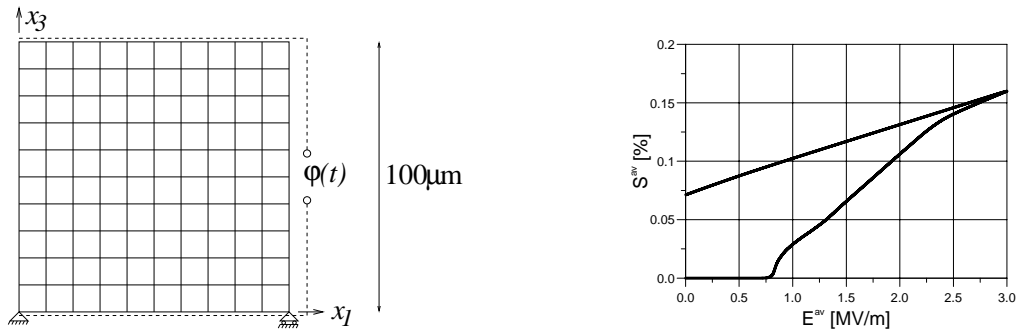


Figure 2: Left: polycrystalline volume element consisting of 10x10 ferroelectric grains. Right: Strain response to electric loading (poling).

### Constitutive Modeling and Finite Element Simulation

In the literature, a general structure for macroscopic constitutive models based on the additive decomposition of polarization and strain into reversible (piezoelectric) and irreversible (remnant) parts has been established, see [1]. A phenomenological constitutive model has been introduced which is based on the introduction of two types of loading criteria [4]. The first type of loading criterion indicates the onset of changing of irreversible polarization and strain,

respectively. The second group of criteria corresponds to a fully switched domain state where no further changes of the irreversible quantities occur. The resulting constitutive model represents all electric, mechanical and electro-mechanical hysteresis properties of ferroelectrics in a simplifying multi-linear manner (left panel of Fig. 3). Exploiting the model structure based on the above mentioned loading criteria, the model has been implemented in the public domain finite element code PSU by means of a customized predictor-corrector algorithm, right panel of Fig. 3 [5].

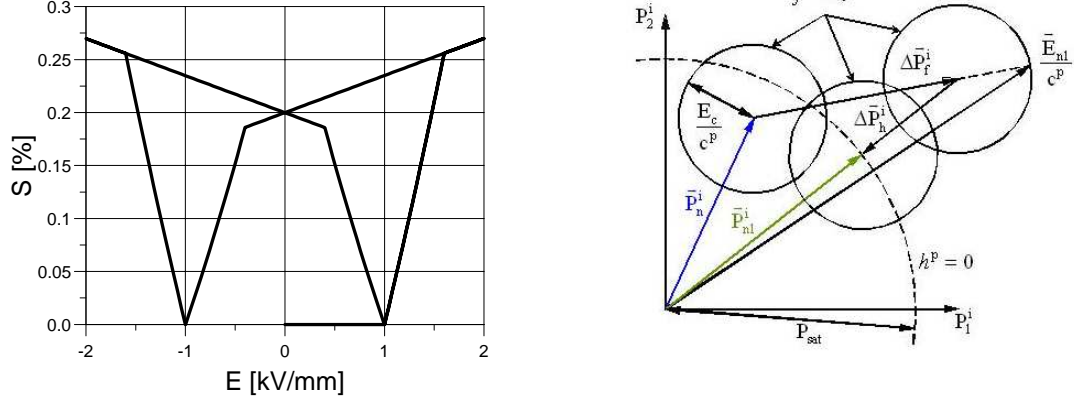


Figure 3: Left: Butterfly hysteresis according to the phenomenological constitutive model [4]. Right: On the predictor-corrector scheme for this model.

In a different constitutive model following a somewhat intermediate approach between pure phenomenological and micromechanical modeling, a step function approximation for the orientation distribution of the domains is introduced, where the parameters of this function serve as internal variables (left panel of Fig. 4). Exploiting the Clausius-Duhem inequality, thermodynamically conjugated driving forces for the internal variables are obtained. The normality rule is applied to a convex switching function to obtain the evolution equations for the internal variables in terms of ordinary differential equations. The right panel of Fig. 4 shows the butterfly hysteresis as it is simulated by this model. For a detailed description see [6]. This constitutive model has been implemented in PSU by means of a Euler backward integration scheme and a numerically computed consistent tangent operator.

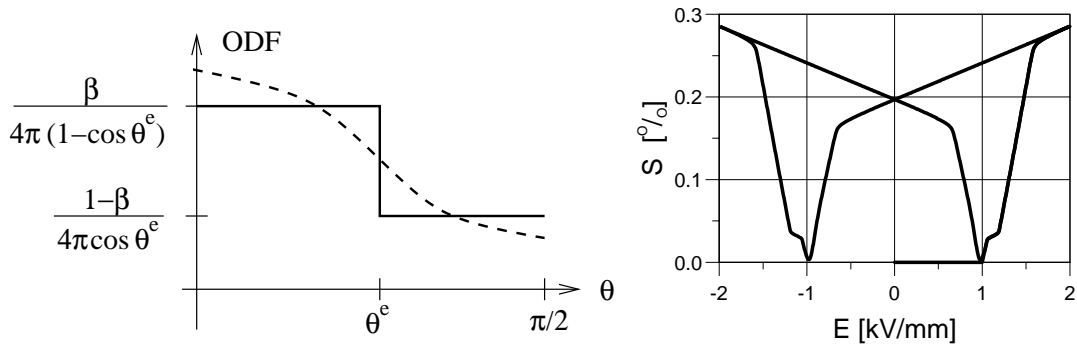


Figure 4: Left: Approximate orientation distribution function. Right: Butterfly hysteresis according to micromechanically motivated constitutive model.

For example, the poling processes in piezoceramic tubes has been analysed. It can be shown

that, depending on the ratio of inner to outer radius, due to a ferroelectric Bauschinger effect, complete radial poling of tubes may be impossible, leading to inhomogeneous electromechanical fields in the tube wall. Fig. 5 refers to a tube with a inner diameter of 17.5mm and a outer diameter of 20.5mm. At the instant of a maximum poling voltage an almost homogenous irreversible polarization state close to the saturation polarization is reached. During unloading, electric depolarization is initiated close to the outer tube surface, since the local electric field assumes neagtive values even beyond the coercive field strength. For a detailed discussion of this phenomenon see [5].

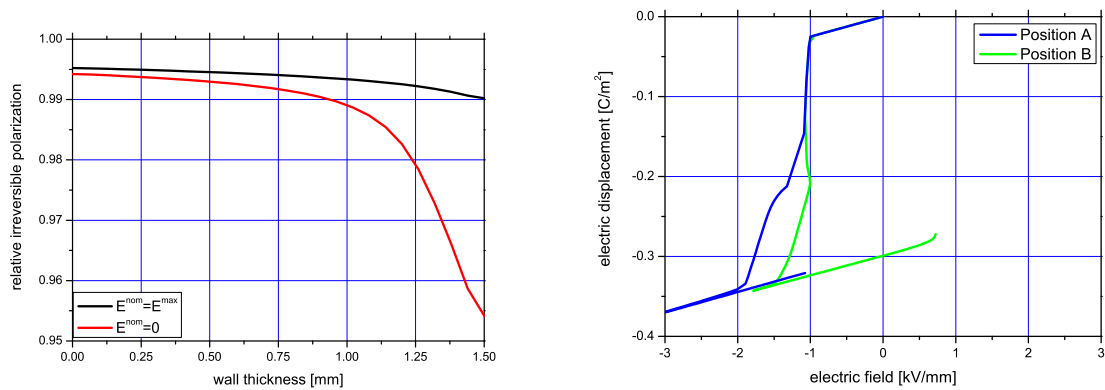


Figure 5: Left: Radial distribution of irreversible polarization in the tube wall for a maximum poling voltage applied in radial direction and after electric unloading. Right: Local electric field-electric displacement history during poling and unloading for positions A and B close to the inner and outer tube surfaces, respectively.

## REFERENCES

- [1] Kamlah, M., “Ferroelectric and Ferroelastic Piezoceramics – Modeling of Electromechanical Hysteresis Phenomena. Review Article,” *Continuum Mech. Thermodyn.* **13**(2001), 219 - 268
- [2] Huber, J.E., Fleck, N.A., Landis, C.M., McMeeking, R.M., “A Constitutive Model of Ferroelectrics,” *J. Mech. Phys. Solids* **47**(1999), 1663 - 1697
- [3] Kamlah, M., Liskowsky, A. C., McMeeking, R. M., Balke, H., “Finite Element Simulation of Polycrystalline Piezoceramic Behavior on the Basis of a Multidomain Single Crystal Switching Model,” *Int. J. Solids Structures* **42**(2005), 2949 - 2964
- [4] Kamlah, M., Tsakmakis, Ch., “Phenomenological Modeling of the Non-Linear Electro-Mechanical Coupling in Ferroelectrics,” *Int. J. Solids Structures* **36**(1999), 669 - 695
- [5] Laskewitz, B., Kamlah, M., Chen, C., “Investigations of the Nonlinear Behaviour of Piezoceramic Hollow Cylinders,” *Journal of Intelligent Material Systems and Structures* **17**(2006), 521 - 532
- [6] Kamlah, M., Wang, Z., “A Thermodynamically and Microscopically Motivated Constitutive Model for Piezoceramics under Uniaxial Loading,” In: Lagoudas, D. C. (ed.): *Active Materials: Behavior and Mechanics*. SPIE Vol. 5387, Bellingham 2004, 390 - 401.

## A CONSTITUTIVE MODEL FOR HYSTERESIS EFFECTS IN FERROELECTRIC CERAMICS

Sven Klinkel<sup>1</sup>

<sup>1</sup>Institut für Baustatik, Universität Karlsruhe(TH)  
Kaiserstr. 12, 76131 Karlsruhe  
e-mail: sk@bs.uka.de

**Abstract.** *This paper is concerned with a macroscopic constitutive law for domain switching effects, which occur in piezoelectric ceramics. The thermodynamical framework of the law is based on two scalar valued functions: the electric free Gibbs energy and a switching surface. In common usage, the remanent polarization and the remanent strain are employed as internal variables. The novel aspect of the present work is to introduce an irreversible electric field, which serves besides the irreversible strain as internal variable. The irreversible electric field has only theoretical meaning, but it makes the formulation very suitable for a finite element implementation, where displacements and the electric potential are the nodal degrees of freedom. The constitutive model reproduces the ferroelastic and the ferroelectric hysteresis as well as the butterfly hysteresis and it accounts for the mechanical depolarization effect.*

### Introduction

Piezoelectric devices are found in a wide range of applications, e.g. ink jet printers or fuel injection systems. The present work is motivated by the necessity to calculate the stress state in piezoceramics as precisely as possible. Macroscopical models which are thermodynamically consistent are based on the electric free energy and on one or more scalar valued switching surfaces. In [1] several switching criteria are used to control the different ferroelastic and ferroelectric hysteresis. For the coupled model of [2] only one switching surface is employed. In [3] a coordinate invariant thermodynamic consistent model is proposed, which accounts for the ferroelectric hysteresis and the butterfly hysteresis. The model of [2] additionally considers the mechanical depolarization effect. A fully coupled contribution is presented in e.g. [1] and allows in addition for the calculation of ferroelastic hysteresis effects. A popular assumption, see e.g. [1], [2], [3], is the one-to-one relationship between the irreversible strain and the remanent polarization, which simplifies the constitutive law and allows remanent polarization to be used as the only internal variable. The main features of the present paper are summarized as:

- A macroscopic constitutive law based on a thermodynamically framework is derived. The formulation is based on the electric free Gibbs energy and on a switching surface.
- An irreversible electric field is introduced. This and the irreversible strain field are used as internal variables to control the switching surface.
- No one-to-one relation between the irreversible strain and the polarization is employed. Here, it is distinguished between an irreversible strain due to stress application and irreversible strain arising from polarization.

- In the paper a finite element implementation in a brick element is provided. The evolution equations for the internal variables are integrated by an implicit integration algorithm.
- The formulation accounts for ferroelastic, ferroelectric and the butterfly hysteresis as well as for mechanical depolarization effect.

### Gradient fields

The strain field reads  $\mathbf{E} = \frac{1}{2}(\nabla \otimes \mathbf{u} + \mathbf{u} \otimes \nabla)$ , where  $\mathbf{u}$  is the displacement vector and  $\nabla$  the Nabla operator. An irreversible strain is obtained when domain switching processes occur due to a stress  $\mathbf{S}$ . An idealized stress strain relation is shown in the Fig. 1a). For  $S_{11} = 0$  and

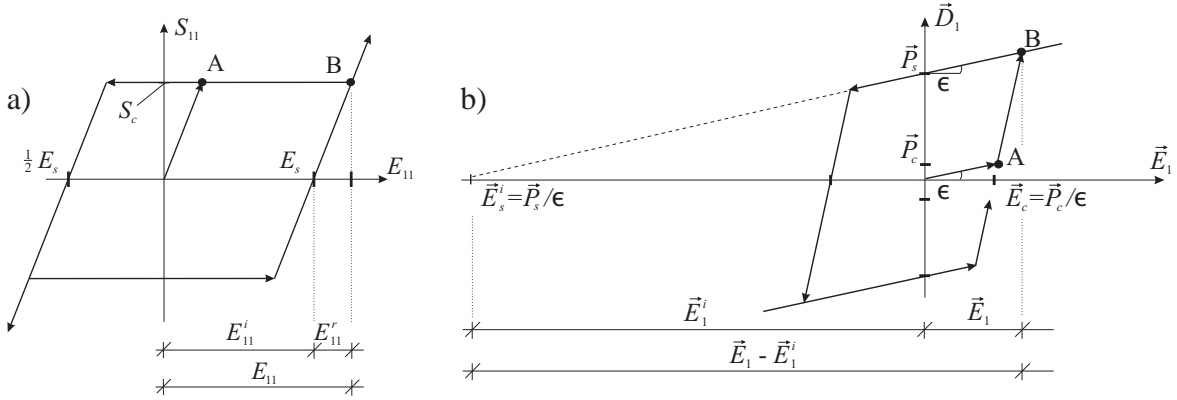


Figure 1: a) Idealized ferroelastic hysteresis and b) idealized dielectric hysteresis

$E_{11} = 0$  an unpolarized ceramic is assumed. Increasing the stress up to the coercive stress  $S_c$  domain switching starts at point A in Fig. 1a). The switching process results in an irreversible strain  $E_{11}^i$ . The process stops when all domains are switched, at point B in Fig. 1a). At this point the maximum irreversible strain  $E_{11}^i = E_s^i$  is obtained. The total strain is defined as  $\mathbf{E} = \mathbf{E}^r + \mathbf{E}^i$ , where  $\mathbf{E}^r$  is the reversible strain.

The electric field is defined as  $\vec{\mathbf{E}} = -\nabla\varphi$ , where  $\varphi$  is the electric potential. In Fig. 1b) an idealized dielectric hysteresis is shown, in which  $\vec{\mathbf{D}}$  is the dielectric displacement. If  $\vec{\mathbf{E}}_1$  is smaller than the coercive field  $\vec{\mathbf{E}}_c$  the material is characterized by the dielectric constant  $\epsilon$ . Alternatively a coercive polarization  $\vec{\mathbf{P}}_c = \vec{\mathbf{E}}_c \epsilon$  is introduced. The domain switching and therefore the polarization process starts at point C and ends at point D, see Fig. 1b). The maximum irreversible polarization is the saturation polarization  $\vec{\mathbf{P}}_s$ , or the irreversible electric saturation field defined as  $\vec{\mathbf{E}}_s^i := \vec{\mathbf{P}}_s / \epsilon$ . This implies the idea of an irreversible electric field  $\vec{\mathbf{E}}^i$ .

### Thermodynamic framework

In this section the constitutive law is developed for poly-crystalline materials under isothermal conditions for rate-independent deformation and polarization processes. The electric free Gibbs energy is defined as

$$\begin{aligned} \psi = & \frac{1}{2}(\mathbf{E} - \mathbf{E}^i) : \mathbb{C} : (\mathbf{E} - \mathbf{E}^i) + \frac{\vec{\mathbf{E}}^i \cdot \mathbf{e}_p}{\vec{\mathbf{E}}_s^i} \vec{\mathbf{E}} \cdot \mathbf{e} : (\mathbf{E} - \mathbf{E}^i) \\ & - \frac{1}{2}(\vec{\mathbf{E}} - \vec{\mathbf{E}}^i) \cdot \epsilon (\vec{\mathbf{E}} - \vec{\mathbf{E}}^i) + \bar{\psi}(\mathbf{E}^i, \vec{\mathbf{E}}^i) \quad . \end{aligned} \quad (1)$$

$\mathbb{C}$  denotes the elasticity matrix,  $\mathfrak{e}$  the piezoelectric modulus and  $\mathbf{e}_p$  is the polarization direction. The hardening function  $\bar{\psi}(\vec{\mathbf{E}}^i, \mathbf{E}^i)$  depends only on the internal variables, for further discussion see [4]. According to the 2nd law of thermodynamics the dissipation inequality reads  $\mathcal{D} = \mathbf{S} : \dot{\mathbf{E}} - \vec{\mathbf{D}} \cdot \dot{\vec{\mathbf{E}}} - \dot{\psi} \geq 0$ . Following standard arguments stress and dielectric displacement are obtained as

$$\begin{aligned} \mathbf{S} &:= \frac{\partial \psi}{\partial \mathbf{E}} = \mathbb{C} : (\mathbf{E} - \mathbf{E}^i) + \frac{\vec{\mathbf{E}}^i \cdot \mathbf{e}_p}{\vec{\mathbf{E}}_s^i} \mathfrak{e}^T \vec{\mathbf{E}} \\ -\vec{\mathbf{D}} &:= \frac{\partial \psi}{\partial \vec{\mathbf{E}}} = \frac{\vec{\mathbf{E}}^i \cdot \mathbf{e}_p}{\vec{\mathbf{E}}_s^i} \mathfrak{e} : (\mathbf{E} - \mathbf{E}^i) - \epsilon (\vec{\mathbf{E}} - \vec{\mathbf{E}}^i) \quad . \end{aligned} \quad (2)$$

The dissipation inequality  $\mathcal{D} = -\partial_{\mathbf{E}^i} \psi : \dot{\mathbf{E}}^i - \partial_{\vec{\mathbf{E}}^i} \psi \cdot \dot{\vec{\mathbf{E}}}^i \geq 0$  motivates the definition of the work conjugate variables as  $\hat{\mathbf{S}} := -\partial_{\mathbf{E}^i} \psi$  and  $\hat{\vec{\mathbf{D}}} := -\partial_{\vec{\mathbf{E}}^i} \psi$ . The vector  $\hat{\mathbf{P}}$  is defined as  $\hat{\mathbf{P}} = \epsilon \vec{\mathbf{E}}^i$  which is the negative polarization vector  $\vec{\mathbf{P}}$ . The evolution equations of the internal variables are derived by the principle of maximum dissipation with the switching surface as constraint, which is defined as

$$\phi := \frac{3 \hat{\mathbf{S}} : \mathbb{P} : \hat{\mathbf{S}}}{2 S_c^2} + \frac{(\hat{\vec{\mathbf{D}}} \cdot \mathbf{e}_p)^2}{\vec{\mathbf{P}}_c^2} + \xi \frac{f(\hat{\mathbf{P}} \cdot \hat{\mathbf{P}})}{S_c^2 \vec{\mathbf{P}}_s^2} - 1 \leq 0 . \quad (3)$$

Here,  $\xi$  is a material parameter and  $\mathbb{P} = \mathbb{I} - \frac{1}{3} \mathbf{1} \otimes \mathbf{1}$  the deviatoric projection tensor. The function  $f$  considers the fact that mechanical depolarization occurs only in polarized ceramics which are subjected to a compression stress, see [4]. A mathematical description of the optimization problem is given with  $\mathcal{L} = -\mathcal{D}(\hat{\mathbf{S}}, \hat{\vec{\mathbf{D}}}) + \lambda \phi(\hat{\mathbf{S}}, \hat{\vec{\mathbf{D}}}, \mathbf{S}, \hat{\mathbf{P}})$ , where  $\lambda$  is the Lagrange multiplier. The evolution equations read

$$\dot{\mathbf{E}}^i = \lambda \frac{\partial \phi}{\partial \hat{\mathbf{S}}} = \lambda \frac{3}{S_c^2} \mathbb{P} : \hat{\mathbf{S}} + \lambda \xi \frac{1}{S_c^2 \vec{\mathbf{P}}_s^2} (\hat{\mathbf{P}} \cdot \mathbf{e}_p)^2 \frac{\partial f}{\partial \hat{\mathbf{S}}} \quad (4)$$

$$\dot{\vec{\mathbf{E}}}^i = \lambda \frac{\partial \phi}{\partial \hat{\vec{\mathbf{D}}}} = \lambda \frac{2}{\vec{\mathbf{P}}_c^2} (\hat{\vec{\mathbf{D}}} \cdot \mathbf{e}_p) \mathbf{e}_p + \lambda \xi \frac{2}{S_c^2 \vec{\mathbf{P}}_s^2} f(\hat{\mathbf{P}} \cdot \mathbf{e}_p) \mathbf{e}_p . \quad (5)$$

An additive decomposition  $\dot{\mathbf{E}}^i = \dot{\mathbf{E}}^{Pi} + \dot{\mathbf{E}}^{Si}$  of the strain into a part arising due to mechanical depolarization  $\dot{\mathbf{E}}^{Si}$  and a part occurring with respect to ferroelectric domain switching effects  $\dot{\mathbf{E}}^{Pi}$  is introduced. Employing the backward Euler implicit time integration scheme, the discrete evolution equations are obtained.

### Variational formulation and finite element approximation

A mechanical force  $\mathbf{t}$  or a displacement  $\mathbf{u}$  may be applied to the boundary of a body  $\mathcal{B}_0$ , which is denoted with  $\partial \mathcal{B}_{0u}$  and  $\partial \mathcal{B}_{0t}$ , respectively. The governing equations are the balance of momentum  $\mathbf{S} \cdot \nabla + \rho_0 \mathbf{b} = \mathbf{0}$  in  $\mathcal{B}_0$  where  $\rho_0 \mathbf{b}$  denotes a body force and the local form of Gauss law  $\vec{\mathbf{D}} \cdot \nabla = 0$  in  $\mathcal{B}_0$ . The corresponding boundary conditions are given as  $\mathbf{S} \mathbf{n} - \mathbf{t} = \mathbf{0}$  on  $\partial \mathcal{B}_{0t}$  and  $\vec{\mathbf{D}} \cdot \mathbf{n} = 0$  on  $\partial \mathcal{B}_{0\sigma}$ , where  $\mathbf{n}$  denotes the normal outward vector on  $\partial \mathcal{B}_0$ . The weak form of the governing equations is given by

$$\delta \pi = \int_{\mathcal{B}_0} \left( \frac{\partial \psi}{\partial \mathbf{E}} : \delta \mathbf{E} + \frac{\partial \psi}{\partial \vec{\mathbf{E}}} \cdot \delta \vec{\mathbf{E}} \right) dV - \int_{\mathcal{B}_0} \rho_0 \mathbf{b} \cdot \delta \mathbf{u} dV - \int_{\partial \mathcal{B}_0} \mathbf{t} \cdot \delta \mathbf{u} dA = 0 . \quad (6)$$

The virtuell gradient fields read  $\delta \mathbf{E} = \frac{1}{2} (\nabla \otimes \delta \mathbf{u} + \delta \mathbf{u} \otimes \nabla)$  and  $\delta \vec{\mathbf{E}} = -\nabla \delta \varphi$ .

The finite element approximation is constructed by dividing the whole domain in element domains with  $\mathcal{B}_0 = \cup_{e=1}^{nelm} \mathcal{B}_e$ , where  $nelm$  is the total number of elements. The hexahedral element has eight nodes and trilinear shape function  $N_I$  at the node  $I = 1..8$ . The approximation of the geometry on element level (index  $e$ ) reads  $\mathbf{X}_e^h = \sum_{I=1}^8 N_I \mathbf{X}_I$ . The vector  $\mathbf{X}_I$  contains the nodal co-ordinates. The interpolation functions  $N_I$  are arranged in the matrix  $\mathbf{N} = [\mathbf{N}_1, \mathbf{N}_2, \mathbf{N}_3, \mathbf{N}_4, \mathbf{N}_5, \mathbf{N}_6, \mathbf{N}_7, \mathbf{N}_8]$  with  $\mathbf{N}_I = \text{diag}[N_I, N_I, N_I, N_I]$ . By means of the isoparametric concept the geometry, the displacements and the electric potential are approximated with the same interpolation functions as  $\mathbf{d}_e^h = [u_e^h, \varphi_e^h]^T = \mathbf{N} \mathbf{v}_e$ . The vector  $\mathbf{v}_e$  is defined as  $\mathbf{v}_e = [\mathbf{u}_1^T, \varphi_1, \mathbf{u}_2^T, \varphi_2, \mathbf{u}_3^T, \varphi_3, \mathbf{u}_4^T, \varphi_4, \mathbf{u}_5^T, \varphi_5, \mathbf{u}_6^T, \varphi_6, \mathbf{u}_7^T, \varphi_7, \mathbf{u}_8^T, \varphi_8]^T$ . The approximations of the gradient fields read  $[\mathbf{E}_e^h, \vec{\mathbf{E}}_e^h]^T = \mathbf{B} \mathbf{v}_e$ . The  $\mathbf{B}$ -matrix contains the derivatives of the shape functions. The approximation of the weak form Eq. (6) is observed on element level as

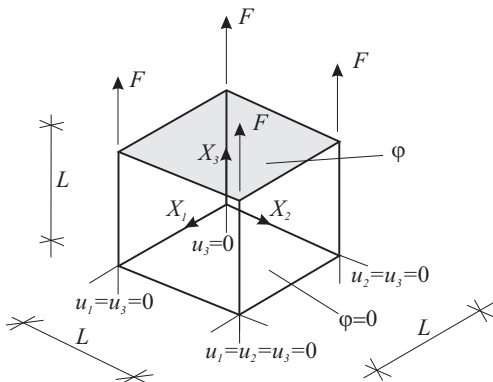
$$\delta \pi_e^h = \delta \mathbf{v}_e^T \left[ \underbrace{\int_{\mathcal{B}_e} \left( \mathbf{B}^T \begin{pmatrix} \frac{\partial \psi}{\partial \mathbf{E}} \\ \frac{\partial \psi}{\partial \vec{\mathbf{E}}} \end{pmatrix} - \mathbf{N}^T \begin{pmatrix} \rho_0 \mathbf{b} \\ \kappa \end{pmatrix} \right) dV - \int_{\partial \mathcal{B}_e} \mathbf{N}^T \begin{pmatrix} \mathbf{t} \\ \sigma \end{pmatrix} dA}_{\mathbf{R}_e^h} \right] . \quad (7)$$

After assembly over all elements  $\delta \pi^h = \mathbf{A}_{e=1}^{nelm} \delta \pi_e^h$  one obtains the residual vector  $\mathbf{R}^h = \mathbf{A}_{e=1}^{nelm} \mathbf{R}_e^h$  and  $\mathbf{v} = \mathbf{A}_{e=1}^{nelm} \mathbf{v}_e$ . Due to the fact that  $\psi$  is a nonlinear function of  $\varphi$  and  $\mathbf{u}$  the equation  $\delta \pi^h = 0$  is solved iteratively by employing the Newton-Raphson within the finite element method. During the load step  $[t_{n+1}, t_n]$  the residual vector (7) at  $t_{n+1}$  is expanded in a Taylor series, which is truncated after the linear element

$$\mathbf{R}_{n+1}^{(k)} + \frac{\partial \mathbf{R}_{n+1}^{(k)}}{\partial \mathbf{v}_{n+1}} \Delta \mathbf{v}_{n+1}^{(k)} = \mathbf{0} . \quad (8)$$

The nodal degrees of freedom are determined by  $\mathbf{v}_{n+1}^{(k+1)} = \mathbf{v}_{n+1}^{(k)} + \Delta \mathbf{v}_{n+1}^{(k+1)}$ , where the superscript  $(k)$  denotes the iteration step. The last equilibrium state is considered as start value for the first iteration and reads  $\mathbf{v}_{n+1}^{(1)} = \mathbf{v}_n$ .

### Numerical example



$$\begin{aligned} E_1 &= E_2 = E_3 = 80 \cdot 10^6 \text{ kN/m}^2 \\ \nu_{12} &= \nu_{13} = \nu_{23} = 0 \\ G_{12} &= G_{13} = G_{23} = 40 \cdot 10^6 \text{ kN/m}^2 \\ \epsilon_{13} &= -12.0 \text{ C/m}^2, \epsilon_{33} = 25.5802 \text{ C/m}^2 \\ \epsilon_{15} &= -12.0 \text{ C/m}^2, \epsilon = 15 \cdot 10^{-6} \text{ C}^2/\text{kN m}^2 \\ E_s^i &= 0.002, \vec{E}_s^i = 20 \cdot 10^3 \text{ kV/m} \\ \vec{P}_c &= 1.5 \cdot 10^{-2} \text{ C/m}^2, S_c = 50 \cdot 10^3 \text{ GN/m}^2 \\ \xi &= 0.27, h = 1 \cdot 10^6 \text{ kN/m}^2, m_t = 1, m_c = 1 \\ k &= \epsilon \cdot 0.999, a = 0.02/\text{arctanh}(1/b) \text{ C/m}^2 \\ b &= 1.00005, \zeta = 0.1 \cdot 10^6 \text{ kN/m}^2 \end{aligned}$$

Figure 2: Boundary and loading conditions along with the applied material parameters

The first example shows that the proposed model is able to capture the different hysteresis loops. A cube with an edge length of  $L = 10$  mm is subjected to either an mechanical force  $F$  or an electric potential  $\varphi$ . The boundary conditions are shown in Fig. 2. The material parameters are chosen as a rough approximation of soft PZT and are summarized in Fig. 2. The hysteresis effects for different load cases are depicted in Fig. 3.

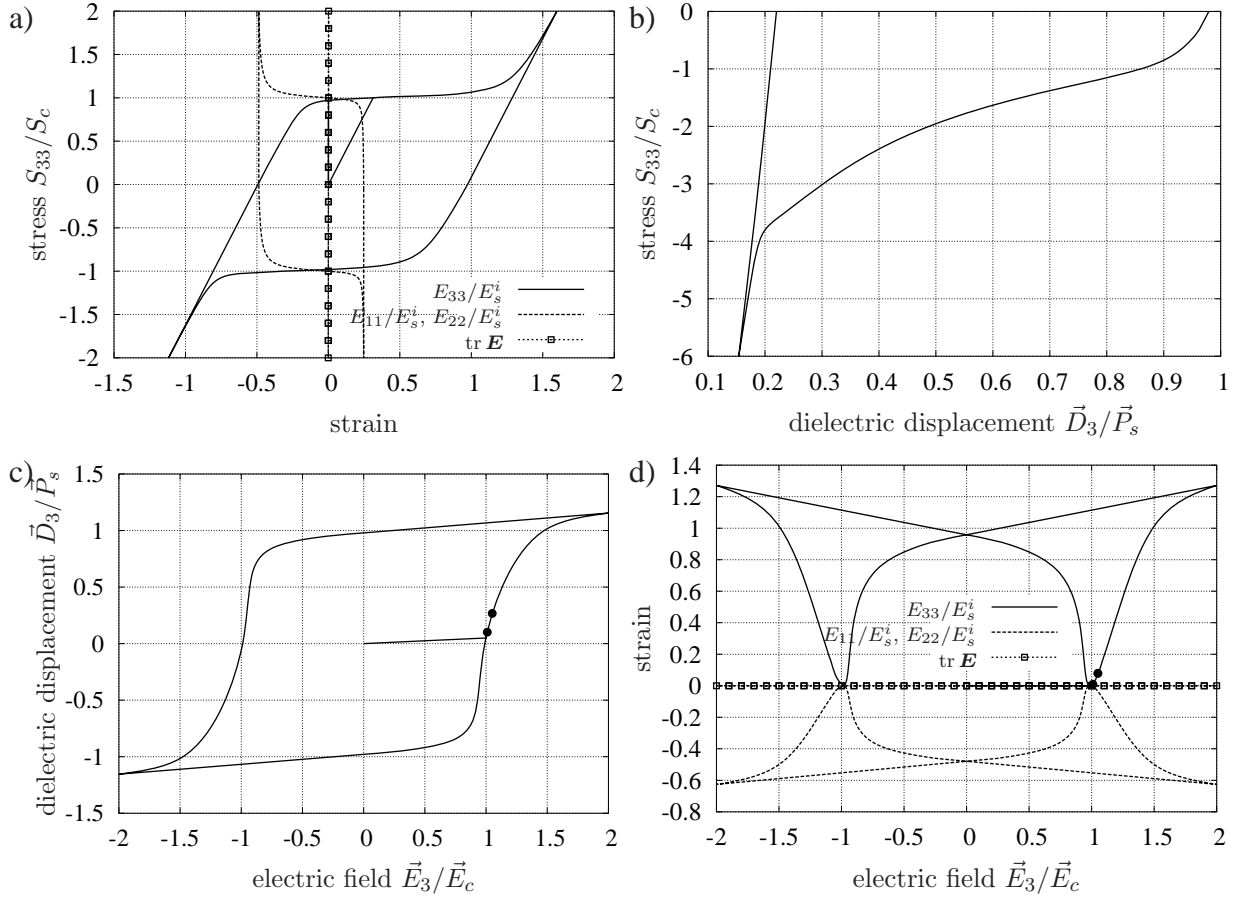


Figure 3: a) Ferroelastic hysteresis, b) mechanical depolarization curve, c) dielectric hysteresis and d) butterfly loop

## REFERENCES

- [1] M. Kamlah, Ferroelectric and ferroelastic piezoceramics – modeling of electromechanical hysteresis phenomena, *Continuum Mech. Thermodyn.*, **13**, 219–268, (2001).
- [2] R.M. McMeeking, C.M. Landis, A phenomenological multi-axial constitutive switching in polycrystalline ferroelectric ceramics, *Int. J. of Eng. Science*, **40**, 1553–1577, (2002).
- [3] J. Schröder, H. Romanowski, A thermodynamically consistent mesoscopic model for transversely isotropic ferroelectric ceramics in a coordinate-invariant setting, *Archive of Applied Mechanics*, **74**, 863–877, (2005).
- [4] S. Klinkel, A phenomenological constitutive model for ferroelastic and ferroelectric hysteresis effects in ferroelectric ceramics, *Int. J. of Solids and Structures*, **43**, 7197–7222, (2006).

## STABILITY AND PERFORMANCE OF COMPOSITE MATERIALS HAVING A NEGATIVE-STIFFNESS PHASE

D. M. Kochmann<sup>1\*</sup>, W. J. Drugan<sup>2</sup>, R. S. Lakes<sup>2</sup>

<sup>1</sup>Lehrstuhl für Allgemeine Mechanik, Ruhr-Universität Bochum  
D-44780 Bochum, Germany

\*e-mail: dennis.kochmann@rub.de

<sup>2</sup>Department of Engineering Physics, University of Wisconsin–Madison  
1500 Engineering Drive, Madison, WI 53706, U.S.A.

**Abstract.** *The stiffness of elastic composite materials depends on the stiffness of each of their constituents. In case one phase with a negative stiffness is included, theory predicts that the overall composite stiffness can increase far beyond the stiffness of each of its constituents. Unfortunately, a negative-stiffness material is unstable by itself – a free standing body must have positive-definite elastic moduli, which prohibits the existence of negative stiffness. We will show that not only can a composite material containing a phase having negative stiffness be stable overall, but also that experimental evidence has been found for the predicted bound-exceeding performance of such composites.*

### Introduction

Composite materials theory limits the attainable overall elastic moduli of a composite in terms of the properties of its constituents, presuming positive-definiteness (positive stiffnesses) for each constituent to ensure overall stability. Paul and Hill as well as Hashin and Shtrikman [1] were at the forefront of investigating the overall stiffness of a two-phase composite material, providing upper and lower bounds on the overall stiffness. Presuming materials with positive stiffness, their results show that the overall stiffness of the composite cannot exceed the stiffness of its stiffest constituent. Admittance of a negative-stiffness phase, however, facilitates the composite material to strongly exceed these classical bounds [2, 3].

It is well known that a body with pure traction boundary conditions (e.g. a free standing body) must have positive-definite elastic moduli (i.e. positive stiffnesses) for stability [4]; a body that is completely geometrically constrained (pure displacement boundary conditions) must have moduli that satisfy the weaker condition of strong ellipticity, which permits negative stiffness (specifically, negative bulk and Young's moduli) [5]. A key means to stabilizing negative stiffness therefore is a sufficient geometric constraint. This suggests that if a material having negative stiffness is trapped in a sufficiently stiff matrix, the matrix functions as a geometric constraint so that the composite can show overall stability.

A two-dimensional (plane strain) model of a simple two-phase composite material is employed in order to obtain restrictions on the elastic moduli of the constituent materials of a composite consisting of a circular inclusion with a concentric coating. Our results show that coated inclusions may indeed have negative stiffness (within the range of strong ellipticity), given a coating with sufficiently stiff elastic moduli (the quantitative restrictions on which we derive), while retaining overall dynamic stability of the composite.

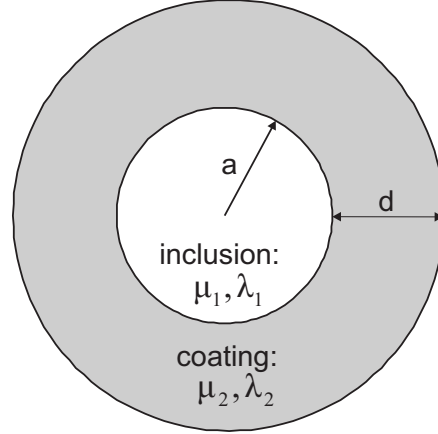


Figure 1: Schematic illustrating the composite model and the definitions used in the present analysis.

Although negative stiffness is unstable by itself, it is possible to realize negative stiffness by making use of the energetic effects of phase transitions: The structural transition of  $\text{BaTiO}_3$  was used to generate particles with negative stiffness in a stiff metal matrix of pure tin by employing the stiffness of tin to prevent the inclusions from undergoing a phase transformation. Viscoelastic experiments [6] on these novel  $\text{Sn-BaTiO}_3$  composites confirmed an extreme increase (that exceeded the classical bounds) in stiffness as well as anomalies in the damping capacity which can only be explained by a negative stiffness in the trapped particles during transformation.

### Theoretical Composite Model

Assume a two-dimensional, homogeneous, isotropic and linear-elastic composite in plane-strain that consists of two phases, viz. a circular inclusion of radius  $a$  and elastic moduli  $\lambda_1$  and  $\mu_1$ , with a concentric coating of thickness  $d$  and elastic moduli  $\lambda_2$  and  $\mu_2$  as sketched in Fig. 1. Drugan [7] showed for this two-dimensional model that, using Hill's energy-based sufficient condition for stability, the inclusion may indeed exhibit merely strong ellipticity if the coating is sufficiently stiff (within positive-definiteness) to ensure overall stability, presuming a very thin coating. Now, let us consider the dynamic stability of the above composite with arbitrary coating thickness.

The composite is governed by Navier's equation

$$\rho \frac{\partial^2}{\partial t^2} \mathbf{u} = \rho \mathbf{B} + \nabla \cdot \boldsymbol{\sigma}.$$

Furthermore, assume linear elasticity and the absence of body forces. Making a separation ansatz and using an infinite sum expansion, one can solve for the general representation of the displacement field  $\mathbf{u}(r, \theta, t)$  for the circular inclusion and the concentric coating in polar coordinates [9]. Finally, applying boundary conditions (traction-free outer surface) and continuity conditions (continuity of tractions and displacements across the interface between inclusion and coating), one can derive the general form of the displacement fields in the inclusion and in the coating for the present composite model, which may be abbreviated

$$\mathbf{u}(r, \theta, t) = \sum_{m=-\infty}^{\infty} \sum_{\omega \in \Psi} \mathbf{U}_m(r) e^{im\theta} e^{\pm i\omega t}$$

where  $r$  and  $\theta$  are the polar coordinates,  $t$  is time,  $\mathbf{U}_m$  is a vector-valued function of  $r$  and  $m$ , with  $\mathbf{U}_{-m} = \overline{\mathbf{U}}_m$ ,  $\Psi$  is the set of (an infinite number of) solutions for  $\omega$  which is obtained from applying boundary conditions.

Define instability as the situation in which an initially small perturbation of the displacement field increases with time. Then, the stability requirement for our composite model simply demands that every  $\omega \in \Psi$  must be real to avoid exponential growth of the displacement field.

Now, the problem of determining admissible ranges for the constituent elastic moduli  $\lambda_i$  and  $\mu_i$  reduces to finding those ranges of  $\lambda_i$  and  $\mu_i$  for which only real solutions for  $\omega$  exist. These ranges are easiest to find by examining imaginary values of  $\omega$  and evaluating the six necessary conditions numerically. From this analysis, one can obtain the sought ranges for the elastic moduli.

Our results confirm those of Drugan [7] for a thin coating, the inclusion can always be merely strongly elliptic (i.e. have negative stiffness) so long as the coating is sufficiently stiff; both energy and dynamic approach give identical moduli requirements for stability (with  $\beta \in [0, 1]$ ):

$$\mu_1 > 0, \quad \lambda_1 > -(1 + \beta)\mu_1, \quad \mu_2 > \frac{\beta a}{2d}\mu_1, \quad \lambda_2 > -\frac{1 - \beta \frac{a}{d} \frac{\mu_1}{\mu_2}}{1 - \frac{\beta a}{2d} \frac{\mu_1}{\mu_2}}\mu_2.$$

For a thick coating, we find the restrictions on the coating moduli become weaker [8] so that the coating may be less stiff while still permitting negative stiffness in the inclusion. We will present explicit representations for these results.

## Experimental Investigation

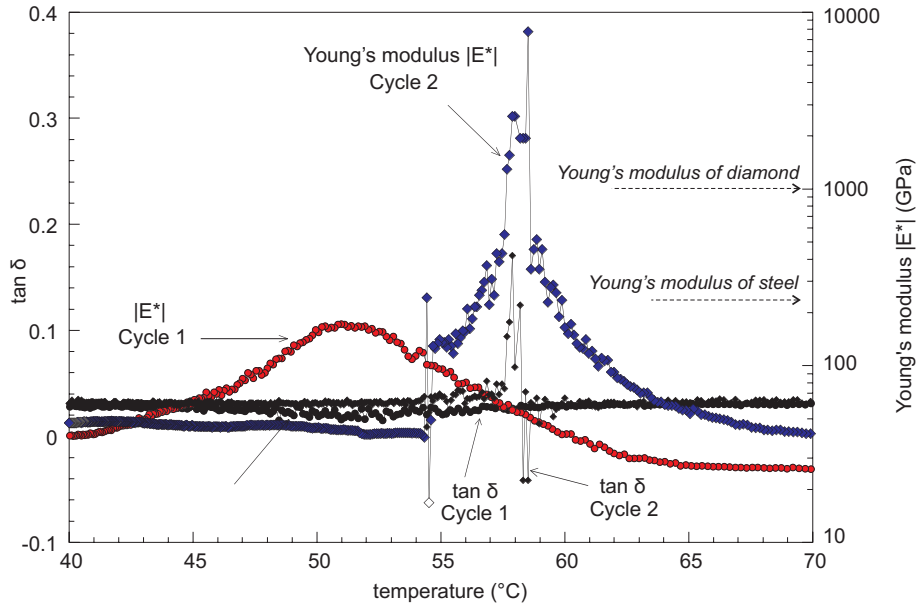


Figure 2: Viscoelastic Young's modulus  $|E^*|$  and damping  $\tan \delta$  vs. temperature of a Sn-BaTiO<sub>3</sub> composite showing an extreme increase in stiffness. Modified after Jaglinski, Kochmann, Stone, Lakes, *Science*, 2007 [6].

Recent experimental results give evidence for bound-exceeding performance of a composite containing one phase with negative stiffness[6, 9, 10]. Again, the key issue is to geometrically constrain the phase with negative stiffness. Barium titanate (BaTiO<sub>3</sub>) is a ferroelastic ceramic which undergoes a structural transition near 120° C, changing its microstructure from cubic to

tetragonal unit cells upon cooling. Governed by Landau's theory of phase transitions, the free energy of the strained  $\text{BaTiO}_3$  body has one global minimum at temperatures above transition which changes into a local maximum below the transition temperature  $T_c$ . After cooling below  $T_c$ , the body is in an unstable equilibrium, facilitating a snap-through effect upon further straining which corresponds to the effect of negative stiffness.

Specimens of pure tin with 3 to 10 vol.-% of  $\text{BaTiO}_3$  particles were prepared (using an ultrasonic casting technique) and tested by employing *Broadband Viscoelastic Spectroscopy* [11] to measure the viscoelastic Young's modulus  $|E^*|$  and the damping  $\tan \delta$  (where  $\delta$  denotes the phase lag between stress and strain) at 100 Hz in bending and in torsion.

Results show that the structural transition in the  $\text{BaTiO}_3$  particles gives rise to extreme anomalies in the composite's Young's modulus and the damping of the overall composite (see Fig. 2), resulting in a Young's modulus that temporarily exceeds that of diamond (1000 GPa) [6]. Such a strong increase in stiffness cannot be accomplished by means of positive-definite materials and is theorized to be due to a temporarily negative bulk modulus in the  $\text{BaTiO}_3$  inclusions.

## REFERENCES

- [1] Z. Hashin, The elastic moduli of heterogeneous materials, *J. Appl. Mech.*, Trans. ASME **84E**, 143-150 (1962).
- [2] R. S. Lakes, Extreme damping in composite materials with a negative stiffness phase, *Physical Review Letters*, **86**, 2897-2900, 26 March (2001).
- [3] R. S. Lakes, W. J. Drugan, Dramatically stiffer elastic composite materials due to a negative stiffness phase?, *J. Mech. Phys. Sol.*, **50**, 979-1009 (2002).
- [4] S. P. Timoshenko, J. N. Goodier, *Theory of Elasticity*, McGraw-Hill, New York, NY (1982).
- [5] T. W. Lord Kelvin, On the reflection and refraction of light, *Phil. Mag.*, **26**, 414-425 (1888).
- [6] T. Jaglinski, D. Kochmann, D. Stone, R. S. Lakes, Composite Materials with viscoelastic stiffness greater than diamond, *Science*, **315** (5812), 620-622 (2007).
- [7] W. J. Drugan, Elastic Composite Materials Having a Negative Stiffness Phase Can Be Stable, *Phys. Rev. Lett.*, **98** (5), 2 February (2007).
- [8] D. M. Kochmann, W. J. Drugan, Dynamic Stability of Elastic Composite Materials Having a Negative-Stiffness Phase, in preparation.
- [9] D. M. Kochmann, Composite Materials with Inclusions of Negative Stiffness – Theoretical Analysis and Experimental Investigations, Master's thesis, University of Wisconsin–Madison (2006).
- [10] R. S. Lakes, T. Lee, A. Bersie, Y. C. Wang, Extreme damping in composite materials with negative stiffness inclusions, *Nature*, **410**, 565-567 (2001).
- [11] R. S. Lakes, Viscoelastic measurement techniques, *Review of Scientific Instruments*, **75** (4), 797-810 (2004).

# MODELING LINEAR PROPERTIES AND NONLINEAR RESPONSE OF FERROELECTRIC/FERROELASTIC POLYCRYSTALLINE MATERIALS

Wolfgang S. Kreher, Alexander Yu. Belov

Technische Universität Dresden, Institut für Werkstoffwissenschaft, 01062 Dresden  
e-mail: wolfgang.kreher@tu-dresden.de

**Abstract.** *We discuss principles of modeling for linear and nonlinear properties of ferroelectric ceramics by means of internal variables. Some recent results are reviewed.*

## Introduction

Ferroelectric materials, in particular ceramics, are gaining increasing interest because of their possible application in smart structures as actuators or sensors. As a consequence of the ferroelectric/ferroelastic phase transformation during cooling from fabrication temperature to ambient temperature, a domain structure is formed inside the grains of a polycrystalline material. Each domain is characterized by a special orientation of electrical polarization and mechanical transformation strain. After a poling process, which creates a non-isotropic distribution of domain orientations, these materials exhibit interesting linear and non-linear electromechanical coupling properties.

The effective (overall) behavior of ferroelectric ceramics is strongly dependent on the single-crystal properties, on the domain configuration and on the grain-grain interaction inside the polycrystalline material. In addition, one has to distinguish between intrinsic properties which are due to the crystal structure itself and extrinsic contributions which are caused by domain reconfiguration processes under the application of external electrical or mechanical fields.

The general relationships between the field quantities stress  $\sigma$ , strain  $\varepsilon$ , electric field  $E$  and electric displacement  $D$  are given by

$$\begin{aligned}\varepsilon_{ik} &= s_{iklm}^E \sigma_{lm} + d_{lik} E_l + \varepsilon_{ik}^s \\ D_i &= d_{ilm} \sigma_{lm} + \kappa_{il}^\sigma E_l + P_i^s\end{aligned}\quad i, k, l, m = 1, 2, 3 \quad (1)$$

where  $s^E$ ,  $\kappa^\sigma$  and  $d$  are the linear elastic, dielectric and piezoelectric constants, respectively. The terms  $\varepsilon^s$  and  $P^s$  describe the remnant strain and polarization, which are due to spontaneous polarization and transformation strain (here for vanishing stress and electric field).

It is convenient to replace the symmetric second order tensors of stress and strain by  $6 \times 1$  column vectors using the standard Voigt replacement of tensor indices. In addition one formally combines the mechanical and electrical field quantities in  $9 \times 1$  column vectors:

$$j = \begin{pmatrix} \varepsilon_\alpha \\ D_i \end{pmatrix} \quad f = \begin{pmatrix} \sigma_\alpha \\ E_i \end{pmatrix} \quad \alpha = 1, 2, \dots, 6 \quad (2)$$

Thus the constitutive equations can be written in the compact notation

$$\dot{j}_p = L_{pq} f_q + j_p^s \quad p, q = 1, 2, \dots, 9 \quad (3)$$

where the material constants  $s^E$ ,  $\kappa^\sigma$  and  $d$  are comprised by  $L$  and the remnant quantities  $\epsilon^s$  and  $P^s$  are included in  $j^s$ . On the single-domain level these properties are given material constants. On the polydomain level and for the macroscopic description, the constants become effective properties which are composition-dependent and, moreover, the remnant quantities become field-dependent.

### Polycrystal-polydomain model

We present a model which is based on the notion of a laminar domain structure with  $90^\circ$  domain walls as typical for tetragonal ferroelectric crystals.

In the first step a laminar stack of two types of domains (with differential thickness) is modeled. This is done for thin layers of homogeneous domains where end effects can be neglected. The resulting homogenized material law has just the form of the local law but is now valid for averaged grain fields:

$$\bar{j}_p^{grain} = L_{pq}^{grain} \bar{f}_q^{grain} + j_p^{s,grain} \quad (4)$$

The effective grain properties depend on the properties of the single domains and on their relative thickness, which is equivalent to their respective volume fractions in the considered grain (denoted by  $\xi^{(1)} = \xi$  and  $\xi^{(2)} = 1 - \xi$ ):

$$L_{pq}^{grain} = L_{pq}^{grain}(\xi, L^{(1)}, L^{(2)}), \quad j_q^{s,grain} = j_q^{s,grain}(\xi, L^{(1)}, L^{(2)}, j^{s(1)}, j^{s(2)}) \quad (5)$$

In a second step the polycrystalline arrangement of homogenized single-crystals is modeled by the standard effective medium approach where the individual crystals are embedded into a matrix which just possesses the still unknown properties. For the solution of the inclusion problem one needs the coupled Eshelby tensor (see e.g. [1]) which describes internal fields for inclusions in an (effectively) homogeneous matrix. After a suitable averaging procedure over all possible grain orientations, one gets an implicit equation from which the effective (macroscopic) properties  $L^*$  and  $j^*$  can be calculated (for details see e.g. [2]).

Depending on the assumption about the local values of the volume fraction  $\xi$  (which may fluctuate from grain to grain), different types of material behavior can be modeled:

- a) If  $\xi$  is kept fixed at a value 0.5 in every grain, one obtains the intrinsic linear response of the polycrystalline material.
- b) If  $\xi$  is allowed to vary by domain wall movement in such a way that the potential energy of the grain interacting with its surroundings is minimized, one gets the extrinsic response which, for low applied fields, is still linear. The extrinsic response contributes to the dielectric and piezoelectric effective constants in the same order as the intrinsic constants.
- c) For larger applied fields (in the range of the coercive field), domain wall motion becomes dissipative since domain pinning points (obstacles) must be overcome by thermal or athermal activation. In the model this can be taken into account by assigning a dissipative specific work to the domain movement. One obtains a large-signal response of the material showing hysteresis.

In case c) the resulting implicit equations are solved numerically in an iterative scheme. Details of the calculation method are provided in [3].

### Semi-phenomenological rate theory

When one is concerned with the application of ferroelectrics in devices with inhomogeneous field distributions (e.g. a multilayer actuator or a foil structure with a special electrode design), one is confronted with a general boundary value problem which determines the inner fields in the device. Although, under service conditions, the material is normally driven in the linear small-signal regime, one nevertheless has to analyze the nonlinear poling process. Then the detailed description of domain processes in a polycrystalline material gets too time-consuming and becomes intractable. Here one needs a more phenomenological approach for the description of effective material behavior which keeps the basic features of ferroelastic/ferroelectric behavior yet is sufficiently simple to be implemented into a finite element code.

A good compromise is inspired by the viscous approach to plasticity: Instead of a definite threshold for the onset of nonlinear domain reconfiguration, one postulates a rate equation for the remnant parts in the constitutive equation. This scheme has been successfully adopted to shape memory alloys by Müller [4] and to ferroelectric materials by Huber&Fleck [5].

The general scheme can be sketched as follows. We introduce a set of structural variables  $\xi_r$  ( $r = 1, 2, \dots, n$ ) with

$$0 \leq \xi_r \leq 1 \quad \sum_{r=1}^n \xi_r = 1 \quad (6)$$

and write the effective remnant strain and remnant polarization as a weighted sum of the corresponding values of a set of  $n$  fixed orientation variants of domains:

$$\varepsilon_{ik}^s = \sum_{r=1}^n \xi_r \varepsilon_{ik}^{s(r)} \quad P_i^s = \sum_{r=1}^n \xi_r P_i^{s(r)} \quad (7)$$

(and with similar equations for the linear material constants comprised in  $L$ ). The unpoled starting state is then described by an equal weight, i.e.  $\xi_r = 1/n$ . Strictly speaking, the weights  $\xi_r$  are not internal variables as it is sometimes assumed, since the energy of surface or interface depolarization fields can not be described in terms of only  $\xi_r$  and requires more detailed information on the domain structure. However, in the sense of a phenomenological approach it should be justified to use  $\xi_r$  as internal variables.

In the literature today one can find many models which differ in the number of variants chosen (from  $n = 2$  for domains with  $180^\circ$  orientation difference, over 6 corresponding to tetragonal ceramics with  $90^\circ$  orientation differences, up to 42 describing 7 systems where each has 6 variants of the  $90^\circ$  type). Another difference in models lies in the assumption for the evolution equation for the internal parameters. Here most models assume that the transition between variants  $r$  and  $s$  is driven by the free enthalpy change  $g_{rs}$ . The relation between the transition rate and the change in free enthalpy requires a certain physical model introducing a corresponding time scale. In our model we assume a thermally activated mechanism of domain wall motion in the field of local (short-range) obstacles and adopt the following equation for the transition rate  $w_{rs}$  from variant  $r$  to variant  $s$  [6, 7, 8]:

$$w_{rs} = w_0 \exp \left( -\frac{\Delta H_0}{kT} \left( 1 - \frac{g_{rs}}{g_c} \right) \right) (\xi_r)^\alpha \quad \dot{\xi}_r = \sum_{s=1}^n (+w_{sr} - w_{rs}) \quad (8)$$

Here  $\Delta H_0$  is the activation barrier height,  $g_c$  describes a transition threshold (obstacle strength), and the prefactor contains a general frequency constant  $w_0$ . The saturation effect related with

structural changes is described by an adjustable parameter  $\alpha$ . The main advantage of this approach lies in the fact that the dependence on temperature  $T$  and also time effects can easily be taken into account. In the talk we demonstrate the applicability of this concept to re-poling processes (a poled material is poled into another direction) [7], frequency-dependent hysteresis curves [6], temperature dependent coercive fields [8] and field simulations in a sheet actuator with interdigitated electrodes [9].

### Summary

Depending on the problem, different models can be utilized to calculate the effective linear and non-linear behavior of ferroelectric/ferroelastic materials. In all cases considered here, a certain set of internal variables is used to describe the complex domain structure met with polycrystalline materials. This reaches from a detailed grain specific description, where the internal parameters are determined from a local equilibrium with an effective surrounding, to a more phenomenological approach with a limited set of internal variables whose time evolution is described by means of rate equations inspired by the theory of thermally activated processes.

### REFERENCES

- [1] J. H. Huang, J. S. Yu, Electroelastic Eshelby tensors for an ellipsoidal piezoelectric inclusion, *Comp. Engng.* **4**, 1169–1182 (1994).
- [2] W. S. Kreher, J. Rödel, Ferroelectric ceramics and composites: Statistical Models for Effective Piezoelectric and Pyroelectric Properties, in: *Proceedings of the Eleventh IEEE International Symposium on Application of Ferroelectrics XI* (eds.: E. Colla, D. Damjanovic, N. Setter), ISAF XI, Montreux, 24–27 August 1998, pp. 455–458, IEEE, Piscataway, 1998.
- [3] J. Rödel, W. S. Kreher, Modeling linear and nonlinear behavior of polycrystalline ferroelectric ceramics, *J. Europ. Ceram. Soc.* **23**, N13, 2297–2306 (2003).
- [4] I. Müller, Micro-macro and meso mechanics of alloys with shape memory, in: *Recent developments in micromechanics* (eds.: D. R. Axelrad, W. Muschik), *Proceedings of the Mini-Symposium on Micromechanics*, June 3-9, 1990, Toronto, pp. 45–62, Springer-Verlag, Berlin, 1991.
- [5] J. E. Huber, N. A. Fleck, Multi-axial electrical switching of a ferroelectric: theory versus experiment, *J. Mech. Phys. Solids* **49**, N4, 785–811 (2001).
- [6] A. Yu. Belov, W. S. Kreher, Viscoplastic models for ferroelectric ceramics, *J. Europ. Ceram. Soc.* **25**, N12, 2567–2571 (2005).
- [7] A. Yu. Belov, W. S. Kreher, Viscoplastic behaviour of perovskite type ferroelectrics, *Mater. Sci. Eng. B* **118**, N1-3, 7–11 (2005).
- [8] A. Yu. Belov, W. S. Kreher, Simulation of microstructure evolution in polycrystalline ferroelectrics-ferroelastics, *Acta mater.* **54**, N13, 3463–3469 (2006).
- [9] A. Yu. Belov, W. S. Kreher, Micromechanics of ferroelectrics: From domain walls to piezoceramic devices, *Ferroelectrics*, in press (2007).

## INVESTIGATION OF LOCAL STRAIN AND TEMPERATURE BEHAVIOR OF SUPERELASTIC NITI WIRES

R. Lammering<sup>1</sup> and A. Vishnevsky<sup>2</sup>

<sup>1</sup> Institute of Mechanics, Helmut-Schmidt-University / University of the Federal Armed Forces Hamburg  
Holstenhofweg 85, 22043 Hamburg, Germany  
e-mail: rolf.lammering@hsu-hh.de

<sup>2</sup> Institute of Materials Research, GKSS Research Center Geesthacht  
Max-Planck Street 1, 21502 Geesthacht, Germany  
e-mail: andriy.vyshnevskyy@gkss.de

**Abstract.** *For investigations on the strongly coupled thermo-mechanical behavior of superelastic NiTi SMA a complex experimental set-up has been developed. It allows for high spatial resolution strain and temperature measurements simultaneously. The experimental program covers the range of strain rates from  $0.001\text{ s}^{-1}$  up to  $0.05\text{ s}^{-1}$  for up to 15 tensile cycles. The highly inhomogeneous transformation process along the axis of the specimen was investigated. Selected stress, strain, and temperature data are presented. A critical evaluation of the dependency of these state variables in view of the strain rate variation and the number of cycles, i.e. the training process, is given. It is shown that the training conditions not only affect the material parameters like transformation stresses or residual strains but also the character of phase transformation.*

### Introduction

Stress induced direct and back phase transformations of superelastic SMA proceed at different stresses and with heat release (exothermic) during loading and heat absorption (endothermic) during unloading. On the other hand the mechanical properties of SMAs are very sensitive to slight temperature changes. Therefore the material behavior of SMAs can only be understood by taking into account the thermo-mechanical coupling.

However, not only thermo-mechanical but also micro-mechanical effects have a distinct influence on the mechanical response of SMAs. The structure of commercially available NiTi SMAs is polycrystalline. The combination of large deformations of single crystals, stipulated by the crystallographic nature of martensitic transformation, and the interaction of arbitrarily oriented grains within the macro body produce a lot of other effects like training effects, residual strain accumulation, hardening at the final stage of direct martensitic transformation etc.

The reasons mentioned above as well as own investigations, cf. [6, 7, 8], and publications of other authors, cf. [1, 2, 3], motivate to perform experiments with a high spatial resolution in order to study the correlation between the macromechanical response of the material on the one hand and the stress, the local strains, and the local temperatures on the other hand.

## Description of test facility and program of experiments

For the basic investigations presented in the following, wire specimens with a circular cross-section have been chosen. Due to the round cross-section and relatively low heat exchange coefficient on the surface the heating process of the specimen is nearly adiabatic at high strain rates. Another reason to choose wire specimens is the fact that they are commercially available at a reasonable price in a known quality. The wire material is a nearly equiatomic NiTi alloy (trade name SE508, manufacturer EUROFlex) with  $Ni - 50.8 \text{ at\%}$ . It shows good superelastic behavior at room temperature.

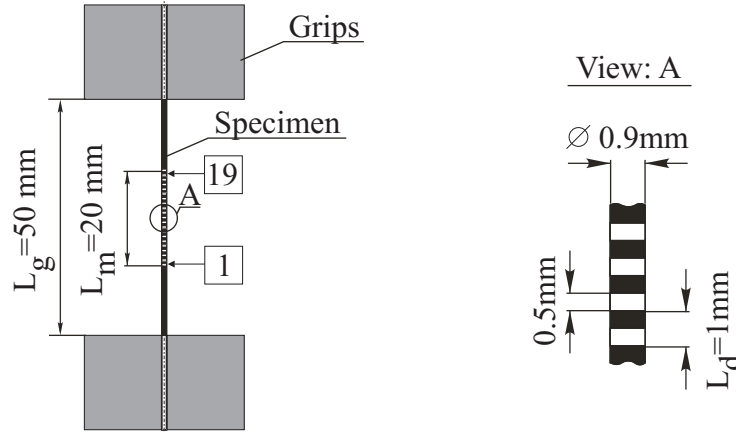


Figure 1: Wire between the grips of the testing machine (left) and specimen preparation (right). The numbers in the boxes indicate the locations of the measuring domains.

The experimental set-up was build around the electro-mechanical testing machine (TIRATest 2410) for uniaxial tension and compression tests. The strain measurements are carried out using a laser extensometer (P-50, Fiedler Optoelektronik), which allows the measurement with the precision  $0.5 \mu\text{m}$  and maximal resolution of  $L_d = 1 \text{ mm}$  (see Fig. 1). 19 measuring domains are placed along the measuring distance  $L_m$  in the middle of specimen. The numbering of the domains is shown in Fig. 1. The surface temperatures in the measuring region were measured by an infrared camera (ThermaCAM<sup>TM</sup> Phoenix, FLIR Systems) with the precision  $0.2 \text{ }^\circ\text{C}$  and resolution approximately  $0.125 \text{ mm}$ . All devices are synchronized for simultaneous data acquisition at a frequency of  $400 \text{ Hz}$ .

The strain controlled experiments cover the range of strain rates from  $\dot{\epsilon} = 0.001 \text{ s}^{-1}$  to  $\dot{\epsilon} = 0.05 \text{ s}^{-1}$ . The cyclic loading is performed without stop before unloading. Each specimen was loaded in tension for 15 cycles. The initial amplitude for each new specimen is  $\epsilon_{max} = 0.001$ . To avoid the drift of the mechanical hysteresis into the region of plastic strains the absolute maximum elongation of the specimen in all cycles was preserved as reported in [4, 5]. Each new tensile test is started at a preload of  $20 \text{ N}$  (the maximum load is about  $500 \text{ N}$ ).

## Experimental results and discussion

### Measurement of spatial strain distribution

In Fig. 2 the spatial distributions of strains along the length of the specimen are shown at various loading steps, i.e. with respect to time.

Fig. 2a depicts the strains in the first cycle with the specimen loaded at a strain rate of  $\dot{\epsilon} = 0.001 \text{ s}^{-1}$ . The diagram shows that one local phase transformation region was built in the

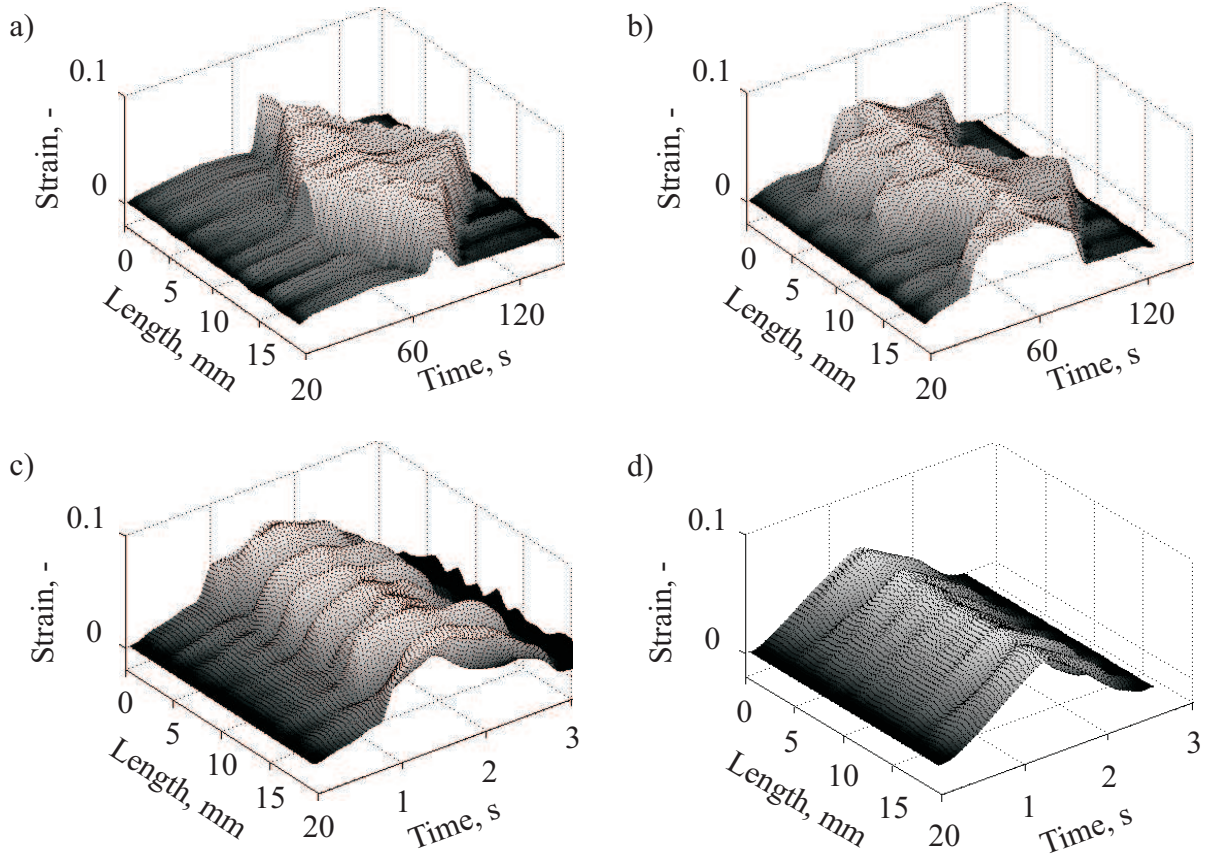


Figure 2: Strains along the length of the specimen with respect to time. Upper row:  $\dot{\epsilon} = 0.001 \text{ s}^{-1}$ , a) 1<sup>st</sup> cycle, b) 15<sup>th</sup> cycle. Lower row:  $\dot{\epsilon} = 0.05 \text{ s}^{-1}$ , c) 1<sup>st</sup> cycle, d) 15<sup>th</sup> cycle.

measuring region. In Fig. 2 the transformation regions are identified by higher local strains compared to the remaining parts of the specimen. It should be noticed that some regions remain untransformed even at maximum global strain. Similar observations of the transformation region development have been reported by other authors [1, 8]. Cyclic loading results in an increasing number of transformation fronts. In Fig. 2b the 15<sup>th</sup> loading cycle is shown. Moreover, it was observed, that from cycle to cycle the spatial positions of the starting and ending points of the transformation fronts hardly ever coincide (not shown in Fig. 2). In contrast to the 1<sup>st</sup> cycle the transformation region covers the whole length of the specimen.

Higher strain rates cause the building of multiple transformation regions already in the 1<sup>st</sup> cycle (see Fig. 2c). The phenomena observed here are analogous to the single moving front under lower strain rate on different time and length scales. In the 15<sup>th</sup> loading cycle at the strain rate  $\dot{\epsilon} = 0.05 \text{ s}^{-1}$  the specimen behaves almost homogeneously (Fig. 2d). However, individual spots (e.g. at app. 2.5 mm length) remain in a non-transformed state in the 1<sup>st</sup> as well as in the 15<sup>th</sup> cycle.

#### *Study of thermo-mechanical behavior*

The study of thermo-mechanical coupling, especially in condition of inhomogeneous phase transformation, requires simultaneous analysis of all measured state variables, e.g. strain, stress, and temperature. For description of the major stages of loading and unloading the strain rate  $\dot{\epsilon} = 0.05 \text{ s}^{-1}$  will be used.

In Fig. 3 the domains 1, 2, and 3 (see Fig. 1) are selected to represent the propagation of the

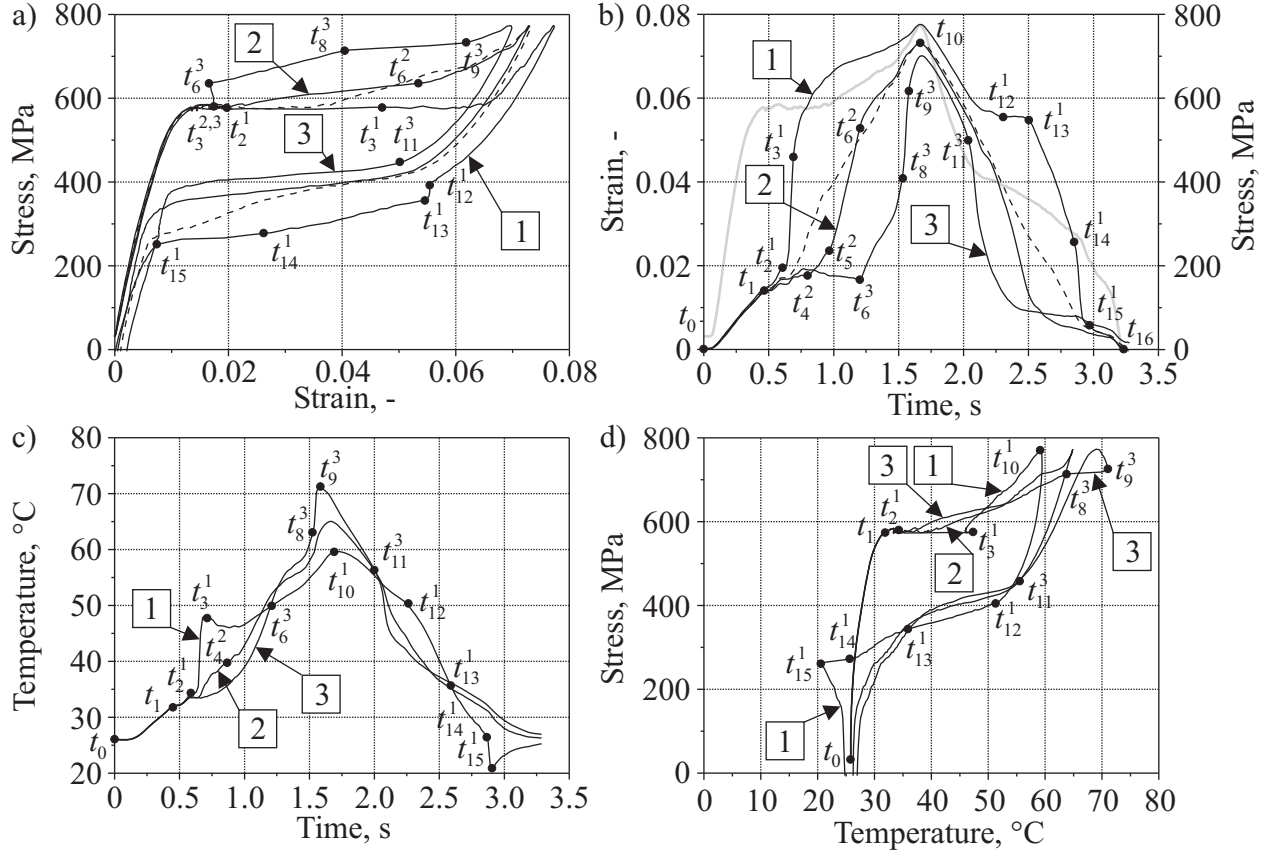


Figure 3: Thermo-mechanical behavior of the wire specimen at a strain rate  $\dot{\epsilon} = 0.05 \text{ s}^{-1}$ , 1<sup>st</sup> cycle.

transformation front from the initiation in the domain 1 until the collision with a neighboring transformation front in domain 3. To improve the readability of the diagrams in Fig. 3 the same time points (indicated by black dots) and variables  $t_j^i$  on the evolution curves are marked, where  $i$  is the domain number and  $j$  denotes the time. The transformation progress in the wire can be subdivided into 3 stages. The first one takes place at the building of the transformation front (domain 1,  $t_2 - t_3$ ). It is characterized by an almost instantaneous rise of the transformation strains and the temperature. At the same time period the macro stresses remain constant. A reasonable explanation of this behavior is an increase of local stresses and a favorable orientation of the grains due to the localization of phase transformation. The second stage is the expansion of the transformation region along the specimen (domain 1, 2, and 3,  $t_3 - t_8$ ). The main highlight of this stage is the strong influence of the stress on the temperature evolution in the stress-strain diagram in Fig. 3a as well as in the stress-time diagram in Fig. 3b (gray line). In Fig. 3a,b the curves of the second stage are located close to the dashed curves representing the entire measuring region. The third stage is a coalesce of the transformation fronts (domain 3,  $t_8 - t_9$ ). This transformation stage is similar to stage 1 and consists in the change of stress state which accelerates the transformation [9].

The process of reverse phase transformation is driven by the accumulated mechanical energy in the material. It depends strongly on the distribution of phase fraction, temperature and accumulated mechanical energy at the beginning of unloading. This makes the description of the reverse martensite-austenite transformation a very difficult problem.

### *Influence of strain rate and cycle number*

Fig. 4 shows the stress-strain curves of the specimens in the 1<sup>st</sup> and 15<sup>th</sup> cycle at the strain rates  $\dot{\epsilon} = 0.001 \text{ s}^{-1}$  and  $\dot{\epsilon} = 0.05 \text{ s}^{-1}$ . They are compared to each other and to the quasistatic case at  $\dot{\epsilon} = 0.0001 \text{ s}^{-1}$  in the 1<sup>st</sup> cycle.

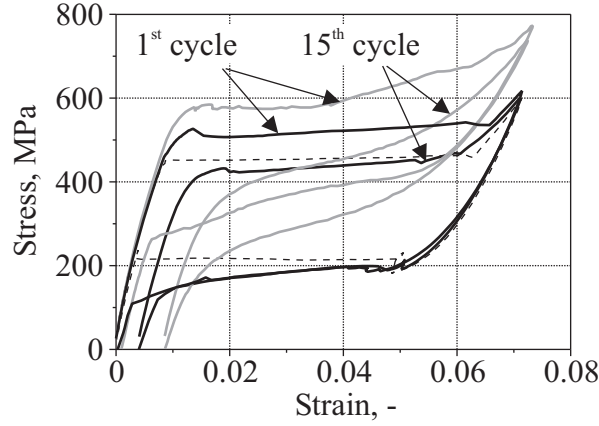


Figure 4: Mechanical diagrams of virgin and trained specimens at different strain rates. Dark curves  $\dot{\epsilon} = 0.001 \text{ s}^{-1}$ , light curves  $\dot{\epsilon} = 0.05 \text{ s}^{-1}$ , dashed line  $\dot{\epsilon} = 0.0001 \text{ s}^{-1}$  in the 1<sup>st</sup> cycle.

It is obvious that the loading rate and training process affect not only the size of the hysteresis area but also the character of the mechanical behavior of the wire specimens. In the previous section the strong dependence of the number of transformation fronts on the strain rate was shown. So the motion of a single transformation front in the 1<sup>st</sup> cycle at  $\dot{\epsilon} = 0.001 \text{ s}^{-1}$  exhibits a large, steady raising plateau of transformation stress. The 1<sup>st</sup> and 3<sup>rd</sup> transformation stages influence only the starting and ending points of the transformation plateau. The hysteresis area is larger compared to the quasistatic case. On the other hand at the strain rate  $\dot{\epsilon} = 0.05 \text{ s}^{-1}$  the multiple 1<sup>st</sup> stages of transformation build the plateau of almost constant stresses. At this loading rate the hysteresis area is again comparable to the quasistatic one.

High inhomogeneity of strains leads to an acceleration of the training process of the specimen. Fig. 4 shows clearly the strong change of the hysteresis area and shape at  $\dot{\epsilon} = 0.05 \text{ s}^{-1}$  compared to  $\dot{\epsilon} = 0.001 \text{ s}^{-1}$  in the 15<sup>th</sup> cycle. An almost absolutely homogeneous behavior of the specimen is observed in the 15<sup>th</sup> cycle at  $\dot{\epsilon} = 0.05 \text{ s}^{-1}$ .

### **Conclusions**

The experiments complement the known fact that the deformation of superelastic NiTi alloy wires in tension tests is highly inhomogeneous along the wire due to phase transformation. The investigations in these experiments allow for further clarification of the influence of local (true) material behavior on to the macro mechanical behavior of superelastic NiTi-material and particularly superelastic NiTi-wires.

The experiments show that the process of deformation homogenization is strongly dependent on the number of cycles. However, the reason for the accelerated homogenization at higher loading rates is obviously the increasing number of start and finish regions of local transformations and their recombination from one cycle to another.

### **Acknowledgement**

The financial support of German Research Foundation (DFG) is gratefully acknowledged.

## REFERENCES

- [1] J.A. Shaw, S.J. Kyriakides, Thermomechanical Aspects of NiTi, *Journal of the Mechanics and Physics of Solids* **43**, 1243–1281 (1995).
- [2] M.A. Iadicola, J.A. Shaw, The Effect of Uniaxial Cyclic Deformation on the Evolution of Phase Transition Fronts in Pseudoelastic NiTi Wire, *Journal of Intelligent Material Systems and Structures* **13**, 157–154 (2002).
- [3] Z.Q. Li, Q.P. Sun, The initiation and growth of macroscopic martensite band in nano-grained NiTi microtube under tension, *International Journal of Plasticity* **18**, 1481–1498 (2002).
- [4] S. Miyazaki, T. Imai, Y. Igo, K. Otsuka, Effects of Cyclic Deformation on the Pseudoelasticity Characteristics of Ti-Ni Alloys, *Metallurgical transactions A* **17A**, 115–120 (1986).
- [5] B. Schroeder, Dämpfungseigenschaften von Formgedächtnislegierungen, PhD-Thesis, University of Stuttgart (2001).
- [6] A. Vishnevsky; R. Lammering, Study on the thermo-mechanical behavior of superelastic NiTi wires, *PAMM Proceedings of GAMM2006* **6(1)**, 273–274 (2006).
- [7] R. Lammering, I. Schmidt, A. Vishnevsky, Characterization of Superelastic NiTi Shape Memory Alloy Specimens from Conventional Material and Sprayed-on Layers, In M. Bernadou, J. Cagnol and R. Ohayon: 16-th International Conference on Adaptive Structures, DEStech Publications, 11–18 (2006).
- [8] I. Schmidt, Untersuchungen zur Dämpfungskapazität superelastischer Nickel-Titan-Formgedächtnislegierungen, PhD-Thesis, Institute of Mechanics, Helmut-Schmidt-University / University of the Federal Armed Forces Hamburg (2004).
- [9] M.A. Indicola, J.A. Shaw, Rate and Thermal Sensitivities of Unstable Transformation Behavior in a Shape Memory Alloy, *International Journal of Plasticity* **20**, 577–605 (2004).

## GEOMETRICALLY, ELECTRICALLY AND THERMALLY NONLINEAR THERMOPIEZOMECHANICS

S. Lentzen<sup>1</sup>, R. Schmidt<sup>2</sup>, and D. Weichert<sup>3</sup>

<sup>1</sup>Institute of General Mechanics  
RWTH Aachen University  
Templergraben 64  
52062 Aachen, Germany  
e-mail: lentzen@iam.rwth-aachen.de

**Abstract.** *The modelling of the fully coupled thermopiezoelectric dipole continuum is presented in curvilinear convective coordinates. No restrictions are made with regard to the range of deformations. Due to the interaction between the polarisation and the electric field, ponderomotoric forces and body moments arise, leading to the electrical nonlinearity. The constitutive laws are developed by Coleman-Noll analysis, using a functional for the Gibb's free energy which is quadratic in all independent quantities, except for the term depending solely on temperature. As a result, linear constitutive laws evolve for the second Piola-Kirchhoff stress and the material electric displacement, and a logarithmic dependency of the entropy on the temperature, to account for large temperature changes.*

### Introduction

Due to the increasing interest in integrating piezoelectric materials into structures for static and dynamic stability control, many models, describing their behaviour, have been developed with varying levels of simplification. In the present work the thermodynamical framework is given for the thermopiezoelectric dipole continuum, with no restrictions to the range of deformations. Two assumptions are made with respect to the electrical equations. The effect of quadrupoles and those of higher order on the effective polarisation is neglected, and the material is assumed to be non-magnetisable, which holds for piezoelectric materials. With this framework, constitutive laws are developed, which are basically linear, with the exception of two terms. A nonlinear dependency of the entropy density on the temperature is assumed to account for large temperature differences. Another nonlinearity arises in the dielectric displacement due to the geometrical nonlinearity. Finally, the weak equations are derived. For the sake of generality, the equations are derived in curvilinear convective coordinates. The interested reader is referred to [1] and [2] for additional information.

### Field equations, mechanical and electrical work

Due to the possibly large deformations it is important to distinguish between spatial and material quantities, which refer respectively to either the deformed or the initial configuration. Spatial quantities and the tensor elements expressed in the deformed base vector system  $\bar{g}_i$  or  $\bar{g}^i$ , are denoted with a bar on top. Further, the investigated object is parameterised by  $\Theta^1$ ,  $\Theta^2$  and  $\Theta^3$ , resulting in the base vectors  $g_i = r_{,i}$ , where  $r$  denotes the position vector and  $[\cdot]_{,i}$  the partial derivative along  $\Theta^i$ . Before continuing with the field equations it is important to note that, due to the interaction between the polarisation and the electric field, body forces and moments

emerge. The infinitesimal polarisation  $d\bar{\mathbf{p}}$  in an infinitesimal volume  $d\bar{V}$  is represented by two infinitesimal charges of equal value, but opposite sign, separated infinitesimally by  $d\mathbf{k} = d\bar{k}^i \bar{\mathbf{g}}_i$ . The total force in the deformed volume is

$${}^e\bar{\mathbf{f}}d\bar{V} = dQ (\bar{\mathcal{E}} + \bar{\mathcal{E}}_{,1} d\bar{k}^1 + \bar{\mathcal{E}}_{,2} d\bar{k}^2 + \bar{\mathcal{E}}_{,3} d\bar{k}^3) - dQ \bar{\mathcal{E}},$$

where  $\bar{\mathcal{E}}$  is the spatial electric field. With the definition of the polarisation  $\bar{\mathbf{p}} d\bar{V} = dQ d\mathbf{k}$ , it follows that

$${}^e\bar{\mathbf{f}} = (\bar{\mathbf{p}} \cdot \bar{\nabla}) \bar{\mathcal{E}} \quad \text{with} \quad \bar{\nabla} = \bar{\mathbf{g}}^k \frac{\partial}{\partial \Theta^k}, \quad (1)$$

which is one part of the ponderomotoric force. The second part normally exists due to the free charges, which are not considered here. The total moment in the deformed volume is

$${}^e\bar{\mathbf{m}}d\bar{V} = d\mathbf{k} \times dQ (\bar{\mathcal{E}} + \bar{\mathcal{E}}_{,1} d\bar{k}^1 + \bar{\mathcal{E}}_{,2} d\bar{k}^2 + \bar{\mathcal{E}}_{,3} d\bar{k}^3).$$

Omitting the terms of higher order results in

$${}^e\bar{\mathbf{m}} = \bar{\mathbf{p}} \times \bar{\mathcal{E}}. \quad (2)$$

The *momentum balance* equation can now be written as

$$\bar{\nabla} \sigma + {}^e\bar{\mathbf{f}} + \bar{\rho} (\bar{\mathbf{b}} - \ddot{\mathbf{v}}) = 0, \quad (3)$$

where  $\sigma$  is the stress tensor, which is normally referred to as Cauchy stress. The spatial mass density  $\bar{\rho}$ , is determined by the *mass conservation* law

$$\bar{\rho} \sqrt{\bar{g}} = \rho \sqrt{g} \quad \text{or} \quad (\dot{\bar{\rho}} + \bar{\rho} \bar{\nabla} \cdot \dot{\mathbf{v}}) d\bar{V} = 0. \quad (4)$$

Further,  $\bar{\mathbf{b}}$ ,  $\mathbf{v}$  and  $\bar{g}$  are the spatial body forces, the displacement vector and the deformed metric determinant  $|\bar{g}|$ , respectively. The symmetry of the Cauchy stress tensor is usually proven by the angular momentum balance, which is now disrupted by the body moment  ${}^e\bar{\mathbf{m}}$ . From the *angular momentum balance* it now follows, that the skew-symmetric part of the stress tensor equals

$$\text{skew}(\sigma) = -\text{skew}(\bar{\mathbf{p}} \otimes \bar{\mathcal{E}}). \quad (5)$$

Two additional field equations have to be considered. Firstly, *Gauss' law*

$$\bar{\nabla} \cdot \bar{\mathbf{D}} = 0 \quad \text{in case of no free charge,} \quad (6)$$

where  $\bar{\mathbf{D}}$  denotes the spatial electric displacement, which is by definition related to the electric field and the polarisation by the following constitutive law

$$\bar{\mathbf{D}} = \varepsilon_0 \bar{\mathcal{E}} + \bar{\mathbf{p}}, \quad (7)$$

where the permittivity of free space  $\varepsilon_0$  equals  $8.8542 \cdot 10^{-12}$  F/m. And secondly the *heat balance* law

$$DQ = (\bar{\rho} \bar{h} - \bar{\nabla} \cdot \bar{\mathbf{h}}) dt d\bar{V}, \quad (8)$$

where  $DQ$ ,  $\bar{h}$  and  $\bar{\mathbf{h}}$  denote the change of heat, the inner heat source and the heat flux, respectively.

With  $\mathbf{F} = \bar{\mathbf{g}}_i \otimes \mathbf{g}^i$  denoting the deformation gradient, the *mechanical work* is expressed as

$$D^m W = \sigma^T : \left( \dot{\mathbf{F}} \mathbf{F}^{-1} \right) dt d\bar{V} + (\bar{\nabla} \sigma + \bar{\rho} (\bar{\mathbf{b}} - \ddot{\mathbf{v}})) \cdot \dot{\mathbf{v}} dt d\bar{V}, \quad (9)$$

and the *electrical work*, regarding (4), is expressed as

$$D^e W = (\bar{\mathbf{f}} \cdot \dot{\mathbf{v}} + \bar{\rho} \bar{\boldsymbol{\varepsilon}} \cdot \dot{\bar{\boldsymbol{\pi}}}) dt d\bar{V} \quad \text{with} \quad \bar{\rho} \bar{\boldsymbol{\pi}} = \bar{\mathbf{p}}, \quad (10)$$

which, under consideration of (3), sum up to

$$DW = \left( \boldsymbol{\sigma}^T : \left( \dot{\mathbf{F}} \mathbf{F}^{-1} \right) + \bar{\rho} \bar{\boldsymbol{\varepsilon}} \cdot \dot{\bar{\boldsymbol{\pi}}} \right) dt d\bar{V}. \quad (11)$$

### Colemann-Noll analysis

According to the *first principle* of thermodynamics, the change of inner energy equals the sum of work done and the change of heat,

$$DU = DW + DQ \quad \text{with} \quad DU = \dot{u} \bar{\rho} dt d\bar{V}.$$

This leads with (8) and (11) to

$$\dot{u} \bar{\rho} = \boldsymbol{\sigma}^T : \left( \dot{\mathbf{F}} \mathbf{F}^{-1} \right) + \bar{\rho} \bar{\boldsymbol{\varepsilon}} \cdot \dot{\bar{\boldsymbol{\pi}}} + \bar{\rho} \bar{h} - \bar{\nabla} \cdot \bar{\mathbf{h}}. \quad (12)$$

The first and second Clausius-Duhem inequality of the *second principle* of thermodynamics can be summarised as the *Meixner inequality*

$$-\bar{\nabla} \cdot \left( \frac{1}{\bar{T}} \bar{\mathbf{h}} \right) + \bar{\rho} \frac{\bar{h}}{\bar{T}} \leq \bar{\rho} \dot{\bar{s}},$$

with  $\bar{T}$  and  $\bar{s}$  denoting the absolute temperature and the entropy density in the deformed configuration. Inserting this inequality into (12) leads to

$$\dot{u} \bar{\rho} - \boldsymbol{\sigma}^T : \left( \dot{\mathbf{F}} \mathbf{F}^{-1} \right) - \bar{\rho} \bar{\boldsymbol{\varepsilon}} \cdot \dot{\bar{\boldsymbol{\pi}}} + \frac{1}{\bar{T}} \bar{\mathbf{h}} \cdot \bar{\nabla} \bar{T} - \bar{\rho} \bar{T} \dot{\bar{s}} \leq 0. \quad (13)$$

Choosing  $\mathbf{F}$ ,  $\bar{\boldsymbol{\varepsilon}}$  and  $\bar{T}$  as independent variables and, in order to obtain constitutive laws for the remaining quantities by parameter identification, the Gibb's free energy is introduced as

$$\bar{G} = \bar{u} - \bar{\rho} \bar{\boldsymbol{\pi}} \cdot \bar{\boldsymbol{\varepsilon}} - \bar{\rho} \bar{T} \bar{s},$$

which leads with (13) to

$$\bar{\rho} \dot{\bar{G}} - \boldsymbol{\sigma}^T : \left( \dot{\mathbf{F}} \mathbf{F}^{-1} \right) + \bar{\rho} \dot{\bar{T}} \bar{s} + \bar{\rho} \bar{\boldsymbol{\pi}} \cdot \bar{\boldsymbol{\varepsilon}} + \frac{1}{\bar{T}} \bar{\mathbf{h}} \cdot \bar{\nabla} \bar{T} \leq 0. \quad (14)$$

Assuming  $\bar{G} = \hat{G}(\mathbf{F}, \bar{\boldsymbol{\varepsilon}}, \bar{T})$ , inserting it into (14), and considering  $\bar{\mathbf{h}} \cdot \bar{\nabla} \bar{T} \leq 0$ , results in the following constitutive laws

$$\boldsymbol{\sigma}^T = \bar{\rho} \frac{\partial \hat{G}}{\partial \mathbf{F}} \mathbf{F}^T, \quad \bar{\boldsymbol{\pi}} = -\frac{\partial \hat{G}}{\partial \bar{\boldsymbol{\varepsilon}}} \quad \text{and} \quad \bar{s} = -\frac{\partial \hat{G}}{\partial \bar{T}}. \quad (15)$$

Due to the principle of *material objectivity*, the Gibb's free energy functional takes on the following specific form

$$\bar{G} = \hat{G}(\mathbf{E}, \bar{\boldsymbol{\varepsilon}}, \bar{T}) \quad \text{with} \quad 2\mathbf{E} = \mathbf{F}^T \mathbf{F} - \mathbf{I} \quad \text{and} \quad \bar{\boldsymbol{\varepsilon}} = \mathbf{F}^T \bar{\boldsymbol{\varepsilon}},$$

where  $\mathbf{E}$  and  $\mathcal{E}$  are the Green-Lagrange strain tensor and the material electric field. Applying the chain rule on (15) and considering  $\mathbf{S} = |\mathbf{F}| \mathbf{F}^{-1} \boldsymbol{\sigma} \mathbf{F}^{-T}$ ,  $\mathbf{p} = |\mathbf{F}| \mathbf{F}^{-1} \bar{\mathbf{p}}$  and  $s = \bar{s}$  leads to

$$\mathbf{S} = \rho \frac{\partial \hat{G}}{\partial \mathbf{E}} - (\mathbf{p} \otimes \mathcal{E}) \mathbf{F}^{-1} \mathbf{F}^{-T}, \quad \mathbf{p} = -\rho \frac{\partial \hat{G}}{\partial \mathcal{E}} \quad \text{and} \quad s = -\frac{\partial \hat{G}}{\partial T},$$

and thus confirming (5). The following functional of the Gibb's free energy is assumed,

$$\rho \hat{G} = \frac{1}{2} (\mathbf{E} : \mathbb{C} : \mathbf{E} - \mathcal{E} \mathcal{D} \mathcal{E}) - \beta \rho \left( \bar{T} \left( \ln \frac{\bar{T}}{T} - 1 \right) + T \right) - \mathcal{E} \mathbb{E} : \mathbf{E} - \mathbf{E} : \mathcal{B} (\bar{T} - T) - \mathcal{E} \cdot \lambda (\bar{T} - T),$$

where  $\mathbb{C}$ ,  $\mathcal{D}$ ,  $\mathbb{E}$ ,  $\mathcal{B}$  and  $\lambda$  contain material parameters, and  $\beta$  is the specific heat at constant strain and electric field.

From  $\bar{\mathbf{h}} \cdot \bar{\nabla} \bar{T} \leq 0$  it can be concluded that  $\bar{\mathbf{h}}$  being an odd function of  $\bar{\nabla} \bar{T}$  is an acceptable choice. With  $\mathbf{h} = |\mathbf{F}| \bar{\mathbf{h}} \mathbf{F}^{-T}$  and considering the principle of *material objectivity*,  $\mathbf{h} = -\mathcal{L} \nabla T$  is taken as the constitutive law for the heat flux, which leads with (7) to the following set of general equations in index notation

$$S^{rs} = \frac{1}{2} (\mathbb{C}^{rsij} + \mathbb{C}^{ijrs}) E_{ij} - \mathbb{E}^{irs} \mathcal{E}_i - \mathcal{B}^{rs} (\bar{T} - T) - p^r \mathcal{E}_k \bar{g}^{ks} \quad (16)$$

$$p^k = \frac{1}{2} (\mathcal{D}^{ik} + \mathcal{D}^{ki}) \mathcal{E}_i + \mathbb{E}^{kij} E_{ij} + \lambda^k (\bar{T} - T) \quad (17)$$

$$D^k = \frac{1}{2} (\mathcal{D}^{ik} + \mathcal{D}^{ki} + 2|\mathbf{F}| \varepsilon_o \bar{g}^{ki}) \mathcal{E}_i + \mathbb{E}^{kij} E_{ij} + \lambda^k (\bar{T} - T) \quad (18)$$

$$s = c_{E,\mathcal{E}} \ln \frac{\bar{T}}{T} + \frac{1}{\rho} \mathcal{B}^{ij} E_{ij} + \frac{1}{\rho} \lambda^i \mathcal{E}_i \quad (19)$$

$$h^i = \mathcal{L}^{ij} \bar{T}_{,j}. \quad (20)$$

### Variational formulation

Multiplying (3) scalar with  $\delta \mathbf{v}$ , (6) and (8) with  $\delta \varphi$  and  $\delta \bar{T}$ , where  $\varphi$  denotes the electric potential, and integrating the results over the deformed volume, assuming no entropy production, and applying Gauss' divergence theorem, ultimately leads to the following weak formulations

$$\int_V (\mathbf{F} \mathbf{S} \mathbf{F}^T) : (\delta \mathbf{F} \mathbf{F}^{-1}) dV - \int_V ((\mathbf{p} \cdot \nabla) (\mathbf{F}^{-T} \mathcal{E}) + \rho (\mathbf{b} - \ddot{\mathbf{v}})) \cdot \delta \mathbf{v} dV - \int_{\partial \bar{V}} (\boldsymbol{\sigma} \delta \mathbf{v}) \cdot \bar{\mathbf{n}} d\bar{A} = 0 \quad (21)$$

$$\int_V \mathbf{D} \cdot \delta \mathcal{E} dV - \int_{\partial V} \mathbf{n} \cdot \mathbf{D} \delta \varphi dA = 0 \quad (22)$$

$$\int_V (\mathbf{h} \cdot (\nabla \delta \bar{T}) - (\bar{T} \dot{s} - \rho h) \delta \bar{T}) dV - \int_{\partial V} \mathbf{n} \cdot \mathbf{h} \delta \bar{T} dA = 0, \quad (23)$$

where  $\bar{\mathbf{n}}$  and  $\mathbf{n}$  denote the surface normal vector in the deformed and the initial configuration, respectively, and  $\bar{\mathcal{E}} = -\bar{\nabla} \varphi$ .

### REFERENCES

- [1] A.C. Eringen, Mechanics of Continua, New York (1980).
- [2] Y. Bařar and D. Weichert, Nonlinear Continuum Mechanics of Solids, Heidelberg (2000).

# A NONLINEAR CONSTITUTIVE MODEL FOR MAGNETOSTRICTIVE MATERIALS

Konrad Linnemann<sup>1</sup>, Sven Klinkel<sup>1</sup>

<sup>1</sup>Institut für Baustatik, Universität Karlsruhe (TH)  
Kaiserstr. 12, 76131 Karlsruhe  
e-mail: kl@bs.uka.de

**Abstract.** *A 3D macroscopic constitutive law for nonlinear effects in giant magnetostrictive materials is presented. The phenomenological model accounts for hysteresis effects and is implemented into a finite element formulation. The novel aspect of the thermodynamically consistent model is an additive decomposition of the magnetic and the strain field in a reversible and an irreversible part. To consider the correlation between the irreversible magnetic field and the irreversible strains a one-to-one relation is assumed. The irreversible magnetic field determines as internal variable the movement of the center of a switching surface. This controls the motion of the domain walls during the magnetization process. The evolution of the internal variables is derived from the magnetic enthalpy function by the postulate of maximum dissipation, where the switching surface serves as constraint. The evolution equations are integrated using the backward Euler implicit integration scheme. The constitutive model is implemented in a 3D hexahedral element which provides an algorithmic consistent tangent stiffness matrix. A numerical example demonstrates the capability of the proposed model to reproduce the ferromagnetic and butterfly hysteresis loops of a Terfenol-D sample.*

## Introduction

The development of giant magnetostrictive alloys has made these materials competitive to other smart materials like piezoelectric ceramics and shape memory alloys. As a result applications in actuating and sensing are found, see [1]. Giant magnetostrictive materials show strong nonlinearities, which have to be considered in the development of constitutive relations. Microscopically motivated models, like [2], [3] consider the behaviour for each crystal and lead to many internal parameters. The published phenomenological macroscopic material models commonly apply on the mathematically and non thermodynamically motivated Preisach model [4] or they are based on a higher order thermodynamic potential [5]. The presented constitutive model is thermodynamically consistent. It is similar to the inelasticity theory of mechanics and uses an additive decomposition of the magnetic field. This results in a convenient model for an efficient finite element implementation.

## The Magnetostrictive Effect

The magnetostrictive coupling defines a deformation of a specimen which is induced by an applied magnetic field. It is an inherent material coupling effect between mechanical and magnetic fields occurring in all ferro- and ferrimagnetic materials. But normally the observed strains are very small. Some alloys of rare-earth elements and iron show a much higher coupling. One of these materials is Terfenol-D with strains up to  $1.6 \cdot 10^{-3}$ . The magnetostrictive

coupling rises from an anisotropic spacing in the crystal lattice depending on the direction of the magnetic moment of the atoms. Strains in magnetostrictive rod are produced when a magnetic field  $\vec{H}$  causes a rotation of the magnetic moments  $\vec{M}$ , see Fig. 1.

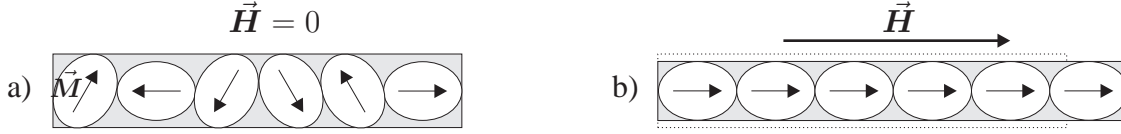


Figure 1: Deformation behaviour of a magnetostrictive rod

## Constitutive Model

The gradient fields for a magnetostrictive coupled problem are given by the strains  $\mathbf{E} = \frac{1}{2}(\nabla \otimes \mathbf{u} + \mathbf{u} \otimes \nabla)$  and the magnetic field  $\vec{H} = -\nabla \varphi$ . Here  $\mathbf{u}$  denotes the displacement vector and  $\varphi$  the magnetic scalar potential. The strains are splitted in a reversible and an irreversible part  $\mathbf{E} = \mathbf{E}^r + \mathbf{E}^i$ . The main idea of the presented model is an additive decomposition of the magnetic field in  $\vec{H} = \vec{H}^r + \vec{H}^i$ . The irreversible magnetic field  $\vec{H}^i$  has no descriptive meaning but it represents the motion of the domain walls as internal variable. To consider the coupling between the internal magnetic state and the irreversible strains a one-to-one relation is assumed as

$$\mathbf{E}^i = \frac{E_s}{(H_s^i)^2} \vec{H}^i \cdot \vec{H}^i \frac{3}{2} (\mathbf{e}_M \otimes \mathbf{e}_M - \frac{1}{3} \mathbf{1}), \quad (1)$$

see also [6] in the context of piezoelectric materials. The quantities  $E_s$  and  $H_s^i$  are saturation values for  $\mathbf{E}^i$  and  $\vec{H}^i$  and are given as material parameters. The vector  $\mathbf{e}_M$  denotes the direction of the magnetization which is fixed during the calculation. The magnetic enthalpy is assumed as 2nd order thermodynamical potential

$$\psi = \frac{1}{2} (\mathbf{E} - \mathbf{E}^i) : \mathbb{C} : (\mathbf{E} - \mathbf{E}^i) + \vec{H} \cdot \mathbf{e} \frac{\vec{H}^i \cdot \mathbf{e}_M}{H_s^i} : (\mathbf{E} - \mathbf{E}^i) - \frac{1}{2} (\vec{H} - \vec{H}^i) \cdot \boldsymbol{\mu} (\vec{H} - \vec{H}^i) + \bar{\psi}(\vec{H}^i). \quad (2)$$

Here,  $\mathbb{C}$  is the elasticity tensor,  $\mathbf{e}$  the piezomagnetic coupling tensor and  $\boldsymbol{\mu}$  denotes the permeability. The hardening function  $\bar{\psi}(\vec{H}^i)$  depends only on the internal variable  $\vec{H}^i$ . With the definition of the mechanical stresses  $\mathbf{S} := \frac{\partial \psi}{\partial \mathbf{E}} = \mathbb{C} : (\mathbf{E} - \mathbf{E}^i) + \mathbf{e}^T \frac{\vec{H}^i \cdot \mathbf{e}_M}{H_s^i} \vec{H}$  and the magnetic flux density  $\vec{B} := \frac{\partial \psi}{\partial \vec{H}} = \mathbf{e} \frac{\vec{H}^i \cdot \mathbf{e}_M}{H_s^i} (\mathbf{E} - \mathbf{E}^i) - \boldsymbol{\mu} (\vec{H} - \vec{H}^i)$  the dissipation inequality of the second law of thermodynamics reads

$$\mathcal{D} = - \frac{\partial \psi}{\partial \vec{H}^i} \cdot \dot{\vec{H}}^i \geq 0. \quad (3)$$

The work conjugated variable  $\mathbf{T} = - \frac{\partial \psi}{\partial \vec{H}^i}$  of the internal quantity  $\vec{H}^i$  is used to formulate a switching criterion as

$$\phi = \frac{\mathbf{T} \cdot \mathbf{T}}{M_c^2} - 1 \leq 0 \quad (4)$$

with the material parameter  $M_c$ . For  $\phi < 0$  a reversible process is assumed,  $\phi = 0$  denotes irreversible behaviour. The postulate of maximum dissipation is considered by the stationarity of a Lagrange functional with the switching criterion as constraint  $\mathcal{L} = -\mathcal{D} + \lambda \Phi$ . The evolution of the internal variable is obtained as  $\dot{\vec{H}}^i = \lambda \frac{\partial \Phi}{\partial \mathbf{T}} = \lambda \frac{2\mathbf{T}}{M_c^2}$ . The evolution equation is integrated using a backward Euler implicit time integration scheme.

The weak form of equilibrium follows with the principle of virtual work from the strong form of equilibrium  $\mathbf{S} \cdot \nabla + \mathbf{b} = \mathbf{0}$  and from the Maxwell equation  $\vec{\mathbf{B}} \cdot \nabla = 0$  and with respect to the boundary conditions  $\mathbf{S} \mathbf{n} = \mathbf{t}$  on  $\partial_t \mathcal{B}_0$  and  $\vec{\mathbf{B}} \cdot \mathbf{n} = 0$  on  $\partial \mathcal{B}_0$

$$\delta \pi = \int_{\mathcal{B}_0} \left( \frac{\partial \psi}{\partial \mathbf{E}} : \delta \mathbf{E} + \frac{\partial \psi}{\partial \vec{\mathbf{H}}} : \delta \vec{\mathbf{H}} \right) dV - \int_{\mathcal{B}_0} \mathbf{b} \cdot \delta \mathbf{u} dV - \int_{\partial_t \mathcal{B}_0} \mathbf{t} \cdot \delta \mathbf{u} dA = 0. \quad (5)$$

Here,  $\mathbf{b}$  is the volume force vector,  $\mathbf{t}$  the surface traction vector and  $\mathbf{n}$  the surface normal vector.

### Finite Element Implementation

The constitutive model is implemented in an 8-node hexahedral element. The geometry of the element is approximated with trilinear shape function  $N_I$  as  $\mathbf{X}_e^h = \sum_{I=1}^8 N_I \mathbf{X}_I$ . Due to the isoparametric concept the same interpolation functions are used to approximate the displacements and magnetic potential as  $\mathbf{d}_e^h = [\mathbf{u}_e^h, \varphi_e^h]^T = \mathbf{N} \mathbf{v}_e$  with  $\mathbf{N} = [N_1, N_2, \dots, N_8]$  consisting of  $N_I = \text{diag}[N_I, N_I, N_I, N_I]$ . The vector  $\mathbf{v}_e$  denotes the nodal degrees of freedom on element level with 3 displacement values and one for the magnetic potential per knot. The virtual gradient fields are ordered in the vector  $\delta \epsilon_e^h = [\delta E_{11}, \delta E_{22}, \delta E_{33}, 2\delta E_{12}, 2\delta E_{13}, 2\delta E_{23}, \delta \vec{H}_1, \delta \vec{H}_2, \delta \vec{H}_3]^T$   $\delta \epsilon_e^h = \mathbf{B} \delta \mathbf{v}_e$ . The matrix  $\mathbf{B}$  contains the derivatives of the shape functions. The approximated weak form on element level reads

$$\delta \pi_e^h = \delta \mathbf{v}_e^T \underbrace{\left[ \int_{\mathcal{B}_e} \left( \mathbf{B}^T \frac{\partial \psi}{\partial \epsilon} - \mathbf{N}^T \begin{bmatrix} \mathbf{b} \\ 0 \end{bmatrix} \right) dV - \int_{\partial \mathcal{B}_e} \mathbf{N}^T \begin{bmatrix} \mathbf{t} \\ 0 \end{bmatrix} dA \right]}_{\mathbf{R}_e^h}. \quad (6)$$

Assembling over all element  $\delta \pi^h = \bigcup_{e=1}^{elem} \delta \pi_e^h = 0$  gives the residual vector  $\mathbf{R}^h = \bigcup_{e=1}^{elem} \mathbf{R}_e^h$  and  $\mathbf{v}^h = \bigcup_{e=1}^{elem} \mathbf{v}_e^h$ . To obtain quadratic convergence for the Newton-Raphson iteration, an algorithmic consistent tangent stiffness is needed. The residual vector at the load step  $\mathbf{t}_{n+1}$  is replaced with a Taylor series which is truncated after the linear element

$$\mathbf{R}_{n+1}^{h(K)} + \frac{\partial \mathbf{R}_{n+1}^{h(K)}}{\partial \mathbf{v}_{n+1}} \Delta \mathbf{v}_{n+1} = \mathbf{0}. \quad (7)$$

The superscript  $(K)$  denotes the iteration step. The nodal degrees of freedom are updated after each iteration step with  $\mathbf{v}_{n+1} = \mathbf{v}_{n+1}^k + \Delta \mathbf{v}_{n+1}^{k+1}$ . The tangent stiffness follows with the chain rule to

$$\mathbf{K}_{eT} := \frac{\partial \mathbf{R}_e^{h(K)}}{\partial \mathbf{v}_{n+1}} = \int_{\mathcal{B}_e} \mathbf{B}^T \mathbb{D}_{T_{n+1}}^{(K)} \mathbf{B} dV. \quad (8)$$

The algorithmic consistent tangent modules is obtained explicitly by

$$\mathbb{D}_{T_{n+1}}^{(K)} = \begin{bmatrix} \frac{\partial \mathbf{S}}{\partial \mathbf{E}} - \frac{1}{\partial_\alpha \bar{T}} \frac{\partial \mathbf{S}}{\partial \alpha} \otimes \frac{\partial \bar{T}}{\partial \mathbf{E}} & \frac{\partial \mathbf{S}}{\partial \vec{\mathbf{H}}} - \frac{1}{\partial_\alpha \bar{T}} \frac{\partial \mathbf{S}}{\partial \alpha} \otimes \frac{\partial \bar{T}}{\partial \vec{\mathbf{H}}} \\ \frac{\partial \vec{\mathbf{B}}}{\partial \mathbf{E}} - \frac{1}{\partial_\alpha \bar{T}} \frac{\partial \vec{\mathbf{B}}}{\partial \alpha} \otimes \frac{\partial \bar{T}}{\partial \mathbf{E}} & \frac{\partial \vec{\mathbf{B}}}{\partial \vec{\mathbf{H}}} - \frac{1}{\partial_\alpha \bar{T}} \frac{\partial \vec{\mathbf{B}}}{\partial \alpha} \otimes \frac{\partial \bar{T}}{\partial \vec{\mathbf{H}}} \end{bmatrix}_{n+1}^{(K)} \quad (9)$$

with  $\bar{T} = \mathbf{T} \cdot \mathbf{e}_M$  and  $\alpha = \frac{\vec{\mathbf{H}}^i \cdot \mathbf{e}_M}{H_s^i}$

### Numerical example

A Terfenol-D cube of edge length  $2\text{ cm}$  in an oscillating magnetic field of  $\vec{H} = -10^5 \dots 10^5\text{ A/m}$  is considered. The magneto-elastic Material constants are given by  $E = 29\text{ GN/m}^2$ ,  $\nu = 0.25$ ,  $e_{33} = 83.9\text{ Vs/m}^2$ ,  $e_{13} = e_{15} = 0$ ,  $\mu_1 = \mu_2 = \mu_3 = 2.8025 \cdot 10^{-6}\text{ Vs/Am}$ . The switching criterion reads  $M_c = 9.0 \cdot 10^{-3}\text{ T}$ . The hardening function is assumed as  $\frac{\partial \bar{\psi}}{\partial \alpha} = H_s^i K \alpha + a \operatorname{arctanh}(\frac{\alpha}{b})$ . The material parameters for the hardening function are  $H_s^i = 185000\text{ A/m}$ ,  $K = 2.8305 \cdot 10^{-6}\text{ Vs/Am}$ ,  $a = 8.078 \cdot 10^{-2}\text{ T}$ ,  $b = 1.05$ . Figure 2 demonstrates the capability of the proposed model to reproduce the typical ferromagnetic and butterfly hysteresis loops of a Terfenol-D sample.

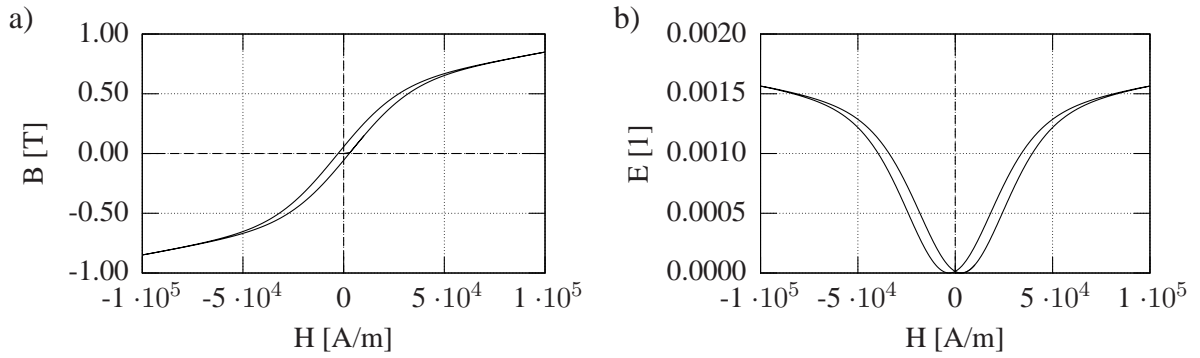


Figure 2: a) ferromagnetic hysteresis, b) butterfly hysteresis

### REFERENCES

- [1] G. Engdahl, Handbook of Giant Magnetostrictive Materials, Academic Press (2000)
- [2] D.C. Jiles, Theory of the Magnetomechanical Effect, Journal of Physics D - Applied Physics **28**, 1537–1546, (1995).
- [3] M. J. Dapino, R. C. Smith, F. T. Calkins, A. B. Flatau, A coupled magnetomechanical model for magnetostrictive transducers and its application to Villari-effect sensors, Journal of Intelligent Material Systems and Structures **13**, 737–747, (2002).
- [4] X. Tan, J. S. Baras, Modeling and control of hysteresis in magnetostrictive actuators, Automatica **40**, 1469–1480, (2004)
- [5] G.P. Carman, M. Mitrovic, Nonlinear Constitutive Relations for Magnetostrictive Materials with Applications to 1-D Problems, J. of Int. Mat. Sys. and Struct. **6**, 673–683 (1995)
- [6] M. Kamlah Ferroelectric and ferroelastic piezoceramics modeling of electromechanical hysteresis phenomena, Continuum Mechanics and Thermodynamics **13**, 219–268, (2001).

# MICROSTRUCTURAL PARAMETERS AND SEMICONDUCTOR PROPERTIES AT THE ORIGIN OF THE MACROSCOPIC BEHAVIOR OF FERROELECTRICS

**Doru C. Lupascu**

Institute of Materials Science  
Dresden University of Technology, Helmholtzstr. 7, 01069 Dresden  
e-mail: doru.lupascu@tu-dresden.de

**Abstract.** *Ferroelectric materials couple stress or strain to electrical fields or displacements and provide remanent memory states. Some of these parameters change during device use due to aging or fatigue. Up to now, it has not become clear which microscopic mechanisms finally determine both effects. This is mostly due to a still poor understanding of the micro- and mesoscopic structural effects. Some problems are of mechanical origin like stresses at grain boundaries, electrode connections, or unfavorable geometrical shapes of the device. For a complete class of other problems the rearrangement of charged defects is the fundamental process. Charged defects change the local electric fields and can thus alter the microscopic domain dynamics. At the same time, the electrical semiconductor properties change considerably. This short report is intended to draw attention to these coupled effects.*

## Introduction

Ferroelectric materials provide two valuable properties. The first is a coupling between mechanical and electrical parameters, e.i. stress or strain on the one hand and electric field or displacement on the other. This coupling is used for all piezoelectric devices. The second is that a remanent state can be externally imposed which can be used for information storage in memory devices. Such a memory state can be an electrical information bit for a computer or potentially a remanent deformation in micromechanical devices. A vast variety of piezoelectric devices is in use today [1] and ferroelectric memories have been implemented [2].

A long term utility of any of such devices can only be assured, if the material as well as the entire device survive the loading during use. The materials at hand should furthermore not alter their properties with time. This is not the case for particular loading conditions or certain materials. Fatigue is a process mostly arising under bipolar loading and thus predominantly affects ferroelectric memories. In thin film memories, this effect has been overcome technologically either by the use of oxide electrode materials on perovskite ferroelectrics or by using bismuth layered compounds and ordinary platinum electrodes. It has been inferred from these findings that the underlying fatigue process is due to electrochemical processes involving charge or vacancy transport. These transport properties depend on the inherent crystallographic structure. Presently, point defects are considered the fundamental culprit of fatigue [3]. On the other hand, it is still under debate in how much these point defects ultimately change the mechanical properties of the material, too. Particularly microcracking occurs as a major contribution to macroscopic material fatigue under bipolar loading [4].

Aging, on the other hand, is the change of material properties with time. It is due to charge carrier drift [5] or defect dipolar re-orientation [6], both mechanisms still being debated. In either case, the interaction is considered to be electrostatic.

### Mechanical Boundaries: Stresses and Strains

The microstructure in ferroelectric ceramics consists of many different internal boundaries (Fig. 1). Fundamentally, there are grain boundaries (A), interfaces to electrodes (C) where a perfect electrical match to the domain system is provided by the free charge carriers in the electrode,  $180^\circ$  domain walls, non- $180^\circ$  domain walls, and interfaces to inclusions or pores. Cubic systems mostly offer approximately  $90^\circ$  domain walls as the non- $180^\circ$  type. In either case regular or charged domain walls exist the latter meaning that the polarization vectors at the domain wall are oriented tip-to-tip or tail-to-tail yielding extremely high local electric fields. Particularly needle tip domains are charged (D). They commonly occur in single crystals during polarization reversal and for harsh boundary conditions, e.g. in samples artificially thinned for transmission electron microscopy (Fig. 1). The highest local stresses develop at intersection points where needle domains within the same crystallite (one grain) meet (B) and even microcracking can be initiated within one crystallite. So far the best description of three dimensional room filling of grains by domains in a ceramic structure has been given by Arlt in his fundamental review on micro-configurations of domain walls [7]. In such compensated structures only very few charged domain walls occur and the total energy is low.

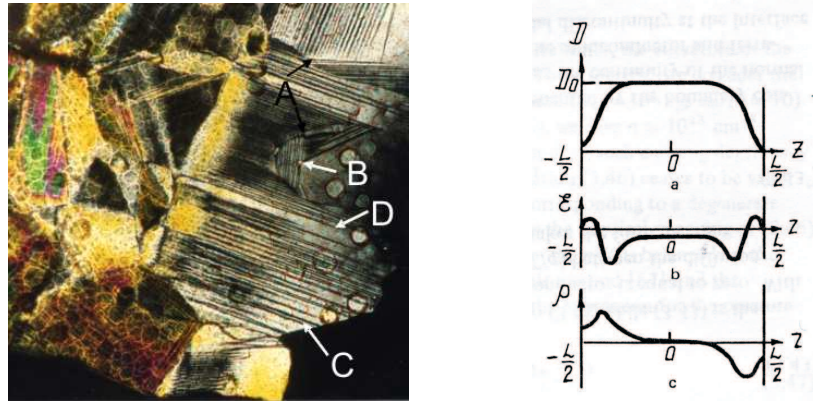


Figure 1: (left) Microstructural features in ferroelectric BaTiO<sub>3</sub> (optical photograph by H. Gorzawski); (right) electric displacement  $\mathbf{D}$ , electric field  $\mathbf{E}$ , and charge density  $\rho$  for a single domain semiconducting ferroelectric [8].

The domain system of a grain terminates at a grain boundary. At an open surface a dented surface morphology develops because no opposing forces exist. Where a grain is embedded into a microstructure a neighboring grain constitutes an elastic medium generating restoring forces. In order for the energy of the entire system to be low, the domain system of the neighbor often matches that of the initial grain. So, domain patterns propagate from grain to grain for moderately off-axis crystallite orientations. As three axes need to be matched in between grains in three dimensions, such an arrangement can only partly compensate the mechanical stresses. While several methods have been developed to display domain systems in microstructures [9], it is very hard to access microscopic stresses and strains. A powerful local X-ray technique is provided by the Kossel technique [10] yielding grain orientations and lattice strains.

## Electrical Boundaries: Displacements and Fields

At first sight it seems that the electrical description of ferroelectrics is simple. Poisson's equation  $\text{div } \mathbf{D} = \rho$  appears to bear everything needed for the electrostatic boundary value problem. The first difficulty arises in anisotropic dielectric constants where electric field and electric displacement can no longer be easily mapped onto each other in 3D. Up to an order of magnitude difference in different crystallographic directions arises in  $\text{BaTiO}_3$ . Lead zirconate-titanate provides less pronounced anisotropies. The second subtlety arises due to semiconductor physics (see beneath). The third difficulty on a long time scale is the mobility of atomic species, mostly oxygen vacancies. Initially they occupy sites in the microstructure, where thermal equilibrium positions them during processing. On the time scale of vacancy motion, the cooling of the ferroelectric to room temperature is equivalent to quenching. Thus, the vacancies are not in thermal equilibrium in the ferroelectric state of the material. Their slow kinetics then determine the development of internal fields and charge compensation at long times and yield the aging effects [5].

## Semiconductor Effects: Localization and Delocalization

According to Ginzburg-Landau-theory the free energy  $F$  of a ferroelectric can be developed into a series in polarization  $P$ , left in Eqn. (2). Originally developed to describe ferroelectric phase transitions, it turned out to be valid across much larger temperature intervals. Under external loading the free energy has to be complemented by the elastic and piezoelectric terms yielding Eqn. (2).

On the other hand, the material is a wide band-gap semiconductor. As such, the free energy  $F_2$  represents electron statistics, Eqn. (3). This is a very relevant addition to the problem. Electrons in band states of semiconductors are completely free to move across a crystal. As such, they do not occupy any particular site in the microstructure only their energy is determined. If fields are present and a sufficient number of charge carriers occupies the band, the material is an ideal conductor, complete compensation occurs, and the material intrinsically becomes field free. Under these circumstances the ferroelectric state can not be switched by external electric fields. Only if the total charge carrier density in the bands is low, the local fields are not compensated. For most ferroelectrics, the band gap is wide so that the thermally excited number of intrinsic charge carriers in the bands is low (Fermi statistics). In chemically doped systems which is the case in all technologically interesting materials the electronic charge carriers attached to the dopant ions can be ionized at much lower temperature than intrinsic charge carriers. An example of the resultant field and charge density distribution is given in Fig. 1 (right). Ions themselves are immobile on the relevant time scales. So charge carriers of one polarity are mobile in the system while the compensating charges, namely the ionized dopant ions, are not. In this case, the field distribution within the microstructure becomes very complex, because the degree of local ionization in turn depends on the local polarization state which means also on the mechanical state in the microstructure. Partial compensation occurs, but a remaining mismatch and thus residual fields are encountered. An electrically equivalent example is drift of vacancies during aging for which an equivalent local field distribution has been calculated [5].

$$F = F_0 + F_1 + F_2 \quad (1)$$

$$F_0(T) = F(P = 0, \sigma = 0, N_i = 0) \quad (2)$$

$$F_1 = \frac{1}{2}\alpha P^2 + \frac{1}{40}\beta P^4 + \frac{1}{6}\gamma P^6 - \frac{1}{2}s_{ik}\sigma_i\sigma_k - P^2\nu_k\sigma_k \quad (3)$$

$$F_2 = \sum_i N_i E_i(T, P, \sigma_k). \quad (4)$$

$s_{ik}$  is the elastic compliance,  $\sigma_i$  mechanical stress,  $\nu_k = \partial^2 F_1 / \partial P \partial \sigma_k$  the electrostriction coefficients,  $N_i$  the density of electronic states, and  $E_i$  the energy of the electronic states.

## Homogenization

Effects on several length scales determine the macroscopic material behavior. So far, mostly the description of homogenized properties of a domain system have been reported [11]. At this length scale, atomic and ionic effects are neglected as well as semiconductor properties.

## Summary

The theoretical description of ferroelectric microstructures is an intricate task. Mechanical stresses, electrical fields, and semiconductor properties interact on the scale of the microstructure. While some theoretical work on the scale of single domain walls or single crystals has been undertaken [8], an analysis for fields in microstructures or a homogenization including semiconductor effects has not been attempted.

## REFERENCES

- [1] K. Uchino, *Piezoelectric Actuators and Ultrasonic Motors*, Kluwer Academic Publishers, Boston, 1997.
- [2] J.F. Scott, C.A. Paz de Araujo, *Ferroelectric Memories*, *Science* **246**, 1400–1405 (1989).
- [3] J.F. Scott, M. Dawber, Oxygen-vacancy ordering as a fatigue mechanism in perovskite ferroelectrics, *Appl. Phys. Lett.* **76**, 3801–3803 (2000).
- [4] Y. Zhang, D.C. Lupascu, N. Balke, J. Rel, Near electrode fatigue in lead zirconate titanate ceramics, *J. Physique IV, France* **128**, 97–103 (2005).
- [5] D.C. Lupascu, Y. Genenko, N. Balke, Aging in Ferroelectrics, *J. Am. Ceram. Soc.* **89**, 224–229 (2006).
- [6] U. Robels, G. Arlt, Domain Wall Clamping in Ferroelectrics by Orientation of Defects, *J. Appl. Phys.* **73**, 3454–3460 (1993).
- [7] G. Arlt, Review: Twinning in ferroelectric and ferroelastic ceramics: Stress relief, *J. Mater. Sci.* **25**, 2655–2666 (1990).
- [8] V. Fridkin, *Ferroelectric Semiconductors*, Consultants Bureau, Plenum Publishing Corporation, New York, 1980.
- [9] M. Alexe, A. Gruverman, *Nanoscale Characterisation of Ferroelectric Materials*, Springer, Heidelberg, 2004.
- [10] J. Bauch, S. Wege, M. Böhlning, H.-J. Ullrich, Improved approaches to measurements of residual stresses in micro regions, *Cryst. Res. Technol.* **39**, 623–633 (2004).
- [11] J. Rödel, W.S. Kreher, Self-consistent modelling of non-linear effective properties of polycrystalline ferroelectric ceramics, *Comp. Mater. Sci.* **19**, 123–132 (2000).

## ON THE MODELLING OF DOMAIN SWITCHING IN FERROELASTIC MATERIALS

A. Menzel<sup>1</sup>, A. Arockiarajan<sup>2</sup>, and S.M. Sivakumar<sup>2</sup>

<sup>1</sup> University of Siegen, Mechanical Engineering  
Institute of Mechanics and Control Engineering – Continuum Mechanics  
Paul–Bonatz–Str. 9–11, D–57076 Siegen, Germany  
e-mail: menzel@imr.mb.uni-siegen.de

<sup>2</sup> Indian Institute of Technology Madras  
Department of Applied Mechanics  
Chennai 600 036, India  
email: rajan@rhrk.uni-kl.de, mssiva@iitm.ac.in

**Abstract.** *In this paper, switching effects of ferroelastic materials are studied by elaborating a micromechanically motivated model. The related energy reduction thereby serves for the definition of a switching criterion so that phase transformations are initiated as soon as the reduction in energy due to possible switching processes exceeds a critical value. Moreover, so-called intergranular effects are accounted for by making use of a phenomenological and probabilistic approach based on a Weibull distribution function.*

### Introduction

Piezoelectric materials, as for instance PZT ceramics, have attracted considerable interest and nowadays are widely commercialised. Naming but a few actuator applications, such materials are used for active vibration suppression, precision positioning, fuel injection valves in automotive engines, and so forth. Under high loading levels and below the Curie temperature, however, piezoceramics exhibit severely nonlinear response due to inherent ferroelectric and ferroelastic domain switching processes stemming from changes in polarisation and so-called spontaneous strains.

In this work we aim at elaborating a finite–element–based model capturing switching effects and accounting for related local changes in the elastic properties of the material. The initially un–poled state is thereby incorporated via randomly initialised material properties or rather unit–cell orientations. To set the stage and to be able to investigate first numerical studies, we do not distinguish between the modelling of domains and grains but rather attach an individual orientation to each finite element. Finally, straightforward volume–averaging techniques enable the comparison of experimental data, take from the literature, with our simulation results.

### Basic constitutive relations

For conceptual simplicity, we restrict ourselves to the consideration of the balance of linear momentum – embedded into a small strain kinematical framework – and to not further emphasise the incorporation of Gauß’ law. Accordingly, the displacement field  $\mathbf{u}$  constitutes the representative degree of freedom determining the total strain contribution which is additively

decomposed into an elastic and a spontaneous part

$$\nabla^{\text{sym}} \mathbf{u} = \boldsymbol{\varepsilon} = \boldsymbol{\varepsilon}^e + \boldsymbol{\varepsilon}^s \quad \text{with} \quad \boldsymbol{\varepsilon}^e = [\boldsymbol{\varepsilon}^e]^t, \quad \boldsymbol{\varepsilon}^s = [\boldsymbol{\varepsilon}^s]^t, \quad \text{and} \quad \text{tr}(\boldsymbol{\varepsilon}^s) = 0. \quad (1)$$

The underlying flux term, as defined by means of the stress tensor, is assumed to take a hyperelastic format

$$\boldsymbol{\sigma} = \partial_{\boldsymbol{\varepsilon}^e} W \quad \text{with} \quad W(\boldsymbol{\varepsilon}^e, \mathbf{m} \otimes \mathbf{m}) \quad \text{and} \quad \mathbf{m} \cdot \mathbf{m} = 1. \quad (2)$$

The unit-vector  $\mathbf{m}$  thereby allows the incorporation of tetragonal symmetries as observed for unit-cells being representative for commercialised piezoceramics. Referring to  $W$  as an isotropic scalar-valued tensor function and restricting  $W$  to be quadratic in  $\boldsymbol{\varepsilon}^e$  we obtain the particular representation

$$\begin{aligned} W = & \frac{1}{2} \lambda \text{tr}^2(\boldsymbol{\varepsilon}^e) + \mu_T \text{tr}([\boldsymbol{\varepsilon}^e]^2) \\ & + \alpha \text{tr}(\boldsymbol{\varepsilon}^e) \mathbf{m} \cdot \boldsymbol{\varepsilon}^e \cdot \mathbf{m} + 2 [\mu_L - \mu_T] \mathbf{m} \cdot [\boldsymbol{\varepsilon}^e]^2 \cdot \mathbf{m} + \frac{1}{2} \beta [\mathbf{m} \cdot \boldsymbol{\varepsilon}^e \cdot \mathbf{m}]^2 \end{aligned} \quad (3)$$

so that the set of material parameters reads  $\boldsymbol{\kappa} = [\lambda, \mu_T, \mu_L, \alpha, \beta]$ .

### Energy-based switching criterion

Nonlinear behaviour of ferroelectric ceramics mainly stems from domain switching effects in the microstructure as reflected by reorientation of the underlying unit-cells. Accordingly, the in this regard characteristic unit-vector  $\mathbf{m}$ , in other words the polarisation direction, may switch under  $90^\circ$  or  $180^\circ$  within a time interval  $\Delta t = t_{n+1} - t_n > 0$  of interest. In this work we adopt an energy-based switching criterion as advocated by McMeeking and Hwang.

Practically speaking, a switching process will be realised as soon as the related reduction in Gibbs free energy (per unit-volume),  $\Delta G$  say, exceeds a certain threshold, namely

$$\Delta G = \boldsymbol{\sigma} : \Delta \boldsymbol{\varepsilon}^s + \frac{1}{2} \boldsymbol{\sigma} : \Delta \mathbf{C} : \boldsymbol{\sigma} > \frac{3}{2} \sigma_0 \varepsilon_0 P \quad \text{wherein} \quad \mathbf{C} = [\partial_{\boldsymbol{\varepsilon}^e} \boldsymbol{\sigma}]^{-1}. \quad (4)$$

Please note that  $\Delta \boldsymbol{\varepsilon}^s$  and  $\Delta \mathbf{C}$  account for the change of the spontaneous strain  $\boldsymbol{\varepsilon}^s$  and the compliance  $\mathbf{C}$  due to the reorientation of  $\mathbf{m}$ . To give an example, consider an orthonormal frame  $\{\mathbf{m}_1, \mathbf{m}, \mathbf{m}_3\}$ . Based on the tetragonal symmetry of the underlying unit-cells, one obtains

$${}^{1,3} \Delta \boldsymbol{\varepsilon}^s = \frac{3}{2} \varepsilon^s [\mathbf{m}_{1,3} \otimes \mathbf{m}_{1,3} - \mathbf{m} \otimes \mathbf{m}]|_{t_n} \quad \text{and} \quad \mathbf{m} \leftrightarrow \mathbf{m}_{1,3}. \quad (5)$$

Apparently, six different polarisation directions come into the picture – monitoring three different spontaneous strain states; the one being realised corresponding the state reflecting the largest (local) energy reduction.

Finally, the probability of domain switching is additionally incorporated by means of the Weibull-type distribution function

$$P = \begin{cases} 1 - \exp\left(-\left[n \frac{2}{3} \frac{\Delta G}{\sigma_0 \varepsilon_0}\right]^k\right) & \text{if } \Delta G < \frac{3}{2} \sigma_0 \varepsilon_0 \\ 1 & \text{if } \Delta G \geq \frac{3}{2} \sigma_0 \varepsilon_0 \end{cases} \quad (6)$$

with  $n$  and  $k$  being non-negative. In summary, the list of parameters now reads  $\boldsymbol{\kappa} = [\lambda, \mu_T, \mu_L, \alpha, \beta, \varepsilon^s, \sigma_0, \varepsilon_0, n, k]$ .

## Numerical Examples

In order to run representative numerical examples, the proposed formulation is embedded into a three-dimensional finite element formulation, whereby each finite element is attached with an individual polarisation direction. The initial state should reflect an un-poled state which is accounted for by a random generation of the element-related orthonormal frames  $\{\mathbf{m}_1, \mathbf{m}, \mathbf{m}_3\}$ . For given boundary conditions the polarisation directions are then updated based on a staggered iteration technique. To be specific, a block-type specimen is considered, the discretisation of which consists of  $9 \times 9 \times 9$  linear elements. Cyclic loading in longitudinal direction,  $\mathbf{e}_3$  say, by means of Neumann boundary conditions is performed and straightforward volume-averaging techniques, namely

$$S = \frac{1}{V} \int_{\mathcal{B}} \mathbf{e}_3 \cdot \boldsymbol{\sigma} \cdot \mathbf{e}_3 \, dv \quad \text{and} \quad \mathbf{e} = \frac{1}{V} \int_{\mathcal{B}} \mathbf{e}_3 \cdot \boldsymbol{\varepsilon} \cdot \mathbf{e}_3 \, dv, \quad (7)$$

enable the comparison with experimental data taken from the literature. Moreover, the material parameters adopted are  $\lambda = 17.48$  [GPa],  $\mu_L = 2.46$  [GPa],  $\mu_T = 11.65$  [GPa],  $\alpha = 1.67$  [GPa],  $\beta = -20.74$  [GPa],  $\varepsilon^s = \varepsilon_0 = 0.0027$ ,  $\sigma_0 = 21.8$  [MPa],  $n = -4.6$  and  $k = 0$  or  $k = 3$  so that the response of PZT-51 is modelled.

The figure below shows stresses ( $S$ ) versus strain ( $e$ ) curves without ( $k = 0$ ) and with ( $k = 3$ ) considering the probability function  $P$ . It is clearly observed that switching processes are initiated when increasing the compressive stresses above  $-20$  [MPa], and the overall behaviour becomes highly nonlinear. Nevertheless, remanent strains saturate at a compressive stress level of  $-90$  [MPa] such that further increasing the applied stresses causes solely a linear response since switching processes are saturated. Upon reversing the loading direction, dissipative effects as reflected by the hysteresis loop are clearly displayed. As far as the comparison with experimental data is concerned, it is observed that the incorporation of the switching probability function  $P$  renders results that even better match with measurements reported in the literature.

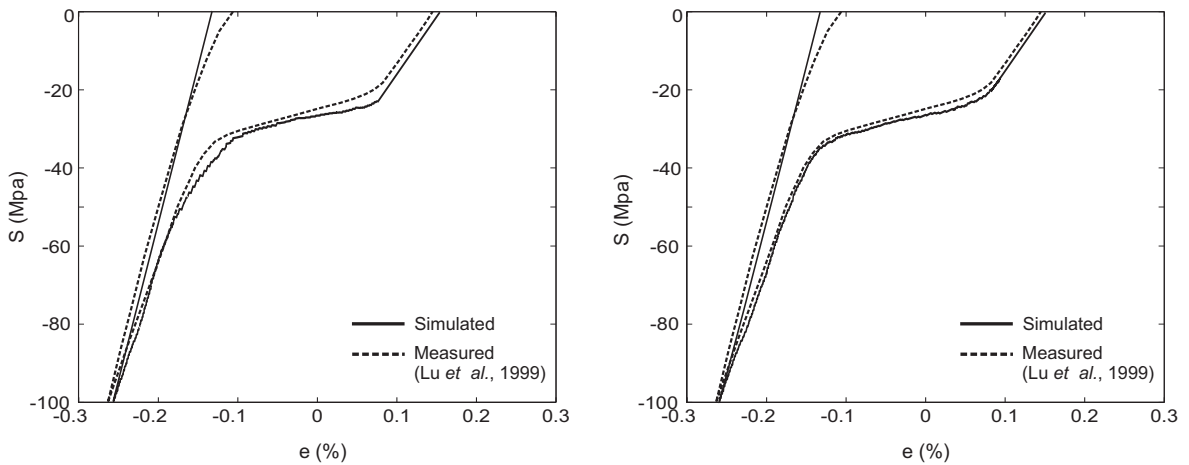


Figure 1: Stresses versus strain curve without ( $k = 0$ , left) and with ( $k = 3$ , right) probability function.

## REFERENCES

- [1] A. Arockiarajan, B. Delibas, A. Menzel, and W. Seemann, Studies on rate dependent switching effects of piezoelectric materials using a finite element model, *Comput. Mater. Sci.* **37**, 306–317 (2006a).
- [2] A. Arockiarajan, A. Menzel, B. Delibas, and W. Seemann, Computational modeling of rate-dependent domain switching in piezoelectric materials, *Euro. J. Mech. A/Solids* **25**, 950–964 (2006b).
- [3] J.P. Boehler, editor, *Applications of Tensor Functions in Solid Mechanics*, Number 292 in CISM Courses and Lectures, Springer (1987).
- [4] J.E. Huber and N.A. Fleck, Ferroelectric switching: a micromechanics model versus measured behaviour, *Euro. J. Mech. A/Solids* **23**, 203–217 (2004).
- [5] M. Kamlah and C. Tsakmakis, Phenomenological modeling of non-linear electromechanical coupling in ferroelectrics, *Int. J. Solids Struct.* **36**, 669–695 (1999).
- [6] W. Lu, D.-N. Fang, C. Li, and K. Hwang, Nonlinear electric–mechanical behaviour and micromechanics modeling of ferroelectric domain evolution, *Acta Mater.* **47**, 2913–2926 (1999).
- [7] D.C. Lupascu, *Fatigue in Ferroelectric Ceramics and Related Issues*, Springer, Heidelberg (2004).
- [8] R.M. McMeeking and S.C. Hwang, On the potential energy of a piezoelectric inclusion and the criterion for ferroelectric switching, *Ferroelectrics* **200**, 151–173 (1997).
- [9] R. Müller, D. Gross, D.C. Lupascu, Driving forces on domain walls in ferroelectric materials and interaction with defects, *Comput. Mater. Sci.* **35**, 42–52 (2006).
- [10] J. Schröder and H.C. Romanowski, A thermodynamically consistent mesoscopic model for transversely isotropic ferroelectric ceramics in a coordinate-invariant setting, *Arch. Appl. Mech.* **74**, 863–877 (2005).
- [11] M.G. Shaikh, S. Phanish, and S.M. Sivakumar, Domain switching criteria for ferroelectrics, *Comput. Mater. Sci.* **37**, 178–186 (2006).
- [12] R.C. Smith, *Smart material systems – Model development*, Society of Industrial and Applied Mathematics, Philadelphia (2005).
- [13] D. Zhou, M. Kamlah and D. Munz, Rate dependence of soft PZT ceramics under electric field loading, In *Proc. SPIE 4333*, 64–70 (2001).

## SIMULATION OF DOMAIN STRUCTURE EVOLUTION IN FERROELECTRIC MATERIALS

R. Müller<sup>1</sup>, D. Gross<sup>1</sup>, and D. Schrade<sup>1</sup>

<sup>1</sup>Solid Mechanics, Department of Civil Engineering, TU Darmstadt  
Hochschulstr. 1, 64289 Darmstadt e-mail: r.mueller@mechanik.tu-darmstadt.de

**Abstract.** *The electro-mechanical properties of ferroelectric materials are determined by the microstructure, i.e. the domain structure of these materials. Understanding the microscopic phenomena is essential in the analysis of the macroscopic behavior of ferroelectrics. Under different loading situations, as for example the application of an external electric field or an external mechanical stress, the domain structure is subject to changes. A numerical tool for simulating the polarization distribution in ferroelectric materials is presented. Using the concept of phase fields a continuum physics model is established. The main feature of the numerical implementation is an implicit time integration of the non-linear evolution equation within in the scope of a finite element implementation. Examples demonstrate the applicability of the model and the influence of defects on domain wall motion.*

### Introduction

Phase field models are well established in many fields of materials physics to model martensitic or diffusive phase transitions. In the field of ferroelectrics the application of these models is more involved on account of the electro-mechanical coupling. But recent works show the numerous possibilities of these models. Without claim of completeness we cite [3, 4, 5]. The implementations frequently use finite difference schemes (sometimes in combination with FFT-techniques) and explicit time integration. In order to derive a robust and a flexible implementation with respect to boundary conditions, we follow a finite element scheme in conjunction with an implicit time integration. A similar approach was used in [3, 5]. In combination with previous works [2, 6, 7] this allows us to introduce defects into the simulation. The incorporation of defect structures is important to realistically simulate macroscopic material behavior, including scenarios with fatigue and time dependent properties.

### Phase field model

The main idea in phase field models is the construction of an energy, from which the dynamics of the system can be derived. In the electro-mechanical setting the electric enthalpy is assumed to depend on the strain  $\epsilon$ , the electric field  $\mathbf{E}$ , and the order parameter (remanent polarisation)  $\mathbf{P}$  and to consist of three parts:

$$H(\epsilon, \mathbf{E}, \mathbf{P}) = H^{\text{ent}} + H^{\text{sep}} + H^{\text{int}}, \quad (1)$$

where the local enthalpy  $H^{\text{ent}}$ , the separation energy  $H^{\text{sep}}$  and the domain wall energy  $H^{\text{int}}$  are defined by

$$\begin{aligned} H^{\text{ent}} &= \frac{1}{2}(\boldsymbol{\varepsilon} - \boldsymbol{\varepsilon}^0) : [\mathbb{C}(\boldsymbol{\varepsilon} - \boldsymbol{\varepsilon}^0)] - (\boldsymbol{\varepsilon} - \boldsymbol{\varepsilon}^0) : (\mathbb{b}^T \mathbf{E}) - \frac{1}{2} \mathbf{E} \cdot (\mathbf{K} \mathbf{E}) - \mathbf{P} \cdot \mathbf{E}, \\ H^{\text{int}} &= \frac{1}{2} \beta \|\nabla \mathbf{P}\|^2, \\ H^{\text{sep}} &= \psi(\mathbf{P}). \end{aligned} \quad (2)$$

Note that in the local enthalpy  $H^{\text{ent}}$  the remanent strain  $\boldsymbol{\varepsilon}^0$  and the piezo-electric tensor  $\mathbb{b}$  are assumed to depend on the order parameter of the system  $\mathbf{P}$ . Details on the dependence can be found in [1, 8]. The interface energy assigns energy to areas with varying polarisation. The separation energy is constructed from invariance arguments. In 2D problems for systems with tetragonal elementary cells, where four orientations are possible, the simplest representation of  $\psi$  requires a fourth order polynomial in  $\mathbf{P}$ , i.e.

$$\psi = a_1 + a_2(P_1^2 + P_2^2) + a_3(P_1^4 + P_2^4) + a_4 P_1^2 P_2^2. \quad (3)$$

From the electric enthalpy constitutive equations are obtained by

$$\boldsymbol{\sigma} = \frac{\partial H}{\partial \boldsymbol{\varepsilon}} = \mathbb{C}(\boldsymbol{\varepsilon} - \boldsymbol{\varepsilon}^0) - \mathbb{b}^T \mathbf{E}, \quad \mathbf{D} = -\frac{\partial H}{\partial \mathbf{E}} = \mathbb{b}(\boldsymbol{\varepsilon} - \boldsymbol{\varepsilon}^0) + \mathbf{K} \mathbf{E} + \mathbf{P}, \quad (4)$$

where  $\boldsymbol{\sigma}$  is the stress and  $\mathbf{D}$  the electric displacement. The Ginzburg-Landau equation gives the evolution of the order parameter by

$$\dot{\mathbf{P}} = -\alpha \frac{\delta H}{\delta \mathbf{P}} = -\alpha \left( \frac{\partial H}{\partial \mathbf{P}} - \text{div} \frac{\partial H}{\partial \nabla \mathbf{P}} \right) = -\alpha \left( \frac{\partial H^{\text{ent}}}{\partial \mathbf{P}} + \frac{\partial \psi}{\partial \mathbf{P}} - \beta \Delta \mathbf{P} \right). \quad (5)$$

The field equations for  $\boldsymbol{\sigma}$  and  $\mathbf{D}$  are given by equilibrium and by electro-statics, i.e.

$$\text{div} \boldsymbol{\sigma} + \mathbf{f} = \mathbf{0}, \quad \text{div} \mathbf{D} = q, \quad (6)$$

with volume forces  $\mathbf{f}$  and volume charges  $q$ . In addition the kinematic and electric field equations are

$$\boldsymbol{\varepsilon} = \frac{1}{2}(\nabla \mathbf{u} + \nabla^T \mathbf{u}), \quad \mathbf{E} = -\nabla \varphi, \quad (7)$$

where  $\mathbf{u}$  is the mechanical displacement and  $\varphi$  the electric potential. The field equations have to be supplemented by proper boundary conditions.

## Implementation into the finite element method

The field equations (6) and the Ginzburg-Landau equation (5) are brought into a weak form. Discretizing in space with finite elements and using an implicit Euler method in time renders a system of non-linear equations to be solved. This can efficiently be done by using a Newton iteration to find the increments in the unknowns  $\mathbf{u}$ ,  $\varphi$  and  $\mathbf{P}$ . Note that due to (5), we have the freedom to chose Dirichelt- or Neumann-type boundary conditions on  $\mathbf{P}$ . In the following we tacitly assume that homogeneous Neumann-type boundary conditions are used for  $\mathbf{P}$ . The implementation requires the calculation of the consistent tangent matrix, to ensure quadratic convergence in the Newton iteration. Details on this implementation are omitted here, for the sake of brevity, but can be found in [8]. It is worth to note that as both (4) and (5) are derived from  $H$  it is possible to end up with a symmetric formulation, which is advantageous for the numerical implementation.

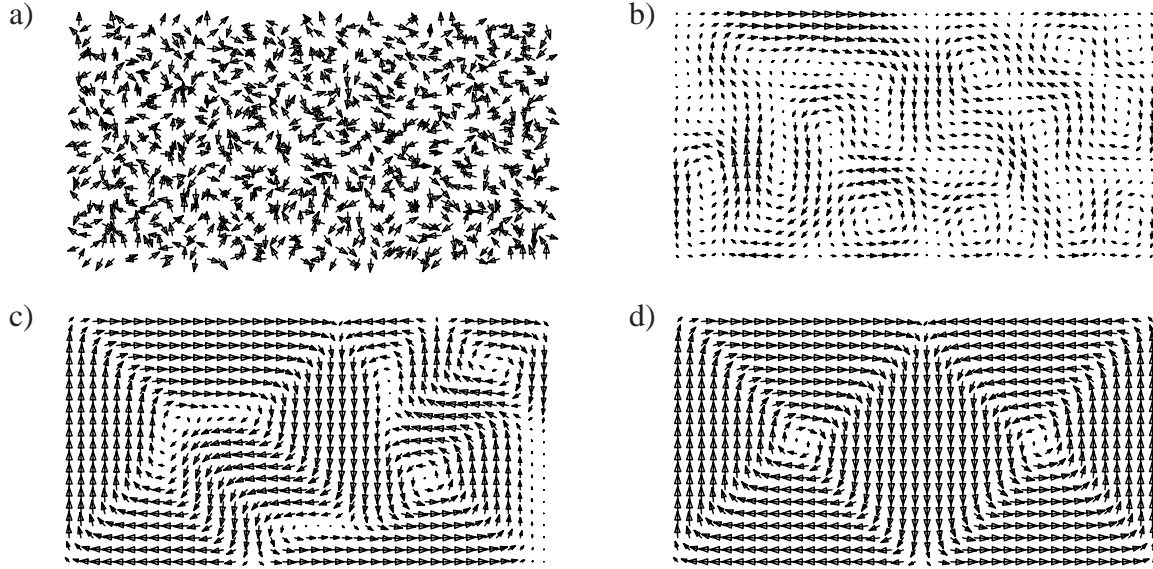


Figure 1: Domain structure evolution starting from random initial polarisation

## Results and Examples

The material parameters, which were used in the following calculations can be found in [8] and are not repeated here. The first example shows the microstructure evolution in a single crystal, starting from a random initial distribution of polarisation. Fig. 1a) depicts this random microstructure. Due to the electric fields caused by the mismatching polarisation a rapid self-organisation of the system takes place. In order to be in agreement with stress-free and charge-free boundary conditions two vortex like distributions of the polarisation develop by forming  $90^\circ$  domain walls.

The next example concerns a sample with a surface defect. The specimen in fig. 2 is loaded by an external field, which is applied by an electric potential difference between top and bottom. To introduce a defect in the top electrode, charge-free boundary conditions are applied in some region of the top surface. The remaining boundary of the specimen is free of surface tractions and of surface charges. Due to the loading a  $180^\circ$  domain wall is moved through the specimen, fig. 2a),b) depict the polarisation vectors, while fig. 2c),d) show the contour of the electric displacement in vertical direction  $D_2$ . Once the domain wall reaches the defect, the forces driving the domain wall reduce and the domain wall is pinned in the defect. This is in agreement with experimental observations and sharp interface calculations in [6]. It is also possible to consider other defects, as for example point defects, which are assumed to be relevant for the fatigue behavior. For details on this type of investigations and the modelling of these defects the reader is referred to [7]. Point defect analysis in conjunction with phase field models can also be found in [5].

## Conclusions

The phase field model implemented in a finite element method together with an implicit time integration renders a stable and robust numerical tool for studying domain structures in ferroelectric materials. The main observations from these simulations are:

- domain walls remain plane and form  $90^\circ$  and  $180^\circ$  domain walls
- boundary conditions can be crucial for the formation of a microstructure

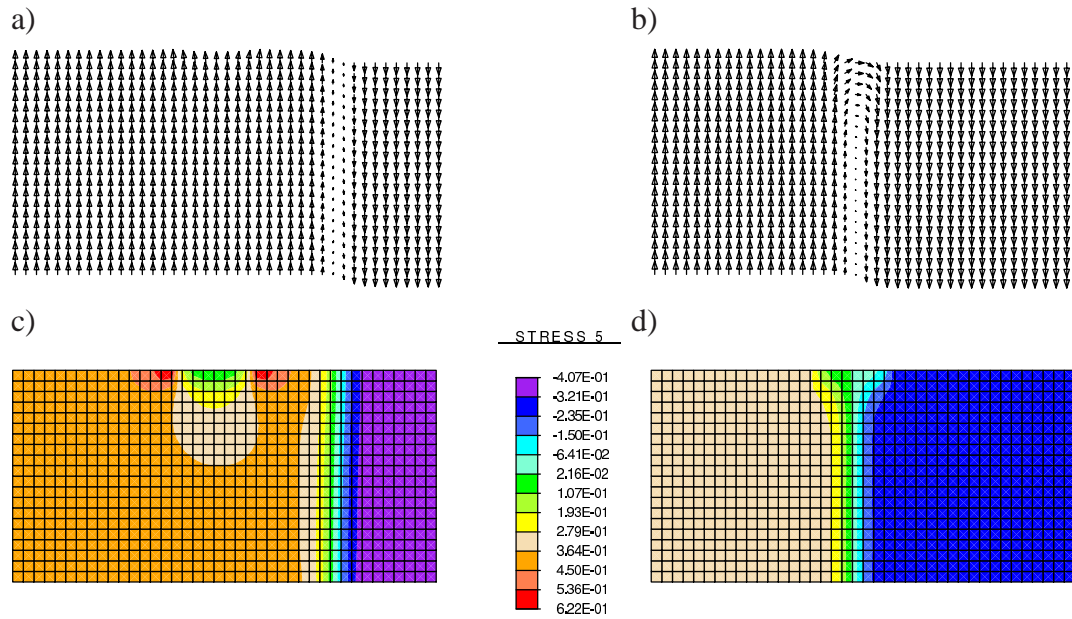


Figure 2: Domain structure evolution starting from random initial polarisation  
Time = 0.00E+00

- an initially random polarisation causes rapid self-organization of the system
- interaction with defects is possible and pinning scenarios can be studied
- pinning obstacles can be surface defects or point defects

## REFERENCES

- [1] M. Kamlah, Ferroelectric and ferroelastic piezoceramics – modeling of electromechanical hysteresis phenomena, *Continuum Mech. Thermodyn.* **13** (2001).
- [2] R. Mueller, D. Gross, D.C. Lupascu, Driving forces on domain walls in ferroelectric materials and interaction with defects, *Comp. Mat. Sci.* **35**, 42–52 (2006).
- [3] Y. Su, C.M Landis, A non-equilibrium thermodynamics framework for domain evolution; phase field models and finite element implementation, *Proceeding to the SPIE* (2006).
- [4] J. Wang, T.-Y. Zhang, Size effects in epitaxial ferroelectric islands and thin films. *Phys. Rev. B* **73** (2006).
- [5] Y. Su, C.M. Landis, Continuum thermodynamics of ferroelectric domain evolution: Theory, finite element implementation, and application to domain wall pinning, *J. Mech. Phys. Solids*, **55**, 280–305 (2007).
- [6] D. Schrade, R. Mueller, D. Gross, T. Utschig, V. Shur, D.C. Lupascu, Interaction of domain walls with defects in ferroelectric materials, *Mechanics of Materials*, **39**, 161–174 (2007).
- [7] O. Goy, R. Mueller, D. Gross, Interaction of point defects in piezoelectric materials ? numerical simulations in the context of electric fatigue, *J. Thero. Appl. Mech.*, accepted for publication (2007).
- [8] D. Schrade, R. Mueller, B.X. Xu, D. Gross, Phase field simulations in ferroelectric materials, *Comp. Meth. Appl. Mech. Eng.*, submitted for publication (2007)

## 3-D MICROSCOPIC MODEL FOR PZT-CERAMICS ACCOUNTING FOR DIFFERENT CRYSTALLOGRAPHIC PHASES

Peter Neumeister, Herbert Balke

Technische Universität Dresden, Institut für Festkörpermechanik  
01062 Dresden, Germany  
e-mail: Peter.Neumeister@tu-dresden.de

**Abstract.** *In the present paper a microscopic model is derived to compute the constitutive behaviour of polycrystalline PZT close to the morphotropic phase boundary (MPB) accounting for grain-to-grain interactions. A simple estimation shows that the assumption of a purely tetragonal structure is not sufficient to describe the large ferroelectric response of these materials, so that the model is enhanced allowing the coexistence of tetragonal and rhombohedral phase. The capabilities of the model are tested by simulating the macroscopic behaviour of the soft PZT PIC151.*

### Introduction

The complex non-linear behaviour of ferroelectric ceramics arises from their crystallographic structure which is based on asymmetric unit cells with characteristic dipole orientations associated with a spontaneous strain  $\varepsilon^S$  and polarisation  $P^S$ . An arrangement of unit cells with equal lattice orientations forms a single crystal in which regions of constant dipole orientation are called domains. The polycrystalline ceramic is a compound of randomly oriented single crystals (grains). The characteristic change (switch) of the dipole orientation is considered as domain wall motion that is induced by applied loads in terms of the mechanical stress  $\sigma_{ij}^a$  and electric field  $E_i^a$  as well as the residual stress  $\sigma_{ij}^i$  and intrinsic electric field  $E_i^i$  due to grain-to-grain interactions. The resulting domain configuration determines the macroscopic ferroelectric properties of the ceramic.

Microscopic models are used by many authors to follow the crystallographic structure, that is the actual dipole orientation distribution, and to describe the switching process taking advantage of the well defined and discrete change of the dipole orientation that simplifies the formulation of a process criterion considering both mechanical and electric loads. Kamlah et al. [1] use such a representative volume element based on a purely tetragonal crystallographic structure and a simplified representation of domains and grains. Grain-to-grain interactions due to incompatibilities caused by different remanent properties are accounted for by means of finite element computations.

### Switching process and material model

Similar to [1] the domain  $\alpha$  inside a grain is represented by means of the volume fraction  $v^\alpha$  with  $\sum_{\alpha=1}^{N^\alpha} v^\alpha = 1$  and  $v^\alpha \geq 0$ , where  $N^\alpha$  is the number of possible dipole orientations considered in the model. From the actual domain configuration the remanent properties of the grain  $\varepsilon_{ij}^r$  and  $P_i^r$  are derived by averaging the spontaneous properties  $\varepsilon_{ij}^{S,\alpha}$  and  $P_i^{S,\alpha}$  of each volume

fraction. Furthermore, the loads  $\sigma_{ij} = \sigma_{ij}^a + \sigma_{ij}^i$  and  $E_i = E_i^a + E_i^i$  acting on the grain are considered constant in the entire grain. It is assumed that  $\sigma_{ij}^i$  and  $E_i^i$  are dominated by the different remanent grain properties whereas the influence of piezoelectric coupling as well as anisotropic mechanical stiffness and dielectric constants can be neglected. Hence,  $\sigma_{ij}^i$  and  $E_i^i$  are computed with the help of a 3-d finite element model representing a sufficient number of grains based on the standard finite element formulation for isotropic electro-mechanical materials (mechanical displacement  $u_i$  and electric potential  $\varphi$ ) using linear elements. One grain is modelled in each integration point. The resulting macroscopic remanent properties of the representative volume element are derived by simply averaging the grain properties.

To describe the domain wall motion the driving force  $f^{\alpha \rightarrow \beta}$  is defined acting on the wall between the domains  $\alpha$  and  $\beta$ :

$$f^{\alpha \rightarrow \beta} = \sigma_{ij} \Delta \varepsilon_{ij}^{S, \alpha \rightarrow \beta} + E_i \Delta P_i^{S, \alpha \rightarrow \beta}. \quad (1)$$

Here,  $\Delta \varepsilon_{ij}^{S, \alpha \rightarrow \beta} = \varepsilon_{ij}^{S, \beta} - \varepsilon_{ij}^{S, \alpha}$  and  $\Delta P_i^{S, \alpha \rightarrow \beta} = P_i^{S, \beta} - P_i^{S, \alpha}$  are the changes of the spontaneous properties when switching from  $\alpha$  to  $\beta$ . For a discrete system with only one moving domain wall and constant loads this driving force is equal to the switching criterion used in [2]. If this force exceeds the critical value  $f_C^{\alpha \rightarrow \beta}$  (resistance force) the domain wall starts to move leading to the volume change rate  $\dot{v}^{\alpha \rightarrow \beta}$  described by an empirical kinetic law:

$$\dot{v}^{\alpha \rightarrow \beta} = \begin{cases} -k_{DW} \left( f^{\alpha \rightarrow \beta} - f_C^{\alpha \rightarrow \beta} \right) v^\alpha & \text{if } f^{\alpha \rightarrow \beta} \geq f_C^{\alpha \rightarrow \beta} \\ 0 & \text{else,} \end{cases} \quad (2)$$

where  $k_{DW}$  is used as a material parameter controlling the rate behaviour of the material. The resistance  $f_C^{\alpha \rightarrow \beta}$  is chosen allowing only the switching type with the smallest change of dipole orientation in every crystallographic phase. The total change of  $v^\alpha$  is obtained by adding the changes due to all switching mechanisms:

$$\dot{v}^\alpha = \sum_{\beta=1}^{N^\alpha} \left( \dot{v}^{\alpha \rightarrow \beta} - \dot{v}^{\beta \rightarrow \alpha} \right). \quad (3)$$

Equation (3) is numerically solved using Euler forward integration together with a sufficient small time step size allowing only small changes of applied loads and volume fractions between each iteration step.

Young's modulus  $Y$ , Poisson's ratio  $\nu$  and dielectric constant  $\varepsilon^d$  give the linear isotropic properties of the bulk material. The first two can be derived from uniaxial compression experiments in the saturated region (large compression stress) as proposed in [3].  $P^S$  and  $\varepsilon^S$  must be given for each present crystallographic phase, where the latter can be derived from measured lattice parameters [4, 5]. Table 1 gives the properties of PIC151 and the tetragonal and rhombohedral phase used in this investigation. Both phases are assumed to have the same bulk properties. A typical  $\varepsilon^d$  is chosen. Following [6],  $P^S$  can be considered equal for both phases. The introduced  $f_C^{\alpha \rightarrow \beta}$  and  $k_{DW}$  remain as fitting parameters to adjust the model to experimental data.

### Purely tetragonal phase model

Equivalent to various publications, a first attempt uses a purely tetragonal structure. However, after several computations it became obvious that this model is not able to describe PZT near the MPB. Although the tetragonal unit cell can switch in 6 different directions it is not able to contribute any remanent strain in its  $\langle 111 \rangle$ -directions. If the ceramic is polarised for example by an applied electric field  $E^a$  some grains show no or only a very small remanent strain

general properties			tetragonal phase		rhombohedral phase	
$Y$ [MPa]	$\nu$	$\varepsilon^d$ [nAs/MVmm]	$\varepsilon_t^S$ [%]	$P_t^S$ [nAs/mm <sup>2</sup> ]	$\varepsilon_r^S$ [%]	$P_r^S$ [nAs/mm <sup>2</sup> ]
144	0.31	8854	2.4	500	0.6	500

Table 1: Bulk properties of PIC151 and ferroelectric properties of crystallographic phases of PZT.

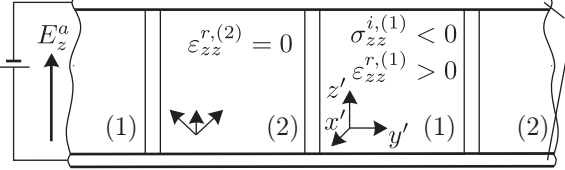
contribution in the direction of  $E^a$  and, hence, cause strong mechanical interactions working against the reorientation of neighbouring grains.

Figure 1 shows a simple periodic arrangement of two grains with different lattice orientations (1):  $\langle 100 \rangle$  and (2):  $\langle 111 \rangle$  in regard to  $E_z^a$ . Initially, both grains have no remanent properties ( $v^\alpha = 1/6$ ), so that the arrangement is stress-free. When applying  $E_z^a$  the reorientation of (1) leads to  $\varepsilon_{zz}^{r,(1)}$  parallel to  $E_z^a$  whereas  $\varepsilon_{zz}^{r,(2)}$  remains zero and causes the compressive stress  $\sigma_{zz}^{(1)}$  which decreases the driving force  $f^{\pm x', \pm y' \rightarrow \pm z'}$  in (1) until no further switching is possible. Using the material constants given in Table 1 the possible averaged remanent strain  $\varepsilon_{zz}^r$  of the arrangement can be derived depending on  $E_z^a$  (4). A realistic load of  $E_z^a = 2\text{kV/mm}$  together with the critical force  $f_C^{90^\circ} = 0.45\text{MPa}$  results in a very small  $\varepsilon_{zz}^r = 0.011\%$  compared to the large ferroelectric strain observed in PZT close to the MPB such as PIC151 [7] of more than 0.2%. In addition, the estimation shows that an increase of  $\varepsilon^S$  would lead to a further reduction of  $\varepsilon_{zz}^r$  (4). The interpretation of this simplified arrangement towards a fully 3-d model is difficult since the worst grain orientation (no strain contribution) is compared with the best (full contribution). However, computations with the complete model yield an averaged remanent strain of the same magnitude. Additionally, decreasing  $\varepsilon^S$  by the factor of two produces about twice of  $\varepsilon_{zz}^r$ .

### Tetragonal and rhombohedral phase model

To enhance the model the observation that a large ferroelectric response occurs only in the immediate vicinity of the MPB is taken into account. [4, 8] implicate this effect with the coexistence of a tetragonal and a rhombohedral phase which increases the number of possible dipole orientations in the  $\langle 111 \rangle$ -directions.

As a first approach toward a multiphase model, every grain has a certain amount (volume fraction) of each phase which is kept constant at any time (no phase transitions considered). Hence, the volume fraction of the tetragonal phase  $v^t$  is required as a new material parameter describing the phase mixture beside the ferroelectric properties of each phase. The best reproduction of PIC151 [7] is found using the parameters of Table 1 together with  $f_C^{90^\circ} = 0.45\text{MPa}$  and  $f_C^{71^\circ} = 0.25\text{MPa}$  for the tetragonal and the rhombohedral phase, respectively,  $k_{DW} = 50/\text{MPa}$  and  $v^t = 30\%$ . Figure 2 shows the results for the first load cycle under homogeneous electric and mechanical load. The dielectric displacement  $D_3$  is calculated from  $D_3 = \varepsilon^d E_3^a + P_3^r$  and



$$\begin{aligned}
 \sigma_{zz}^{i,(1)} &= -\frac{1}{2}Y\varepsilon_{zz}^{r,(1)} \\
 f^{\pm x', \pm y' \rightarrow \pm z'} &= E_z^a P^S + \frac{3}{2}\sigma_{zz}^{i,(1)}\varepsilon^S \geq f_C^{90^\circ} \\
 \varepsilon_{zz}^{r,(1)} &= \frac{4}{3}(E_z^a P^S - f_C^{90^\circ}) / (Y\varepsilon^S) \\
 \varepsilon_{zz}^r &= \frac{1}{2}\varepsilon_{zz}^{r,(1)} \sim 1/\varepsilon^S
 \end{aligned}
 \tag{4}$$

Figure 1: Periodic arrangement of two grain orientations demonstrating the locking effect caused by the crystallographic structure.

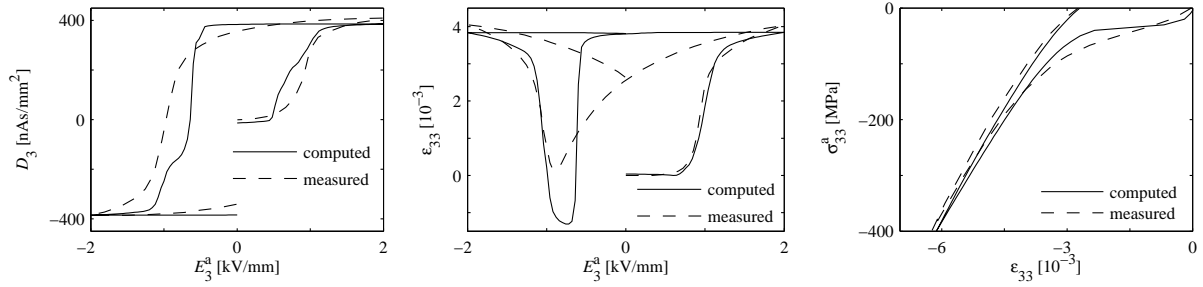


Figure 2: Computed and measured macroscopic response of PIC151 due to homogeneous loads beginning in virgin state: electrical poling with a) hysteresis and b) butterfly curve; c) mechanical compression.

the strain is given as  $\varepsilon_{33} = \sigma_{33}^a / Y + \varepsilon_{33}^r$  neglecting macroscopic piezoelectric coupling.

## Conclusion

The coexistence of tetragonal and rhombohedral phase allows the simulation of the large ferroelectric response typical for PZT close to the MPB. However, the curves do not show the characteristics of the soft PZT PIC151. This may be due to donor materials used to "soften" the material whose impact on the switching process is not considered in this model. Nevertheless, the model seems to be able to reproduce the behaviour of hard PZT.

**Acknowledgement** The authors thank the DFG for financial report under contract no. Ba 14411/12.

## REFERENCES

- [1] M. Kamlah, A.C. Liskowsky, R.M. McMeeking and H. Balke, Finite element simulation of a polycrystalline ferroelectric based on a multidomain single crystal switching model, *Int. J. Sol. Struc.* **42**, 2949–2964 (2005)
- [2] S.C. Hwang, C.S. Lynch and R.M. McMeeking, Ferroelectric/ferroelastic interactions and a polarization switching model, *Acta metall. mater.* **43**, 2073–2084 (1995)
- [3] T. Fett, D. Munz and G. Thun, Young's modulus of soft PZT from partial unloading tests, *Ferroelectrics* **274**, 67–81 (2002)
- [4] B. Noheda, D.E. Cox, G. Shirane, J.A. Gonzalo, L.E. Cross and S-E. Park, A monoclinic ferroelectric phase in  $\text{Pb}(\text{Zr}_{1-x}\text{Ti}_x)\text{O}_3$  solid solution, *Appl. Phys. L.* **74**, 2059–2061 (1999).
- [5] D.L. Corker, A.M. Glazert, R.W. Whatmore, A. Stallard and F. Fauth, A neutron diffraction investigation into the rhombohedral phases of the perovskite series  $\text{PbZr}_{1-x}\text{Ti}_x\text{O}_3$ , *J. Phys.: Condens. Matter* **10**, 6251–6269 (1998)
- [6] H. Fu and R.E. Cohen, Polarization rotation mechanism for ultrahigh electromechanical response in single-crystal piezoelectrics, *Nature* **403**, 281–283 (2000).
- [7] D. Zhou, Experimental investigations of non-linear constitutive behavior of PZT piezoceramics, Dissertation, Karlsruhe (Germany) (2003)
- [8] A.P. Wilkinson, J. Xu, S. Pattanaik and S.J.L. Billinge, Neutron scattering studies of compositional heterogeneity in sol-gel processed Lead Zirconate Titanates, *Chem. Mater.* **10**, 3611–3619 (1998)

# INVESTIGATION OF LARGE STRAINS AND FRACTURE IN SINGLE CRYSTAL SILICON STRUCTURES BY MEANS OF A MIXED ATOMISTIC - CONTINUUM MECHANICAL APPROACH

**O. Papes**

Eidgenössische Technische Hochschule Zürich  
Institut für mechanische Systeme / Zentrum für Mechanik / CLA G31  
Tannenstrasse 3, 8092 Zürich, Switzerland  
phone: +41 44 632 7754  
fax: +41 44 632 1145  
e-mail: [ondrej.papes@imes.mavt.ethz.ch](mailto:ondrej.papes@imes.mavt.ethz.ch)

**Abstract.** *It is demonstrated on the example of single crystal silicon how concepts from solid state physics and nonlinear continuum mechanics can be unified for the purpose of fracture prediction within an easy-to-use FE methodology. Well-established molecular potentials (Stillinger-Weber and Modified Embedded Atom Method) are reformulated in terms of a strain energy density function of diamond structure silicon. Consequently, stress and stiffness tensors are derived from this function, are implemented and linked to a commercial FE software using a constitutive interface. Not only is thus obtained tool capable of solving the nonlinear deformation problem for an arbitrary geometry, the local information about the acoustic and optical  $\Gamma$ -phonons becomes available as well, as the constitutive law is based on the underlying molecular structure, its kinematics and its energetics. By the identification of soft phonons, the onset of material decohesion is predicted and found in very good agreement with a reported experiment.*

## Introduction

The investigation of crystalline solids at high mechanical strains has become a revitalized area of research in the last years. Upon straining the atomic lattice, the electronic structure of a solid rearranges, which can result in dramatic changes of almost any physical property, be it mechanical, chemical or electronic. Thus, the possibility of bringing a crystal into a controlled state of large deformation makes a classical material truly multifunctional and opens the doors to new, fascinating technological fields. For instance, it was demonstrated in recent experiments [1] that mechanical straining of a silicon p-channel MOSFET leads to a considerable increase in the mobility and saturation current, hence to a speedup of the device. However, the desired modifications of the electronic structure at high tensile strains go hand in hand with an unwanted mechanical destabilization of the atomic lattice. Due to strong covalent and directional bonds in group IV semiconductors, such materials are brittle. In the presence of stress fields, a local loss of material cohesion can quickly initiate a progressive debonding: a crack runs through the material and destroys the device.

The prediction of brittle fracture is a demanding discipline of both physical and engineering interest. For a specific material, the stress field is determined by the device geometry and boundary conditions (prescribed displacements and / or tractions). However, as the crack typically originates in a localized stress amplifier at the atomic scale (e.g. defect or notch), this problem is intrinsically multiscale. Even in the case of micron-sized electromechanical devices, five to six orders of magnitude separate the device dimensions from the bond length. In order to link boundary conditions to fracture initiation, the deformation field must be calculated, critical overstressed sites have to be identified, the nearby stress field is

resolved down to the atomic scale and criterions indicating loss of cohesion must be formulated.

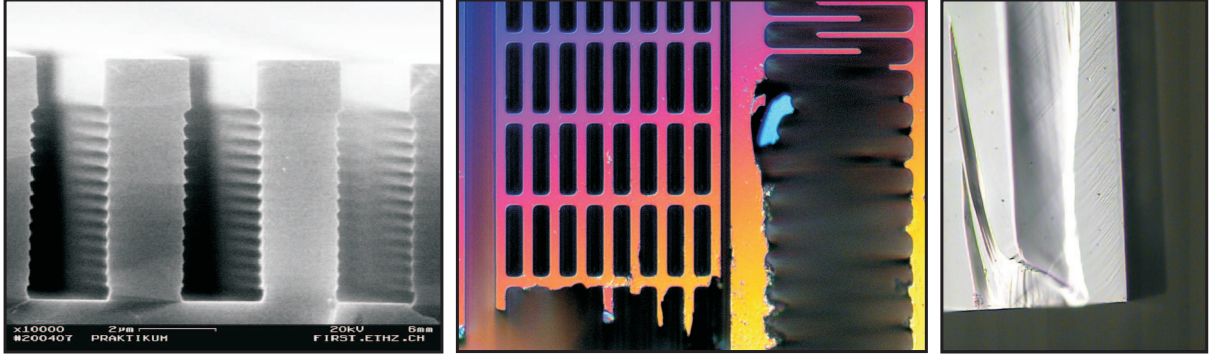


Figure 1: At critical loads single crystal silicon structures suffer from brittle fracture. The damage occurs suddenly, one or several cracks start at localized stress raisers, cleave the structure and leave atomically flat surfaces.

In the past, the question of deformation was mostly treated within the framework of linear elastic field theory, which provides a good approximation to the underlying nonlinear theory as long as strains are small enough and do not exceed  $\sim 1\%$ . However, it is currently recognized that debonding of group IV semiconductors occurs at considerable tensile strains, quantum mechanical *ab initio* calculations indicate critical strains of  $\sim 20\%$  [2]. The stress-strain curves at such high strains deviate from the linear Hooke's law  $\sigma = E\varepsilon$ . Not only fails linear elasticity in describing such nonlinearities, it does not explain fracture at all. As there is a proportionality between applied boundary conditions and the stress field, the theory provides solutions for arbitrary high loads. Due to this shortcoming of linear continuum mechanics and the fact that material decohesion concerns atoms and bonds, it is often anticipated that either fracture mechanics or molecular dynamics (equipped with empirical or *ab initio* potentials) are the right tools to treat such problems.

A promising alternative to this approach is presented in this paper. By incorporation of nonlinear continuum mechanics it was shown that physics of atoms and the continuum theory can be merged together to provide a tool for the investigation of crystal mechanics, be it on the macroscopic or almost atomic scale [3]. Here, a continuum mechanical formulation of well-established molecular potentials from solid state physics literature is set up. The constitutive response is coded within a material routine, for which there are interfaces in most commercial finite element method (FEM) toolboxes. Equipped with a FE software and such material models, the scientist or engineer is provided with a versatile and easy-to-use tool for the investigation of crystalline devices subject to large deformations. One is free to define geometry and boundary conditions for which deformation fields can be calculated. Aspects of the phonon spectrum (acoustic wave speeds, Raman frequencies) are spatially resolved by investigating the local stiffness tensors. By the identification of soft phonons, it is shown on the example of a silicon structure that the prediction of brittle fracture becomes possible.

In the authors' opinion, one of the central issues in recognition of multifunctional capabilities of materials lies in the acquisition of a unified and accurate physical picture, in which different phenomena are understood and explained as manifestations of the same underlying physics. The work presented here is hopefully a successful realization of this philosophy.

## Elastostatics of crystals

From a continuum mechanical point of view [4], a crystal is a continuous collection of material points. Static deformations of solids are described by the assignment of the current position  $\mathbf{x} \in \omega \subset \mathbb{R}^3$  to the initial position  $\mathbf{X} \in \Omega \subset \mathbb{R}^3$  for each material particle.  $\Omega$  and  $\omega$  are regions of space occupied by the solid in the undeformed (referential) and deformed (spatial) configurations, respectively. The goal is to find the mapping  $\mathbf{x} \rightarrow \mathbf{x}(\mathbf{X})$ , which for prescribed external loads and boundary conditions gives a deformation that satisfies force equilibrium. For conservative systems, a potential energy  $U$  can be

assigned to any deformation and force equilibrium is equivalent to the stationarity condition  $\delta U = 0$  for all admissible perturbations  $\delta \mathbf{x}$ . In the absence of body forces,  $U$  is a simple functional of  $\mathbf{x}(\mathbf{X})$ :

$$U[\mathbf{x}] = \int_{\Omega} W(\mathbf{F}) dV \quad , \quad \mathbf{F} = \partial \mathbf{x} / \partial \mathbf{X}$$

$\mathbf{F}$  is the deformation gradient which provides the local mapping of the three undeformed lattice vectors  $\mathbf{A}_{\alpha}$  with  $\alpha = 1, 2, 3$  onto the deformed lattice vectors  $\mathbf{a}_{\alpha}$  according to  $\mathbf{a}_{\alpha} = \mathbf{F} \cdot \mathbf{A}_{\alpha}$ . The scalar valued function  $W(\mathbf{F})$  is the strain energy density. For energetic solids the strain energy density is with good accuracy defined as the limit  $W(\mathbf{F}) = \lim_{V \rightarrow \infty} E_0 / V$ .  $V$  is a arbitrary volume of the initially unstrained crystal and  $E_0$  is the electronic ground state energy of the respective crystal portion that is homogeneously deformed in such a way that an arbitrary lattice point of initial position  $\mathbf{X}$  is found at  $\mathbf{x} = \mathbf{F} \cdot \mathbf{X}$ . Since  $W$  must be invariant under rigid body rotations when  $\mathbf{F} \in \text{SO}(3)$ ,  $W$  depends on  $\mathbf{F}$  through the right Cauchy-Green tensor  $\mathbf{C} = \mathbf{F}^T \cdot \mathbf{F}$ . If all functions are sufficiently smooth, the application of standard variational procedures and the Piola identity allow for the derivation of the partial differential equations of elastostatics in the spatial picture, which follow from  $\delta U = 0$  if  $\delta \mathbf{x}$  is arbitrary:

$$\text{div}(\boldsymbol{\sigma}) = \mathbf{0} \quad , \quad \boldsymbol{\sigma} = J^{-1} \mathbf{F} \cdot \mathbf{S} \cdot \mathbf{F}^T \quad , \quad \mathbf{S} = 2 \frac{\partial W}{\partial \mathbf{C}}$$

Here  $\boldsymbol{\sigma}$  is the Cauchy (true) stress tensor and the divergence is taken with respect to spatial coordinates  $\mathbf{x}$ .  $J = \det(\mathbf{F})$  is the volume ratio and  $\mathbf{S}$  is the second Piola-Kirchhoff stress tensor. The equations of elastostatics can be solved using the FEM [5]. However, before this can be realized: (i) a formulation of the strain energy density  $W$  as a function of deformation must be defined and (ii) stress and stiffness tensors required by the FE codes must be derived from  $W$ .

### Definition of the strain energy density

Since accurate ab initio ground state energy calculations are numerically quite expensive, good empirical approximations for  $E_0$  are necessary if computational efficiency is an issue. Unfortunately, it is a fact that empirical potentials are typically capable to represent material properties in accordance with experiment only near specific states to which the potentials were explicitly fitted [6]. It is the responsibility of the user to check whether a potential is suitable for the application at hand.

In the situation discussed here, two promising formulations of inter-atomic potentials for single crystal silicon were chosen: the Stillinger-Weber potential (StW) [7] and the Modified Embedded Atom Method (MEAM) [8]. The former was chosen for its formal simplicity, while the latter for its abilities to approximate correctly the elasticities and a realistic fracture behavior [9]. The potentials were transferred into constitutive laws by taking into account only first neighbour interactions, setting up the corresponding strain energy densities and its analytical derivatives. The following procedure for the above issue can be followed:

1. A crystallographic unit cell is chosen and characterized by the three lattice vectors  $\{\mathbf{A}_{\alpha}\}$ , and an  $N$ -atom basis is chosen and characterized by  $N$  vectors  $\{\mathbf{R}_k\}$ ,  $k = 1, \dots, N$ .
2. The lattice is subject to an affine deformation  $\mathbf{a}_{\alpha} = \mathbf{F} \cdot \mathbf{A}_{\alpha}$  while the basis is allowed to deform in a non affine way  $\mathbf{R}_k \rightarrow \mathbf{r}_k$  (sublattice shifts),
3. The energy contributions of all bonds, bond angles or embeddings corresponding to one unit cell are added and the strain energy density  $W$  is obtained by dividing the resulting total energy  $E_0$  by the undeformed unit cell volume  $V = \mathbf{A}_1 \cdot (\mathbf{A}_2 \times \mathbf{A}_3)$ .
4. By differentiating the strain energy density with respect to  $\mathbf{C}$  and all inner displacements, stress and stiffness tensors are obtained as nonlinear functions of these arguments.

This approach becomes especially simple for short range interactions and first neighbour formulations, in which no kinematical objects extending over several unit cells enter the energy expression. Within a minimal representation, the diamond structure of silicon is obtained by occupying a special nonorthogonal lattice with a two atom basis. One single inner displacement vector  $\mathbf{Z}$  is sufficient to describe the energetically relevant relative shift of the two initially face centered cubic sublattices. The deformed versions of the four normalized bond vectors  $\mathbf{N}_I$ ,  $I = 1, 2, 3, 4$  connecting first neighbours are thus defined as  $\mathbf{m}_I = \mathbf{F} \cdot (\mathbf{N}_I + \mathbf{Z})$ .

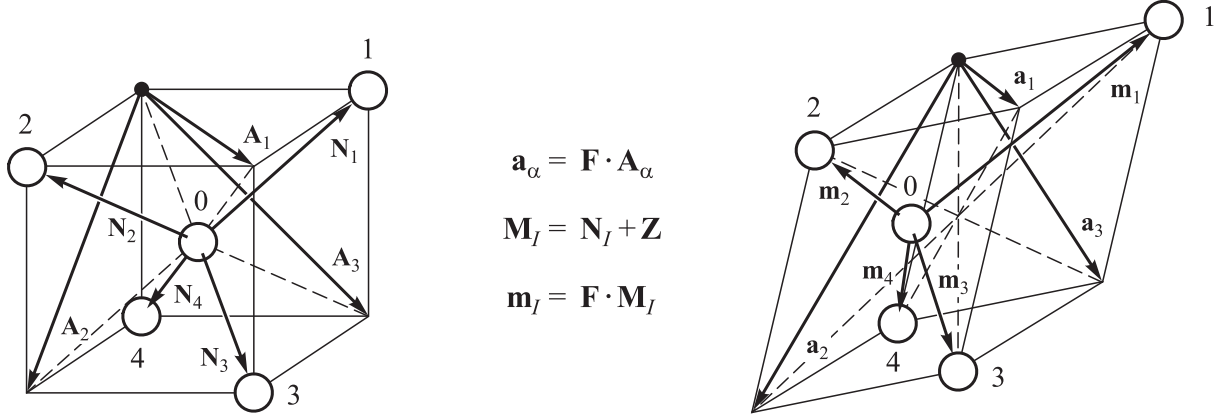


Figure 2: A cut-out of the undeformed (left) and homogeneously deformed (right) diamond lattice. Atom No. 0 leaves its central position, thus violating affinity and making it necessary to introduce a sublattice shift vector.

By the use of the spatial vectors  $\mathbf{m}_I$ , the dimensionless bond stretch  $\lambda_I = \sqrt{\mathbf{m}_I \cdot \mathbf{m}_I}$  of bond  $I$  and the cosine  $\phi_{IJ} = \cos(\varphi_{IJ}) = (\mathbf{m}_I/\lambda_I) \cdot (\mathbf{m}_J/\lambda_J)$  between the two bonds  $I$  and  $J \neq I$  can be expressed as functions of  $\mathbf{C}$  and  $\mathbf{Z}$ . The kinematical objects  $\lambda_I$  and  $\phi_{IJ}$  can directly enter energy contributions attributed to bond stretching and bond bending. For instance, the analytical expression for the first neighbour strain energy density function of the Stillinger-Weber potential reads as:

$$W(\mathbf{C}, \mathbf{Z}) = \sum_{I=1}^4 f(\lambda_I) + \sum_{I=1}^4 \sum_{\substack{J=1 \\ J \neq I}}^4 g(\lambda_I, \lambda_J, \phi_{IJ})$$

$$f(\lambda_I) = \begin{cases} \epsilon A \left( B \left( \frac{\lambda_I}{\sigma} \right)^{-p} - \left( \frac{\lambda_I}{\sigma} \right)^{-q} \right) e^{\frac{1}{\lambda_I/\sigma - a}} & \text{for } \lambda_I < a\sigma \\ 0 & \text{else} \end{cases}$$

$$g(\lambda_I, \lambda_J, \phi_{IJ}) = \begin{cases} \epsilon \lambda e^{\frac{\gamma}{\lambda_I/\sigma - a}} e^{\frac{\gamma}{\lambda_J/\sigma - a}} (\phi_{IJ} + \frac{1}{3})^2 & \text{for } \lambda_I < a\sigma \text{ and } \lambda_J < a\sigma \\ 0 & \text{else} \end{cases}$$

The parameters  $A$ ,  $B$ ,  $p$ ,  $q$ ,  $a$ ,  $\lambda$  and  $\gamma$  can be found in the original publication [7], the remaining two parameters  $\epsilon = 8.670'614'369$  GPa and  $\sigma = 0.890'898'718'149'725'5$  are the equivalents of the original parameters, here suitably reformulated for the homogenized formulation. With the same methods as shown above, the strain energy densities for other crystal structures and more involved potentials, such as the MEAM or bond order potentials, can be defined.

### Stress tensor, elasticity tensors and the Cauchy-Born rule

As shown above, the definition of the strain energy density  $W$  formally allows to close the equations of elastostatics. However, the resurrection of the constitutive behaviour induced by  $W$  within an FE environment requires some additional effort. To assure a deformation  $\mathbf{x}(\mathbf{X})$  satisfies stress equilibrium or to propagate a nonequilibrium towards stationarity with Newton-Raphson iterations, the second order Cauchy stress tensor  $\boldsymbol{\sigma}$  and the corresponding tangent operator, the fourth order elasticity tensor  $\mathbb{C}$ , are required, respectively. In order to make the later numerical implementation of the constitutive

law efficient, well ordered analytical expressions should be opted for. For instance, an appropriate formula for the first neighbour Stillinger-Weber Cauchy stress writes as follows and might be counterchecked by the interested reader:

$$\boldsymbol{\sigma} = \frac{1}{J} \sum_{I=1}^4 T_1(\lambda_I) (\mathbf{m}_I \otimes \mathbf{m}_I) + \frac{2}{J} \sum_{I=1}^4 \sum_{\substack{J=1 \\ J \neq I}}^4 T_2(\lambda_I, \lambda_J, \phi_{IJ}) (\mathbf{m}_I \otimes \mathbf{m}_I) + T_3(\lambda_I, \lambda_J, \phi_{IJ}) (\mathbf{m}_I \otimes \mathbf{m}_J)$$

$$T_1(\lambda_I) = \frac{1}{\lambda_I} \frac{\partial f}{\partial \lambda_I}, \quad T_2(\lambda_I, \lambda_J, \phi_{IJ}) = \frac{1}{\lambda_I} \left( \frac{\partial g}{\partial \lambda_I} - \frac{\phi_{IJ}}{\lambda_I} \frac{\partial g}{\partial \phi_{IJ}} \right), \quad T_3(\lambda_I, \lambda_J, \phi_{IJ}) = \frac{1}{\lambda_I \lambda_J} \frac{\partial g}{\partial \phi_{IJ}}$$

Furthermore, a rule must be given how to determine the lattice shift vector  $\mathbf{Z}$ . Here the Cauchy-Born rule provides a fruitful approach [10]. In energetic solids, free internal degrees of freedom arrange in such a way that the energy is instantaneously minimized. This will result in a zero-Kelvin model, which for silicon at room temperature seems to be not a too severe simplification. So the constitutive routine must in addition contain an inner algorithm which minimizes  $W$  with respect to  $\mathbf{Z}$ . A stationary point is identified by a vanishing inner force  $\mathbf{G} = \partial W / \partial \mathbf{Z} = \mathbf{0}$ . However, if inner equilibrium is lacking, an efficient algorithm must search for the energy minimum. Then the calculation of the inner elasticity tensor  $\mathbf{E} = \partial^2 W / \partial \mathbf{Z} \otimes \partial \mathbf{Z}$  is advantageous for driving  $\mathbf{Z}$  quickly towards a stationary point using Newton steps.

So a diversity of tensors must be derived by analytical differentiation of  $W$ . Without presenting further details, the following table summarizes the required objects. For all referential quantities (denoted by capital letters), there exist spatial counterparts (lower case letters) and are obtained by a corresponding push forward operation. For early work on this topic see [11].

name	definition (referential)	push forward (spatial)
stress tensor	$\mathbf{S} = 2 \partial W / \partial \mathbf{C}$	$\sigma_{ij} = J^{-1} F_{ik} F_{jl} S_{kl}$
inner force vector	$\mathbf{G} = \partial W / \partial \mathbf{Z}$	$g_i = J^{-1} F_{ik}^{-T} G_k$
partial elasticity tensor	$\mathbb{C}^0 = 4 \partial^2 W / \partial \mathbf{C} \otimes \partial \mathbf{C}$	$\mathbb{C}_{ijkl}^0 = J^{-1} F_{iq} F_{jr} F_{ks} F_{lt} \mathbb{C}_{qrst}^0$
force-strain coupling	$\mathbf{D} = 2 \partial^2 W / \partial \mathbf{Z} \otimes \partial \mathbf{C}$	$d_{imn} = J^{-1} F_{ik}^{-T} F_{mq} F_{nr} D_{kqr}$
inner elasticity tensor	$\mathbf{E} = \partial^2 W / \partial \mathbf{Z} \otimes \partial \mathbf{Z}$	$e_{mn} = J^{-1} F_{mq}^{-T} F_{nr}^{-T} E_{qr}$
total elasticity tensor	$\mathbb{C}_{ijkl} = \mathbb{C}_{ijkl}^0 - E_{mn}^{-1} D_{mij} D_{nkl}$	$\mathbb{C}_{ijkl} = J^{-1} F_{iq} F_{jr} F_{ks} F_{lt} \mathbb{C}_{qrst}$

### Conditions for material stability

Constitutive laws derived from molecular potentials in the above sense possess only conditional material stability, i.e. material stability is lost at critical deformations, see [12] for further details. For instance, a truly elastic body is able to carry acoustic waves (here: acoustic phonons near  $\Gamma$ ) with real valued wave speeds. There is a mathematical criterion to check whether this ability is ensured: the Legendre-Hadamard or rank-1-convexity condition [13], denoted here as R1C. The construction of an indicator of the same name should have the property of being real valued, nonnegative if R1C is ensured and negative if it is violated:

$$\text{R1C} = \chi \left( \rho^{-1} \min_{\mathbf{u}, \mathbf{v}} [\boldsymbol{\sigma} : (\mathbf{v} \otimes \mathbf{v}) + (\mathbf{u} \otimes \mathbf{v}) : \mathbb{c} : (\mathbf{u} \otimes \mathbf{v})] \right) , \quad \chi(x) = \text{sgn}(x) \sqrt{\text{abs}(x)}$$

Here  $\rho = \rho_0/J$  is the true, spatial density of the homogeneously deformed silicon crystal ( $\rho_0 = 2'329 \text{ kg/m}^3$  is the referential density),  $\mathbf{u}$  and  $\mathbf{v}$  are arbitrary unit vectors and the minimization is carried out over all possible pairs,  $\text{sgn}(x)$  is the signum function and  $\text{abs}(x)$  gives the absolute value of the argument. If R1C is nonnegative, it will return the smallest true wave speed of an acoustic wave propagating in the homogeneously strained crystal. A negative value of R1C indicates the existence of standing modes with amplitudes exponentially growing in time, so instability of the state of homogeneous deformation with respect to acoustic perturbations.

A second stability indicator addresses the question of whether the internal stiffness tensor  $\mathbf{e}$  is positive semidefinite, which is a necessary condition for the existence of a local minimum of  $W$  with respect to perturbations of the lattice shift vector. Since the eigenvalues of  $\mathbf{e}$  are related to the Raman frequencies (the frequencies of optical phonons at  $\Gamma$ ), a good definition is:

$$\text{RAF} = \frac{1}{\pi R_0} \chi \left( \rho^{-1} \min_{\mathbf{u}} [\mathbf{e} : (\mathbf{u} \otimes \mathbf{u})] \right)$$

Here  $R_0 = 235.2 \text{ pm}$  is the initial, undeformed bond length. A positive RAF gives the smallest Raman frequency and the minimization is carried out over all unit vectors  $\mathbf{u}$ . If RAF becomes negative, this indicates instability of the crystal energy with respect to the arrangement of atoms inside the chosen unit cell. Since the arguments of the R1C and RAF indicators are nonlinear functions of  $\mathbf{F}$ , the indicators will take different values for different states of strain and can finally go through zero at critical configurations. From a physical point of view, the indicators are well defined since they access the acoustic and optical  $\Gamma$ -phonons of the homogeneously deformed solid.

### Referential properties and tensile curves

Constitutive routines in the above sense were implemented in Fortran using the silicon Stillinger-Weber potential and the Modified Embedded Atom Method in the first neighbour formulation. For a given deformation gradient  $\mathbf{F}$  the routines find the relaxed lattice shift vector  $\mathbf{Z}$  and calculate the stress and stiffness tensors  $\boldsymbol{\sigma}$  and  $\mathbb{c}$ , respectively. In addition, the Raman frequencies and the stability indicators R1C and RAF are calculated. The routines process several hundred constitutive evaluations per second on a P4/3GHz/2GB personal computer running under Windows XP. Hence it is possible to link the routines to FE programs and finish complex elastostatic calculations within reasonable times.

The models were thoroughly tested and verified. As one of several checks the referential elasticities were determined by investigating the elasticity tensors and the Raman frequencies in the undeformed state  $\mathbf{F} = \mathbf{I}$ . The elasticities of the models were found in perfect agreement

with computational results from literature [14], [8]. The StW potential is well known of being incapable to give the experimentally observed values since its elastic constants are restricted by the Harrison-Huntington relation [15]. The MEAM is much better in this respect, but in return the Raman frequencies are in serious disagreement with experiment.

	$C_{11}$	$C_{12}$	$C_{44}$	$C_{44}^0$	$E_{100}$	$E_{110}$	$E_{111}$	$f_R$
Exp.	165.773	63.924	79.619		130.193	169.159	187.904	15.530
StW	151.350	76.385	56.422	109.703	100.110	129.029	142.777	17.841
	-8.7%	+19.5%	-29.1%		-23.1%	-23.7%	-24.0%	+14.9%
MEAM	164.152	64.692	76.638	250.336	127.577	164.653	182.314	26.686
	-1.0%	+1.2%	-3.7%		-2.0%	-2.7%	-3.0%	+71.8%

Table 1: The elastic constants (GPa), elastic moduli (GPa) and the triply degenerate Raman frequency (THz) for single crystal silicon at the stress free reference configuration. The experimental data is from [16] and [17].

The uniaxial tensile curves in the [110] and [111] directions show the behavior as expected for a material with internal degrees of freedom and dissociating bonds. With increasing strain the stress first goes up until a maximum, the ultimate strength, is reached. After this point cohesion is weakening and the stress gradually drops back to zero again. The MEAM [111] stress curve is close to the corresponding ab initio prediction [2] while StW considerably overshoots it. The R1C indicator and the Raman frequencies are dropping for increasing strain and finally go through zero at strains which perfectly correlate with the occurrence of ultimate strength, thus justifying the roles of R1C and RAF as stability indicators.

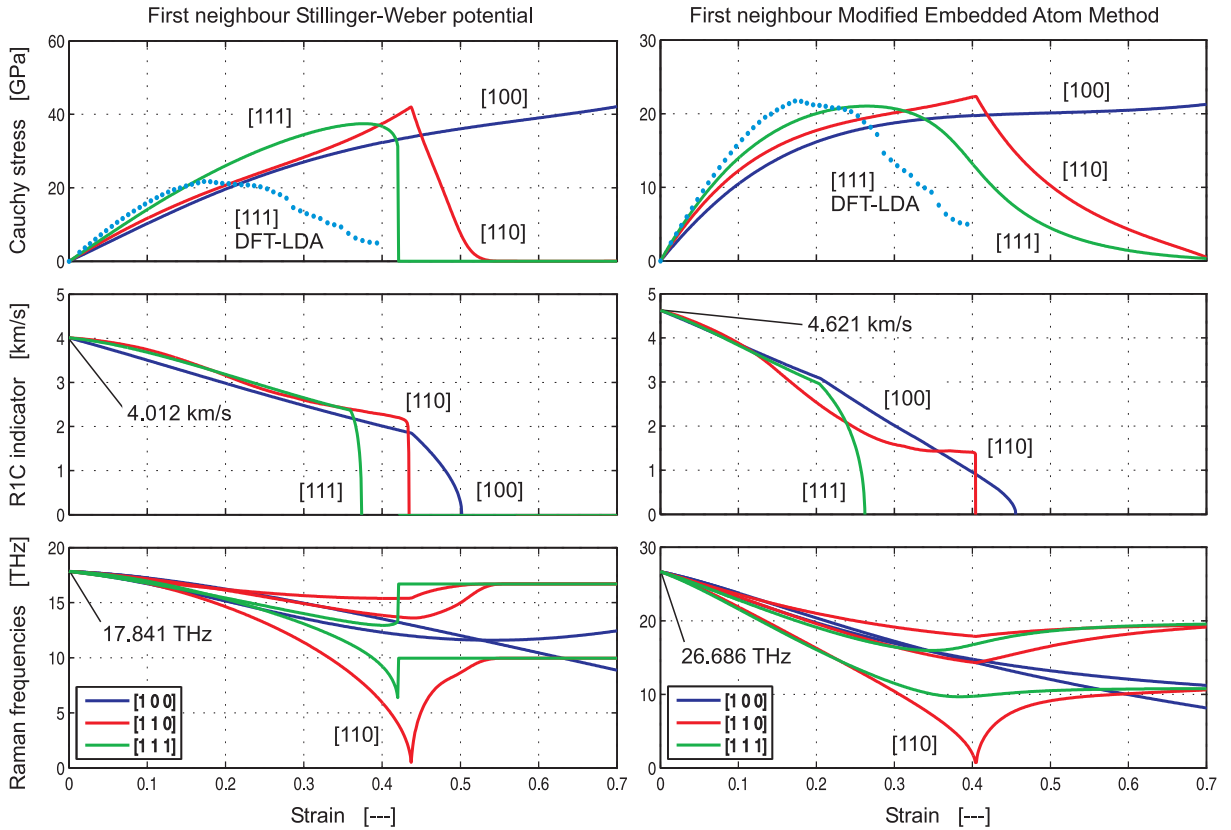


Figure 3: Stress-strain curves, the R1C indicator and the Raman frequencies for uniaxially stressed (laterally free) silicon in different crystallographic directions. The ab initio DFT-LDA data for [111] is from reference [2].

## FEM aided prediction of brittle fracture

The full 3D capabilities of the constitutive routines were used to conduct finite element calculations on realistic mechanical structures loaded until fracture. For such calculations the routines are linked to an FE software by a constitutive interface. For instance, in the commercial program ABAQUS this is the UMAT subroutine [18]. The FE software calls the constitutive routine in every increment and in all integration points and uses the returned stress and elasticity tensors for the assembly of global force vectors and stiffness matrices. With the help of these objects the FE code solves - increment by increment - the nonlinear elastostatic problem for the unknown displacement and stress fields.

The case used for the here reported numerical study was experimentally investigated in [19], see figure 4 for details. It is a micron-sized single crystal silicon tensile specimen, of which several realizations were made and stretched in the [010] direction until fracture. The specimens were manufactured by anisotropic etching in KOH. This process leads to perfectly flat surfaces which are oriented along crystallographic plains. As a consequence however, very sharp notches result from the intersection of two such plains, in fact the notches were classified as atomically sharp using electron microscopy. The specimens were stretched and the applied force and the strain in the bridge (cross section dimensions  $90 \times 50 \mu\text{m}^2$ ) were measured. By dividing this force through the cross section area, the nominal stress  $\bar{\sigma}$  in the bridge is defined. Experimentally, fracture occurred at an average nominal stress  $\bar{\sigma}_{\text{crit}} = 0.586 \text{ GPa}$  with a small standard deviation of only 3% and the cracks initiated from one of the sharp notches, where a strong stress concentration occurs.

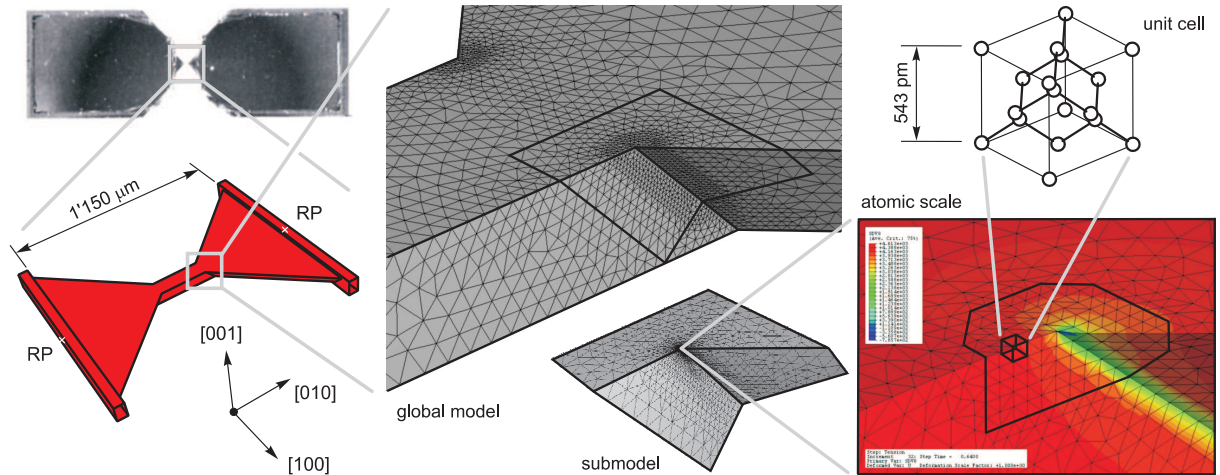


Figure 4: Details of the investigated specimen and the FE mesh. The mesh near the notch is refined down to the atomic scale and adapted to the crystal lattice. The corner element is most critical with respect to material stability.

Within the numerical simulation, this well known geometry is discretized with 49'733 quadratic tetraeder elements. In order to resolve accurately the stress field in the vicinity of the critical notch base, the mesh there is refined down to the atomic scale using a submodel with another 101'684 elements. At the atomic scale, the mesh is adapted to the structure of the crystal lattice, i.e. elements are forced to occupy regular cubes of side length 357 pm, which is the lattice constant of diamond structure silicon. With quadratic elements, the density of nodes then corresponds to the number of silicon atoms per volume. A simulation is performed by assigning the StW or MEAM material to the discretized FE specimen. The tensile force is applied to the model and slowly ramped up.

The stability indicators R1C and RAF are calculated in all elements, and if plotted as fields on the geometry, are soon found most critical in the corner element adjacent to the notch base. With both material models, R1C indicates instability first. The positive outcome of the approach presented here consists in a strong correlation between the simulated load at which local loss of material stability occurs and the experimentally observed fracture load. In figure 5 the minimum of the R1C field for the StW and MEAM simulations is plotted against the nominal stress  $\bar{\sigma}$ , now defined as the simulated tensile force divided by the referential cross section area  $90 \times 50 \mu\text{m}^2$ . At elevated loads the R1C indicator breaks down and passes through zero, so the affected elements are transferred into a state of material instability. This happens for the StW material at a simulated load of  $\bar{\sigma} = 0.788 \text{ GPa}$ , thus overshooting the experimentally found fracture stress  $\bar{\sigma}_{\text{crit}}$  by 34.5 %. For the MEAM however, R1C indicates instability at  $\bar{\sigma} = 0.582 \text{ GPa}$ , which is only 0.7% below  $\bar{\sigma}_{\text{crit}}$  and thus in good agreement with experiment.

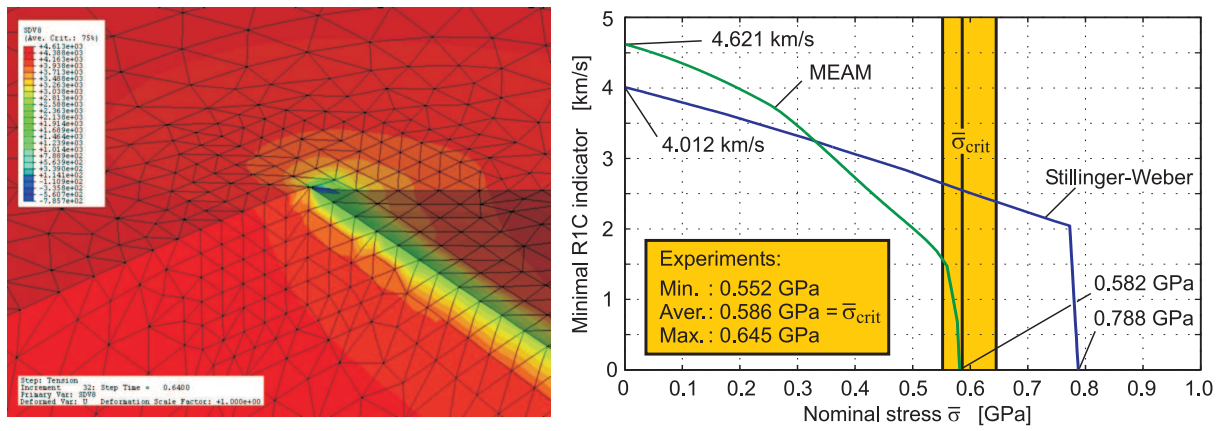


Figure 5: Left: the R1C field for MEAM silicon at the first occurrence of material instability. Right: the minimum of the R1C field for the StW and MEAM simulations, plotted against increasing nominal stress  $\bar{\sigma}$ . The experimentally investigated specimens failed at loads  $\bar{\sigma}$  within the shaded region, the average was  $\bar{\sigma}_{\text{crit}}$ .

So a material law derived from an appropriate molecular potential, properly transferred into a continuum mechanical framework and paired with the concepts of material stability in the sense of R1C and RAF gives a good tool for the prediction of fracture strength of brittle silicon for the considered test case. From the point of view of application the method presented here is not different from a standard nonlinear FE calculation and in this sense requires no excessive training of the operator since the full information concerning the mechanics of the material and the destabilization mechanism are contained in the constitutive subroutine. The only duty of the operator is the detailed modeling of crucial geometrical features leading to stress concentration.

## Conclusions

A ready-for-use FEM based procedure for the prediction of brittle fracture of single crystal silicon structures was presented that yields results in good agreement with experiment. This is especially interesting in consideration of the fact that not a single manipulation was undertaken to make theory and experiment fall together. The original formulations of the StW and MEAM potentials remained unchanged including the parameters, of which not a single one was varied. The freedom in choosing the kinematical objects describing the crystal was used such that the numerically most efficient model resulted, i.e. the primitive unit cell and thus the minimal atom basis were chosen. The FE discretization at the critical site was refined in such a way that the mesh geometry and density of nodes match the crystal structure, so even in this elsewhere often

crucial point there is no ambiguity. The stability indicators address properties of phonons, thus draw upon a sound physical theory and can be derived from a purely mathematical investigation of the linearized system of equations of motion.

But besides these positive findings there are still open questions. First, the method has to be applied to more examples and compared with corresponding experimental data before its reliability can be rated. Second, there are intrinsic shortcomings to every local continuum theory resulting from homogenization. For example nonlocality due to long range atomic interactions is lacking, the influence of a most probably oxidised surface, of material imperfections or dislocations are not contained and the effect of temperature is missing. If there is a connection between such issues and the structural strength, there is possibly no other way than treating the problem within a detailed atomistic picture. Third, the potential formulation plays a crucial role. Today the conceptual validity of the potential energy surface - and so the strain energy density - is generally accepted but it is difficult to find efficient algorithms for computing it precisely. Any approximation simplifying the originally quantum mechanical problem will most probably lead to errors, so empirical potentials like the ones presented here will generate inevitable deviations from the observed physics.

Nevertheless, the positive outcome of this work and the unambiguous way on which the results were obtained encourage further investigations in this direction. Future projects will deal primarily with the application of the method to realistic geometries, in particular to topologies as obtained from dry etching. A further goal will be the generalization of the method to different materials and crystal structures.

## REFERENCES

- [1] Belford RE et al.: "Strain enhanced p-type metal oxide semiconductor field effect transistors", J. Appl. Phys. 100 (6): 2006
- [2] Roundy D, Cohen ML: "Ideal strength of diamond, Si, and Ge", Phys. Rev. B 64 (21): 2001
- [3] Fago M, Hayes RL, Carter EA, Ortiz M: "Density-functional-theory-based local quasi-continuum method: Prediction of dislocation nucleation", Phys. Rev. B 70 (10): 2004
- [4] Holzapfel GA: "Nonlinear solid mechanics: A continuum approach for engineering", John Wiley & Sons, 2000
- [5] Belytschko T, Liu WK, Moran B: "Nonlinear finite elements for continua and structures", John Wiley & Sons, 2000
- [6] Godet J, Pizzagalli L, Brochard S, Beauchamp P: "Comparison between classical potentials and ab initio methods for silicon under large shear", J. Phys. Cond. Mat. 15 (41): 2003
- [7] Stillinger FH, Weber TA: "Computer simulation of local order in condensed phases of silicon", Phys. Rev. B 31 (8): 1985
- [8] Baskes MI: "Modified embedded-atom potentials for cubic materials and impurities", Phys. Rev. B 46 (5): 1992

- [9] Bailey NP, Sethna JP: "Macroscopic measure of the cohesive length scale: Fracture of notched single-crystal silicon", *Phys. Rev. B* 68 (20): 2003
- [10] Pitteri M, Zanzotto G: "Continuum models for phase transitions and twinning in crystals", Chapman & Hall/CRC, 2003
- [11] Cousins CSG: "Internal strain in diamond structure elements: A survey of theoretical approaches", *J. Phys. C* 15 (9): 1982
- [12] Elliott RS, Triantafyllidis N, Shaw JA: "Stability of crystalline solids - I: Continuum and atomic lattice considerations", *J. Mech. Phys. Sol.* 54 (1): 2006
- [13] Ciarlet PG: "Mathematical elasticity", North-Holland, 1988
- [14] Cowley ER: "Lattice dynamics of silicon with empirical many-body potentials" *Phys. Rev. Let.* 60 (23): 1988
- [15] Martin JW: "Many-body forces in solids: Elastic constants of diamond-type crystals", *J. Phys. C* 8 (18): 1975
- [16] McSkimin HJ, Andreatch P: "Measurement of third-order moduli of silicon and germanium", *J. Appl. Phys.* 35 (11): 1964
- [17] Yin MT, Cohen ML: "Theory of lattice-dynamical properties of solids: Application to Si and Ge", *Phys. Rev. B* 26 (6): 1982
- [18] ABAQUS online documentation, version 6.4, copyright ABAQUS Inc. 2003
- [19] Mazza E, Dual J: "Mechanical behavior of a  $\mu$ m-sized single crystal silicon structure with sharp notches", *J. Mech. Phys. Sol.* 47 (8): 1999

## LOCOMOTION SYSTEMS BASED ON MAGNETISABLE, HIGHLY ELASTIC MATERIALS

**J. Popp<sup>1</sup>, V. Böhm<sup>1</sup>, V. Naletova<sup>2</sup>, I. Zeidis<sup>1</sup>, and K. Zimmermann<sup>1</sup>**

<sup>1</sup>Technische Universität Ilmenau, Faculty of Mechanical Engineering, PF 100565, 98693 Ilmenau, Germany  
e-mail: jana.popp@tu-ilmenau.de, valter.boehm@tu-ilmenau.de

<sup>2</sup> M.V.Lomonosov Moscow State University, Department of Mechanics and Mathematics, Leninskye gory,  
119992, Moscow, Russia  
e-mail: naletova@imec.msu.ru

**Abstract.** *Colloidal, superparamagnetic fluids as well as ferroelastomers and gels are substances which respond to an external magnetic field by a strong change of position and shape. By these characteristics the magnetisable, highly elastic materials are well adapted as a basis of locomotion principles. At present applications using ferrofluids are i.g. seals, dampers, pumps and a microdosage pipette [2, 3, 4, 5]. Ferrofluids has been discovered as an actuation medium in general, in partucular as a basis for locomotion systems since a few years. In this paper three applications will be discussed with respect to passive locomotion systems based on a free ferrofluid surface and active locomotion sytems based on ferroelastomers.*

### Introduction

Colloidal paramagnetic fluids (in short: ferrofluids) as well as ferroelastomers and gels are substances which respond to an external magnetic field by a strong change of position and shape. That is to say, nanometer sized volumes align nearly unaffected by each other following the magnetic field and thus deform and move the whole fluid volume [1].

By these characteristics the magnetisable, highly elastic materials are well adapted as a basis of locomotion principles. At present applications using ferrofluids are e.g. seals, dampers, pumps and a microdosage pipette [2, 3, 4, 5]. Ferrofluids has been discovered as an actuation medium in general, in partucular as a basis for locomotion systems since a few years [6].

This kind of locomotion, using magnetisable, highly elastic materials, utilises the resulting force of surface effects and magnetic interaction for the locomotion purposes. Locomotion in general is classified by passive and active locomotion, see Fig. 1. According to the definition in [7] the magnetoelastomaterial is stationary in a passive system. Whereas in an active system the magnetisabel, highly elastic material is an element of the locomotive structure [7].

In our paper three applications will be discussed with respect to passive locomotion systems based on a free ferrofluid surface and active locomotion sytems based on ferroelastomers.

### Applications of locomotion systems based on magnetoelastomaterials

Locomotion driven by a locally and temporally changing magnetic field on a free ferrofluid surface operates on an array of electromagnets. The resulting ferrofluid soliton and the force

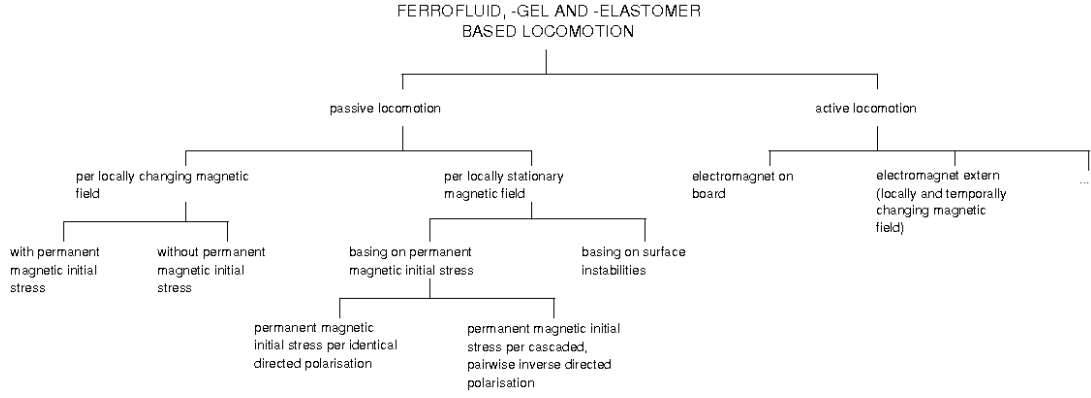
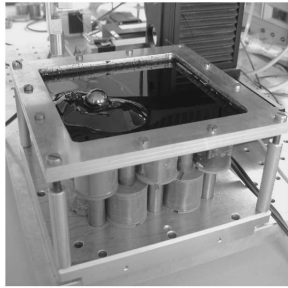
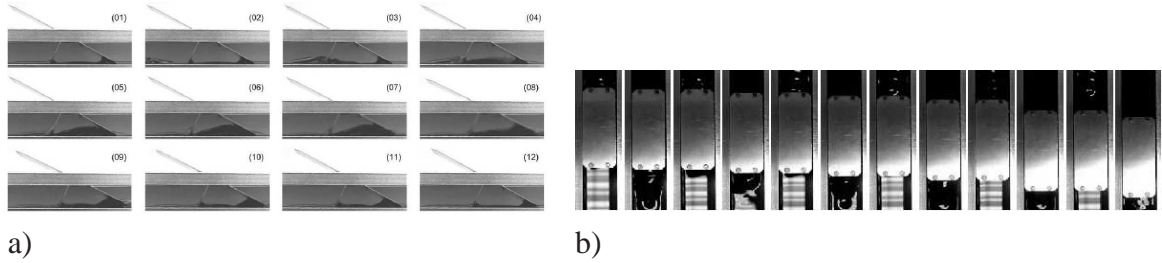


Figure 1: A possible classification of locomotion systems based on magnetoelastomaterials.

acting within, respectively, are moving an object either by a swimming or by a pushing operation. An onedimensional and a twodimensional alignment are introduced in Fig. 2 and Fig. 3.



type of passive, onedimensional locomotion.

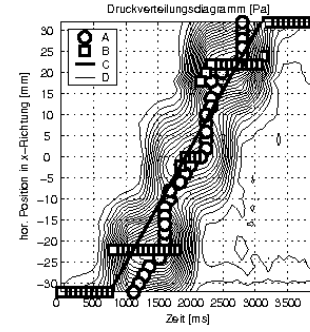
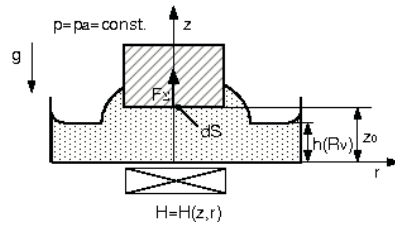


Figure 3: Passive, twodimensional locomotion of an object.

The theoretical background of Fig. 3 is presented in equation (1). A total force mainly resulting from atmospheric and magnetic and hydrostatic effects is characterized by

$$F_{\Sigma} = \int_S (\rho_f g (h(R_V) - z_0) + \frac{H_0^2(z_0, r)}{8\pi} (\mu_f - 1) - \frac{H_0^2(z = h(R_V), r)}{8\pi} (\mu_f - 1)) dS. \quad (1)$$

Whereas  $\rho_f$  and  $\mu_f$  are the density and the permeability of the fluid, respectively, and  $H_0$  is the magnetic field intensity unaffected by the fluid. This areal force is experimentally determined by static and dynamic measurements. The distribution of pressure maxima<sup>1</sup>

<sup>1</sup> 'A' marks the locally depended and 'B' the temporally depended maxima.

on a 12mm-diametered sensor area is depicted in Fig. 3c). The thick solid line 'C' is the position-time-graph of the ferrofluid soliton.

The system of Fig. 4 is classified as a passive locomotion system, which basis of the locomotion is a free ferrofluid surface, a locally fixed but temporally changing magnetic field and a permanent magnetic initial stress. The polarisation of the latter is cascaded in locomotion direction and pairwise inverse directed, which causes a ripple structure on the fluid surface. If a homogeneous, alternating magnetic field, applied by electromagnets, is added, the the surface pattern changes periodically. Subsequently, an object, placed on the surface, is lifted and gliding horizontally in the next pattern sink. In series of a periodic process a locomotion is accomplished.

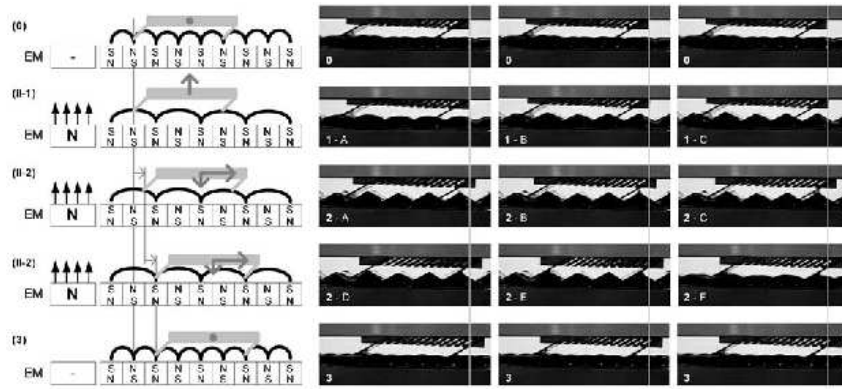


Figure 4: Prototype of a passive, linear locomotion system.

The actuation mechanism of active locomotion systems, which base on magnetoelastomers, gels and covered ferrofluids, comprises two principles. The first is achieved by an expansion and compression like the biological archetype earthworm, see Fig. 5a), and the second by a change of bending, see Fig. 5b) and c). The devices use a change of length and are advancing due to a non-symmetric friction, in case of Fig. 5a) and b) by inclined bristles.

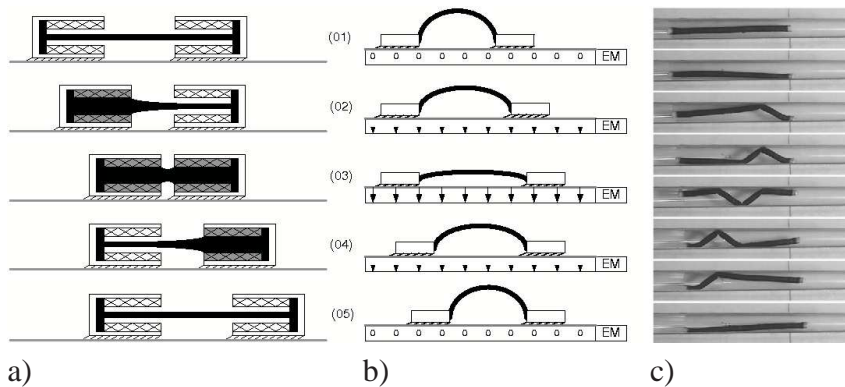


Figure 5: Active locomotion systems based on expansion and compression or on a change of the bending rate of the magnetoelastomaterial.

Fig. 5c) shows a worm made of an elastic cylindrical capsule filled with ferrofluid. It is positioned in a channel surrounded by electromagnets. While the magnetic field is alternating

with a frequency of  $f = 5.800\text{Hz}$ , the worm undulates in a periodically traveling magnetic field and thus is moving along the channel in opposite direction of the traveling magnetic field. The velocity of the capsule depends on the geometry of its own shape, of the channel and of the frequency. Theoretical and experimental analysis concerning the capsule velocity yields similar results for frequencies below  $50\text{Hz}$ . From  $700\text{Hz}$  the experimental values diverge from the theoretically predicted due to inertia forces.

The currently available magnetisable, highly elastic materials, like ferrofluids, elastomers, gels, can only render comparatively minor forces within the 1-digit newton range. Thus, the following requirements, which have to be considered in the development of similar systems, arise:

- mass and volume reduction of the systems,
- usage of powerful and lightweighting magnets,
- reduction of the thermal energy loss at the magnets.

Locomotion systems based on these magnetisable, highly elastic materials, solely receive their locomotion energy and information from the magnetic field, thus a high degree of autonomy is obtained. Especially this fact provides the great attractiveness of these materials in an engineers view.

## Acknowledgements

This work is supported by Deutsche Forschungsgemeinschaft (DFG, ZI 540/7-1) and the Russian Foundation for Basic Research (project 05-01-04001 and Grant Sci.Sc.-1481.2003.1).

## REFERENCES

- [1] R. E. Rosensweig, *Ferrohydrodynamics*, Dover Pubns **1** (1997).
- [2] S. Odenbach, Ferrofluide - ihre Grundlagen und Anwendungen, *Physik in unserer Zeit* **3**, 122–127 (2001).
- [3] U. Lange and L. Zipser, Geregelte magnetorheologische Stoß- und Schwingungsdämpfer, *A&D Kompendium* **21**, 91 (2003).
- [4] H. Hartshorne, C. J. Backhouse and W. E. Lee, Ferrofluid-based microchip pump and valve, *Sensors and Actuators B: Chemical* **99**, 592–600 (2004).
- [5] N. E. Greivell and B. Hannaford, The Design of a Ferrofluid Magnetic Pipette, *Biomedical Engineering, IEEE Transactions* **44**, 129–135 (1997).
- [6] K. Zimmermann, V. A. Naletova, I. Zeidis, V. Böhm and E. Kolev, Modelling of locomotion systems using deformable magnetizable media, *Journal of Physics: Condensed Matter* **18**, 2973–2983 (2006).
- [7] E. Forth and E. Schewitzer, *Meyers Taschenlexikon Bionik*, VEB Bibliographisches Institut Leipzig **2**, 229–230 (1976).

# ON THE DETERMINATION OF THE OVERALL ELASTIC MATERIAL BEHAVIOUR OF TEXTILE REINFORCED CONCRETE WITH MICRO- AND MACRO-CRACKS USING HOMOGENISATION

M. Richter<sup>1</sup>, B. W. Zastrau<sup>2</sup>

Institute of Mechanics and Shell Structures  
Technische Universität Dresden  
01062 Dresden, Germany

<sup>1</sup> e-mail: mike.richter@tu-dresden.de

<sup>2</sup> e-mail: bernd.zastra@tu-dresden.de

**Abstract.** *This paper is concerned with the development of mechanical models for the analytical determination of the macroscopic material behaviour of textile reinforced concrete (TRC) using a multi scale approach. Therefore the heterogeneous structure of TRC is modelled on the mesoscopic level followed by the homogenisation of the heterogeneous structure. Based on the micro-mechanical solution for a single inclusion embedded in an elastic matrix according to ESHELBY for the multi-directional reinforced concrete an effective field approximation is used. This approach considers the interaction between the different orientated rovings and the micro-cracks in an average sense. For the mechanical modelling of the bond behaviour between roving and matrix after initiating of the macro-cracking a slip-based bond model with a multiple linear shear stress-slip relation is used.*

## Introduction

In the last years textile reinforced concrete (TRC) as a new composite material has shown its high potential for application in the field of civil engineering for the fabrication of new structural elements and the strengthening of existing constructions [1]. The textile reinforcement consists of rovings which are bundles of a huge number of continuous filaments. TRC shows a complex material behaviour which can be classified in a linear-elastic part for low loading, the micro-cracking and the macro-cracking. For the determination of the overall macroscopic material behaviour the heterogeneous structure of TRC is modelled on the mesoscopic level followed by a homogenisation of the elastic fields. To reduce the numerical costs with regard to an intended multi-scale computation of TRC structures analytical homogenisation techniques are used.

## Linear-elastic behaviour

For a low macroscopic loading the material behaviour is approximately linear-elastic. Basis of the analytical homogenisation is the micro-mechanical solution of the average strain in a single inclusion embedded in an elastic matrix according to ESHELBY [2]. In the case of ellipsoidal inclusions the strain in the inclusion is constant and with the ESHELBY tensor  $\mathbf{S}^\alpha$  the overall elasticity tensor  $\overline{\mathbf{C}}$  can be written as

$$\overline{\mathbf{C}} = \mathbf{C} + \sum_{\alpha=1}^n f_\alpha \left( (\mathbf{C}^\alpha - \mathbf{C})^{-1} + \mathbf{S}^\alpha : \mathbf{C}^{-1} \right)^{-1}. \quad (1)$$

Herein are  $\mathbf{C}$  and  $\mathbf{C}^\alpha$  the elasticity tensors of concrete matrix and inclusion  $\alpha$  and  $f_\alpha$  the volume fraction of the inclusions. This solution neglects any interaction between the inclusions and is called the dilute solution. In extension of this solution for multi-directional reinforcements an effective field approximation (EFA) is used [3]. This approach considers the interaction between the different orientated rovings in an average sense. Now the different orientated rovings are assumed to be in a matrix (volume fraction  $f_m$ ) with the still unknown average matrix strain  $\bar{\epsilon}^m$ . This problem can be solved analytically and leads to an equation for the direct computation of the overall elasticity tensor [6]:

$$\bar{\mathbf{C}} = \mathbf{C} + \sum_{\alpha=1}^n f_\alpha (\mathbf{C}^\alpha - \mathbf{C}) : \left\{ \mathbf{K}^\alpha + \sum_{\beta=1, \beta \neq \alpha}^n f_\beta (\mathbf{K}^\beta - f_\beta \mathbf{1})^{-1} : (\mathbf{K}^\alpha - f_\alpha \mathbf{1}) \right\}^{-1} \quad (2)$$

with

$$\mathbf{K}^\alpha = (f_m + f_\alpha) \mathbf{1} - f_m \mathbf{S}^\alpha : (\mathbf{1} - \mathbf{C}^{-1} : \mathbf{C}^\alpha). \quad (3)$$

Compared to Eq. (1) in Eq. (2) now the different orientated rovings are coupled.

A roving is a loose bundle of filaments and we assume in the mechanical model, that the embedded roving has only a longitudinal stiffness and acts transverse to its axis like a hole in the matrix. As shown in the example of a bidirectionally reinforced matrix in Fig. 1 we obtain the interesting result, that the decrease of the YOUNGS modulus perpendicular to the roving axis is larger than the increase of the modulus in direction of the roving.

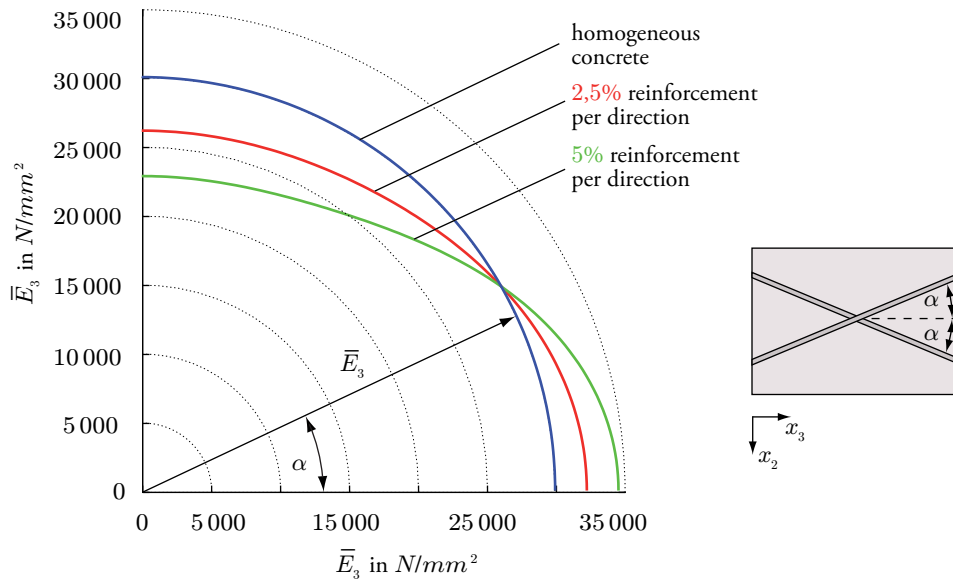


Figure 1: YOUNGS modulus  $\bar{E}_3$  in  $x_3$ -direction of a bidirectionally reinforced matrix depending on the roving orientation  $\alpha$  (plotted in polar coordinates).

### Micro-cracks

If the matrix stress exceeds a critical value micro-cracks are developing. The additional strain due to the micro-cracks  $\bar{\epsilon}^c$  can be expressed by the definition of a forth order tensor  $\mathbf{J}^c$  and the prescribed macroscopic strain  $\bar{\epsilon}^0$  [4]:

$$\bar{\epsilon}^c = \mathbf{J}^c : \bar{\epsilon}^m. \quad (4)$$

In the sense of the analytical homogenisation it is assumed, that there are no direct interactions between the micro-cracks among themselves and between micro-cracks and rovings, but the

application of the effective field approximation allows the consideration of these interactions in an average sense.  $\mathbf{J}^c$  can be obtained by integration over the crack opening displacement (COD) [6] which is known from fracture mechanical solutions.

For the characterisation of the actual state of micro-cracking we define a so-called *crack density parameter*  $f_c$  as product of the total number of cracks per unit area and the squared half crack length [4, 6]. Therewith we can describe the evolution of the micro-cracks with only one parameter, and the tensor  $\mathbf{J}^c$  depends on  $f_c$ . Using this parameter we don't need to know the lengths and the distribution of the cracks. However, the calculation of stress singularities is not possible.

Figure 2 shows as an example a bidirectionally reinforced matrix under uniaxial tension in  $x_3$ -direction. In this example the elastic properties of the matrix and the rovings are  $E_m = 30000 \text{ N/mm}^2$ ,  $\nu_m = 0.2$ ,  $E_r = 76000 \text{ N/mm}^2$  and the volume fractions of the rovings are  $f_1 = 5\%$  in  $x_3$ -direction and  $f_2 = 1\%$  in  $x_2$ -direction. The damage evolution due to the micro-

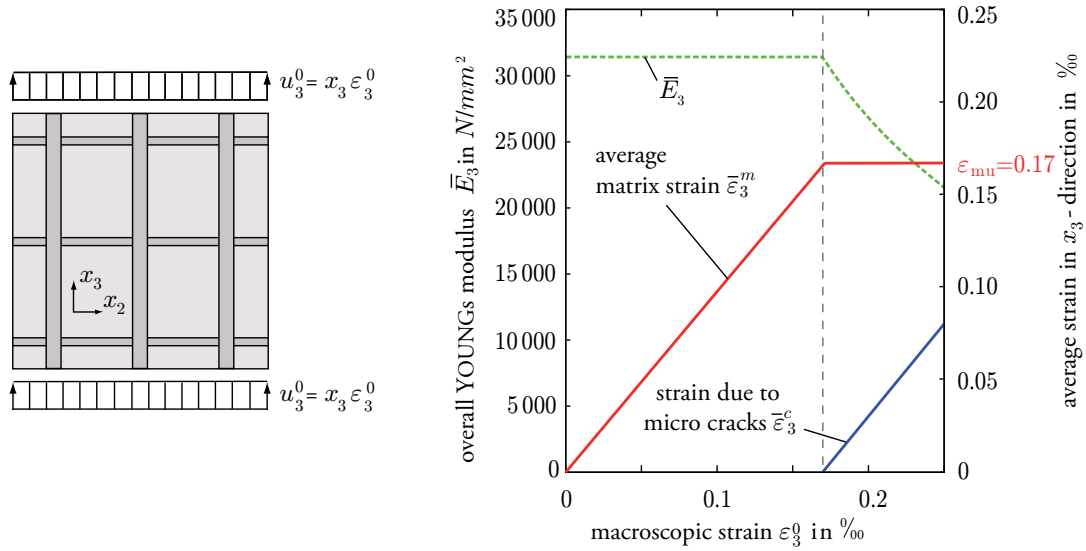


Figure 2: YOUNGS modulus and average strains of a bidirectionally reinforced matrix including micro-cracking.

cracks can be described as follows. With increasing macroscopic strain  $\epsilon_3^0$  also the matrix strain  $\bar{\epsilon}_3^m$  is increasing. If the matrix strain obtains its limit (here:  $\epsilon_{mu} = 0,17\%$ ), micro-cracks are developing. After the initiation of micro-cracking the average matrix strain  $\bar{\epsilon}_3^m$  cannot exceed the ultimate matrix strain  $\epsilon_{mu}$ . Hence, with increasing macroscopic strain  $\epsilon_3^0$  the strain  $\bar{\epsilon}_3^c$  due to the micro-cracks must increase. For a continuously increasing uniaxial tensile loading the matrix strain remains constant at  $\epsilon_{mu}$  and the overall YOUNGS modulus  $\bar{E}_3$  decreases. This decrease is non-linear. The current state of the damage due to the micro-cracks is characterised by the parameter  $f_c$  which is irreversible.

### Macro-cracks

In the mechanical model it is assumed, that the micro-cracks accumulate to macro-cracks if the micro-crack density reaches a critical value. After initiation of the macro-cracking the bond behaviour between roving and matrix dominates the overall macroscopic material behaviour. For the modelling of the bond behaviour a slip-based bond model with a multiple linear shear stress-slip relation is used [5, 6]. A multiple linear approach allows the closed form analytical solution of the bond problem. At least three linear sections are necessary to consider the perfect

bond zone, the partly damaged bond zone and the complete debonded zone. The function of the shear stress-slip relation can be determined by pullout experiments.

### Example

As an example a strain specimen is analysed. The specimen has a width of 100 mm and a thickness of 8 mm. In the experiment the elongation is measured between two measurement marks with a distance of 200 mm. The specimen is reinforced in three layers. The elastic properties of the concrete matrix and the rovings and also the ultimate stresses are given. Figure 3 shows the comparison between the measurement data and the analytical solution and demonstrates the applicability of the presented analytical model.

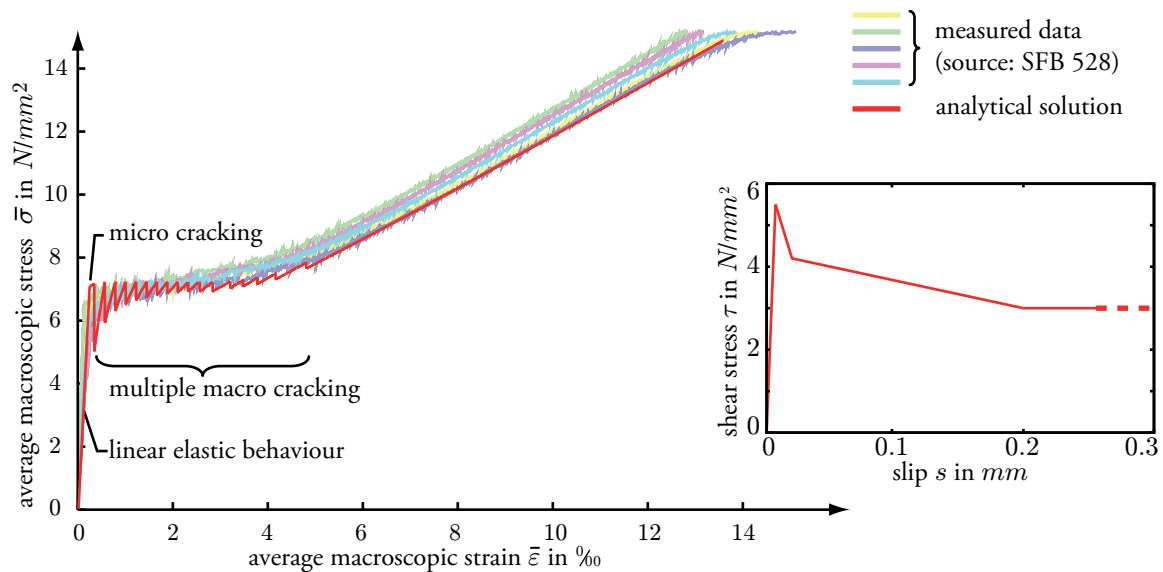


Figure 3: Macroscopic material behaviour of a TRC specimen under tensile loading and implemented material behaviour of the roving-matrix interface.

### REFERENCES

- [1] W. Brameshuber (Edt.), Textile reinforced concrete, State-of-the-art report of RILEM committee 201-TRC **36** (2006).
- [2] J. D. Eshelby, The determination of the elastic field of an ellipsoidal inclusion and related problems, Proceedings of the Royal Society of London **A 241**, 376–396 (1957).
- [3] T. Mori, K. Tanaka, Average stress in matrix and elastic energy of materials with misfitting inclusions, Acta Metallurgica **21**, 571–574 (1973).
- [4] T. Mura, Micromechanics of defects in solids, Kluwer Academic Publisher, Dordrecht (1993).
- [5] M. Richter, I. Lepenies, B. W. Zastrau, On the influence of the bond behaviour between fiber and matrix on the material properties of textile reinforced concrete, International Symposium of Anisotropic Behaviour of Damaged Materials, 1–24, Kraków (2002).
- [6] M. Richter, Entwicklung mechanischer Modelle zur analytischen Beschreibung der Materialeigenschaften von textilbewehrtem Feinbeton, Ph.D. thesis, Berichte des Instituts für Mechanik und Flächentragwerke **2**, Dresden (2005).

# AN INCREMENTAL VARIATIONAL FORMULATION FOR THE COUPLED ELECTROMECHANICAL RESPONSE OF PIEZOCERAMICS

D. Rosato<sup>1</sup> and C. Miehe<sup>2</sup>

<sup>1</sup>Institut für Mechanik (Bauwesen) Lehrstuhl I  
Universität Stuttgart  
70550 Stuttgart, Pfaffenwaldring 7  
e-mail: rosato@mechbau.uni-stuttgart.de

<sup>2</sup> Institut für Mechanik (Bauwesen) Lehrstuhl I  
Universität Stuttgart  
70550 Stuttgart, Pfaffenwaldring 7  
e-mail: cm@mechbau.uni-stuttgart.de

**Abstract.** *The paper presents continuous and discrete variational formulations for the treatment of the non-linear response of piezoceramics under multiaxial electromechanical loading. The point of departure is a general internal variable formulation that determines the hysteretic response of the material as a generalized standard medium in terms of an energy storage and a dissipation function. Consistent with this type of standard dissipative continua, we develop an incremental variational formulation of the coupled electromechanical boundary value problem. We specify the variational formulation for a setting based on a of smooth switching-surface which governs the hysteretic response. An important aspect is the numerical implementation of the coupled problem. The discretization of the two-field problem appears, as a consequence of the proposed incremental variational principle, in a symmetric format. The performance of the proposed methods is demonstrated by means of a spectrum of benchmark problems.*

## A COMPUTATIONAL MESO-MACRO TRANSITION PROCEDURE FOR ELECTRO-MECHANICAL COUPLED CERAMICS

J. Schröder<sup>1</sup>, H. Romanowski<sup>1</sup> and I. Kurzhöfer<sup>1</sup>

<sup>1</sup> Institute of Mechanics, Department of Civil Engineering, University of Duisburg-Essen  
Universitätsstr. 15, 45117 Essen, Germany  
e-mail: j.schroeder@uni-due.de

**Abstract.** *Ferroelectric materials exhibit a spontaneous polarization, which can be reversed by an applied electric field of sufficient magnitude. The resulting nonlinearities are expressed by characteristic dielectric and butterfly hysteresis loops. These effects are correlated to the structure of the crystal and especially to the axis of the spontaneous polarization in case of single crystals. On our representative meso scale we assume that the domains consist of unit cells with equal spontaneous polarization. Each domain is modeled within a coordinate invariant formulation for an assumed transversely isotropic material as presented in Schröder and Romanowski [6], in this context see also Schröder and Gross [5]. In this investigation the macroscopic polycrystalline quantities are obtained via a simple homogenization procedure, where discrete orientation distribution functions are used to approximate the different domains.*

### Introduction

A first macroscopic theory for the description of the hysteresis loops has been based on rate equations for the alignment of dipoles; which characterize the consequences of domain switching in a macroscopic sense, see e.g. Chen and Peercy [3]. A thermodynamic phenomenological formulation for the description of the electromechanical hysteresis effects has been proposed by Bassiouny, Ghaleb and Maugin [1]. The authors introduced the remanent strains and remanent polarization as internal variables and derived associated evolution equations as well as loading conditions. It should be remarked, that their proposed poling model can be considered as a generalization of Chen's model on a thermodynamic basis. Generally the considered materials are built by the repetition of structure elements in the three-dimensional space. In heterogeneous materials we differ between different scales of modeling: the macro-, the meso- and the micro-scale. In order to model piezoelectric material behavior we have to differentiate between the macroscopic boundary value problem, the mesoscopic domain configuration and the microscopic unit cells. The appearance of different polarization orientations on the micro-scale are the reason for the generation of the sub-domains on the meso-scale. One characteristic feature of ferroelectric material behavior is the appearance of a spontaneous polarization in a certain temperature range which can be reversed by an applied electric field.

### Macroscopic boundary value problem.

Let  $\mathcal{B} \subset \mathbb{R}^3$  be the macroscopic body of interest which is parameterized in  $\bar{\mathbf{x}}$ . Furthermore, let  $\bar{\mathbf{u}}$  be the macroscopic displacement field. The basic kinematic variable is the macroscopic strain tensor  $\bar{\boldsymbol{\varepsilon}}$ , which is defined by the symmetric part of the macroscopic displacement gradient. As the basic electric field variable we choose the macroscopic electric field vector  $\bar{\mathbf{E}}$ , given

by the negative gradient of the macroscopic scalar potential  $\bar{\phi}$ , where  $\bar{\nabla}$  denotes the gradient operator with respect to  $\bar{\mathbf{x}}$ . The governing field equations from the macroscopic point of view are the balance of momentum and Gauss law.

Mechanical part	Electrical part
$\bar{\boldsymbol{\varepsilon}} = \text{sym}[\bar{\nabla}\bar{\mathbf{u}}]$	$\bar{\mathbf{E}} = -\bar{\nabla}\bar{\phi}$
$\text{div}\bar{\boldsymbol{\sigma}} + \bar{\mathbf{f}} = \mathbf{0} \quad \text{in } \mathcal{B}$	$\text{div}\bar{\mathbf{D}} = \bar{\rho}_{\text{free}} \quad \text{in } \mathcal{B}$
$\bar{\mathbf{u}} = \bar{\mathbf{u}}_b \quad \text{on } \partial\mathcal{B}_u$	$\bar{\phi} = \bar{\phi}_b \quad \text{on } \partial\mathcal{B}_\phi$
$\bar{\mathbf{t}} = \bar{\boldsymbol{\sigma}}\bar{\mathbf{n}} \quad \text{on } \partial\mathcal{B}_t$	$-\bar{q} = \bar{\mathbf{D}} \cdot \bar{\mathbf{n}} \quad \text{on } \partial\mathcal{B}_D$

Table 1: Basic equations of the macroscopic electromechanical BVP.

Here  $\bar{\boldsymbol{\sigma}}$  represents the macroscopic symmetric Cauchy stress tensor,  $\bar{\mathbf{f}}$  the given body force,  $\bar{\mathbf{D}}$  the vector of macroscopic electric displacements and  $\bar{\rho}_{\text{free}}$  is the given density of free charge carriers. In order to treat the electromechanical boundary value problem, the surface of the considered body is divided in mechanical and electrical parts  $\partial\mathcal{B} = \partial\mathcal{B}_u \cup \partial\mathcal{B}_\sigma$  and  $\partial\mathcal{B} = \partial\mathcal{B}_\phi \cup \partial\mathcal{B}_D$  respectively, with  $\partial\mathcal{B}_u \cap \partial\mathcal{B}_\sigma = \emptyset$  and  $\partial\mathcal{B}_\phi \cap \partial\mathcal{B}_D = \emptyset$ .

### Meso-Macro-Transition.

In order to derive different constraint/boundary conditions for the considered body on the meso-scale, the representative volume element, we postulate a generalized macro-homogeneity condition which equates the mesoscopic and macroscopic electromechanical power, in this context see the well known Hill condition. In the following we assume a decoupling of the mechanical and electrical contributions and focus on continuous bodies without holes. The two decoupled macro-homogeneity conditions are defined as

$$\mathcal{P}_1 := \frac{1}{V} \int_{\mathcal{RV}\mathcal{E}} \boldsymbol{\sigma} : \dot{\boldsymbol{\varepsilon}} \, dv - \bar{\boldsymbol{\sigma}} : \dot{\bar{\boldsymbol{\varepsilon}}} \quad \text{and} \quad \mathcal{P}_2 := \frac{1}{V} \int_{\mathcal{RV}\mathcal{E}} \mathbf{D} \cdot \dot{\mathbf{E}} \, dv - \bar{\mathbf{D}} \cdot \dot{\bar{\mathbf{E}}}. \quad (1)$$

Simple conditions, here denoted as constraints on the meso-structure, satisfying equation (1) are  $\boldsymbol{\sigma} = \bar{\boldsymbol{\sigma}} = \text{const.}$  or  $\dot{\boldsymbol{\varepsilon}} = \dot{\bar{\boldsymbol{\varepsilon}}} = \text{const.}$  and  $\mathbf{D} = \bar{\mathbf{D}} = \text{const.}$  or  $\dot{\mathbf{E}} = \dot{\bar{\mathbf{E}}} = \text{const.}$ . The first condition is associated to the well known Reuss-bound and contains the assumption that the stresses are place invariant during the deformation process and always equal to the volume average  $\bar{\boldsymbol{\sigma}}$ . In a similar manner the other part is associated with the Voigt-bound. In this contribution the volume average  $\bar{\boldsymbol{\sigma}}$  is rendered by the consideration of orientation distribution functions. Our approach is to construct a consistent distribution of orientation to pay respect to the many directions of polarization in a polycrystal. In plane the construction of this distribution functions is very simple. The orientations are uniformly distributed over the unit circle. For a spatial distribution of orientations the generation is not that easy. A consistent segmentation of the two angles which describe a point on a unit sphere would lead to a compaction of orientations in the neighborhood of one axis. A feasible access to the construction of consistent spatial distribution functions is the partitioning of the sphere surface into parts of equal areas. An innovative treatment of the problem was given by RICHARD BUCKMINSTER FULLER who separated the surface of the sphere into equilateral congruent triangles. The resulting constructions of a dome are denoted by the expressions geodesic spheres or geodesic domes. They were

presented to a wider audience during the world exhibition 1967 in Montreal where the american pavillon was constructed in the mentioned manner.

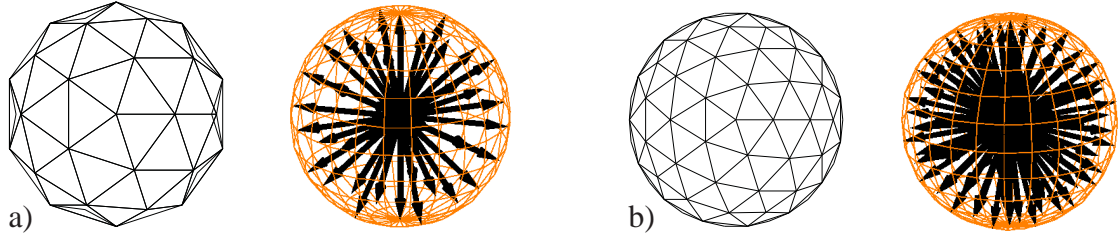


Figure 1: Geodesic spheres and their distribution of orientations, a) 42 orientations and b) 92 orientations.

### Thermodynamically consistent framework

The key assumption in the proposed model is an additive decomposition of the strains and the electric displacements into reversible and remanent (irreversible) parts. Let us now assume the existence of a thermodynamic potential  $H = \hat{H}(\varepsilon, \varepsilon^r, \mathbf{E}, \mathbf{P}^r)$ . The evaluation of the second law of thermodynamic yields the constitutive expressions for the stresses and electric displacements and a reduced dissipation inequality remains. In order to model the dissipation process we have to construct evolution equations for the remanent quantities. For this purpose the existence of a switching surface  $\Phi$  is assumed, where the optimization conditions  $\partial_{(\bullet)}\mathcal{L}$  of the Lagrangian functional  $\mathcal{L}(\tilde{\sigma}, \tilde{\mathbf{E}}, \lambda)$  lead to associated flow rules for the remanent quantities and related loading and unloading conditions (postulate of maximum remanent dissipation). The complete set of equations for the proposed model is summarized in Table 1.

additive decomposition	$\varepsilon = \varepsilon^e + \varepsilon^r$ and $\mathbf{D} = \mathbf{D}^e + \mathbf{P}^r$
thermodynamic potential	$H = \hat{H}(\varepsilon, \varepsilon^r, \mathbf{E}, \mathbf{P}^r)$
stresses and electric displacements	$\boldsymbol{\sigma} = \partial_{\varepsilon} H$ and $\mathbf{D} = -\partial_{\mathbf{E}} H$
conjugated stresses and electric field	$\tilde{\boldsymbol{\sigma}} = -\partial_{\varepsilon^r} H$ and $\tilde{\mathbf{E}} = -\partial_{\mathbf{P}^r} H$
reduced dissipation inequality	$\mathcal{D} = \tilde{\boldsymbol{\sigma}} : \dot{\varepsilon}^r + \tilde{\mathbf{E}} \cdot \dot{\mathbf{P}}^r \geq 0$
switching surface	$\Phi = \hat{\Phi}(\tilde{\boldsymbol{\sigma}}, \tilde{\mathbf{E}}) \leq 0$
Lagrangian functional	$\mathcal{L}(\tilde{\boldsymbol{\sigma}}, \tilde{\mathbf{E}}, \lambda) = -\mathcal{D}(\tilde{\boldsymbol{\sigma}}, \tilde{\mathbf{E}}) + \lambda \phi(\tilde{\boldsymbol{\sigma}}, \tilde{\mathbf{E}})$
flow rules for remanent quantities	$\dot{\varepsilon}^r = \lambda \partial_{\tilde{\boldsymbol{\sigma}}} \Phi = \lambda \tilde{\mathbf{m}}$ and $\dot{\mathbf{P}}^r = \lambda \partial_{\tilde{\mathbf{E}}} \Phi = \lambda \tilde{\mathbf{n}}$
loading/unloading conditions	$\lambda \geq 0; \Phi \leq 0$ and $\lambda \Phi = 0$

Table 2: Set of equations for the proposed model

### Numerical example

To clarify the macroscopic procedures an electric inhomogeneous example, the piezoelectric actuator, is presented. In this example we reduce the actuator to a two dimensional section with 576 Elements. The dimensions of the meshed region were taken in adaption to Kamlah and Böhle [4]. This means in detail we compute with a height of  $h = 57.5\mu m$  and the magnitude of each fragment of the actuator is given by  $l_1 = l_2 = 205\mu m$ . A poling process is modeled

by applying an cycling electric potential with maximum value of  $\phi_{max} = -333V$ . The boundary conditions and connection between the load factor and the time are presented in Figure 2. A spacial distribution of 42 orientations is assigned to each Gauss Point of the elements. For the clarification of the poling process Figure 3 shows the contour plot of the norm of the electric field and the vector plot of the macroscopic remanent polarization over the isolines of the electric potential.

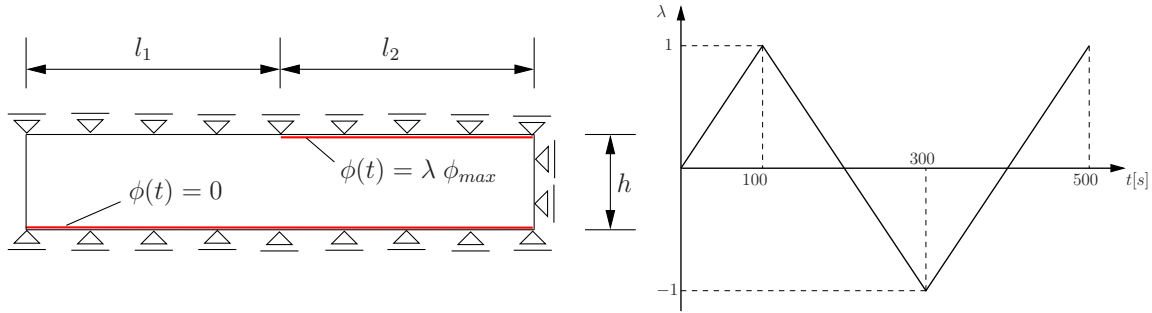


Figure 2: Boundary conditions and cyclic loading.

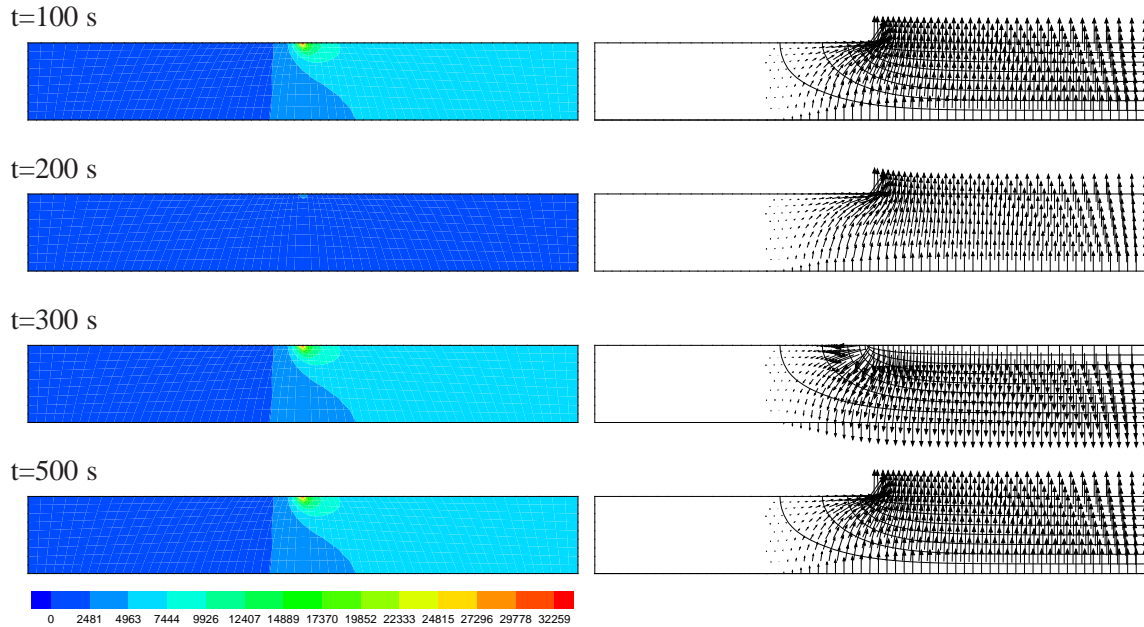


Figure 3:  $|\mathbf{E}|$  and  $\bar{\mathbf{P}}^r$  at different time steps of the computation.

## REFERENCES

- [1] E. Bassiouny et al., International Journal of Engineering Science **26**, 1279–1295 (1988).
- [2] J.P. Boehler, Applications of Tensor Functions in Solid Mechanics, CISM Course No. 292 (Springer, Heidelberg, 1987).
- [3] P.J. Chen and P.S. Peercy, Acta Mechanica **31**, 231–241 (1979).
- [4] M. Kamlah and U. Böhle, Int. Journal of Solids and Structures **38**, 605–633 (2001).
- [5] J. Schröder and D. Gross, Archive of Applied Mechanics **73**, 533–552 (2004).
- [6] J. Schröder and H. Romanowski, Archive of Applied Mechanics **74**, 863–877 (2005).

## HERSTELLUNG UND CHARAKTERISIERUNG VON PIEZOELEKTRISCHEN GRADIENTENKERAMIKEN

Ralf Steinhausen<sup>1</sup>, Christoph Pientschke<sup>1</sup>, and Horst Beige<sup>1</sup>

<sup>1</sup>Martin-Luther-Universität Halle-Wittenberg  
Friedemann-Bach-Platz 6, 06108 Halle  
e-mail: ralf.steinhausen@physik.uni-halle.de

**Abstract.** *Piezoelektrische Gradientenmaterialien bestehen aus mindestens zwei Komponenten mit unterschiedlichen piezoelektrischen Eigenschaften. Die piezoelektrischen Koeffizienten ändern sich dabei innerhalb des Materials stetig (ein- oder mehrdimensionaler Gradient). Dadurch wird beim Anlegen eines elektrischen Feldes eine stetige Änderung der lokalen Dehnung hervorgerufen, was sich z.B. in einer Reduzierung innerer mechanischer Spannungen bemerkbar macht. Die Eigenschaften eines solchen Materials werden am Beispiel eines Biegeaktuators diskutiert.*

*Es werden verschiedene Herstellungsmöglichkeiten für piezoelektrische Gradientenmaterialien vorgestellt. Bei der gebräuchlichsten Methode wird ein chemischer Gradient durch einen Polungsprozess in einen piezoelektrischen Gradient umgewandelt. Die Polungsmechanismen werden an Hand eines Polungsmodells vorgestellt. Die Vor- und Nachteile verschiedener Materialkombinationen werden diskutiert. Die theoretischen Ergebnisse werden mit experimentellen Untersuchungen von monolithischen Gradientenbiegern verglichen.*

### Introduction

Für die Herstellung eines piezoelektrischen Gradienten in monolithischen Keramiken sind verschiedene Verfahren bekannt. So kann der piezoelektrische Koeffizient z.B. durch eine unterschiedliche lokale Dichte in einer Keramik beeinflusst werden, die ihrerseits z.B. über einen Porositätsgradienten eingestellt werden kann. Eine weitere Möglichkeit ist die Präparation eines Korngrößengradienten. Die am häufigsten verwendete Methode ist jedoch die Präparation eines chemischen Gradienten, der erst durch den Polungsprozess in einen piezoelektrischen Gradienten umgewandelt wird. Auch hier sind aus der Literatur verschiedene Herstellungsverfahren bekannt, die auf Technologien wie dem Pulverpressen, Folien gießen oder FreeForm-Techniken beruhen.

Herkömmliche Biegeaktuator bestehen aus mindestens zwei miteinander fest verbundenen Schichten, die sich beim Anlegen eines elektrischen Feldes unterschiedlich stark ausdehnen. Die Schichten werden z.B. miteinander oder mit einer passiven Schicht in der Mitte, die gleichzeitig auch als Mittelelektrode dienen kann, verklebt. Die Biegeauslenkung ist dabei umso besser je größer der Unterschied in den Dehnungen der Ober- und Unterseite des Biegers ist.

Auf Grund der unterschiedlichen Dehnung kommt es an der Verbindungsstelle zwischen den Schichten zu großen mechanischen Spannungen, die zu Rissbildung oder sogar zum Ablösen der Schicht und damit zur Schädigung des Bauteils führen können. Durch einen Dehnungsgradienten können die mechanischen Spannungen deutlich reduziert werden, ohne das die Biegeauslenkung deutlich darunter leidet.

## Materialauswahl und Pulverpressverfahren

Bei der Auswahl der Materialien, die für einen chemischen Gradienten verwendet werden, müssen verschiedene Aspekte beachtet werden. Im einfachsten Fall geht man von zwei Materialien aus, so dass sich die chemische Zusammensetzung stetig von Material A zu Material B ändert. Material A sollte dann o.E.d.A. einen möglichst hohen piezoelektrischen Koeffizienten (bei Biegeaktuatoren ist dies der Koeffizient  $d_{31}$ ) und eine vergleichsweise kleine Dielektrizitätskonstante besitzen, damit ein möglichst großer Anteil der angelegten Spannung in dieser Schicht abfällt. Für das Material B kommen verschiedene Möglichkeiten in Frage. Es kann ein piezoelektrisch inaktives oder schwach piezoelektrisches Material mit einer hohen Dielektrizitätskonstante gewählt werden, z.B. paraelektrisch/elektrostriktive Materialien, aber auch leitfähige Keramiken oder Relaxorferroelektrika kommen in Betracht. Die Kombination eines ferroelektrisch harten mit einem ferroelektrisch weichen Material bietet darüber hinaus die Möglichkeit, einen piezoelektrischen Gradienten mit wechselndem Vorzeichen zu induzieren.

Beim Pulverpressverfahren werden Pulverschichten mit unterschiedlicher chemischer Zusammensetzung zu einem Grünling gepresst. Je nach Anzahl und Grad der Variation der chemischen Zusammensetzung kann der spätere Gradient variiert werden. Während des Sinterprozesses kommt es durch Diffusion zu einem *Verschmieren* der Übergänge.

## Grundlagen der Biegetheorie von Mehrschichtbiegern

In erster Näherung kann ein Material mit einem eindimensionalen Gradienten als Mehrschichtsystem betrachtet werden. Die einzelnen Schichten sind dabei homogen mit konstanten piezoelektrischen, dielektrischen und elastischen Koeffizienten. Wird ein reiner piezoelektrischer Gradient vorausgesetzt, d.h. die dielektrischen und elastischen Eigenschaften sind für alle Schichten gleich, so ergibt sich die Auslenkung eines einseitig eingespannten Mehrschichtbiegeaktuators aus  $N$  Schichten nach [1] aus

$$\delta(N) = \frac{E_3 L^2 d_{31}^{max}}{h} \left( \frac{N+1}{N} \right). \quad (1)$$

Dabei wird der piezoelektrische Koeffizient von einem positiven Maximalwert  $d_{31}^{max}$  zu einem negativen Maximalwert  $-d_{31}^{max}$  schrittweise verändert. Die angelegte Feldstärke ist  $E_3$ ,  $h$  ist die Gesamtdicke des Biegers und  $L$  dessen freie Länge. Die mechanischen Spannungen sind in lateraler Richtung, senkrecht zur Feldrichtung, am größten. Die Komponente  $T_1$  in Längsrichtung des Biegers ändert dabei am Interface zwischen den Schichten das Vorzeichen (Wechsel von Zug- und Druckspannung). Das Maximum dieser Spannung tritt dabei immer zwischen den jeweils beiden äußeren Schichten auf und kann nach

$$T_{1max}(N) = E_3 Y d_{31}^{max} \left( \frac{N+2}{N^2} \right) \quad (2)$$

berechnet werden [2].  $Y$  ist hier der Youngs- oder Elastizitätsmodul, der hier für alle Schichten als konstant angenommen wird. Die Auslenkung nimmt mit zunehmender Schichtzahl leicht ab und strebt einem Grenzwert von ca. 2/3 des Wertes für die Zweischichtstruktur (herkömmlicher Bieger) zu (Abb. 1). Die mechanische Spannung hingegen nimmt deutlich ab und nähert sich für einen idealen Gradienten  $N \rightarrow \infty$  der Null.

## Polungsmodell

Mit der chemischen Zusammensetzung ändern sich neben den Kleinsignaleigenschaften in starkem Maße auch die nichtlinearen (Großsignal-)Eigenschaften. Dabei ist insbesondere die

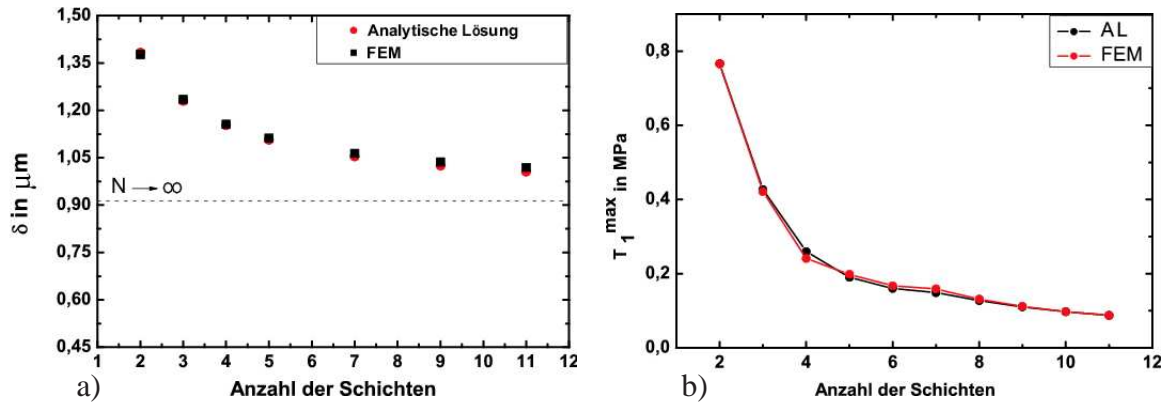


Figure 1: Auslenkung (a) und maximale mechanische Spannung (b) von Mehrschichtbiegern in Abhängigkeit von der Schichtanzahl  $N$

Abhängigkeit der Polarisierung von der angelegten Feldstärke  $P(E)$  für das Polungsverhalten von entscheidender Bedeutung. Das bereits beschriebene Mehrschichtmodell kann durch ein einfaches Ersatzschaltbild aus in Reihe geschalteten RC-Gliedern beschrieben werden. Der Einfluß der Dehnung der Einzelschichten und daraus resultierende Effekte durch mechanische Klemmung werden vernachlässigt. Von den Schichten müssen neben der elektrischen Leitfähigkeit  $\sigma$ , die Abhängigkeit  $P(E)$  und deren zeitliche Ableitung  $P'(E)$  bekannt sein. Für den einfachsten Fall eines Zweischichtsystems erhält man ein System von einfachen Differentialgleichungen

$$\sigma_1 E_1 + \epsilon_0 \dot{E}_1 + P'_1 \dot{E}_1 = \sigma_2 E_2 + \epsilon_0 \dot{E}_2 + P'_2 \dot{E}_2 \quad (3)$$

$$\dot{E}_{\text{appl}} = \frac{d_1}{d} \dot{E}_1 + \frac{d_2}{d} \dot{E}_2, \quad (4)$$

wobei  $E_1$  und  $E_2$  die lokale elektrische Feldstärke in den Schichten sowie  $d_1$  und  $d_2$  die Schichtdicke sind. Die angelegte Feldstärke  $E_{\text{appl}}$  in Gl. 2 ist die angelegte Spannung pro Gesamtdicke  $d$ .

Die ferroelektrischen Hysteresen  $P(E)$  sowie deren Ableitung können z.B. mit tanh-Funktionen [3] oder dem Preisach-Modell [4] beschrieben werden. Das Modell liefert Aussagen über den zeitlichen Verlauf der lokalen Feldstärke in den einzelnen Schichten, sowie über die lokale Polarisierung des Materials. In der Abb. 2 ist der zeitliche Verlauf dieser Größen für ein Zwei-schichtsystem aus einem ferroelektrischen Material (BTS7.5) und einem hysteresefreien Relaxor (BTS15) dargestellt. Die Polungsfeldstärke für das Gesamtsystem wird dabei langsam erhöht, bleibt dann 50 Sekunden konstant und wird dann wieder langsam auf Null verringert.

## Experimentelle Ergebnisse

Es wurden Gradientenstrukturen hergestellt und untersucht, die auf  $\text{BaTiO}_3$  Keramiken basieren. Dabei wurden verschiedene Mischkristallsysteme und Dotierungen untersucht, um bleifreie monolithische Biegeaktuatoren herzustellen. Das Mischkristallsystem von  $\text{BaTiO}_3$  und  $\text{BaSnO}_3$  erlaubt es, die ferroelektrischen Eigenschaften in einem weiten Bereich zu ändern. So wird bei einem Sn-Gehalt von 7,5 mol% (BTS7.5) an der orthorhombisch-rhomboedrischen Phasengrenze ein Maximum der spontanen Polarisierung, verbunden mit einem großen  $d_{31}$  und einer kleinen Dielektrizitätskonstante, beobachtet. Bei einem Sn-Gehalt von 15 mol% zeigt  $\text{Ba}(\text{Ti},\text{Sn})\text{O}_3$  (BTS15) bereits Relaxor-Verhalten mit einer verschwindenden remanenten Polarisierung und kleinen piezoelektrischen Koeffizienten. Das Polungs- und Biegeverhalten

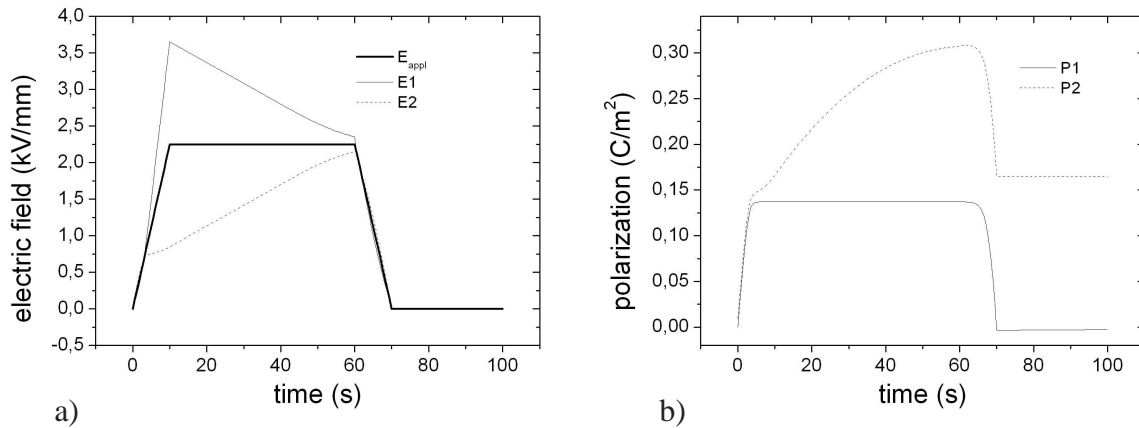


Figure 2: Zeitliche Abhängigkeit der lokalen Feldstärke (a) und der lokalen Polarisation (b) in einem Zweischichtsystem während des Polungsvorgangs

von Proben mit unterschiedlich starker Ausprägung des Gradienten wurde untersucht und mit Ergebnissen der Modellierung verglichen.

Wird  $\text{BaTiO}_3$  mit 2mol% La dotiert, so erhöht sich die Leitfähigkeit um ein Vielfaches und das Material kann als keramische Elektrode eingesetzt werden. Eine Kombination von piezoelektrischen  $\text{BaTiO}_3$  und leitfähigem  $\text{BaTiO}_3+\text{La}$  kann ebenfalls als Biegeaktuator verwendet werden. Die Biegeeigenschaften können durch eine Änderung der Dicke der La-dotierten Schicht variiert werden.

Die bereits genannte Kombination eines ferroelektrisch harten und weichen Materials wurde mit Keramiken aus  $\text{BaTiO}_3$  und Mn-dotiertem  $\text{BaTiO}_3$  realisiert. Es konnte gezeigt werden, dass es durch ein geeignetes Polungsregime möglich ist, in einer Schichtstruktur entgegengesetzte Polarisierungen zu erzeugen. Dadurch wird im Betrieb beim Anlegen einer elektrischen Spannung in einer Schicht eine positive und in der anderen Schicht eine negative Dehnung erzeugt, was die Biegung des Aktuators verbessert.

## REFERENCES

- [1] M.A. Marcus, Performance characteristics of piezoelectric polymer flexure mode devices, *Ferroelectrics* **57**, 203 (1984).
- [2] A. Kouvatov, R. Steinhausen, W. Seifert, T. Hauke, H.T. Langhammer, H. Beige and H. Abicht, Comparison Between Bimorphic and Polymorphic Bending Devices, *Journal of European Ceramic Society* **19**, 1153–1156 (1999).
- [3] Y. T. Or and C. K. Wong, B. Ploss, F.G. Shin, Polarization behavior of ferroelectric multilayered composite structures, *Journal of Applied Physics* **93**, 4112–4119 (2003).
- [4] C. Pientschke, R. Steinhausen, A. Kouvatov, H. T. Langhammer, H. Beige, Comparison Between Bimorphic and Polymorphic Bending Devices, *Ferroelectrics* **319**, 181–190 (2005).

## A DATABASE APPROACH TO HOMOGENIZATION

İlker Temizer, Peter Wriggers

Institute of Mechanics and Computational Mechanics  
Leibniz University of Hannover  
Appelstr. 9A, 30167 Hannover, Germany  
e-mail: temizer or wriggers@ibnm.uni-hannover.de

**Abstract.** *In this contribution, an adaptive numerical homogenization technique is described for macroscopically anisotropic, nonlinearly elastic heterogeneous materials. The concept of a material map, where one identifies the constitutive behavior of a material in a discrete sense through interpolation among various RVE states in the stress-strain space, is discussed together with its implementation in the finite element method. The homogenization of the heterogeneous material is then realized through the computation of its material map. An application of this approach to the analysis of a two-scale periodic particulate composite is presented in an adaptive multi-level finite element setting that renders the methodology applicable over a wide range of deformations.*

### Introduction

Homogenization of microheterogeneous materials for the linear elastic analysis of macrostructures is well-established. In the nonlinear elasticity regime, the homogenization process is more challenging. In this regime, one identifies the macroscopic stress  $\mathbf{P}^*$  and the deformation gradient  $\mathbf{F}^*$  at a point of the macrostructure as the volume average of microscopic stress and deformation fields over a statistically representative volume element (RVE)<sup>2</sup>. Explicitly,  $\mathbf{P}^* = \langle \mathbf{P} \rangle_{\mathcal{V}_o}$  and  $\mathbf{F}^* = \langle \mathbf{F} \rangle_{\mathcal{V}_o}$  where  $\mathcal{V}_o$  denotes the undeformed configuration of the RVE, and  $\mathbf{P}$  and  $\mathbf{F}$  denote microscopic 1<sup>st</sup> Piola-Kirchhoff stress and deformation gradient tensors, respectively. These macroscopic quantities are determined by subjecting the RVE to boundary conditions that satisfy Hill's energy criterion, which reads  $\langle \mathbf{P} \cdot \dot{\mathbf{F}} \rangle_{\mathcal{V}_o} = \langle \mathbf{P} \rangle_{\mathcal{V}_o} \cdot \langle \dot{\mathbf{F}} \rangle_{\mathcal{V}_o}$ . One then defines other kinetic and kinematic quantities using  $\mathbf{P}^*$  and  $\mathbf{F}^*$ . In particular,  $\mathbf{S}^* \stackrel{\text{def}}{=} (\mathbf{F}^*)^{-1} \mathbf{P}^*$  is the effective 2<sup>nd</sup> Piola-Kirchhoff stress tensor and  $\mathbf{E}^* \stackrel{\text{def}}{=} \frac{1}{2} ((\mathbf{F}^*)^T \mathbf{F}^* - \mathbf{I})$  is the effective Lagrangian strain tensor, where  $\mathbf{I}$  is the identity tensor. Moreover, assuming that the constituents of the heterogeneous material are hyperelastic then so is the macroscopic material. Therefore, if one identifies  $\mathcal{W}^* = \langle \mathcal{W} \rangle_{\mathcal{V}_o}$  where  $\mathcal{W}$  is the microscopic strain energy, then  $\mathbf{S}^* = \frac{\partial \mathcal{W}^*}{\partial \mathbf{E}^*}$ .

If the heterogeneous material displays macroscopic isotropy, the most general form of the constitutive equation of this material is  $\mathbf{S}^* = \phi_0^* \mathbf{I} + \phi_1^* \mathbf{E}^* + \phi_2^* (\mathbf{E}^*)^2$  where  $\phi_i^*$  are functions of the set of invariants of  $\mathbf{E}^*$ :  $\phi_i^* = \phi_i^*(I_{\mathbf{E}^*}, II_{\mathbf{E}^*}, III_{\mathbf{E}^*})$ . However, explicit forms of the functions  $\phi_i^*$  are not known *a priori* so material test data is required in order to characterize the

<sup>2</sup>The notation  $(\cdot)^*$  denotes the macroscopic equivalent of a microscopic quantity. The volume average of a quantity  $\mathcal{Q}$  with respect to a domain  $\Psi$  is defined as  $\langle \mathcal{Q} \rangle_{\Psi} \stackrel{\text{def}}{=} \frac{1}{|\Psi|} \int_{\Psi} \mathcal{Q} d\Psi$ .

macroscopic constitutive behavior. The usual method for this characterization involves proposing relatively general forms for  $\phi_i^*$ , or alternatively for  $\mathcal{W}^* = \mathcal{W}^*(I_{\mathbf{E}^*}, II_{\mathbf{E}^*}, III_{\mathbf{E}^*})$ , with free parameters which are determined by an optimization procedure that makes use of the test data. An alternative method is the direct usage of the material test data by referring to a database of RVE computation results during the macrostructural analysis, as attempted in [1]. This approach has been pursued in [2] for the homogenization of macroscopically isotropic heterogeneous materials, where a database (referred to as the *material map*) for the values of  $\phi_i^*$  was created in the eigenvalue space  $(\lambda_1, \lambda_2, \lambda_3)$  of  $\mathbf{E}^*$ . The use of this map during a macrostructural analysis essentially corresponds to interpolation among known RVE stress-strain states in order to generate a continuous stress-strain relationship that characterizes the macroscopic behavior of the heterogeneous material. In this contribution, a similar approach is described for the analysis of microstructures that display macroscopic anisotropy. For clarity, the homogenization methodology is presented in a two-dimensional setting.

### Homogenization in anisotropic nonlinear elasticity

Consider a periodic composite which displays macroscopic orthotropy. In the absence of microstructural bifurcations, the RVE ( $\mathcal{V}_o$ ) is identified as the unit cell of the periodic composite, and the macroscopic stress may be computed by imposing periodic boundary conditions (PR-BCs) which control  $\langle \mathbf{F} \rangle_{\mathcal{V}_o}$ .

Let the unit vector  $\mathbf{n}$  denote the material orientation characterizing orthotropy. The macroscopic constitutive behavior of this composite is described by  $\mathcal{W}^* = \mathcal{W}^*(\mathbf{E}^*, \mathbf{n})$ . Although the tensorial dependence of  $\mathbf{S}^*$  on  $\mathbf{E}^*$  and  $\mathbf{n}$  may be derived from  $\mathcal{W}^*$  using  $\mathbf{S}^* = \frac{\partial \mathcal{W}^*}{\partial \mathbf{E}^*}$  [3], the number of unknown functions (similar to  $\phi_i^*$ ) that appear in the resulting form for  $\mathbf{S}^*$  may not match the number of equations available through the components of  $\mathbf{S}^*$ , contrary to the macroscopic isotropy case. This indeterminacy may be avoided by creating a material map for the components of  $\mathbf{S}^*$ .

The material test space  $(\lambda_1, \lambda_2, \theta)$  is used for the generation of the map, where  $\theta$  denotes the orientation of the eigenvector basis  $\{\mathbf{v}_1, \mathbf{v}_2\}$  of  $\mathbf{E}^*$  with respect to  $\mathbf{n}$ . The test space is meshed in a manner similar to the generation of a finite element mesh. The components  $[\mathbf{S}^*]_{11}^v$ ,  $[\mathbf{S}^*]_{22}^v$  and  $[\mathbf{S}^*]_{12}^v$  of  $\mathbf{S}^*$  are determined at the map mesh nodes, and the continuity of the map is ensured via interpolation using map element shape functions. Explicitly,  $[\mathbf{S}^*]_{AB}^v = [\mathbf{S}^*]_{AB}^{v,I} \Phi_I$  where  $[\mathbf{S}^*]_{AB}^{v,I}$  is the nodal value of the stress component, and  $\Phi_I = \Phi_I(\lambda_1, \lambda_2, \theta)$  is a map element shape function. Here, the notation  $[\cdot]_{AB}^v$  denotes the components of a tensor with respect to the eigenvector basis of  $\mathbf{E}^*$ .

The macrostructural calculations require the macroscopic tangent stiffness  $\mathbf{L}^* \stackrel{\text{def}}{=} \frac{\partial \mathbf{S}^*}{\partial \mathbf{E}^*}$  at each integration point of the macroscopic finite element mesh. For this purpose, the tangent induced by the material map may be employed via  $\mathbf{L}^* = \frac{\partial \mathbf{S}^*}{\partial \mathbf{E}^*} = \frac{\partial \mathbf{S}^*}{\partial \lambda_1} \frac{\partial \lambda_1}{\partial \mathbf{E}^*} + \frac{\partial \mathbf{S}^*}{\partial \lambda_2} \frac{\partial \lambda_2}{\partial \mathbf{E}^*} + \frac{\partial \mathbf{S}^*}{\partial \theta} \frac{\partial \theta}{\partial \mathbf{E}^*}$ . Here,  $\mathbf{S}^* = [\mathbf{S}^*]_{AB}^{v,I} \Phi_I \mathbf{v}_A \otimes \mathbf{v}_B$  so that the derivatives  $\frac{\partial \mathbf{S}^*}{\partial \lambda_i}$  and  $\frac{\partial \mathbf{S}^*}{\partial \theta}$  may be computed using the dependence of  $\Phi_I$  on the test space parameters. The remaining derivatives are kinematical quantities. A more robust approach is to explicitly record a database and generate a material map using the components  $[\mathbf{L}^*]_{ABCD}^v$  of the macroscopic tangent  $\mathbf{L}^*$ , which may be obtained using a perturbation scheme that monitors the variation in  $\mathbf{S}^*$  for a given variation in the  $\mathbf{E}^*$  that is imposed on the RVE.

A natural restriction to the application of the generated material maps is the range of deformations over which the map is applicable. In order to render the material maps applicable when one or more eigenvalues of  $\mathbf{E}^*$  violate the limits of the database, one may employ schemes

referred to as *multi-level (ML) schemes* in the context of finite elements. Such schemes extract the macroscopic stress and the macroscopic tangent corresponding to a given  $\mathbf{F}^* = \mathbf{\Phi}$  at an integration point of a finite element mesh by conducting RVE analyses (i.e. additional finite element analyses) at this point. In order to employ this ML-scheme in an adaptive finite element analysis where the material map is employed, after each Newton iteration one flags integration points where the map limits are exceeded and computes the next Newton iteration by employing ML-schemes at these integration points (*ML-points*).

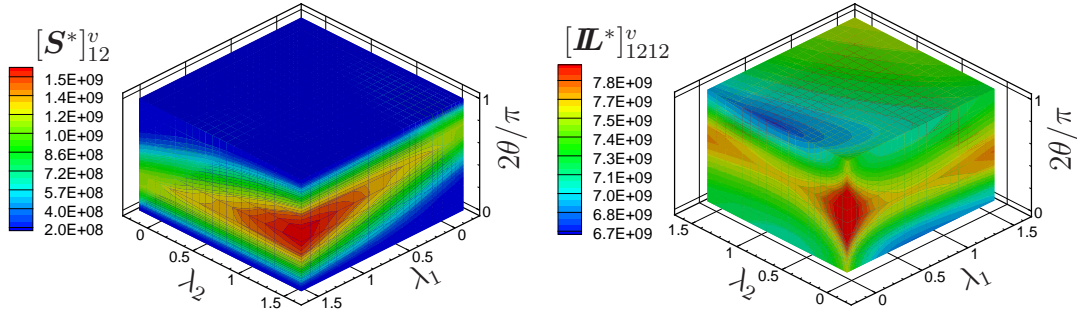


Figure 1: The material map for the stress component  $[S^*]_{12}^v$  and the tangent component  $[L^*]_{1212}^v$  of the periodic composite described.

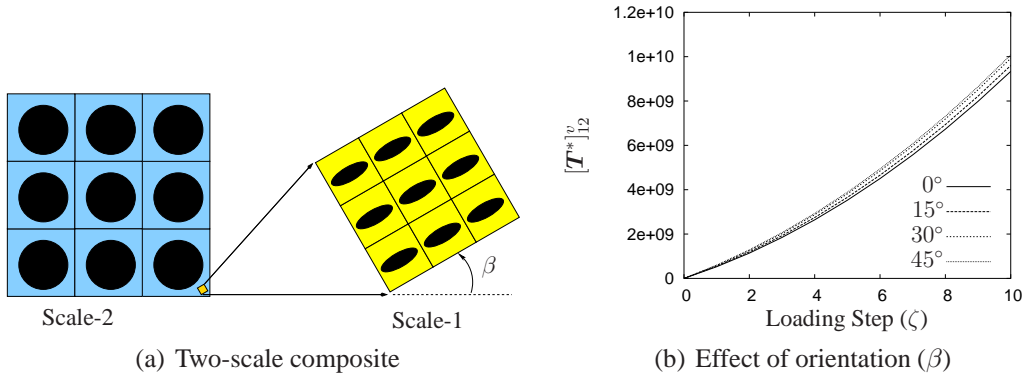


Figure 2: (a) The two-scale composite analyzed is depicted. (b) The variation of the macroscopic Cauchy stress component for the Scale-2 unit cell is shown for the case when the unit cell is subjected to PR-BCs parametrized by  $\mathbf{\Phi} = \mathbf{I} + (\zeta/50)\mathbf{1}$  and for various values of the orientation angle  $\beta$ .

$\kappa^0$ (GPa)	$\mu^0$ (GPa)	$\kappa^1$ (GPa)	$\mu^1$ (GPa)	$\kappa^2$ (GPa)	$\mu^2$ (GPa)	$v_1$ (%)	$v_2$ (%)
10	6	40	24	60	36	25	40

Table 1: Test parameters used in calculations.

## A numerical example

Consider a two-scale periodic particulate composite material, where the matrix of the composite (Scale-2) is also identified as a periodic particulate composite (Scale-1), as depicted in Figure 2(a). For experimental purposes, the strain energy functions of the constituents are chosen as a modified Kirchhoff-St. Venant type for which  $\mathcal{W} = \frac{\kappa_1}{2}(\ln J)^2 + \frac{\kappa_2}{2}(\text{tr}(\mathbf{E}))^2 + \mu \mathbf{E}' \cdot \mathbf{E}'$ . Here,  $J = \det \mathbf{F}$  and  $\kappa_1 + \kappa_2 = \kappa$ , where  $\kappa$  and  $\mu$  are the bulk and shear moduli, respectively, and  $(\cdot)'$  denotes the deviatoric part. In particular,  $\kappa_1 = \kappa_2 = \frac{\kappa}{2}$  is employed. The simulation

parameters used are given in Table 1, where 0 denotes matrix of Scale-1, 1 denotes the particles of Scale-1, 2 denotes the particles of Scale-2 and  $v_i$  denotes the volume fraction of the particles for the corresponding scale. The particles of Scale-1 are elliptical with an aspect ratio of 2, and those of Scale-2 are circular.

The material map characterizing the macroscopic  $[\mathbf{S}^*]_{12}^v$  and the tangent component  $[\mathbf{L}^*]_{1212}^v$  stress component of the Scale-1 composite is shown in Figure 1. The computed material map is subsequently used in the analysis of the Scale-2 composite in order to observe its macroscopic behavior. The dependence of the  $[\mathbf{T}^*]_{12}^v$  component of the macroscopic Cauchy stress at Scale-2 is plotted for increasing deformation in Figure 2, where the dependence of this stress on the orientation ( $\beta$ ) of the Scale-1 composite is also shown.

In order to demonstrate the mentioned adaptive procedure, the two-scale composite example is used with the orientation angle set to  $\beta = 0^\circ$ . The macroscopic deformation imposed on the unit cell of the Scale-2 composite is parameterized by  $\Phi = \mathbf{I} + \xi \mathbf{1}$ . At the solution state, the mesh elements of the unit cell that contain ML-points are shown in Figure 3(a). Comparing this figure with Figure 3(b) where the distribution of the deformation magnitude  $\|\mathbf{F}\|$  throughout the unit cell is shown, it is clearly seen that the adaptation points correspond to regions of high deformation where the map limits are exceeded.

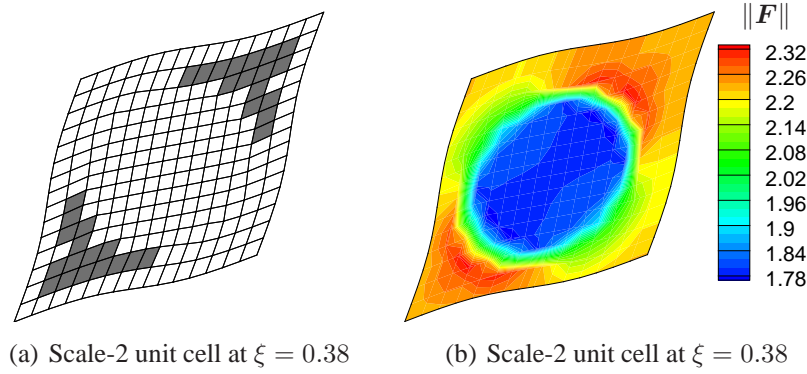


Figure 3: (a) Mesh elements of the unit cell that contain ML-points. (b) The deformation gradient magnitude ( $\|\mathbf{F}\|$ ) distribution in the Scale-2 composite for  $\xi = 0.38$ .

## REFERENCES

- [1] N. Takano and M. Zako and Y. Ohnishi, Macro-micro uncoupled homogenization procedure for microscopic nonlinear behavior analysis of composites, Materials Science Research International 2(2) p.81-86, 1996.
- [2] İ. Temizer and T. I. Zohdi, A Numerical Method for Homogenization in Non-Linear Elasticity, Computational Mechanics, 2006. (available on the journal website)
- [3] I.-S. Liu, Continuum Mechanics, Springer Berlin Heidelberg, 2002.

# **SIMULATION OF TEMPERATURE AND STRESS INDUCED PHASE TRANSFORMATION OF SHAPE MEMORY ALLOYS USING CELLULAR AUTOMATON AND THE FINITE ELEMENT METHOD**

**Andy Ungethüm<sup>1</sup> and Rolf Lammering<sup>2</sup>**

Helmut-Schmidt-University/University of the Federal Armed Forces Hamburg  
Holstenhofweg 85, D-22043 Hamburg

<sup>1</sup>e-mail: andyunge@hsu-hh.de <sup>2</sup>e-mail: rl@hsu-hh.de

**Abstract.** *In this work a combined model based on a cellular automaton and the finite element method is presented which describes the Austenite-Martensite phase transformation of superelastic shape memory alloys.*

## **Introduction**

Shape memory alloys show a very complex coupled thermo-mechanical material behaviour. From the literature various models are known which describe the material behaviour in a phenomenological, thermodynamical or micromechanical way. In this work a new approach will be presented using a combination of the theory of cellular automata and the finite element method to describe the phase transformation. In computer simulations the parallelised calculation of the phase transformation reduces the calculation time efficiently.

## **Shape Memory Alloys**

Shape memory alloys (SMA) are materials capable of very large recoverable inelastic strain (of the order of 10%). For this property they have been extensively investigated over the past three decades as potential control materials. The source of the distinctive mechanical behaviour of these materials is a crystalline phase transformation between a high symmetry, highly ordered parent phase (austenite), and a low symmetry, less ordered product phase (martensite). Martensitic structure is obtained from austenite with application of mechanical load or decrease in temperature. Upon heating or reduction of stress, the austenitic structure is recovered. This is the cause of the two most significant phenomena that characterise the mechanical behaviour of SMAs: the pseudoelastic response and the shape memory effect (SME). For further information see [1].

## **Cellular Automaton**

Cellular automata (CA) serve for the modelling of spatially discrete dynamic systems, whereby the development of individual cells at the time  $t_{n+1}$  depends primarily on the cell conditions of a given neighbourhood and from the own condition at the time  $t_n$ . A CA is characterised by the following parameters (see [2]): the cellular space, a defined neighbourhood, a condition quantity, and the condition transition function. The CA may be one- or two-dimensional, or even higher in its dimensions. The way of operation of a CA is defined in such a way that a mapping from the cell area into the condition quantity is obtained, i.e. one assigns

a condition to each cell of the automaton. The transition of a cell at time  $t_n$  from a condition (local configuration)  $z_n$  into the subsequent condition  $z_{n+1}$  at time  $t_{n+1}$  is defined by condition transition functions  $f$ , which can be deterministic or stochastic. The basic formulation of the local rule is as follows:

$$z_{n+1}(i, j) = f(N(z_n(i, j))) \quad (1)$$

where  $i, j$  are the coordinates of the cell,  $z$  is the condition and  $N$  defines the neighbourhood, cf. [3]. The condition transitions take place for all cells according to the same transfer function and at the same time.

### Algorithmic Implementation

Within the developed programme a CA is directly coupled with the Finite Element (FE) - programme. The FE - programme computes the temperature and stress fields, while the CA analyses the state of the cells and a possible phase transformation.

#### Structure of the CA

In the subsequent investigations, the cellular area consists of a two-dimensional lattice, which covers the specimen under consideration. The area is composed of squares equal in size. The cells have the same shape as the rectangle thermal and stress elements which are used by the FE - programme. For the computations periodic boundary conditions are assumed. All phases of a SMA can be illustrated by a binary condition quantity. The condition 1 indicates austenite and the condition 0 martensite.

#### Condition Transition Function

The condition transition function (or local rule) determines the behaviour of the CA and its proper definition is essential for the quality of the model. Here the temperature hysteresis (see figure 1a) and the growth of the martensitic needles have to be modelled.

A probability function is chosen as the local rule taking into account that the temperature induced transformation takes place within a certain range.



Figure 1: a) Temperature hysteresis b) Condition transition functions.

The probability functions result in a basis formulation of the local rule (see figure 1b) for the austenitic transformation

$$P(X = x_n) = (1 - e^{-\frac{\phi \Delta t}{\rho c_p}}) \frac{1}{1 + e^{-(x_n - A_0)}} \quad (2)$$

and the martensitic transformation

$$P(Y = y_n) = (1 - e^{-\frac{\phi \Delta t}{\rho c_p}}) \frac{1}{1 + e^{(y_n - M_0)}} \quad (3)$$

where  $x_n$  and  $y_n$  are the values of the probability variables,  $\phi$  is the density of the heat source,  $\Delta t$  the time increment,  $\rho$  the density,  $c_p$  the specific heat capacity and  $A_0$  and  $M_0$  are the mean transformation temperatures.

With these probabilities the latent heat due to phase transformation can be represented. In order to simulate the growing of martensitic plates, the cell environment must be merged into the local rule. The simulation starts from a single crystal SMA under mechanical and thermal load, e.g. in the austenitic state. The first martensitic needles grow unhindered into the austenitic region. The changed stress state of the crystal lattice affects the growth of following structures. In order to take the influence of neighbouring structures on the lattice cells into consideration, the state of the cell environment has to be included into the formulation of the local rule, too. As a result of the organisation of the cell environment also the preferential diagonal growth direction arises which is also experimentally observed.

### Programme Sequence

The underlying problem is solved numerically by coupling of FE - programme and CA. The FE - programme computes the stress and temperature fields due to the mechanical and thermal load vectors. The nodal stresses and temperatures are interpolated by averaging in order to obtain the stress and temperature in the centre of the rectangular element. The stresses and temperatures are stored in their fields according to their positions in the FE - grid. Using the equation for Gibbs free enthalpy the transformation temperature  $T = T_0 + (\tau \epsilon V) / \Delta s$  is calculated according to the stress field, where  $T_0$  is the mean transformation temperature,  $\tau$  the shear stress,  $\epsilon$  the strain,  $V$  the volume and  $\Delta s$  the change of entropy.

The local rule computes the transformation probabilities of each individual cell  $Z(i, j)$  due to the temperature  $T_n(i, j)$  and the cell environment in the cellular area, cf. equation (2) and (3). Afterwards this is compared to the corresponding probability  $P_{max}(i, j)$  which is the maximum probability that has been reached as yet. Transformation takes place if  $P(i, j) > P_{max}(i, j)$ . If the local rule entails a phase transformation, the cell state  $z_{n+1}(i, j)$  changes.

If a cell converts the Young's modulus changes and an amount of energy  $du$  is released at martensitic transformation due to its exothermal nature. In case of a transformation from martensite to austenite the energy  $du$  is absorbed. This energy and the changed Young's modulus are taken into account in the FE - analysis. Therefore corresponding thermal loads are added to the external thermal load vector. The phase transition of a cell thus directly influences the data basis of the FE - programme and causes thereby a change in the mechanical properties and the temperature distribution for the next time step, therefore also in the temperature field.

### Results of Simulation

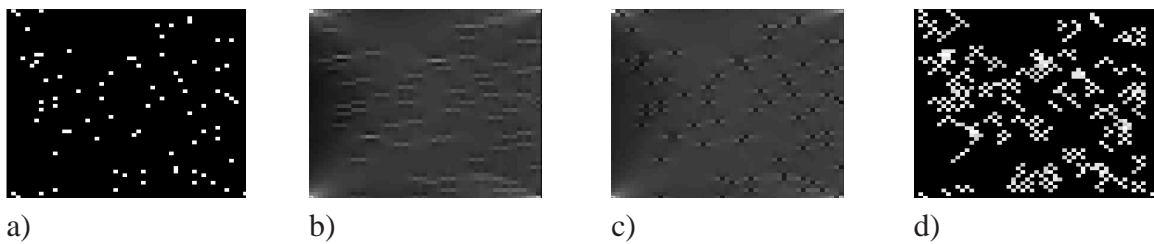


Figure 2: a) Starting configuration b) Stress field c) Transformation temperature d) Austenite-martensite-field after first time step.

During heating the phase transformation from martensite to austenite takes place and finally leads to the result shown in figure 3a after reaching the destination temperature in accordance with the local rule.

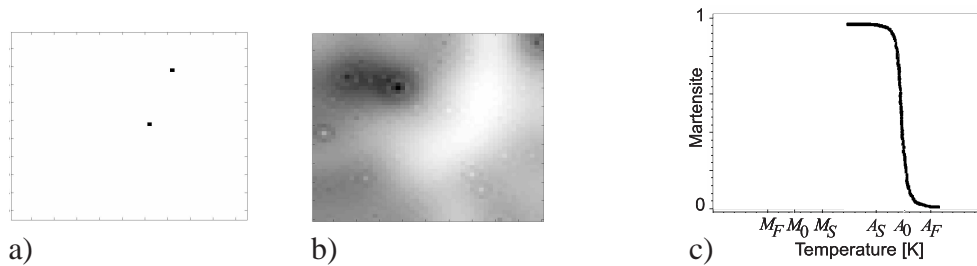


Figure 3: a) Martensite-austenite-distribution after first heating period b) Corresponding temperature-field c) Martensite fraction during heating.

The martensite is nearly completely converted, recognisably are only two isolated martensite cells. This behaviour can be observed also in experiments. The temperature distribution represented in figure 3b shows how the transformation of a cell affects its environment. In the upper left corner of the picture two cells are visible which have been converted in the last time steps. They extract energy from their adjoining cells during the transformation, shown in the undercooling of the environment. In figure 3c the temperature curve of the austenitic transformation shown in figure 1a is presented. The temperature is averaged over the whole field. Moreover the temperature curve is in accordance with the characteristic temperatures of the material. They are determined by the parameters in the probability processes. The programme shows the same behaviour in case of repeated heating. Generally, it can be stated that the methodology described above is able to capture the material behaviour. Further work will be concerned with the refinement of the model and adjustment.

## REFERENCES

- [1] L. C. Brinson and M. S. Huang, Simplification and Comparison of Shape Memory Alloy Constitutive Models, *Journal of Intelligent Material Systems and Structures* **7**, 108–114 (1996).
- [2] K. Cattell, Shujian Zhang, M. Serra and J. C. Muzio, 2-by-n hybrid cellular automata with regular configuration: theory and application, *IEEE Transactions on Computers* , 285–295 (1999).
- [3] R. Alonso-Sanz, Reversible cellular automata with memory: two-dimensional patterns from a single site seed, *Physica D* , 1–30 (2003).

## A THEORY FOR KIRKENDALL VOID GROWTH IN MEMS

Kerstin Weinberg\*

\*Dr. Kerstin Weinberg, Technische Universität Berlin, Institut für Mechanik, Einsteinufer 5, 10587 Berlin,  
Germany address  
e-mail: kerstin.weinberg@tu-berlin.de

**Abstract.** *Microelectronic systems consist of the functional chip unit itself and its packaging, which includes several electro-mechanical connections, e.g., solder joints between different metal layers. Experimental evidence shows that aging of the solder alloy as well as the formation and growth of so-called Kirkendall voids significantly contributes to the degradation of joint strength and drop impact reliability.*

*In this contribution we model a typical visco-plastic solder material with a certain porosity. The proposed mesoscopic theory links the mechanisms of diffusion and deformation induced growth of voids to parameters which describe the macroscopic material response. Numerical simulations on the material point level provide inside into the (not yet completely understood) mechanisms of failure by formation and growth of Kirkendall voids.*

### Voids in Solder Joints

The functional unit of Micro-Electro-Mechanical-Systems (MEMS) is typically a Si-chip, however, different metallic joints are required to provide electrical and mechanical connections. The principle is illustrated in Figure 1 where Pb-Sn solder joints as well as small lead-free joints (which are typically made of Cu-Sn alloys) hold the multi-layered unit in position. The life expectation of these joints determines the reliability of the MEMS. In addition to the challenges posed by the replacement of lead in solder joints the miniaturisation of microelectronic components is changing the failure mode of interest from conventional thermal cycling induced fatigue to drop impact induced (dynamic) solder joint fracture.

The formation and growth of so-called Kirkendall voids significantly contributes to the failure of joints. Typically, the Si-chips are fixed at the copper substrate by means of solder materials (e.g., Sn-Ag-Cu) in which Intermetallic Compounds (e.g.,  $\text{Cu}_3\text{Sn}$  or  $\text{Cu}_6\text{Sn}_5$ ) are formed near the solder-substrate interface, cf. Figure 1. The Kirkendall voids appear between the Cu substrate and the thin  $\text{Cu}_3\text{Sn}$  layer due to the migration of Cu atoms from  $\text{Cu}_3\text{Sn}$  into  $\text{Cu}_6\text{Sn}_5$ , which is much faster than the Sn-diffusion from  $\text{Cu}_6\text{Sn}_5$  towards  $\text{Cu}_3\text{Sn}$ , cf. Figure 2. This unbalanced Cu-Sn interdiffusion generates atomic vacancies at the lattice sites which coalesce to the KIRKENDALL voids. Plastic deformation of the solder joint as well as stress induced diffusion (and other mechanisms) assist in the process of void growth and material degradation.

For a continuum mechanical approach to such processes the question is: How can the additional information about the micro-structural development be included in a constitutive model? We suggest here the use of a general mesoscopic concept, firstly introduced by Muschik and his co-workers (see [2] and cited works) to describe a certain microstructure with continuum mechanical methods. The basic idea of this concept is the extension of the space-time domain by a

set of additional mesoscopic variables. Moreover, a mesoscopic distribution function provides a statistical addition to the classical continuum theory.

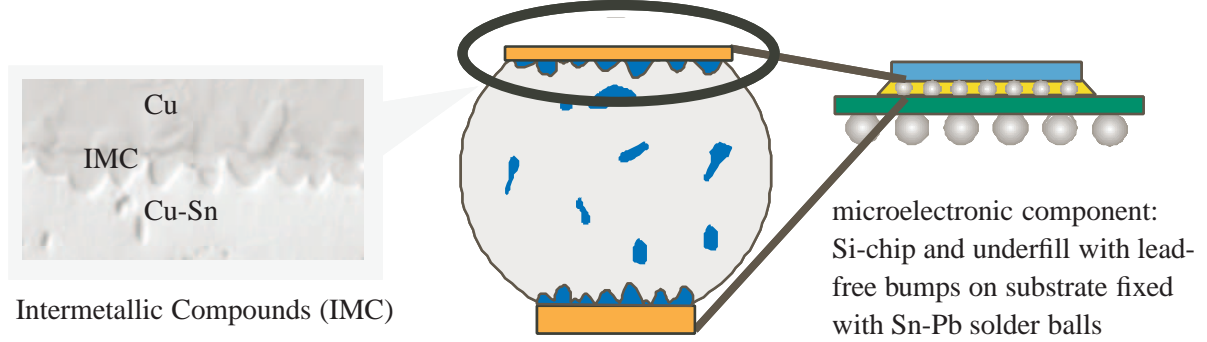


Figure 1: Intermetallic compounds at copper-solder interfaces in microelectronic components.

### A Mesoscopic Theory for Void Growth

In classical (five-field) continuum mechanics the wanted fields are the mass density  $\rho(\mathbf{x}, t)$ , the material velocity  $\mathbf{v}(\mathbf{x}, t)$  and the (mass-specific) internal energy  $u(\mathbf{x}, t)$ . These fields are defined on the space-time domain  $(\mathbf{x}, t)$  and follow universal balance equations. In order to solve the balances one must specify the material through constitutive equations, which are defined on the *state space*. The central idea of the mesoscopic concept is the extension of the space-time domain  $(\mathbf{x}, t) \in \mathbf{R}^3 \times \mathbf{R} \rightarrow (\mathbf{m}, \mathbf{x}, t) \in \mathcal{M} \times \mathbf{R}^3 \times \mathbf{R}$  to the *mesoscopic space*, where  $\mathbf{m}$  are 'suitable' variables of arbitrary tensorial order describing the microstructure and  $\mathcal{M}$  is the manifold according to  $\mathbf{m}$ , [2].

For our problem we identify the mesoscopic variables to be the radii of the (spherically assumed) voids,  $\mathbf{m} \equiv a$ , and,  $\mathcal{M} \subset \mathbf{R}$ . Moreover, we model the material as an ensemble of isotropic spherically voids plus surrounding matrix with a certain given initial void volume fraction and an initial distribution, cf. [4] for more details. Consider now *one* spherical shell and let it expand for some reason. Presuming an incompressible deformation it holds for all  $r \in [a, b]$ :

$$\frac{d}{dt} \frac{4\pi}{3} (r^3 - a^3) = 0, \quad b = (b_0^3 - a_0^3 + a^3)^{1/3}, \quad v_r \stackrel{(\text{def})}{=} \frac{dr}{dt} = \frac{a^2}{r^2} \dot{a}, \quad \dot{\varepsilon} \stackrel{(\text{def})}{=} \frac{\partial \dot{r}}{\partial r} = \frac{2a^2}{r^3} \dot{a}, \quad (1)$$

where an index 0 refers to the initial state and  $\dot{a}$  denotes *velocity of void expansion*.

Then, a (normalized) mesoscopic distribution function  $\tilde{d} \equiv d(a, \mathbf{x}, t)$  can be found representing the number of the voids  $\tilde{N}_V$  with radius  $a$  relatively to the total number of voids  $N_V$  at position  $\mathbf{x}$  and time  $t$  (to omit the arguments a tilde in the variables refers to the mesoscopic space):

$$\tilde{d} \stackrel{(\text{def})}{=} \frac{\tilde{N}_V}{N_V} \quad \text{and} \quad N_V = \int_{a_0}^{a_{\max}} \tilde{N}_V da \quad . \quad (2)$$

With this additional information a reformulation of the balances is necessary, in which occur now derivatives and fluxes due to  $\mathbf{m}$  and  $\mathcal{M}$ , respectively, for a detailed derivation see [3]. In particular, the (local) mass balance and the balance of the distribution function read:

$$\frac{\partial \tilde{\rho}}{\partial t} + \nabla \cdot (\tilde{\rho} \mathbf{v}) + \frac{\partial}{\partial a} (\tilde{\rho} \dot{a}) = 0 \quad \text{and} \quad \frac{\partial \tilde{d}}{\partial t} + \nabla \cdot (\tilde{d} \mathbf{v}) + \frac{\partial}{\partial a} (\tilde{d} \dot{a}) = 0, \quad (3)$$

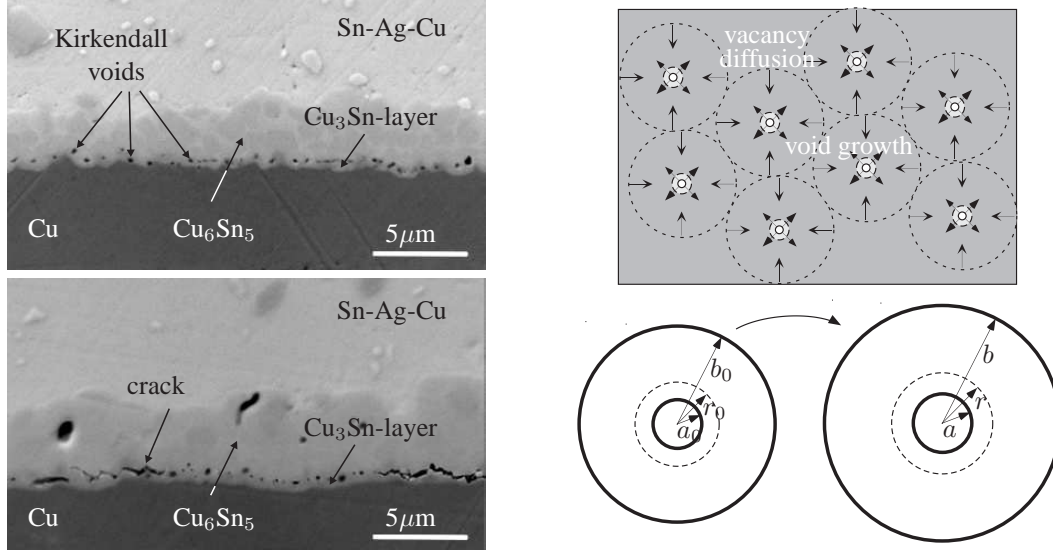


Figure 2: Kirkendall voids between Cu-Ag-Sn solder and Cu substrate, [6], model of vacancy diffusion and spherical shell model of a single void before and after the deformation.

where we presume a solid state of the material,  $\mathbf{v} = \tilde{\mathbf{v}}$ , and no void production,  $\dot{N}_V = 0$ . Eq. (3)<sub>2</sub> determines the temporal development of arbitrary distributed voids in a material. For its (numerical) solution a material law for  $\dot{a} \equiv \dot{a}(a, \mathbf{x}, t)$  is required.

To this end let us consider a small void surrounded by a vacancy concentration  $c_\infty$  generated, e.g., by plastic deformation. Let us assume a steady state vacancy concentration profile and a spherical symmetry of the problem, cf. Figure 2. Then, the diffusion equation reduces to:

$$\frac{\partial}{\partial r} \left( r^2 \frac{\partial c}{\partial r} \right) = 0 \quad \text{with} \quad c(r = \infty) = c_\infty \quad \text{and} \quad c(r = a) = c_a = c_0 e^{d/a}, \quad (4)$$

where  $d = \frac{2\gamma V_V}{kT}$  and  $c_0 = e^{-E_v/kT}$  is the equilibrium vacancy concentration near a free surface;  $\gamma$  is the surface energy,  $V_V$  the atomic volume,  $k$  the Boltzmann constant and  $E_v$  is the free-energy change per vacancy added into the system. The solution of Eq. 4 yields a relation for the rate of growth of the voids due to vacancy flux, cf. [1], with the result

$$\dot{a} = \frac{D}{a} (c_\infty - c_0 e^{d/a}), \quad (5)$$

where  $D$  is the diffusion coefficient. Let us now ask, which energy contributions are necessary to deform *one* void with surrounding spherical shell. In case of dynamic loading these are: **(a)** the energy of irreversible deformation  $\tilde{W}(\sigma_e, \varepsilon)$ , **(b)** the kinetic energy  $\tilde{K}(v_r)$  and **(c)** surface energy  $\tilde{S}(a)$ . Setting the external power equal the “sum of the internal powers”,  $\tilde{P} = d(\tilde{W} + \tilde{S} + \tilde{K})/dt$  and adding a diffusion rate potential obtained from Eq. 5 yields an ODE for the void expansion velocity,  $\dot{a}(a, \mathbf{x}, t)$ , which can be solved (numerically) for *all* different void sizes.

$$0 = -pa^2\dot{a} + \frac{2}{3}\sigma_e a^2\dot{a} \log\left(\frac{b^3}{a^3}\right) + 2a\gamma\dot{a} + \frac{E_v\dot{a}^2}{D} - \frac{E_v\dot{a}}{a}(c_\infty - c_a) + \frac{\rho_0}{2} \left[ 2\ddot{a}a^3 + 3\dot{a}^3a^2 - \frac{a^3}{b(a)} \left( 2\ddot{a}a + 4\dot{a}^3 - \frac{a^3\dot{a}^3}{b^3(a)} \right) \right] \quad (6)$$

### Evolution of Void Distribution

In order to investigate dynamic void expansion we apply to the material element a rapid pressure impulse which is typical for a drop impact test,  $p(t)$ , Figure 3 (left). In the centered plot of

Figure 3 two different voids with the initial radii of  $a_0 = 0.1 \mu\text{m}$ ,  $1 \mu\text{m}$  and the initial void volume fraction  $f_{v0} = a_0^3/b_0^3 = 10^{-4}$  were considered. Obviously the void growth continues after  $p(t)$  finished. This fact is caused by inertia effects due to the kinetic energy  $\tilde{K}$ . Furthermore, smaller voids grow faster than bigger voids, they can even “overtake” the bigger voids.

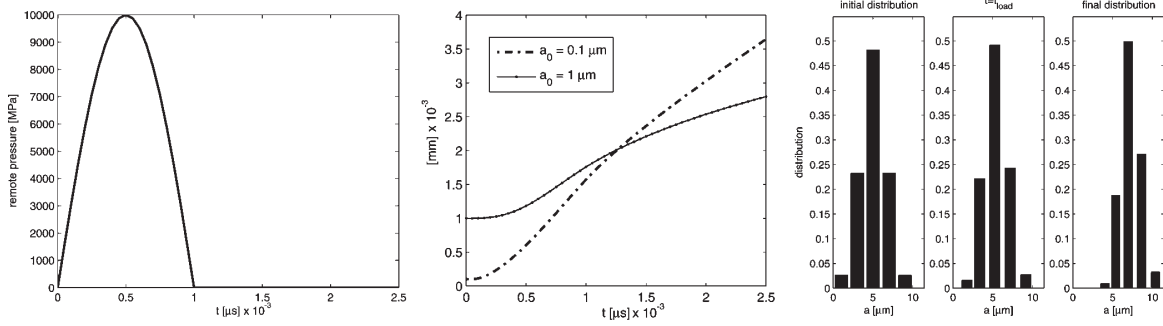


Figure 3: The remotely applied pressure impulse, the subsequent expansion of two different voids and the temporal evolution of five different void radii in the dynamic loading regime.

The temporal development of a discrete (Gaussian) void distribution function with five different initial void radii is also displayed in Figure 3 (right). Due to the fact that smaller voids grow faster than bigger voids the initial symmetric distribution change to an asymmetrical distribution in such a manner that the fraction of smaller voids decrease. Such results can be also found in so-called LSW-theories (Ostwald ripening), although the driving forces are different.

Note that, following the strategy of [5], the model which is here studied on the material point level, can be employed in a finite-element code to study the structural response of solder joints in general loading conditions.

## REFERENCES

- [1] A. Cuitino and M. Ortiz. Ductile fracture by vacancy condensation in fcc single crystals. *Acta Metallurgica*, 44:427–436, 1995.
- [2] W. Muschik, C. Papenfuss, and H. Ehrentraut. A sketch of continuum thermodynamics. *Journal of Non-Newtonian Fluid Mechanics*, 96:255–290, 2001.
- [3] K. Weinberg and T. Böhme. Mesoscopic Modeling for Continua with Pores: Biological Soft Tissue. *to appear in: Non-Equilibrium Thermodynamics*, 2006.
- [4] K. Weinberg and T. Böhme. Mesoscopic Modeling for Continua with Pores: Dynamic Void Growth in Visco-Plastic Metals. *to appear in: Non-Equilibrium Thermodynamics*, 2006.
- [5] K. Weinberg, A. Mota, and M. Ortiz. A Variational Constitutive Model for Porous Metal Plasticity. *Computational Mechanics*, 37(2):142 – 152, 2006.
- [6] Luhua Xu and John H.L. Pang. Interfacial IMC and Kirkendall void on SAC solder joints subject to thermal cycling. *Proceedings of the 7th Electronics Packaging Technology Conference*, 2, 2005.

# HOMOGENIZATION OF GRANULAR MATERIALS MODELED THROUGH A THREE-DIMENSIONAL DISCRETE ELEMENT MODEL

Christian Wellmann<sup>1</sup>, Peter Wriggers<sup>2</sup>

Institute of Mechanics and Computational Mechanics  
Leibniz University Hannover

Appelstr. 9a, 30167 Hannover, Germany

<sup>1</sup>e-mail: wellmann@ibnm.uni-hannover.de

<sup>2</sup>e-mail: wriggers@ibnm.uni-hannover.de

**Abstract.** *A homogenization strategy for granular materials is introduced and applied to a three-dimensional Discrete Element Model (DEM), in which the particles are represented by superellipsoids. Macroscopic quantities are derived from the microscopic quantities resulting from a DEM simulation by averaging over representative volume elements (RVEs). The implementation of a RVE is described regarding the definition and discretization of the RVE boundary. The homogenization strategy is validated by means of DEM simulations of a compression and shear test of a cohesionless granular assembly. Finally an elasto-plastic material is fit to the resulting stress-strain curves.*

## Introduction

Since the pioneering work of [1] Discrete Element Models (DEMs) have become the leading computational method for analyzation of complex phenomena exhibited by granular materials. Most of todays three-dimensional DEM codes use spherical particles due to the minimum computational effort for contact detection. However, it is well known that geometries of real soil particles are not well described by spheres. A comparison of spherical and ellipsoidal particles in [2] showed that the main problem with spherical particles is their small resistance against rolling and their lacking ability to show particle interlocking. To overcome this problem superellipsoid particles are used here, compare [3]. The individual particles are considered as rigid bodies which interact in terms of contact forces. A penalty-type contact formulation is used that allows a small overlap of two particles, whereas the elastic repulsive force is proportional to the overlapping distance. The normal and tangential components of the contact force are coupled by COULOMB'S friction law. Cohesion forces acting between the particles are neglected in this contribution. The homogenization strategy is described in the next section, followed by a discussion of the RVE implementation. Finally results of the numerical tests are presented and the fitting procedure is depicted.

## Homogenization

The information obtained from the DEM simulation, i.e. the contact forces and the particle motions, is transferred to a continuum mechanical description in terms of stresses and strains by a homogenization approach, which was applied to a two-dimensional DEM in [4]. The initial point of this approach is the introduction of representative volume elements (RVEs), that serve as averaging volumes for the macroscopic quantities. Hence three systems are considered which

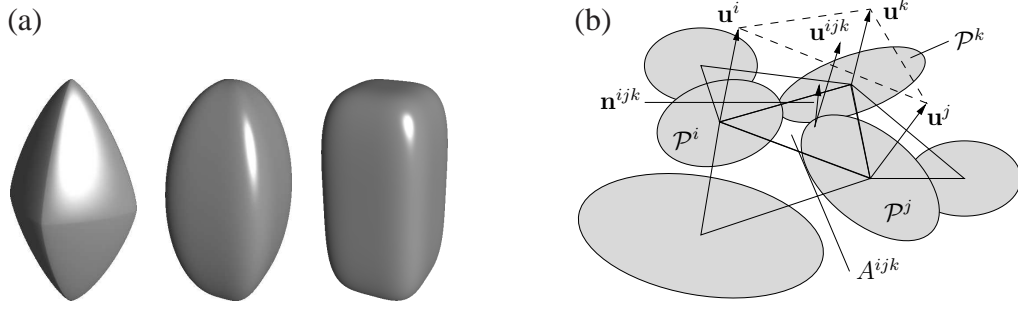


Figure 1: (a) Superellipsoids. (b) Part of triangular mesh for strain calculation.

are defined on different length-scales: First, on the macroscale, the body  $\mathcal{B}$  consisting of a huge number of particles and with a characteristic length  $D$ , second, on the mesoscale, the RVE  $\mathcal{R}$  with a characteristic length  $d$  and third, on the microscale, a single particle  $\mathcal{P}^i$  with a diameter  $\delta$ . The key assumption for the derivation of volumetric averages of the macroscopic quantities is that the scale separation  $D \gg d \gg \delta$  is satisfied. Applying this to the balance of momentum of a RVE  $\mathcal{R}$  inside  $\mathcal{B}$ , the volumetric contributions are neglected with respect to the surface contributions yielding the static equilibrium condition for  $\mathcal{R}$ . From this the expression for the RVE average of the stress tensor is derived

$$\langle \sigma \rangle = \frac{1}{V_{\mathcal{R}}} \sum_{i=1}^{N_{\partial\mathcal{R}}} \mathbf{f}^i \otimes \mathbf{x}_M^i. \quad (1)$$

$V_{\mathcal{R}}$  denotes the volume of  $\mathcal{R}$ ,  $N_{\partial\mathcal{R}}$  is the number of boundary particles of  $\mathcal{R}$ , i.e. the number of particles that are in contact with particles not belonging to  $\mathcal{R}$ ,  $\mathbf{f}^i$  is the resultant of the outward contact forces acting on  $\mathcal{P}^i$  and  $\mathbf{x}_M^i$  is the center position of  $\mathcal{P}^i$ . Considering static equilibrium and a small particle size compared to the RVE size ( $\delta/d \rightarrow 0$ ) this expression is symmetric, compare [5]. The same approach is applied to the RVE average of the linear strain tensor. In contrast to the stress calculation, where a discretization of the boundary  $\partial\mathcal{R}$  is given naturally in terms of contact forces, it has to be determined explicitly here. Therefor a triangular mesh is generated with the boundary particle centers serving as vertices yielding the expression for the RVE average of the linear strain tensor

$$\langle \epsilon \rangle = \frac{1}{2V_{\mathcal{R}}} \sum_{ijk \in I_{\mathcal{T}}} (\mathbf{u}^{ijk} \otimes \mathbf{n}^{ijk} + \mathbf{n}^{ijk} \otimes \mathbf{u}^{ijk}) A^{ijk}. \quad (2)$$

Herein  $\mathbf{u}^{ijk}$  is the center displacement,  $\mathbf{n}^{ijk}$  is the outward-oriented unit normal and  $A^{ijk}$  is the area of the triangle  $\mathcal{T}^{ijk}$ . The center displacement is calculated from the vertex displacements assuming a linear displacement field. Since small displacements are assumed, the discretization is only determined once at the beginning of the DEM simulation.

## Implementation

For the discretization of the boundary convex shaped RVEs are advantageous. An approximately spherical shaped RVE is generated by choosing a basis point  $\mathbf{x}_{\mathcal{R}}$  inside  $\mathcal{B}$  and a radius  $r_{\mathcal{R}}$  and selecting all particles  $\mathcal{P}^i$  with  $\|\mathbf{x}_{\mathcal{R}} - \mathbf{x}_M^i\| < r_{\mathcal{R}}$ . The crucial point for the determination of a boundary discretization is which particles should be considered as boundary particles for strain calculation. Using the same particles as for stress calculation leads to the problem that there are several possible triangular meshes that use their centers as vertices. Furthermore the discretization is only determined once at the beginning of the DEM simulation, while the set

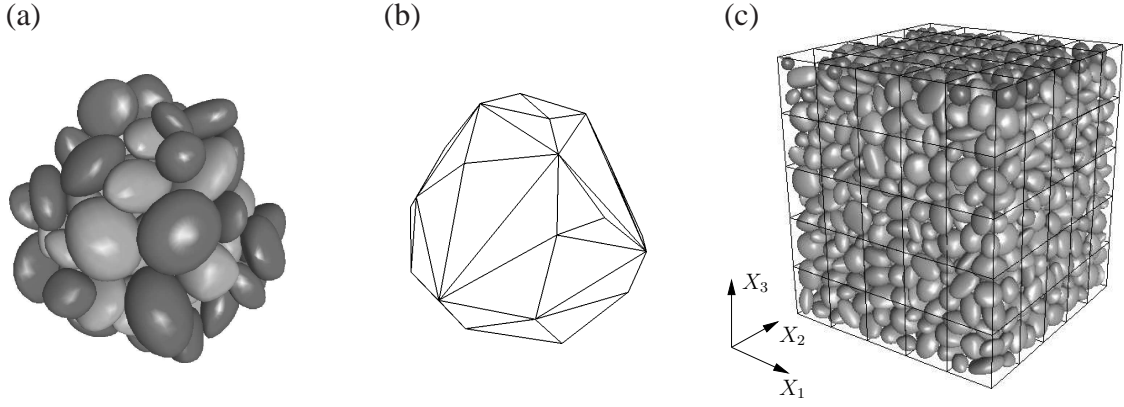


Figure 2: (a) RVE consisting of 76 particles. The centers of the darker particles specify the convex hull depicted in (b). (c) Model used for numerical tests. The lighter particles are randomly generated superellipsoids. The darker particles are spheres that were added in order to raise the number of particle-boundary contacts at the top side of the box.

of particles that are in contact with particles outside the RVE changes in the course of the simulation. Hence, another well-defined set of particles is chosen, namely those particles whose centers specify the convex hull of all centers in the RVE. These are determined by a DELAUNAY triangulation which yields the triangular mesh and the enclosed volume right away. Since different boundary definitions are used for stress and strain calculation the averaging volumes  $V_{\mathcal{R}}$  differ too. To estimate the volume for stress calculation from the known volume enclosed by the triangular mesh a strategy is used that utilizes the approximately spherical shape of a RVE.

### Validation of the homogenization strategy

The homogenization strategy is validated by means of strain driven compression and shear tests of a cuboid sample consisting of 1609 randomly generated particles. Loads are applied incrementally in a quasi-static way. Macroscopic quantities are always recorded right before a loading step using eight RVEs with an average number of about 80 particles. Since the numeri-

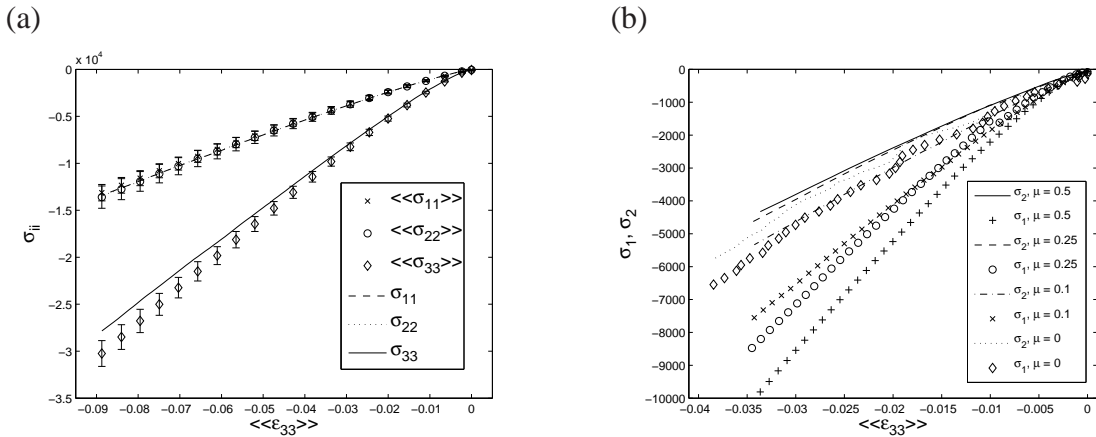


Figure 3: Compression test results. (a) Comparison of RVE average ( $\langle\langle \bullet \rangle\rangle$ ) and macroscopic normal stresses. (b) Influence of local friction coefficient  $\mu$  of DEM contact formulation on principal stresses.

cal tests performed yield homogeneous macroscopic strains, the results are evaluated by calculating average values with corresponding error bars. First, the particle sample is compressed in the vertical  $X_3$  direction. It shows a linear elastic response and there is good agreement of RVE and macroscopic quantities, whereat macroscopic stresses are obtained from particle-boundary

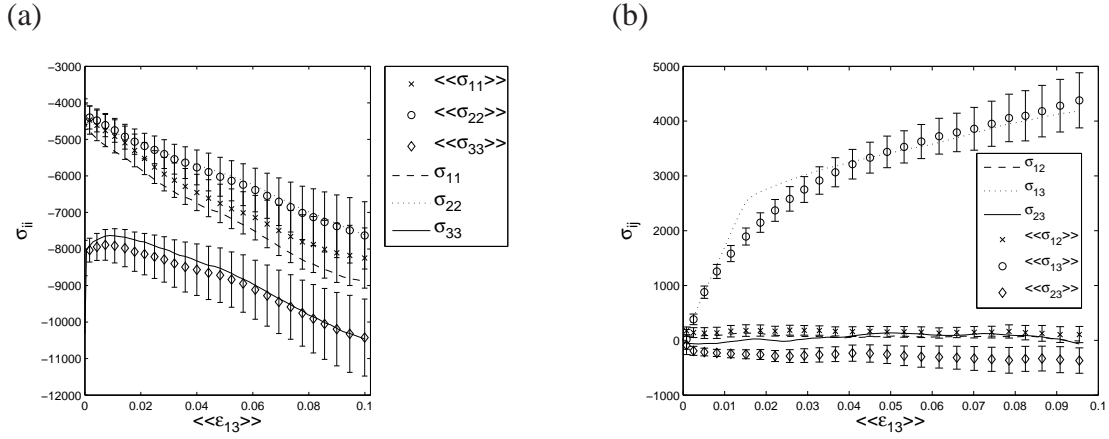


Figure 4: (a) Shear test results. Comparison of RVE average ( $\langle\langle \bullet \rangle\rangle$ ) and macroscopic normal stresses. (b) Results of fitting procedure. Comparison of RVE average shear stresses ( $\langle\langle \bullet \rangle\rangle$ ) and the shear stresses computed from the constitutive equation.

contact forces.

Next the sample gets sheared in the  $X_1, X_3$  plane. There is an approximately linear rise of normal stresses with shear strain. The main shear stress component shows a nonlinear behavior. The shear modulus decreases until a shear strain of about 4% and remains constant from there on.

### Fitting the results to a macroscopic constitutive equation

The particle sample shows a material response which can be modeled using a standard elastoplastic constitutive equation. For this purpose the DRUCKER-PRAGER soil model is applied whereas the elastic part is described by HOOKE's law. A modification has to be applied to the standard predictor-corrector scheme to account for the dilatancy effect that the particle sample exhibits under shear loading. First, the bulk and shear modulus are fit to the stress-strain curve of the compression test, where the particle sample's response is purely elastic. Subsequently, the plastic parameters are fit to the shear test results. Here the cohesion parameter of the Drucker-Prager model is set zero a priori, because no cohesion forces act between the particles in the DEM. The procedure results in reasonable values for the material parameters.

### REFERENCES

- [1] P. A. Cundall and O. D. L. Strack, A discrete numerical model for granular assemblies, *Geotechnique* **29**, (1979).
- [2] X. Lin and T.-T. Ng, A three-dimensional discrete element model using arrays of ellipsoids, *Geotechnique* **47**, (1997).
- [3] J. R. Williams and A. P. Pentland, Superquadrics and modal dynamics for discrete elements in interactive design, *Engineering computations* **9**, (1992).
- [4] G. A. D'Addetta, E. Ramm, S. Diebels and W. Ehlers, A particle center based homogenization strategy for granular assemblies, *Engineering Computations* **21**, (2004).
- [5] J. P. Bardet and I. Vardoulakis, The asymmetry of stress in granular media, *International Journal of Solids and Structures* **38**, (2001).

## NUMERISCHE UND ANALYTISCHE DREIDIMENSIONALE FUNDAMENTALLÖSUNGEN FÜR PIEZOELEKTRIKA ZUR ANWENDUNG IN DER BEM

K. Wippler, M. Kuna

Institut für Mechanik und Fluidodynamik  
Lampadiusstr. 4, 09599 Freiberg  
e-mail: karsten.wippler@imfd.tu-freiberg.de  
e-mail: meinhard.kuna@imfd.tu-freiberg.de

**Abstract.** *Die Basis jeder Randelementemethode (BEM) bilden die Fundamentallösungen (FL), die sowohl vom Werkstoff, aber auch von der Problemstellung selbst abhängen können. Lösungen für den isotrop elastischen Fall sind in geschlossener analytischer Form schon lange bekannt. Für Piezoelektrika können unter Ausnutzung transversaler Isotropieeigenschaften ebenfalls analytische Fundamentallösungen (AFL) gefunden werden. Eine Darstellung von FL für eine allgemeine Anisotropie gelingt unter Verwendung der RADON-Transformation. Ziel dieses Beitrages ist es, sowohl analytische als auch numerisch gefundene Fundamentallösungen (NFL) für Piezoelektrika aus Sicht ihrer Anwendung im konkreten BEM-Code zu beleuchten.*

### Einleitung

Betrachtet man den Aufbau moderner Maschinen und Anlagen, so fällt auf, dass zu deren Beschreibung immer weniger das Wort Mechanik, sondern eher das Wort Mechatronik treffend erscheint. Im Zuge der Ausstattung mit Regelungs- und Steuerungseinrichtungen finden hier vielfach Piezo-Aktoren und -Sensoren Anwendung. Als Piezoelektrika werden industriell Funktionskeramiken eingesetzt, die zumeist spröde sind, herstellungsbedingt häufig Mikrokdefekte enthalten und oftmals hohen elektromechanischen Beanspruchungen im Betrieb ausgesetzt sind. Aus diesen Gründen erwächst die Frage nach der Festigkeit, Zuverlässigkeit und Lebensdauer. Zur Beantwortung dieser Frage existieren numerische Werkzeuge, namentlich die Methode der finiten Elemente (FEM) und die Methode der Randelemente (BEM). Letztere soll Gegenstand dieses Beitrags sein, wobei im Besonderen auf ihre Basis – die Fundamentallösungen – eingegangen wird.

### Grundlagen Piezoelektrika

Um sowohl mechanische als auch elektrische Feldgrößen gemeinsam beschreiben zu können, wird eine verallgemeinerte Notation verwendet. Der verallgemeinerte Verschiebungsvektor  $U_K$  besteht hierbei aus den Verschiebungen  $u_k$  und dem elektrischen Potential  $\varphi$ . Dabei laufen Indizes mit Kleinbuchstaben von 1 bis 3 während Indizes mit Großbuchstaben von 1 bis 4 reichen. Den verallgemeinerten Verzerrungstensor  $S_{Kl}$  erhält man durch entsprechende Differentiation nach den drei Raumrichtungen.

$$U_K = \begin{cases} u_k & \text{für } K = 1, 2, 3 \\ \varphi & \text{für } K = 4 \end{cases} ; \quad S_{Kl} = U_{K,l} = \begin{cases} u_{k,l} & \text{für } K = 1, 2, 3 \\ \varphi_{,l} & \text{für } K = 4 \end{cases} . \quad (1)$$

Die verallgemeinerten Spannungen  $\Sigma_{iJ}$  (mechanische Spannungen  $\sigma_{ij}$ , dielektrische Verschiebung  $D_i$ ) und verallgemeinerte Verzerrungen  $S_{Kl}$  können durch die folgende Beziehung verknüpft werden.

$$\Sigma_{iJ} = \begin{cases} \sigma_{ij} & \text{für } J = 1, 2, 3 \\ D_i & \text{für } J = 4 \end{cases} = E_{iJKl} S_{Kl}; \quad E_{iJKl} = \begin{cases} C_{ijkl} & \text{für } J, K = 1, 2, 3 \\ \epsilon_{lij} & \text{für } J = 1, 2, 3; K = 4 \\ \epsilon_{ikl} & \text{für } J = 4; K = 1, 2, 3 \\ -\kappa_{il} & \text{für } J, K = 4 \end{cases} \quad (2)$$

$E_{iJKl}$  ist der verallgemeinerte Materialtensor, wobei  $C_{ijkl}$ ,  $\epsilon_{ikl}$  und  $\kappa_{il}$  die Tensoren der elastischen, piezoelektrischen und dielektrischen Konstanten sind.

## Piezoelektrische Fundamentalösungen

### Numerische Fundamentallösungen NFL

Die Verschiebungsfundamentallösungen  $U_{IJ}^*$  folgen aus der Lösung von:

$$E_{kMJl} U_{IJ,lk}^* = -\delta(p, Q) \delta_{MI}. \quad (3)$$

Hierin ist  $\delta(p, Q)$  die DIRACsche Delta-Funktion und  $\delta_{MI}$  die Einheitsmatrix. Auf eine Darstellung der Traction-Fundamentallösung soll hier verzichtet werden. Die FL stellen den Zusammenhang zwischen einer verallgemeinerten Kraft (3 Kräfte, 1 Punktladung) an einem Raumpunkt  $Q$  (Quellpunkt) und den verallgemeinerten Verschiebungen an einem anderen Raumpunkt  $p$  (Feldpunkt) dar. Für die zur FL führenden Inversen der RADON-Transformation erhält man aus Gl.(3):

$$U_{IJ}^*(\rho, \theta_1, \theta_2) = \frac{1}{8\pi\rho^2} \oint_0^{2\pi} (\mathcal{K}_{IJ}^{zz}(\phi, \theta_1, \theta_2))^{-1} d\phi. \quad (4)$$

Die Berechnung piezoelektrischer FL mit Hilfe der RADON-Transformation wurde schon 1980 von Deeg [2] in seiner Dissertation vorgeschlagen.  $\rho$  ist in Gl.(4) der Abstand zwischen Feld- und Quellpunkt. Den Integrand in Gl.(4) erhält man durch

$$\mathcal{K}_{IJ}^{zz}(\phi, \theta_1, \theta_2) = E_{kIJl} z_k(\phi, \theta_1, \theta_2) z_l(\phi, \theta_1, \theta_2) \quad (5)$$

Die Vektoren  $z_i$  stehen senkrecht auf dem Abstandsvektor zwischen Quell- und Feldpunkt. Sie werden für die Rücktransformation bezüglich des Einheitskreises, über den integriert wird, parametrisiert. In Gl.(4) ist das Linienintegral über den Umfang eines Einheitskreises der einzige numerisch zu erbringende Teil während der Berechnung der FL. Der Integrand bzw. dessen Inverse können entgegen [1] in geschlossener algebraischer Form dargestellt werden.

### Analytische Fundamentallösungen AFL

Die gesuchten FL aus Gl.(3) lassen sich für Transversalisotropie analog [3] auch aus harmonischen Potentialfunktionen geschlossen konstruieren. Hierzu werden konjugiert komplexe tangentielle Verschiebungen der Form  $u = u_x + iu_y$  und  $\bar{u} = u_x - iu_y$  eingeführt. Mit dieser, auf Fabrikant [4] zurück gehenden Notation, lässt sich die zu den FL führende POISSONSche

Differentialgleichung (3) lösen. Für die Verschiebungsfundamentallösung  $U$  ergibt sich:

$$U = -\frac{1}{8\pi C_{44}\Omega^*} \sum_{j=1}^3 \hat{M}_j^* \left[ \frac{q^2 \bar{T}}{R_j(R_j + z_j)^2} - \frac{T}{R_j} \right] + \frac{\gamma_4^*}{8\pi C_{44}} \left[ \frac{q^2 \bar{T}}{R_j(R_4 + z_4)^2} - \frac{T}{R_4} \right] \quad (6)$$

$$- \frac{1}{4\pi(e_{15}^2 + C_{44}\kappa_{11})\Omega^*} \sum_{j=1}^3 \left( \hat{N}_j^* T_z + \hat{L}_j^* Q \frac{q}{R_j(R_j + z)} \right)$$

Hierin sind  $T, \bar{T}, T_z, Q$  die Punktlasten, also Kräfte und Ladungen in komplex und konjugiert komplexer Form.  $R_j$  ist der Abstand zum Koordinatenursprung, d.h. zum Quellpunkt, es gilt  $R_j = \sqrt{x^2 + y^2 + z_j^2}$  mit  $z_j = z/\gamma_j$ . Die Eigenwerte  $\gamma_j$  wie auch die weiteren, hier nicht näher erläuterten Größen in Gl.(6), hängen nach [3] ausschließlich von den Materialtensoren  $C_{ij}, e_{kl}, \kappa_{ij}$  (VOIGT-Notation) ab.

### Vergleich und Anwendung

Bei der Umsetzung zeigt sich, dass die NFL im Rahmen der Verwendung von Computeralgebrasystemen auf direktem Weg abzuleiten und zu implementieren sind, was eine fehlerfreie Umsetzung erlaubt. Darüber hinaus ist mit diesem Zugang auch die Bestimmung von FL für vollständig anisotrope Materialien möglich. Die vorgestellten AFL sind für eine direkte Anwendung in einem universellen BEM-Code weniger gut geeignet, da sie ausschließlich für transversalisotrope Werkstoffe gelten. Für die Leistungsfähigkeit jeder Randelemente-Software ist die schnelle und genaue Ermittlung der FL ein entscheidender, kritischer Aspekt.  $10^9$  Funktionsaufrufe sind auch bei kleineren Problemen realistisch. Ursache ist das mit dem Abstand von Quell- und Feldpunkt singuläre Verhalten der FL. Eine Verwendung adaptiver Integrationsalgorithmen ist unumgänglich. Da an jedem GAUSSpunkt ein Funktionswert der entsprechenden FL zu ermitteln ist, muss eine schnelle Berechnung der Funktionswerte der FL Ziel sein. Tabelle 1 stellt den Zeitbedarf bei der Ermittlung der Funktionswerte ins Verhältnis. Dabei werden analytische FL, numerische FL als auch ihre Bestimmung aus einem Kennfeld mittels linearer oder kubischer LAGRANGEinterpolation verglichen. Dieser Kennfeldzugang ist möglich, da sich die Abstandsabhängigkeit der FL abspalten lässt. Hier zeigt sich ein großer Geschwindigkeitsvorteil zu Gunsten der Interpolation. Wird linear interpoliert, gewinnt man über 70 Prozent, eine direkte Verwendung numerisch bestimmter Fundamentallösungen schließt sich aus. Verwendet man ein Interpolationschema auf Basis der NFL, stellt sich die Frage

	analytisch	numerisch	LAGRANGE	linear
Zeit	1.0	3.42	0.76	0.27

Table 1: Relativer Rechenzeitbedarf für die Funktionswertermittlungen

nach dessen Genauigkeit. In Bild (1a) ist  $U_{xx}$  als Funktion des Abstandes zum Quellpunkt dargestellt. Bild (1b) gibt den relativen Fehler der NFL zur AFL wieder, der mit  $8 \cdot 10^{-8}$  Prozent als vernachlässigbar bezeichnet werden kann. Die Verwendung der implementierungsseitig überlegenen NFL ist also legitim.

Ausgehend von den NFL soll nun die Genauigkeit in Abhängigkeit von der Anzahl der Stützstellen und dem verwendeten Interpolationsalgorithmus untersucht werden. Bild (2a) und (2b) stellen den relativen Fehler zur AFL auf einer logarithmischen Skala dar. Es zeigt sich,

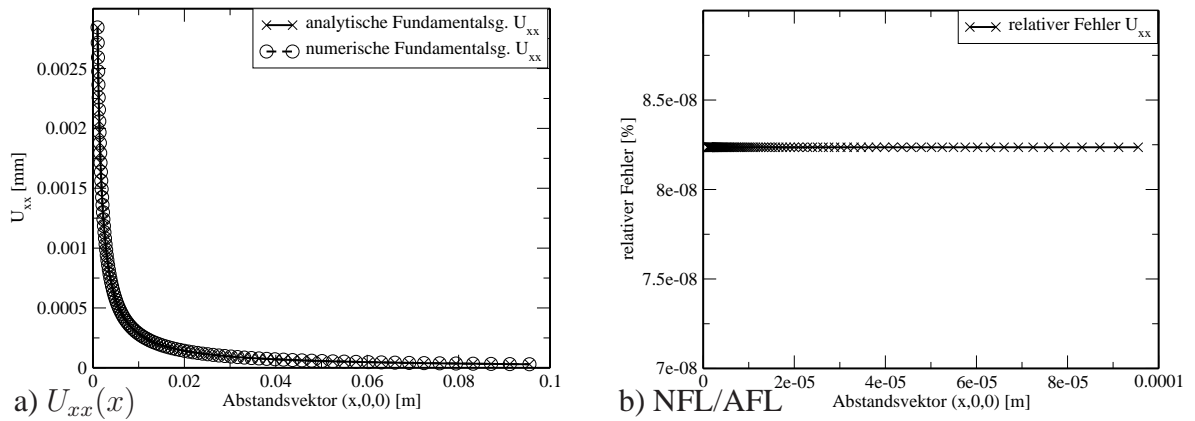


Figure 1: Analytische und numerische Fundamentallösungen im Vergleich

dass die mittels kubischer LAGRANGEinterpolation (Bild (2b)) gewonnenen Funktionswerte der FL schneller sehr hohe Genauigkeiten erreichen. Vor dem Hintergrund der deutlich höheren Ausführungsgeschwindigkeit ist aber eine lineare Interpolation (Bild (2a)) vorzuziehen, deren Genauigkeit bei 400x400 Stützstellen ausreichend ist.

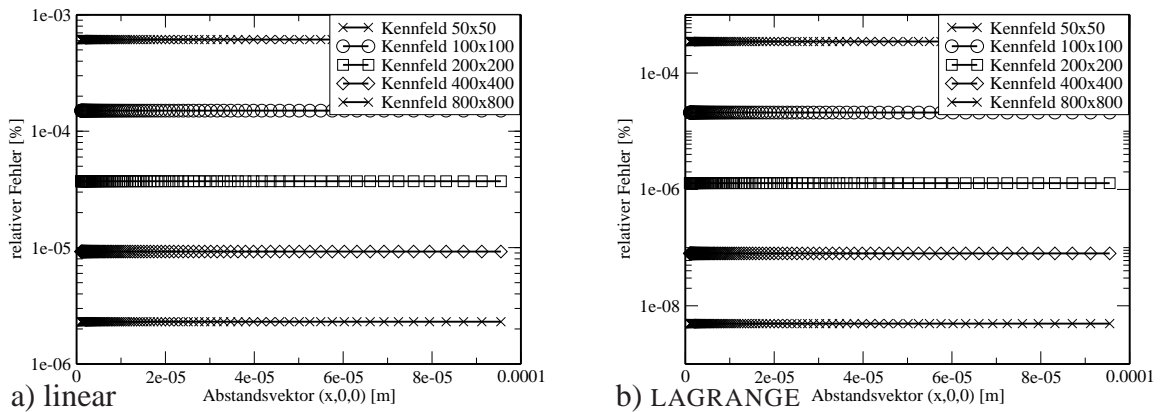


Figure 2: Funktionswert-Fehler abhängig von Kennfeldauflösung und Interpolationsalgorithmus

## Zusammenfassung

Ausgangsbasis zur Implementierung von Randelementemethoden für Piezoelektrika bilden die Fundamentallösungen (FL). Sie stellen neben genauen und robusten Integrationsalgorithmen die größte Herausforderung dar. Die FL können sowohl analytisch als auch numerisch bestimmt werden. Bei der konkreten Anwendung zeigt sich, dass zur Geschwindigkeitsoptimierung ein Interpolationsschema unumgänglich ist. Ist die Stützstellendichte hier hoch genug, so ergeben sich vernachlässigbare Genauigkeitseinbußen bei 70 Prozent Geschwindigkeitsvorteil.

## REFERENCES

- [1] E. Pan, F. Tonon, Three-dimensional Green's functions in anisotropic piezoelectric solids, *International Journal of Solids and Structures* **37**, 943–958 (2000)
- [2] W.F. Deeg, *The Analysis of Dislocation, Crack and Inclusion Problems in Piezoelectric Solids*, Stanford University 1980
- [3] E. Karapetian, I. Sevostianov, M. Kachanov, Point force and point electric charge in infinite and semi-infinite transversely isotropic piezoelectric solids, *Philosophical magazine B* **80**, 331–359 (2000).
- [4] V.I. Fabrikant, *Applications of potential theory in mechanics. Selection of new results*, Kluwer (1989)

## FERROELECTRIC AND FERROELASTIC PROPERTIES OF PIEZOCERAMICS: AN EXPERIMENTAL INVESTIGATION

Dayu Zhou, Marc Kamlah, Zhenggui Wang, Bernd Laskewitz, and Yixiang Gan

Forschungszentrum Karlsruhe, Institut fuer Materialforschung II, Hermann-von-Helmholtz-Platz 1, D-76344  
Eggenstein-Leopoldshafen, Germany  
e-mail: dayu.zhou@imf.fzk.de

**Abstract.** *Piezoceramics are presently being used increasingly as sensors and actuators in a wide variety of electromechanical applications, for instance, piezoelectric fuel injectors in common rail diesel and gasoline engines. In the attempt to improve the performance and especially, the reliability of the components, considerable efforts have been made in the development of predictive constitutive models for the coupled and non-linear electromechanical behavior of piezoceramics. The success of such constitutive models depends strongly on the availability of suitable measurements. Supported by DFG, fruitful experimental work has been carried out for a commercial soft PZT polycrystalline material (PIC151, PI Ceramic) under co-axial, coupled electromechanical loading at room temperature.*

### Mechanical preload dependence of dielectric and piezoelectric performance

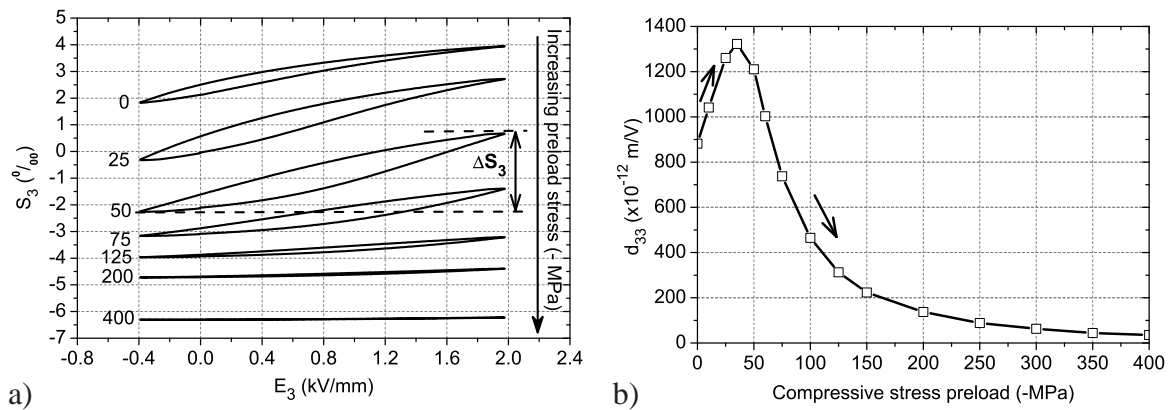


Figure 1: a) Uni-polar high electric field induced strains measured under different compressive stress preloads; b) Piezoelectric coefficient  $d_{33}$  as a function of prestress.

A series of tests has been performed to understand the electromechanical properties of piezoceramics under loading conditions simulating the in-service environment, e.g. driving by a high E-field and operating under a significant compressive preload [1]. Fig. 1 shows the mechanical preload dependence of the piezoelectric performance. The piezoelectric coefficient  $d_{33}$  can be determined by a measure of the uni-polar high field induced strain at different prestress levels. A significant enhancement of the piezoelectric performance is observed within a small prestress range. At much higher preload levels, the mechanical depolarization effect becomes predominant and makes the material exhibit hardly any piezoeffects.

## Ferroelectric and ferroelastic behavior under coupled electromechanical loading

Systematic measurements have been performed to investigate the fundamental ferroelectric and ferroelastic domain switching behavior.

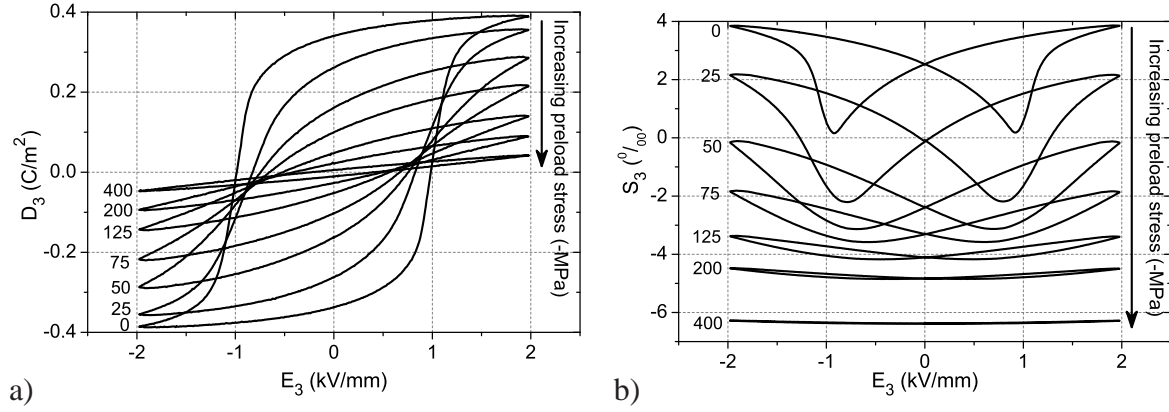


Figure 2: a) Polarization and b) butterfly strain hysteresis loops measured under different compressive stress preloads.

Fig. 2 shows the bipolar, cyclic field induced polarization and butterfly strain hysteresis loops measured over a wide range of compressive stress preloads [2]. The investigation reveals that the superimposed stress reduces the remnant polarization, decreases the coercive field, and also significantly changes the shape and amplitude of the ferroelectric hysteresis curves. With an increase in preload, the hystereses in polarization and strain loops become less and less pronounced, as the compressive stress prevents full alignment of the domains and induces mechanical depolarization.

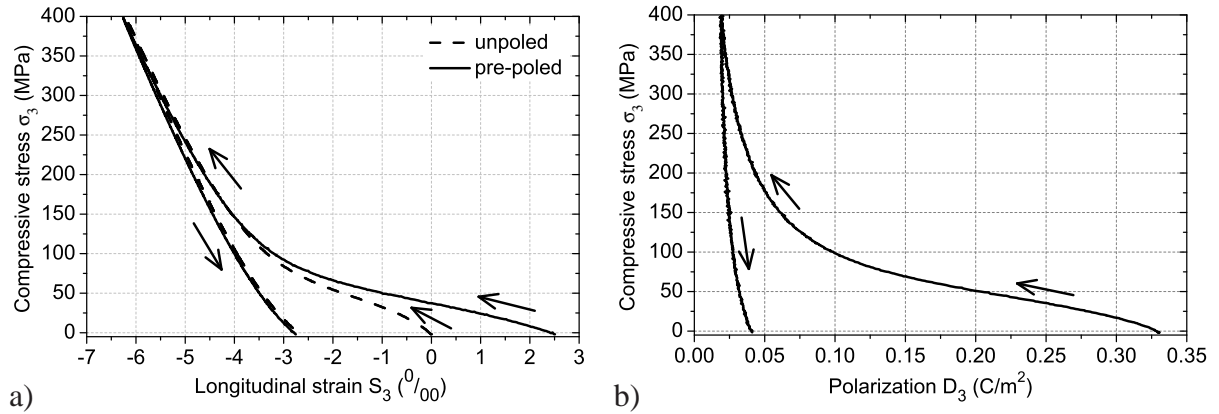


Figure 3: a) Compressive stress-strain curves of initially unpoled and pre-poled specimens; b) Mechanical depolarization of a pre-poled specimen.

The compressive stress-strain and mechanical depolarization curves are shown in Fig. 3. Significant nonlinearity is observed during the period of compression loading. After removing the stress, an irreversible remnant strain is induced. The macroscopic nonlinearity and residual deformation are due to the microscopic ferroelastic domain switching process. The influence of DC bias field on the non-linear ferroelastic behavior has also been studied in detail [3]. A bias field parallel to the initial poling direction has the tendency to maintain the existing domain configuration and inhibit mechanically ferroelastic domain switching, whereas an anti-parallel

bias field acts the other way around. The coercive stress has been found to be linearly dependent on the bias field, increasing with an increase in parallel bias field.

### Multi-axial loading tests

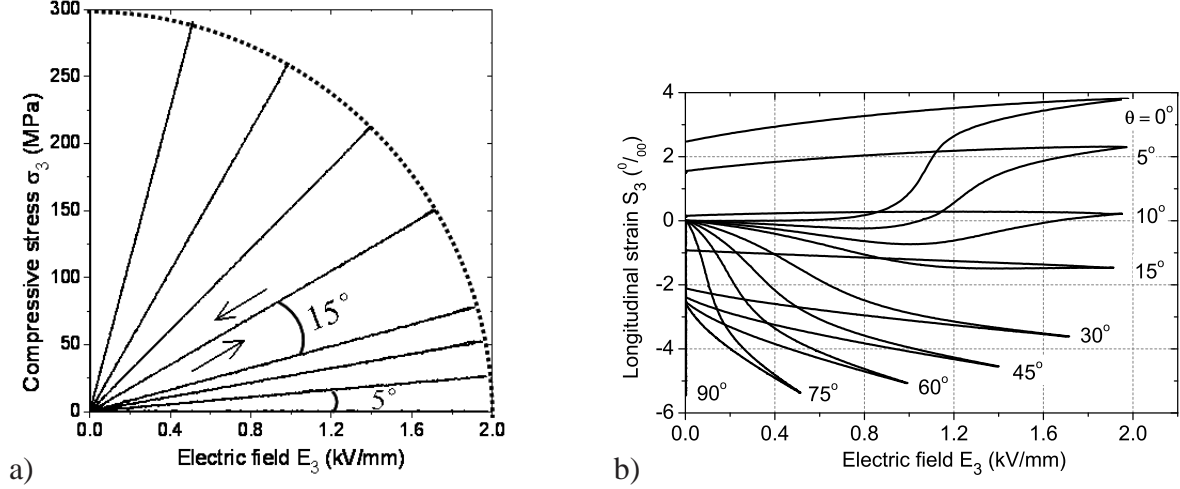


Figure 4: a) Loading paths of coaxial, proportional electromechanical tests; b) Longitudinal strain as a function of electric field, measured with different electric field-stress proportions.

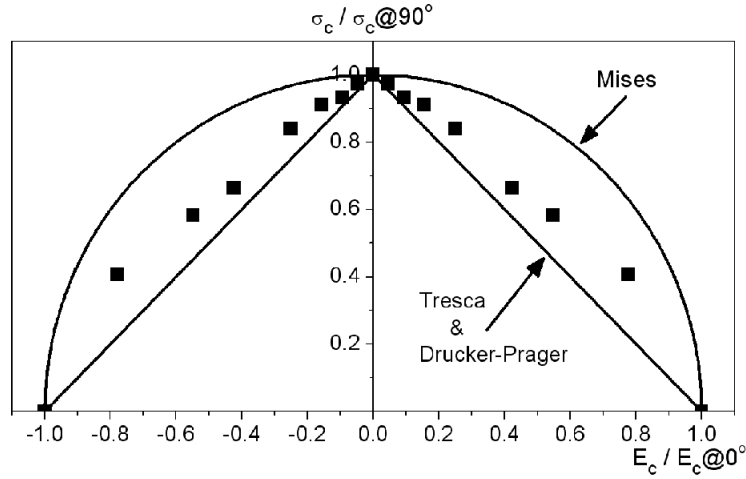


Figure 5: Comparison of switching surface corresponding to an offset of 1 % remanent strain with the Tresca, Drucker-Prager, and Mises prediction criteria.

For the purpose of evaluating the accuracy of existing micromechanical and phenomenological models for ferroelectric switching, systematic polarization and strain measurements have been performed for initially unpoled specimens under coaxial, proportional electromechanical loading [4]. Fig. 4 shows the loading paths and the results of strain measurement. Based on the conventional offset method, initial domain switching surface is constructed in the biaxial electric field-stress space and compared with several criteria existing in the literature. As seen in Fig. 5, the experimental data are found to be close to the Tresca and Drucker-Prager switching condition.

Recently, multi-axial polarization rotation tests have been performed for pre-poled specimens re-loaded by an electric field at an angle to the original poling direction [5]. The anisotropic domain distribution results in significantly different non-linear responses measured

at different angles. In the bi-axial electric field space, polarization and strain measurements gave rise to different domain switching surfaces with respect to size and shape. In contrast to the circular yielding surfaces of an isotropic unpoled specimen, the switching surface obtained from polarization measurement for pre-poled specimens exhibits a distortion in shape and an evident translation in the pre-poling direction. In the case of the strain measurement, an apparent softening with respect to the unpoled state was observed.

It is worthy of noting that the non-linear ferroelectric and ferroelastic behavior of piezoceramics are strongly time-dependent. When subjected to a constant electric field or mechanical stress load, significant creep in both strain and polarization has been observed in experimental investigations [6, 7].

## REFERENCES

- [1] D. Zhou and M. Kamlah, High-field dielectric and piezoelectric performance of soft lead zirconate titanate piezoceramics under combined electromechanical loading, *J. Appl. Phys.* **96**, 6634–6641 (2004).
- [2] D. Zhou, M. Kamlah and D. Munz, Effects of uniaxial prestress on the ferroelectric hysteretic response of soft PZT, *J. Eur. Ceram. Soc.* **25**, 425–432 (2005).
- [3] D. Zhou, M. Kamlah and D. Munz, Effects of bias electric fields on the non-linear ferroelastic behavior of soft lead zirconate titanate piezoceramics, *J. Am. Ceram. Soc.* **88**, 867–874 (2005).
- [4] D. Zhou, Z. Wang and M. Kamlah, Experimental investigation of domain switching criterion for soft lead zirconate titanate piezoceramics under coaxial proportional electromechanical loading, *J. Appl. Phys.* **97**, 084105 (2005).
- [5] D. Zhou, M. Kamlah and B. Laskewitz, Multi-axial non-proportional polarization rotation tests of soft PZT piezoceramics under electric field loading, in *Smart Structures and Materials 2006: Active Materials: Behavior and Mechanics*, edited by William. D. Armstrong, Proceedings of SPIE (SPIE, Bellingham, WA, 2006), **6170**, 617009 (2006).
- [6] D. Zhou and M. Kamlah, Room-temperature creep of soft PZT under static electrical and compressive stress loading, *Acta Mater.* **54**, 1389–1396 (2006).
- [7] D. Zhou and M. Kamlah, Determination of room-temperature creep of soft lead zirconate titanate piezoceramics under static electric fields, *J. Appl. Phys.* **98**, 104107 (2005).

# Traveling wave solutions for phase field models for diffusionless phase transitions in ferroelectrics

## H.-D. Alber and Peicheng Zhu

In recent years the authors have developed a program for the formulation of phase field models for diffusionless phase transitions in solids, which for example occur in ferroelectric materials at domain boundaries. The formulation of the models is based on ideas, which extend far beyond the modelling of the evolution of diffusionless phase transitions. They are applicable to the modelling of interface motion by interface diffusion, crack propagation and the evolution of dislocations in metals.

In the talk I show how to construct traveling wave solutions of the phase field model and explain the model properties at the behavior of these traveling wave solutions. These traveling wave solutions show that the solutions of the phase field model converge to solutions of the sharp interface model if a parameter of regulation tends to zero.

Moreover, I compare the behavior of these traveling wave solutions to the behavior of traveling wave solutions for the Allen-Cahn and Chan-Hilliard model, which model diffusion dominated phase transformations.

## References

- [1] H.-D. Alber: Evolving microstructure and homogenization. *Continuum Mech. Thermodyn.* **12** (2000), 235-287.
- [2] H.-D. Alber, Peicheng Zhu: Solutions to a Model with nonuniformly parabolic terms for phase evolution driven by configurational forces. *SIAM J. Appl. Math.* **66,2** (2006), 680-699.
- [3] H.-D. Alber, Peicheng Zhu: Evolution of phase boundaries by configurational forces. *Archive for Rational Mechanics and Analysis*, in press.
- [4] H.-D. Alber, Peicheng Zhu: Solutions to a model for interface motion by interface diffusion. Submitted to *Proc. Royal Soc. Edinburgh A*.

# Theory and computation of a micro - macro monocrystalline model for martensitic phase transformation at finite strains

Erwin Stein and Gautam Sagar

Institute of Mechanics and Computational Mechanics  
Leibniz University of Hannover Appelstrasse 9A Hannover  
E-mail: stein@ibnm.uni-hannover.de; sagar@ibnm.uni-hannover.de

## Abstract

The presentation is based on the theory with linear kinematics by Govindjee and Miehe (2001) with computational extension by Stein and Zwickert (2006). A major theoretical and numerical difficulty in this paper is the quasi-convexification of the finite deformation phase transformation problem for arbitrary many phase variants,  $n = 1, 2, 3, \dots$ . A lower bound of the mixing energy for arbitrary many variants is provided by the Reuß bound in case of linear kinematics proven by Govindjee, Mielke and Hall (2003). An approximation of free energy of mixing for finite strains using also the Reuß bound is presented here which generally yields a lower bound for  $n \leq 2$ , Stein and Sagar (2006).

Abaqus is used for implementation of 3D finite elements in space, via UMAT-interface for integrating the phase evolution rule in time which requires Jaumann rate of Cauchy stresses. Deterministic validation of the used micro-macro material model is presented by comparing verified numerical results with experimental data for  $\text{Cu}_{82}\text{Al}_{14}\text{Ni}_4$  monocrystals for quasiplastic phase transformation, provided by Xiangyang et al. (2000). Improvement of numerical results at finite strains compared with linearized strains is emphasized.

## 1 Introduction

Martensitic phase transformation (PT) is a diffusionless first-order PT between 'high' temperature austenite and 'low' temperature martensitic phases of shape memory alloys (SMAs). The specific feature of martensitic phase transformations (PTs) is the ability of SMAs to 'remember' their initial state. We investigate the following PT cycle: 1.) Micro deformation from austenite to twinned and further to detwinned martensite,  $A \rightarrow M_{detw}$ , by cooling (which is not visible in computation), followed by elastic deformation due to mechanical loading at equilibrium temperature  $\theta_0$ ,  $\theta_0 = (A_s + M_s)/2$ , ( $A_s$ : austenite start temperature,  $M_s$ : martensite start temperature,  $\theta_0 < A_f$ ,  $A_f$ : austenite finish temperature); 2.) fast quasi-plastic PT at a critical stress at  $M_f$ ,  $M_f \approx \theta_0$  ( $M_f$ : martensite finish temperature); 3.) elastic unloading at  $\theta_0$ ; and finally 4.) back-PT to austenite,  $M \rightarrow A$ , by heating up to second critical temperature  $\theta_{crit}$ ,  $\theta_{crit} > A_f$  ( $A_f > A_s$ ). This fourth step characterizes the shape memory effect (SME).

Different from SME, superelastic PT (called SE) takes place for certain SMAs if the back transformation takes place within the unloading process without external heating.

## 2 A unified micro-macro mathematical model for phase transformation of monocrystals

The micro-macro PT material model based on Cauchy-Born hypothesis and the concept of habit planes as proposed by Patoor et al. (1995), presented by Govindjee and Miehe (2001) and computationally extended by Stein and Zwickert (2006) at small strains for multiple phase variants is extended to finite strain kinematics, Stein and Sagar (2006). The mathematical model is based on the multiplicative decomposition of the total deformation gradient  $\mathbf{F}$  into elastic  $\mathbf{F}^e$  and transformation part  $\mathbf{F}^t$ . The Neo-Hookean hyperelastic material model is used. Mass conservation with respect to phase fractions on the micro scale has the same form as in linear kinematics. The concept of quasi-convexified free energy is used for monocrystalline shape memory alloys in order to get the  $C^1$ -continuous macroscopic constitutive model at large strains where transformation strains during phase transition can reach up to 15% according to available experimental data.

The extension of the total free energy by a Lagrangian functional  $\mathcal{L}$  accounts for kinematic constraints and mass conservation of the material with martensitic PT cycles under cooling, mechanical loading and heating. Stress tensor, phase transformation vector and vector of thermodynamical forces are obtained in a canonical way as partial derivatives of  $\mathcal{L}$  with respect to the conjugate field variables. The PT-criteria together with the evolution law for internal variables ( $\boldsymbol{\xi}$  = phase transformation vector,  $\lambda$  = strain-controlled load factor,  $\delta$  = Lagrangian parameter for mass conservation and  $\boldsymbol{\gamma}$  = partial phase energy vector) completes the PT model.

### 2.1 Free energy and thermodynamical forces

Based on the assumption by Ball and James (1987) the macroscopic free strain energy of a crystal is given by the minimum of the energies of all possible i.e. compatible  $n$  phase variants,

$$\Psi = \min_{i=1..n} [\psi_i^{el}(\mathbf{b}_i^e, J_i^e) + \psi_i^{ch}] , \quad (1)$$

where  $\mathbf{b}_i^e = \mathbf{F}(\mathbf{U}_i^t)^2)^{-1}\mathbf{F}^T$  is elastic left Cauchy-Green deformation tensor, with PT stretch tensor  $\mathbf{U}_i^t$  for phase  $i$ .  $\psi_i^{ch}$  is the so-called chemical energy of the  $i$ -th phase variant. The phase variants are described through internal variables. The added constraints concern the explicit 'mass' conservation of the phases and positiveness of phase fractions, eq. (5).

Using Gibbs mixture potential and applying Legendre transformation yields the explicit form of the quasi-convexified free energy for linearized elasticity, Govindjee et al. (2003), by a supremum condition as

$$\Psi(\boldsymbol{\epsilon}, \boldsymbol{\xi}) = \boldsymbol{\xi} \cdot \boldsymbol{\psi}(\boldsymbol{\epsilon}) + \Psi_{LS}^M(\tilde{\boldsymbol{\epsilon}}^t, \boldsymbol{\xi}) , \quad (2)$$

where  $\tilde{\boldsymbol{\varepsilon}}^t$  is the phase transformation strain tensor and  $\Psi_{LS}^M(\tilde{\boldsymbol{\varepsilon}}^t, \boldsymbol{\xi})$  is the mixed representation of the convexified free energy for linear strains.

Similarly, the extension of the vector of quasi-convexified free energies for the phase fractions from small to finite strains,  $\Psi(\boldsymbol{\varepsilon}, \boldsymbol{\xi}) \longrightarrow \Psi(\mathbf{b}, \boldsymbol{\xi})$ , reads,

$$\Psi(\mathbf{b}, \boldsymbol{\xi}) = \boldsymbol{\xi} \cdot \boldsymbol{\psi}(\mathbf{b}) + \Psi_{FS}^M(\mathbf{b}^t, \boldsymbol{\xi}), \quad (3)$$

with the vector of phase fractions  $\boldsymbol{\xi} = \sum_{i=1}^n \xi_i \mathbf{e}_i$ ,  $\mathbf{e}_i \cdot \mathbf{e}_j = \delta_{ij}$  (1 austenite phase and n-1 martensitic phases), the mass conservation condition that all scaled phases have to sum up to 1 ( $\Rightarrow \mathbf{e}^* \cdot \boldsymbol{\xi} - 1 = 0$ ,  $\mathbf{e}^*$  the normal vector of the (n-1)-dimensional PT-polytope,  $\mathbf{e}^* = \sum_{i=1}^{n-1} \mathbf{e}_i^* \mathbf{e}_i$ ,  $\mathbf{e}_i^* \cdot \mathbf{e}_i = 1$ ) where the phase fractions have to be positive semi-definite ( $\Rightarrow \xi_i \geq 0$ ) and  $\mathbf{b}^t$  is PT left Cauchy-Green tensor.  $\boldsymbol{\psi}$  is the vector of phase energies with

$$\boldsymbol{\psi}(\mathbf{b}) = \sum_{i=1}^n \psi_i(\mathbf{b}_i, \boldsymbol{\xi}) \mathbf{e}_i, \quad \mathbf{e}_i \in \mathbb{R}^n \text{ and } \boldsymbol{\psi} \in \mathbb{R}^n. \quad (4)$$

$\Psi_{FS}^M(\boldsymbol{\xi})$  follows from a mixed representation of the approximated convexified free energy for finite strains.

The presence of kinematic constraints of the material suggests the enhancement of the free energy function, eq. (3), by a Lagrangian functional now presented as

$$\mathcal{L}(\mathbf{b}, \boldsymbol{\xi}, \boldsymbol{\gamma}, \delta) = \Psi(\mathbf{b}, \boldsymbol{\xi}) - \boldsymbol{\gamma} \cdot \boldsymbol{\xi} + \delta(\mathbf{e}^* \cdot \boldsymbol{\xi} - 1), \quad (5)$$

with the vector  $\boldsymbol{\gamma}$  and the scalar  $\delta$  as Lagrangian multipliers for n phases fulfilling the Kuhn-Tucker conditions of the saddle point problem

$$\gamma_i \geq 0, -\xi_i \leq 0; i = 1 \text{ to } n \text{ and } \boldsymbol{\gamma} \cdot \boldsymbol{\xi} = 0. \quad (6)$$

The extension of the free energy to a Lagrangian functional is called 'unified model', as introduced by, e.g., Patoor et al. (1995) for a two-phase material.

The energy dissipation condition for the driving force (thermodynamical conjugate force)  $\mathbf{f} = \partial \mathcal{L} / \partial \boldsymbol{\xi}$  and a local maximum dissipation principle reads

$$\mathcal{D} = \mathbf{f} \cdot \dot{\boldsymbol{\xi}} \geq 0, \quad \mathbf{f} \cdot \dot{\boldsymbol{\xi}} \rightarrow \text{Max}. \quad (7)$$

With analogies to the theory of stable inelastic deformations in elastoplasticity it is deduced that the 'transformation function'  $\phi$  has to be convex (similar to a convex yield function)

$$\phi = \|\mathbf{f}\| - f_c \leq 0, \quad (8)$$

with the critical driving force  $f_c$  as an energy barrier for initiating PT.

## 2.2 Free elastic energy of hyperelastic material model

Consistent with the assumption of elastic and thermal isotropy the stored split elastic energy for  $i$ -th phase  $\psi_i^{el}$  reads

$$\psi_i^{el}(\mathbf{b}_i^e, J_i^e) = W_i(J_i^e) + \overline{W}_i(\overline{\mathbf{b}}_i^e), \quad (9)$$

with the deviatoric part of elastic left Cauchy-Green tensor  $\overline{\mathbf{b}}_i^e := J_i^{e-2/3} \mathbf{F}_i^e \mathbf{F}_i^{eT}$ , where  $W_i : \mathbb{R}_+ \rightarrow \mathbb{R}_+$ .  $W_i\{0\}$  is a convex function of  $J_i^e := \det \mathbf{F}_i^e$ .  $W_i(J_i^e)$  and  $\overline{W}_i(\overline{\mathbf{b}}_i^e)$  are the volumetric and deviatoric parts of  $\psi_i^{el}$ , respectively. The following explicit forms are considered

$$\boxed{\begin{aligned} W_i(J_i^e) &:= \frac{1}{2} \kappa \left[ \frac{1}{2} (J_i^{e2} - 1) - \ln J_i^e \right], \\ \overline{W}_i(\overline{\mathbf{b}}_i^e) &:= \frac{1}{2} \mu (\text{tr}[\overline{\mathbf{b}}_i^e] - 3) \end{aligned}} \quad (10)$$

where  $\mu$  and  $\kappa$  are the shear modulus and bulk modulus for linearized strains, respectively.

## 2.3 Free energy of mixing at finite strains

The problem of quasi-convexification at finite strains is treated here by starting with the explicit form of the lower Reuss bound for small strains given by Govindjee et al. (2003).

The extension of the free energy of mixing from small to finite strains,  $\Psi_{LS}^M(\tilde{\boldsymbol{\varepsilon}}^t, \boldsymbol{\xi}) \rightarrow \Psi_{FS}^M(\mathbf{b}^t, \boldsymbol{\xi})$ , for hyperelastic material with convex stress-strain function reads

$$\Psi_{FS}^M(\mathbf{b}^t, \boldsymbol{\xi}) \approx - \sum_{i=1}^n \xi_i \psi_i^t(\mathbf{b}_i^t, J_i^t) + \sum_{i=1}^n \sum_{j=1}^n p_{ij}(\mathbf{b}_i^t, \mathbf{b}_j^t) \xi_i \xi_j \boldsymbol{\sigma}_i^t(\mathbf{b}_i^t, J_i^t) : \left[ \frac{1}{2} \ln(\mathbf{b}_j^t) \right], \quad (11)$$

where  $p_{ij} \in \mathbb{R}, i \neq j$  are scalar integration factors and account for the non-linearity of the stress-strain functions; they can be determined for each given pair of left Cauchy-Green PT strain tensors  $\mathbf{b}_i^t$  and  $\mathbf{b}_j^t$  according to the condition

$$p_{ij} \boldsymbol{\sigma}_i^t(\mathbf{b}_i^t) : \frac{1}{2} \ln(\mathbf{b}_j^t) \stackrel{!}{=} \int_{\mathbf{b}_j^{*t}=1}^{\mathbf{b}_j^t} \boldsymbol{\sigma}_i^t(\mathbf{b}_i^{*t}) : d \left( \frac{1}{2} \ln(\mathbf{b}_j^{*t}) \right), \quad (12)$$

$\psi_i^t(\mathbf{b}_i^t, J_i^t)$  is the PT energy with non-linear kinematics which takes the form of eq. (9) and  $\boldsymbol{\sigma}_i^t(\mathbf{b}_i^t, J_i^t)$  Cauchy PT-stress for phase  $i$ . If the variables  $\mathbf{b}_i^{*t}$  and  $\mathbf{b}_j^{*t}$  are not depending on each other we directly get  $p_{ij} = 1$  for  $i \neq j$ . With this restrictive assumption the lower bound still holds for finite strains which have size of up to 15% in practical cases if additional instabilities of energy wells due to kinematic non-linearity are excluded.

The approximation of free energy of mixing,  $\Psi_{FS}^M(\mathbf{b}^t, \boldsymbol{\xi})$ , for a 2-phase system (1 means austenite, 2 means martensite) follows from eq. (11) as

$$\Psi_{FS}^M(\mathbf{b}^t, \boldsymbol{\xi}) \approx -\xi_2 \psi_2^t(\mathbf{b}_2^t, J_2^t) + \xi_2 \xi_2 \psi_2^t(\mathbf{b}_2^t, J_2^t), \quad (13)$$

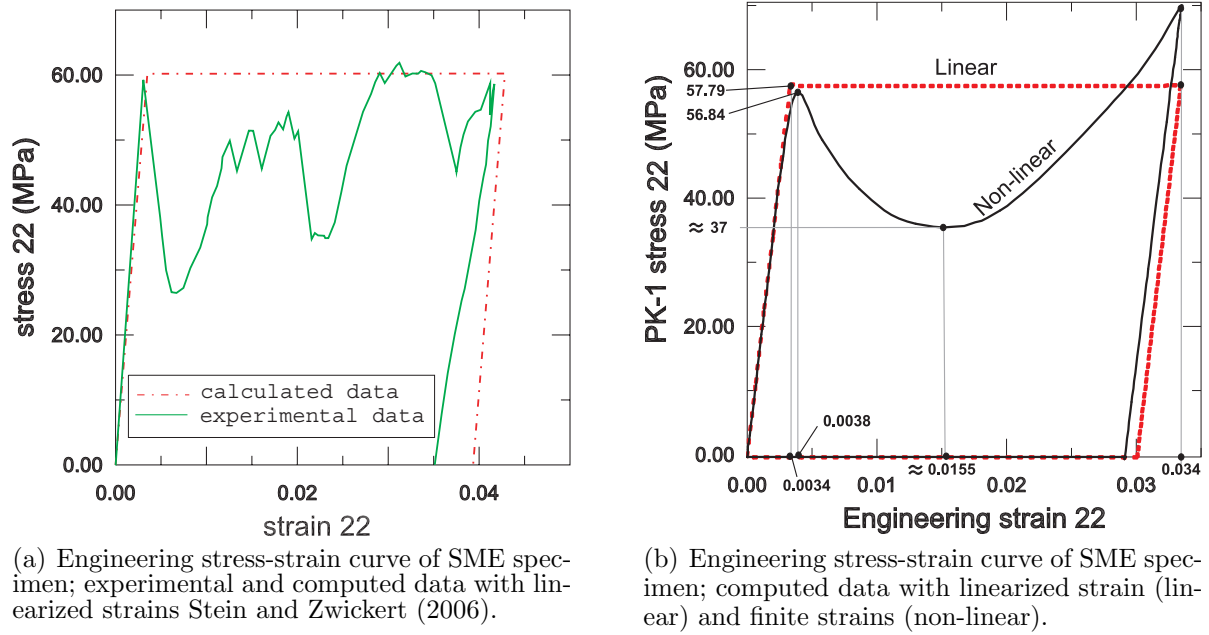


Figure 1: Comparisons of experimental and computed engineering stress-strain data.

because  $\mathbf{b}_1^t = \mathbf{1}$ ,  $\frac{1}{2} \ln(\mathbf{b}_1^t) = \mathbf{0}$  and  $\psi_1^t(\mathbf{b}_1^t, J_1^t) = 0$ . Therefore, the integration factors  $p_{ij}$  do not influence quasi-convexification for 2-phase system what essentially simplifies the achievement of the minimum property, eq. (1).

In PT process of  $\text{Cu}_{82}\text{Al}_{14}\text{Ni}_4$  treated here only martensitic phase number 6 is active beside the austenitic parent phase i.e. in total two phases. Therefore, the lower bound problem of mixing energy holds anyway.

The detailed discussions on stress response, algorithmic tangent and implementation in Abaqus are given in Stein and Sagar (2006).

### 3 Verification and validation of mathematical PT-model

The material model was implemented into Abaqus via UMAT-interface which requires Jaumann rate of Cauchy stresses. Model validation for one loading type is done in a deterministic way by comparing the experimental data for  $\text{Cu}_{82}\text{Al}_{14}\text{Ni}_4$  monocrystals obtained by Xiangyang et al. (2000) with verified computational results, using three regularly refined hexahedral B-bar finite element meshes (with 48, 56 and 176 elements) as well as automatic time stepping.

Comparison of experimental stress-strain behavior of SME-specimen with the numerically obtained data at linearized PT strains is shown in fig. 1a and comparison of numerical stress-strain behavior at finite PT strains with such for linearized strains is presented in fig. 1b, both for full SME-PT cycles (loading as well as elastic unloading

at equilibrium temperature and heating).

Different from linear theory, the presented theoretical model and finite element computations are able to describe the average decrease and increase of experimental stresses within the PT process after reaching the critical stress. Fig. 1a,b show that PK1-transformation-stress with non-linear kinematics is 1.6% less than with linear kinematics, and approximately 2% less than the experimentally measured stress. The residual PT strains after elastic unloading for non-linear kinematics are smaller by 3% than those with linear strain.

The numerical results of the finite strain PT-model are capturing more detailed information for stress-strain behavior during quasiplastic PT. The zigzag type experimental stress-strain curve within phase transformation at loading, called 'yield tooth', is approximated within the finite element analysis by a smoothly decreasing and then increasing axial stress - axial strain curve which could not be achieved with linearized kinematics yielding a constant axial stress during PT, as given in Stein and Zwickert (2006) and also presented here for comparison, fig. 1a. The presented model can also be used for simulation of superelastic PT-effect.

## References

- J. M. Ball and R. D. James. Fine phase mixtures and minimizers of energy. *Archive for Rational Mechanics and Analysis*, 100(1):13–52, 1987.
- S. Govindjee and C. Miehe. A multi-variant martensitic phase transformation model: formulation and numerical implementation. *Computer Methods in Applied Mechanics and Engineering*, 191(3–5):215–238, 2001.
- S. Govindjee, A. Mielke, and G. J. Hall. The free energy of mixing for n-variant martensitic phase transformations using quasi-convex analysis. *Journal of the Mechanics and Physics of Solids*, 51(4):I–XXVI, 2003.
- E. Patoor, A. Eberhardt, and M. Berveiller. Micromechanical modelling of superelasticity in shape memory alloys. *Journal de Physique IV*, (C8-5):277–292, 1995.
- E. Stein and G. Sagar. Theory and finite element computation of cyclic martensitic phase transformation at finite strain. *International Journal for Numerical Methods in Engineering*, in review, 2006.
- E. Stein and O. Zwickert. Theory and finite element computations of a unified cyclic phase transformation model for monocrystalline materials at small strain. *Computational Mechanics*, online printed first: 17 pages, 2006.
- Z. Xiangyang, S. Qingping, and Y. Shouwen. A non-invariant plane model for the interface in CuAlNi single crystal shape memory alloys. *Journal of the Mechanics and physics of solids* 48, 2163–2182, 2000.